THE UNIVERSITY
of ADELAIDE

Development of dual-wavelength pumped mid-infrared fibre laser

by

Ori Henderson-Sapir

Supervisors:
Dr. David J. Ottaway
Prof. Jesper Munch

A thesis submitted in fulfilment of the
degree of Doctor of Philosophy

in the
Faculty of Science
School of Physical Sciences

July 2015

Declaration of Authorship

I, Ori Henderson-Sapir, declare that this thesis titled 'Development of dual-wavelength pumped mid-infrared fibre laser' and the work presented in it are my own. I confirm that:

- This work contains no material which has been accepted for the award of any other degree or diploma in any university or other tertiary institution to Ori Henderson-Sapir and, to the best of my knowledge and belief, contains no material previously published or written by another person, except where due reference has been made in the text. In addition, I certify that no part of this work will, in the future, be used in a submission in my name for any other degree or diploma in any university or other tertiary institution without the prior approval of the University of Adelaide and where applicable, any partner institution responsible for the joint award of this degree.

- I give consent to this copy of my thesis, when deposited in the University Library, being made available for loan and photocopying, subject to the provisions of the Copyright Act 1968.

- I acknowledge that copyright of published works contained within this thesis (as listed below) resides with the copyright holder(s) of those works.

- I also give permission for the digital version of my thesis to be made available on the web, via the University's digital research repository, the Library Search, the Australasian Digital Theses Program (ADTP) and also through web search engines, unless permission has been granted by the University to restrict access for a period of time.

Signed:

_____

Date:

_____

For **Annetay**, *who deserves a PhD in patience.*

THE UNIVERSITY OF ADELAIDE

Abstract

Faculty of Science
School of Physical Sciences

Doctor of Philosophy

by Ori Henderson-Sapir

THERE is an urgent need for efficient and compact sources of coherent mid-infrared wavelength radiation (3-5 μm). Cost-effective and bright mid-infrared sources will lead to exciting new sensing applications, ranging from the remote sensing of greenhouse gases, such as CO_2 and methane, to analysis of trace gases in exhaled breath for disease marker identification.

The last decade has seen a continuing increase in the output power of various types of mid-infrared sources, such as optical parametric oscillators and amplifiers, quantum cascade lasers and fibre lasers. However, advances in brightness, efficiency, peak power and tunability are still necessary for many applications.

In this thesis, we describe a new concept for a fibre laser based on Er^{3+} doped ZBLAN glass that operates in the mid-infrared with lasing centred around 3.5 μm. We used a novel dual-wavelength pumping (DWP) scheme to achieve world-leading efficiency for this material and an output power of 260 mW.

The DWP technique uses long-lived excited states in our Er^{3+} ion doped ZBLAN glass gain medium to improve the Stokes efficiency. A low power, 985 nm pump source excites ions from the $^4I_{15/2}$ ground state to the long lived $^4I_{11/2}$ state. A large fraction of the ion population can be stored in this level because of its long lifetime, creating a "virtual ground state." A concurrent 1973 nm pump source is then used as the main pump source. This pump excites the ions further to the upper laser level $^4F_{9/2}$. Post lasing, the 1973 nm pump cycles the ions between the "virtual ground state" at $^4I_{11/2}$ and the $^4F_{9/2}$ level. The first pump at 985 nm maintains the population in the "virtual ground" as this population is diminished by spontaneous emission and energy-transfer processes, which eject ions from the lasing cycle.

In this thesis, we review the literature and the current state-of-the-art in mid-infrared fibre lasers. An overview of the spectroscopic properties of Er^{3+}:ZBLAN relevant to mid-infrared operation is presented. The difficulties and issues associated with the creation of mid-infrared radiation are discussed and our spectroscopic investigations of ZBLAN glass and glass fibres are summarised.

Multiple wavelengths were used as pump sources for our DWP laser. Our investigation of the optimal wavelength for the DWP technique and the development of suitable sources is described as well. The 3.5 μm laser system is discussed, including the full characterisation of the laser. The thesis is concluded with a summary of the results and an outlook for the future.

Acknowledgements

First and foremost, I would like to thank my supervisors David Ottaway and Jesper Munch. Without their guidance and advice this work would not have been possible.

During my PhD, I had the pleasure of working with a great bunch of people. The academics and students from the Optics Group, Alex Dinovitser, Andrew Malouf, David Hosken, Eleanor King, Huichao Luo (Nicky), Ka Wu, Keiron Boyd, Matt Heintze, Miftar Ganja, Murray Hamilton, Myles Clark, Muddassar Naeem, Nick Chang, Nikita Simakov, Peter Veitch and Sophie Hollit, were always available and happy to lend a hand or equipment and to provide advice.

Many others within the Institute for Photonics and Advanced Sensing (IPAS) have also helped along the way with advice and equipment including: Alexandre Frabcois, Andre Luiten, Andrew Richardson, Chris Kalnins, Chris Perella, Dale Godfrey, David Lancaster, Elodie Janvier, Eric Schartner, Fiorina Piantedosi, Georgios Tsiminis, Heike Ebendorff-Heidepriem, Herbert Fu, James Anstie, Kevin Kuan, Kristopher Rowland, Matt Henderson, Michael Oermann, Nigel Spooner, Olivia Towers, Philip Light, Piers Lincoln, Richard White, Sara Leggatt, Sean Manning, Sebastian Ng, Shahraam Afshar, Tanya Monro and Tilanka Munasinghe.

Special thanks are due to the School of Physical Sciences professional staff who were always there to help: Adrian Giffen, Adrian Selby, Alastair Dowler, Blair Middlemiss, Bob Chivell, Carol Maelzer, Jeanette Roulston, John Cameron, Katie Burton, Mary Odlum, Trevor Waterhouse, Ramona Adjoran, Sharon Leech, Neville Wild, Wayne England and Wendy Brown.

Last but not least is my family who was always there for me, my parents Aya and Yossi Sapir, my brother Yoav and sister Tali and Barbara, Bill and Benjamin Henderson, who always believed in me and provided encouragement and support. I am thoroughly indebted to all of you, for long phone conversations and your physical presence in Australia during some difficult times. Finally, I would like to thank my wife, partner and friend, Annetay, for her enduring love and support throughout this long journey. Without her I would have never made it to the finish line.

Thank you.

Contents

List of Figures

List of Tables

Abbreviations

Abbreviation	Meaning
AM	**A**mplitude **M**odulation
AR	**A**nti-**R**eflective
ASE	**A**mplified **S**pontanous **E**mission
BPF	**B**and **P**ass **F**ilter
CaF$_2$	**C**alcium **F**luoride
CW	**C**ontinous **W**ave
CR	**C**ross-**R**elaxation
DUT	**D**evice **U**nder **T**est
DWP	**D**ual-**W**avelength **P**umping
EDFA	**E**rbium **D**oped **F**ibre **A**mplifier
Er	**E**rbium
ESA	**E**xcited **S**tate **A**bsorption
ET	**E**nergy **T**ransfer
ETU	**E**nergy-**T**ransfer-**U**pconversion
FBG	**F**ibre **B**ragg **G**rating
FTIR	**F**ourier **T**ransform **I**nfra**R**ed
GSA	**G**round **S**tate **A**bsorption
HeNe	**H**elium **Ne**on
HR	**H**ighly **R**eflective
InGaAs	**I**ndium **G**alium **A**rsenide
InSb	**I**ndium **S**tibium (antimonide)

LD	**L**aser **D**iode
LIA	**L**ock **I**n **A**mplifier
LPF	**L**ong **P**ass **F**ilter
MIR	**M**id **I**nfra**R**ed
MP	**M**ulty **P**honon
NA	**N**umerical **A**perture
OAP	**O**ff-**A**xis **P**arabola
PbSe	**P**lumbum (lead) **S**elenide
RE	**R**are-**E**arth
SBS	**S**timulated **B**rillouin **S**cattering
SE	**S**timulated **E**mission
Si	**S**ilicon
SCS	**S**uper **C**ontinuum **S**ource
SRS	**S**timulated **R**aman **S**cattering
TEC	**T**hermo **E**lectric **C**ooler
Tm	**T**hulium
TFL	**T**hulium **F**ibre **L**aser
TTL	**T**ransistor **T**ransistor **L**ogic
ZBLAN	**Z**irconium **B**arium **L**anthanum **A**luminium **N**atrium (sodium)

Symbols

Symbol	Meaning
A_{clad}	Inner cladding area of a double-clad fibre
A_{core}	Area of fibre core
A_{ed}, A_{md}	Electric and magnetic dipole transitions radiative rates
A_{ij}	Radiative decay rate from level i to level j
A_r, A_{nr}, A_m	Radiative, non-radiative and measured decay rates of an energy level
b_i	Boltzmann factor for level energy i
c	Speed of light
C	Material dependant constant
C_s	Number of Stark levels in manifold
dl	Discretisation length of a fibre
e	Charge of electron
E, E_0	Absorbance and background absorbance
E_{ij}	Energy difference between each Stark level to the lowest Stark level of the same manifold
E_{s0}	Separation between the lowest Stark levels of two manifolds
f_{pump}, f_{probe}	Pump and probe beam modulation/chopping frequencies
g_0	Small signal gain coefficient
g_i	Degeneracy of level i
h	Planck constant

h_c Convective heat transfer coefficient

I_0 Launched intensity

$I_{1973nm\,with\,pump}(\lambda_2)$, $I_{1973nm}(\lambda_2)$ Transmitted intensity of the 1973 nm band light with and without pump

I_{in} Incident intensity

$I_{incident\,800nm}(\lambda_1)$ Incident 800 nm band intensity on fibre

I_{out} Transmitted intensity

$I_{out\,800nm\,pump}(\lambda)$, $I_{out800nm}(\lambda_1)$ 800 nm band light intensity transmitted through the fibre with and without pump

I_s Saturation intensity

I_{single}, I_{double} Fluorescence intensity from a single or double pass along a pumped fibre

I_u, I_p Transmitted probe beam intensity in the unpumped and pumped cases

I_z Fluorescence intensity at location z along the fibre

J Total angular momentum

K Host dependant constant

K_s Slope of curve

k_B Boltzmann constant

k_i Thermal conductivity of layer i

l Fibre length

LS Host-independent reduced matrix parameters for specific dopant specie

Δl Segment of fibre

m_e Mass of electron

n Refractive index

n_{inv}, $n_{inv\,th}$	Inversion average density and average density at laser threshold
$\hat{n}$	Parameter based on refractive index used in Judd-Ofelt analysis
$N_{^4I_{9/2}}$, $N_{^4I_{11/2}}$, $N_{^4I_{13/2}}$	Ion population density at the $^4I_{9/2}$, $^4I_{11/2}$ and $^4I_{13/2}$ levels
NA_b	Numerical aperture of cladding of fibre
N_e, $N_{excited}$	Total excited ion population
$\overline{N_e}$	Average over fibre of excited ion density
N_g, N_{ground}	Ground state population
$N_{ground\,with\,pump}$	Ground state population when pump is on
N_{Higher}	Population density of all excited states combined
N_i	Population density at energy level i
$N_i(z)$	Population density at energy level i at position z along a fibre
N_{Er}	Doping density
N_l, N_u	Partition function of lower and upper laser level manifolds
p	Number of phonons
P	Power
P_1	Power of first pump source
P_2	Power of second pump source
P_{abs}, P_l	Absorbed and launched pump power
P_{ed}, P_{md}	Calculated electric and magnetic dipole oscillator strength
P_{exp}	Measured dipole oscillator strength
$P_{in_i}(z, \lambda)$	Launched power of pump i at position z along the fibre and wavelength λ
$P_{inc_i}(\lambda)$	Incident power of pump i at wavelength λ

P_{out}	Laser output power
P_{sat}	Pump saturation power
P_{th}	Pump power at laser threshold
R, R_1, R_2	Mirror reflectivity
R'_1, R'_2	Equivalent reflectivity
R_F	Fresnel reflection
Q_0	Heat load density
r_{core}	Radius of fibre core
$R_{P_1\,GSA}$, $R_{P_1\,ESA}$	Ground and excited-state absorption rate of the first pump
$R_{P_2\,ESA}$	Excited-state absorption rate of the second pump
$R_{SE\,ij}$	Stimulated emission rate from level i to level j
T	Temperature
T_0	Temperature at centre of fibre core
T_c	Temperature of coolant
$T_I(r)$, $T_II(r)$	Temperature in regions I and II at radial coordinate r relative to centre of fibre core
$\|U^{(t)}\|$	Host-independent reduced matrix parameters for specific dopant type
$V_{v\,core}$	Doped core volume
$V_{\#\,core}$	Normalised frequency (V-number) of the fibre core
W_{ij}	Rate of two ion cross-relaxation or energy-transfer upconversion process involving ions from energy levels i and j
$W_{MP}(T)$	Multi-phonon rate
W_P	Pump rate
$W_{P_{GSA}}$, $W_{P_{ESA}}$	Ground state and excited-state absorption pump rates

α	Absorption coefficient
α', α''	Host dependant constants
α_c, α_d	Absorption coefficient in the core and cladding of a fibre (in cm^{-1})
$\alpha_{cdB/m}$	Absorption coefficient in the core (in dBm^{-1})
$\alpha_{eff_i}(z, \lambda)$	Effective absorption coefficient of pump i in the cladding of a fibre, at position z along the fibre and wavelength λ
β_{ij}	Branching ratio from level i to level j
γ	Inversion factor
δ	Cavity losses coefficient
ΔE	Energy gap
ΔT	Temperature difference
ϵ	Net free energy difference between the manifolds of two energy levels
η	Efficiency coefficient
η_B	Overlap coefficient between laser and pump modes
η_{in_i}	Launch efficiency of pump i
$\eta_{internal}$	Laser internal slope efficiency i
η_{op2op}	Optical-to-optical efficiency of a dual-wavelength pumped laser
η_s	Laser slope efficiency
η_{St}	Stokes efficiency (Quantum defect)
$\eta_{NR,GSA}$, $\eta_{NR,ESA}$	Fractions of energy lost to heat with every ground-state or excited-state absorption transition
$\eta_{R\,GSA}(\lambda)$, $\eta_{R\,ESA}(\lambda)$	Fractions of ions undergone ground-state and excited-state absorption transition

η_Q	Quantum efficiency
$\eta_{Q_{pump}}$	Fraction of absorbed pump power that is deposited as heat in the fibre
λ	Wavelength
λ_b	Absorption band barycentre
λ_{pi}	Wavelength of pump i
$h\nu_{max}$	Maximum phonon energy
ν_b	Absorption wavenumber barycentre
ν_{Laser}	Laser frequency
$\sigma_{800nm}(\lambda_1)$	Ground state absorption cross-section at a certain wavelength within the 800 nm band
$\sigma_{ESA\,1970nm}(\lambda_2)$	Excited-state absorption cross-section at a certain wavelength within the 1973 nm band
σ_{abs}	Absorption cross-section
σ_e	Emission cross-section
$\sigma_{ESA_{4_{I_{13/2}}}}(\lambda_1),$ $\sigma_{ESA_{4_{I_{11/2}}}}(\lambda_1)$	Excited-state absorption of 800 nm band light on the $^4I_{13/2} \rightarrow {}^2H_{11/2}$ and $^4I_{11/2} \rightarrow {}^4F_{3/2}$ transition, respectively
$\sigma_{P_1\,GSA}, \sigma_{P_1\,ESA}$	Ground and excited-state absorption cross-sections of the first pump
$\sigma_{P_1\,GSA\,em}, \sigma_{P_1\,ESA\,em}$	Emission cross-sections on the GSA and ESA transitions of the first pump
σ_{P_2}	Excited-state absorption cross-section of the second pump
$\sigma_{P_2\,em}$	Emission cross-section on the transition of the second pump
σ_{SE}	Emission cross-section
τ_f	Upper laser level intrinsic lifetime

$\tau_{i_{eff}}$	Effective lifetime of energy level i with energy-transfer processes
$\tau_i,\ \tau_{i_{int}}$	Intrinsic lifetime of energy level i
τ_{r_i}, τ_r	Radiative lifetimes of an energy level
$\tau_{nr},\ \tau_m$	Non-radiative and measured lifetimes of an energy level
ϕ	Photon flux density
ω	Angular frequency
Ω_t	Judd-Ofelt parameters

"Seek and you will find"

"יגעת ומצאת – תאמין"

Matthew 7:7

בבלי מגילה ו׳ ב׳

Chapter 1

Introduction and literature review

1.1 Introduction

THERE is an urgent need for convenient, efficient sources of coherent light in the mid-infrared (MIR) wavelength band of 3-5 μm. In the last decade, the output of fibre lasers has reached further into the infrared, with recent results achieving significant power at 3 μm [1]. This has led to significant new applications in communications [2, 3], defence, [4] environmental monitoring [5–7] and medicine [8, 9]. In this thesis, we present an erbium doped ZBLAN glass fibre laser that operates at 3.5 μm with a continuous-wave (CW) output power in excess of 250 mW. This is more than 30 times the power previously reported on this transition and is the first rare-earth (RE) doped fibre laser to operate at room temperature with a wavelength significantly beyond 3 μm with power considerably exceeding 10 mW.

The MIR (3-5 μm) range of the electromagnetic spectrum offers significant opportunities for exciting scientific breakthroughs because it is a key enabler for advanced sensing technologies. The exploitation of this part of the electromagnetic spectrum has been limited by the lack of bright sources of MIR radiation. The unfavourable laser dynamics of RE doped laser sources operating in this part of the spectrum often make them inefficient, resulting in low output for practical use.

Since laser operation was first demonstrated by Maiman in 1960 [10], a host of new opportunities has emerged. The first lasing observed was within the visible spectrum and infrared (IR) lines were demonstrated soon thereafter [11]. Many practical applications were quickly found for the laser even though it was thought to be "a solution looking for a problem" [12]. Lasers are now used for diverse purposes including welding, missile

defence applications, medical applications such as eye surgery and essential components in many consumer electronics.

"Traditional" lasers which cover the range of wavelengths between 3-5 μm were based on two related physical mechanisms. When the wavelength is relatively short, i.e. closer to the visible spectrum, infrared transitions are the result of electronic transitions within the lasing medium. This holds for wavelengths as long as 4 μm with notable exceptions extending to 5 μm [13]. Beyond this range, laser transitions can only be the result of transitions between combinations of vibrational and rotational energy levels of molecular materials. Throughout this work we will be using the terms near-infrared (NIR) and MIR often. The definition of both can vary significantly according to the source used. In the context of this work, we refer to the NIR as the wavelength range between visible wavelengths and 2.7 μm. The MIR range is defined here as the wavelength range spanning between 2.7 and 5 μm.

Most of the initial work in lasers occurred in the visible and NIR parts of the spectrum, but some MIR lasers were demonstrated early on. These lasers used either a gaseous gain medium (for example HeNe 3.391 μm, HeXe 2.0-12.9 μm [14]) which are limited to tens of milliwatts power levels or chemical (such as DF 3.6-4.2 μm and HCl 3.7-4.0 μm [15]) that can achieve power levels of hundreds of kilowatts [16]. Others used cryogenically cooled lead salts [7]. Today, most high power and short pulse MIR coherent emission is produced using non-linear processes such as optical parametric oscillation (OPO) [17, 18] and amplification (OPA) which can produce a hundred watts of widely tunable emission [18]. Semiconductor energy level engineering allowed for the development of quantum cascade (QC) laser diodes [19–21], which perform best at longer wavelengths and with pulsed operation. Those demonstrated operated at between 4-12 μm with up to 10% tunability and demonstrated power levels of many watts at the longer end of this wavelength range. Inter-sub-band cascade (ICL) laser diodes [22, 23], extended to the 3-5 μm wavelength range while operating at lower power. Additional methods for MIR generation include supercontinuum generation (SC) [24–26], Raman-based lasers [27–29] and free-electron lasers (FEL) [30, 31]. Each of these approaches have strengths and weaknesses. Among the weaknesses are low efficiencies (gas lasers), complicated design (OPO and especially FEL) and relatively moderate power levels (QC between 3-4 μm, SC low spectral power density). These limitations prevent them from being a general purpose solution for MIR applications.

In this chapter, we discuss possible applications for cost-effective MIR lasers which can produce watt-level output efficiently. We then review MIR fibre lasers operating within the 2.75 μm to 5 μm spectral range. These are emerging as a possible solution for an efficient, watt-level source in the MIR with inherently excellent beam quality and the

possibility of wavelength tunability. We then introduce the DWP method we developed to improve the energy efficiency of this family of lasers.

1.2 Applications of 3-5 μm lasers

There are many diverse applications that utilise 3-5 μm MIR lasers. In this section, we present a short overview of the main applications that would benefit from improved MIR sources with emphasis on the advantage of using fibre lasers. The list of applications presented below is by no means exhaustive, and additional applications will be conceived in the future when new rugged, cost effective light sources become available.

1.2.1 Gas sensing

Many organic and inorganic molecules have strong absorption lines in the MIR spectral region (see example between 2.5-4 μm in Figure 1.1). These absorption lines constitute "fingerprints" which enable their identification.
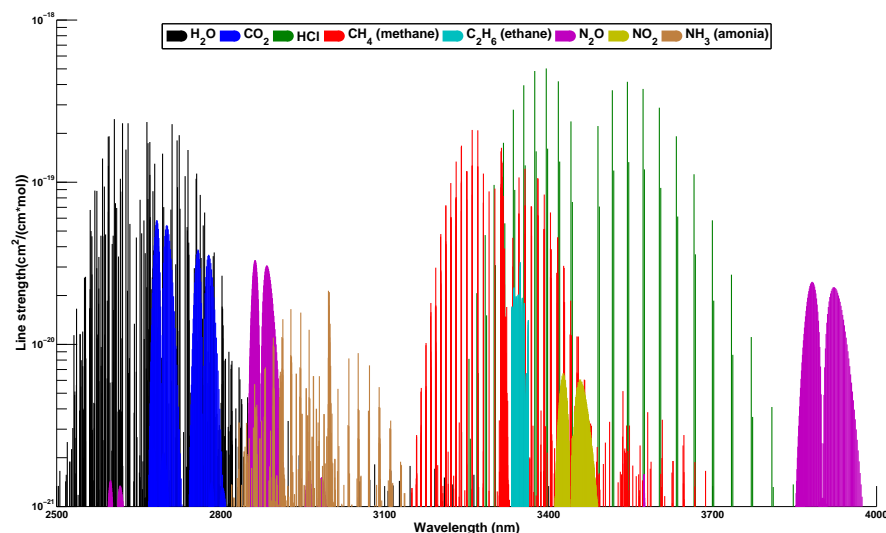
Figure 1.1: Absorption of various gasses in the 2.5-4 μm spectral range. Note that the three most important greenhouse gases, water, carbon-dioxide and methane, are all present.

These absorption lines are due to the fundamental vibrational-rotational modes of molecular bonds. The atmosphere has numerous open "spectral window" where light can propagate with relatively low absorption by the atmospheric gasses. One of these

windows is between 3.3 μm and 5 μm and is the result of reduced attenuation by water vapour which, together with carbon-dioxide, is the main overall MIR absorber within this wavelength range [32].

It is therefore possible to monitor the concentration of aforementioned gases remotely using laser-radars that utilise MIR lasers tuned to relevant absorption lines. It is possible to determine the isotopic concentration by using exact tuning of the wavelength [33].

MIR laser sources allow the monitoring of water vapour and carbon-dioxide which are both important greenhouse-gases. The lesser known but very potent greenhouse gasses methane and ethane can also be monitored using MIR lasers [5, 6, 22, 33, 34]. Beyond the value of environmental monitoring for scientific reasons, consideration is being given by regulatory bodies around the world to mandating monitoring of these gasses prior to and during oil and gas drilling activities [35]. Advanced MIR lasers systems can detect the concentration of methane with sensitivity down to the particles-per-billion range, which is more sensitive than the natural background concentration [7].

Laser absorption spectroscopy monitoring of other gasses can be beneficial in other fields. For example, ethylene monitoring is of high importance in agriculture as it is the plant hormone that regulates fruit ripening. Ethanol, methanol and ammonia are industrial pollutants that can also be monitored using the same laser absorption spectroscopy methods while obtaining very high detection sensitivities [33].

The long lifetime of excited states typical in common fibre lasers allows for large energy storage and enables high peak power. The guidance of fibres leads to excellent beam quality and a high overlap between the pump light absorption and the lasing mode resulting in high efficiency. Laser radars for atmospheric monitoring can benefit from all these qualities.

1.2.2   Medical applications

Lasers operating in the near infrared have been used as surgical scalpels because their non-contact nature makes laser scalpels sterile. The heat generated by these lasers tends to burn the end of blood vessels, helping the coagulation process and preventing bleeding. It has been shown recently [36] that biological tissues have the highest absorption cross-section of light within the two spectral bands due to strong light absorption by lipids and proteins. The first band is centred around 3 μm and the second at 6.5 μm. This effect is especially pronounced in the skin, cornea and brain tissue but appears to be prominent in most soft tissues in the body [36, 37]. A laser operating within these bands can cut

faster, creating cleaner incisions. Fibre lasers, which seamlessly combine the generation and the delivery of laser light, can significantly simplify the construction of laser scalpels. In addition, the inherent excellent beam quality should allow for cleaner, more precise incisions, causing less collateral damage.

Another emerging field is the early detection of disease using breath analysis [8, 38–40]. The human body produces a host of organic compounds which are associated with metabolic processes and specific diseases. Many of these compounds are volatile and can be directly linked to a specific condition. For example, the presence of acetone in exhaled breath has been linked with diabetes [41] and ethane is associated with lipid peroxidation [38]. Direct imaging of tissue using MIR lasers is also gathering traction, with strong indications that cancerous skin cells can be detected using MIR sources [42]. Both fields are developing rapidly, but the lack of commercially affordable sources often makes these medical tools available only in large laboratories and research institutes. If such devices were affordable for outpatient clinics, they could provide an attractive, rapid, non-invasive medical diagnostic tool [40].

1.2.3 Military applications

The available information on military applications is limited because much of it is classified. Publicly available sources point to two main uses for MIR lasers: The first is using an extremely high power MIR laser as a directed energy weapon. Few examples of this sort have been described in the literature. The best known examples are the HF/DF chemical lasers (operating on 2.8 μm and 3.4 μm lines, respectively) that were originally developed to intercept and destroy nuclear ballistic missiles [16, 43]. These lasers achieved megawatts of CW output power, but were only used as technology demonstrators and were never field deployed to the best of our knowledge.

MIR sources are also finding applications in jamming and neutralising heat-seeking missiles [4, 44]. The plumes from the jet engines of aircrafts have high thermal emission in the MIR spectral range. While weak sources are useful in confusing the electronics in such missiles, powerful sources, often based on OPOs [18], can be used for blinding and destroying the sensitive detectors in the seeker head of the missile. The combination of light generation and ease of aiming when using fibre lasers is important to this application. Another advantage is the ability to achieve tight focusing at a distance due to fibre lasers' excellent beam quality, which allows high power density on a distant moving object.

Another emerging application is the stand-off detection of explosives using MIR illumination [45]. Broadband or swept wavelength illumination can be used to observe various distinct absorption lines which make it possible to distinguish explosives from other materials.

1.2.4 Future applications

A cost-effective MIR source operating with high spectral power density, good beam quality and with the option for wavelength tunability can open the door for applications which are not foreseen at the moment. Such applications might be ones which are currently not mature, impractical, or too expensive outside of a laboratory setting. Two examples can be found in optical communication and metrology.

MIR laser communication might enable more robust point-to-point communications. Operating in the MIR enables communication links which are eye-safe, covert, jam-proof and require less power than visible ones are possible [46, 47]. This is due to the better penetration of MIR light, specifically at 3.5-4.0 μm, through rain and fog and its greater immunity to scattering from dust and Rayleigh scattering of the atmosphere.

In metrology, many labs are pursuing the development of MIR frequency combs [48–50]. The direct generation of dense swaths of coherent MIR laser lines, which have absolute wavelength accuracy, can enable rapid parallel molecular spectroscopy with unprecedented accuracy. Various methods for generation of MIR combs have been demonstrated, including difference-frequency-generation [48], direct generation in solid-state crystals [51], OPOs [52] and crystalline micro-resonators [53]. MIR frequency combs have already found applications in spectroscopy and are expected to be adapted for other applications as well. Such applications include, for example, MIR calibration of astronomical spectrographs, assisting in the generation of atto-second laser pulses and dual-comb optical coherence tomography [50].

1.3 Mid-IR fibre lasers

1.3.1 Overview

Fibre lasers are a very attractive solution for robust and low maintenance laser systems. A monolithic laser can be made by directly splicing all fibre components together, resulting in a very simple laser system without free space optics and no need for alignment. In addition, fibre lasers have an inherently high overlap between the laser and pump modes which, combined with their long gain lengths, can achieve lasing with high power and a low threshold [1]. This is particularly important for lasing on low gain transitions. The very large surface area to volume ratio of fibres results in easier thermal control compared with other types of solid state lasers. This, in conjunction with the development of double-clad fibres, has enabled the development of kW class fibre lasers with diffraction-limited beam quality [54].

In recent years much work has been done on extending the operational range of fibre based laser devices towards the MIR. The bulk of this work concentrated on using non-linear phenomena. Broadband approaches such as supercontinuum generation [25, 26, 55, 56] and frequency combs [48] demonstrated a total power of a few watts over the entire band. Stimulated Raman scattering (SRS) based fibre lasers have progressed further into the MIR with a recent demonstration of a laser operating at 3.77 μm [29]. In the context of this work, however, we concentrate on fibre lasers using electronic transitions in RE doped glasses. Figure 1.2, which is reproduced from [1], shows the maximum power demonstrated from RE doped fibre lasers at the end of 2012.
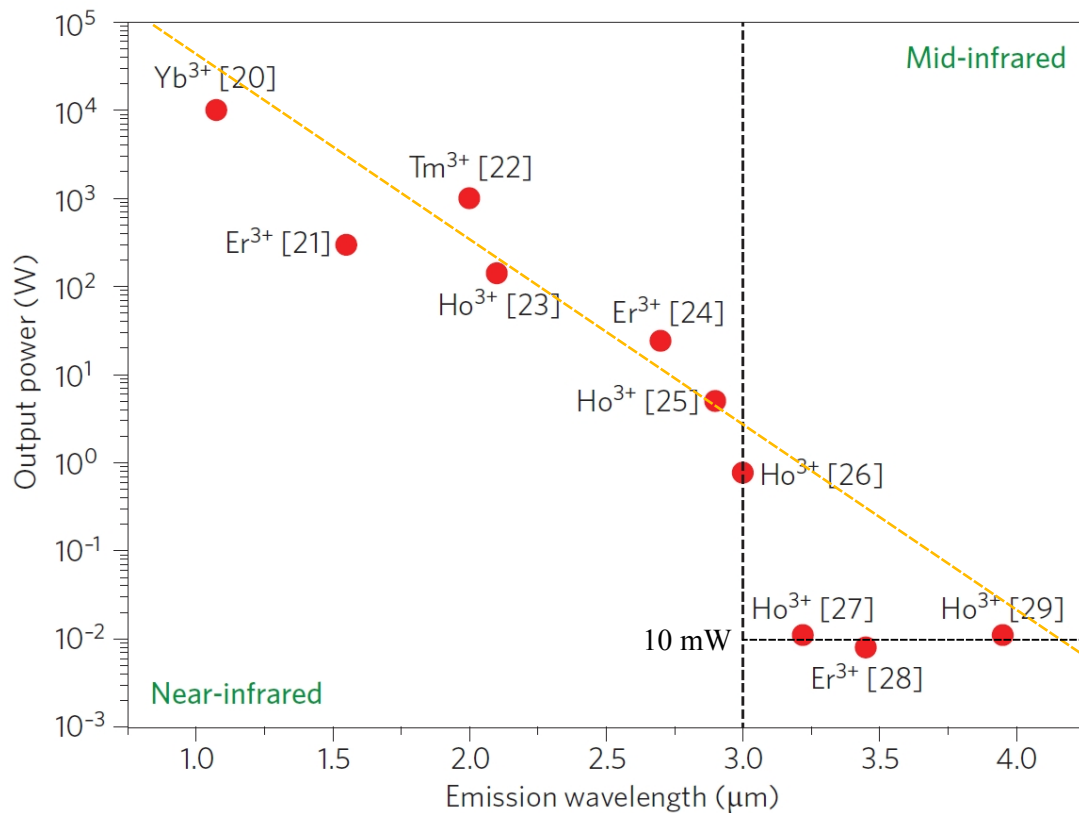
Figure 1.2: Output power from published demonstrations of infrared fibre lasers as a function of the emitted wavelength. Cryogenic cooling of the fluoride fibre was needed to demonstrate emission at 3.9 μm. Orange line represents trend as a guide to the eye. Adapted from [1] by permission from Macmillan Publishers Ltd: Nature Photonics, copyright 2012.

The figure shows that output power decreases exponentially with a linear increase in the laser wavelength as shown by the trend line in Figure 1.2. This trend is maintained until the 3 μm threshold is crossed. At this point, the reported power levels drop significantly below the trend line and plateau at about 10 mW of laser output power.

1.3.2 Challanges in obtaining MIR transitions in RE doped fibre lasers

There are multiple reasons for the difficulty associated with achieving efficient high power operation from RE doped fibre lasers operating on long wavelength transitions. Three of these are specific to long wavelength transition and host combinations: the choice of host, high quantum-defect and bottlenecking in excited states. Additional spectroscopic issues such as excited-state absorption and various forms of radiation-less energy-transfer processes also contribute to the complexity of obtaining lasing at long wavelengths.

1.3.2.1 The choice of host glass

The first thing to consider when designing a MIR fibre laser is the host glass. Silica is the glass of choice for most fibre laser applications because of its strength, durability and very low optical losses in the NIR region. However, silica is opaque in the MIR. The transparency issue arises due to the high phonon-energy of silica, which causes strong attenuation beyond 2.2 μm and makes it practically opaque for samples thicker than 1 mm at wavelengths longer than 4 μm [57].

Phonons are the quantisation of lattice vibrational energy. "Optical" or transverse lattice vibrations are generated from the absorption of light of long wavelength by the fundamental and overtones stretching modes of dipoles within the glass [58]. The vibrations of the glass matrix constituents modulate the Stark field surrounding the RE ions dopants. The field fluctuations induce non-radiative transitions from higher energetic states [59]. The probability of a multi-phonon quenching process decreases very rapidly when the gap between the energy levels involved increases because the number of phonons required to quench such a transition increases. The phonon quenching rate is dependent on the material's temperature, as seen in Equation 1.1 [60].

$$W_{MP}(T) = C \cdot exp(-\alpha \Delta E) \left[1 - exp(-\frac{h\nu_{max}}{k_B T}) \right]^{-\frac{\Delta E}{h\nu_{max}}} \quad (1.1)$$

Here $W_{MP}(T)$ is the multi-phonon rate, ΔE is the energy gap between the two levels, $h\nu_{max}$ is the maximum phonon energy and $k_B T$ is the thermal energy. A smaller gap requires less phonons to bridge and results in a faster rate of multi-phonon quenching. The lifetime of excited states with a small energy gap to a lower energy level is strongly quenched, unless the host glass has a low phonon energy.

Multi-phonon quenching has a strong impact on the viability of a material for MIR lasing. Efficient MIR operation can only be obtained with a low-phonon-energy material.

A number of low phonon energy crystals supporting mid-IR lasing up to 7.24 μm have been demonstrated. These include lead salts [7], YLF [61, 62], ZnSe [63] and various others [13], with lead salt based diodes demonstrated at even longer wavelengths [64].

It is not currently possible to create long fibres from low-phonon-energy crystalline materials because the addition of a low index crystalline cladding is a significant issue [13]. Therefore, MIR fibre lasers use glasses with phonon energies that are significantly lower than the phonon energy of silica, which is 1100 cm^{-1} [65, 65]. Glasses based on heavy metals and fluoride (such as ZBLAN), oxides of germanium and tellurium and chalcogenide glasses based on sulphur, selenium or antimony have been used for the creation of MIR fibre lasers [29, 65–67]. Figure 1.3 lists the phonon energies and shows the multi-phonon rates associated with different optical glasses.
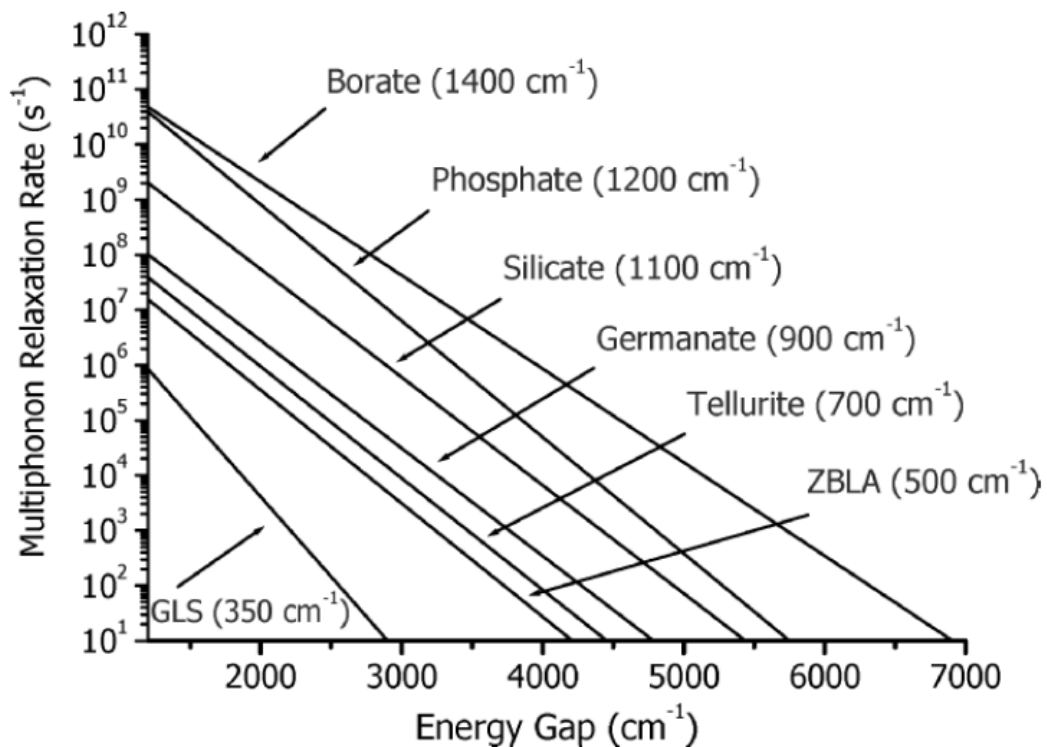
Figure 1.3: Multi-phonon relaxation rates of various glass types as a function of energy gap. Reproduced from [65] with kind permission from Springer Science and Business Media.

ZBLAN glass is currently the most mature of the low phonon energy glasses available for fibre drawing. ZBLAN is a soft glass, i.e. it is a non-silica based glass which melts at low temperature. It is a fluoride based glass and it receives its name from its constituents: zirconium (Zr), barium (Ba), lanthanum (La), aluminium (Al) and sodium (Na), all of which are chemically bound to fluorine (F). The maximum phonon energy of ZBLAN is about 565 cm^{-1}, which is considerably lower than silica glass (1100 cm^{-1}). Therefore,

ZBLAN is transparent up to wavelengths of about 5 μm [65] but is practically opaque for samples thicker than 1 mm at wavelengths longer than 8 μm [57].

ZBLAN can be doped with RE ions up to relatively high concentrations of about 7 $mol\%$ in the case of Er^{3+} ions [68]. The relative maturity of ZBLAN glass fibres and their commercial availability make ZBLAN a promising choice for the creation of fibre lasers. Many fibre lasers operating from the UV to 3.95 μm have been demonstrated using ZBLAN glass fibres [69–73]

The intrinsic optical transparency of ZBLAN glass due to low phonon energy is not sufficient to support lasing of RE-doped fibre lasers. The process of creating the glass and then drawing it into a fibre can introduce contaminants into the fibre which can significantly reduce transparency. Commercially available raw materials must be purified to significantly higher purity levels. This is necessary to reduce both broadband and strong narrow-band absorption in the glass due to contaminants [74]. In addition, glass transparency in the MIR is strongly affected by the residual water in the glass. Residual water and O-H bonds must be minimised in ZBLAN glass to increase MIR transparency and improve the mechanical strength of the glass [75].

1.3.2.2   High quantum defect - low Stokes efficiency

Many long wavelength transitions in commonly used RE ions (i.e. Er^{3+}, Ho^{3+} Tm^{3+}) are located high above the ground state. Examples of such transitions in Er^{3+} and Ho^{3+} are shown in Figure 1.4.
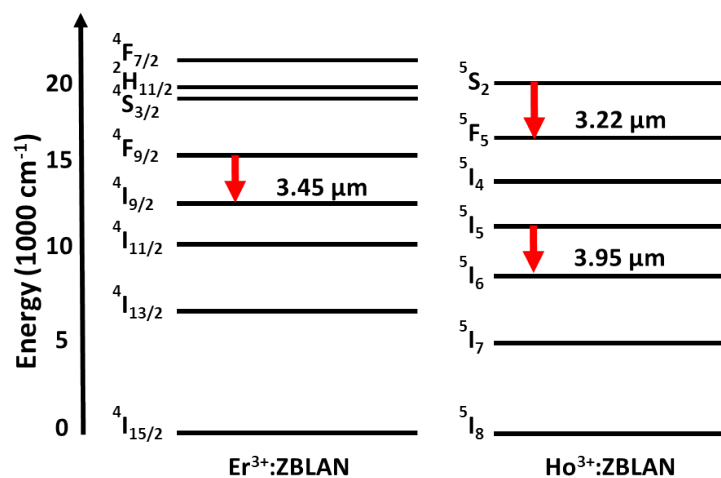
Figure 1.4: Examples of MIR transitions in RE ions which are located high above the ground state.

An ordinary laser which is pumped directly from the ground state to the upper laser level of a laser transition high above the ground state results in a high quantum defect and loss of energy to heat. Quantum defect is defined as the difference in energy between the pump and laser photons $h\nu_p - h\nu_s$. We can define another useful figure of merit for the theoretical efficiency of the pumping process. This is the ratio between the laser and pump photon energies ν_s/ν_p, which is often referred to as "Stokes efficiency" [74, 76, 77]. The Stokes efficiency is the theoretical upper limit on a laser slope efficiency under ordinary linear operation. The high quantum defect for MIR transitions combined with less mature glasses and significantly less efficient pump sources [74] are the main reasons behind the declining trend in laser power shown in Figure 1.2.

A high quantum defect means that the significant energy difference between a pump photon and a lasing photon is wasted and a fraction of it is deposited as heat in the fibre. This heat must be removed for effective laser operation. Fibre lasers are intrinsically good at removing heat passively by conduction and convection because of the large ratio between surface area and volume. However, the same fibre geometry also makes it difficult to actively remove the heat from fibres, for example by thermo-electric cooling, because the heat sink must be in contact with the entire fibre surface. In the case of MIR transitions, the strong heating of the fibre can have some adverse effects. Silica glass can withstand significant heating caused by high pump powers because of its high transition temperature of 1160°C [57]. However, fluoride and chalcogenide glasses have much lower softening and melting temperatures. ZBLAN glass in particular has a very low transition temperature of 260°C [57], which can result in the destruction of the fibre when significant heat is deposited during high power laser operation. Effective heat management of the fibre laser is therefore critical to achieving high-power MIR output in soft glasses.

1.3.2.3   Bottlenecking

A unique problem to low phonon energy materials is the long lifetimes of excited states that are below the upper lasing state. Quantum mechanics postulates that many transitions in REs are radiatively forbidden, due to parity conservation. However, RE ions in crystal and glass hosts interact with the crystal field or lattice vibrations. This causes mixing of states with different parities, therefore aiding those transitions [78]. Such mixing enables those transitions to occur radiatively due to interaction with the host glass matrix. In low phonon energy glasses, the radiative lifetimes of those "forbidden" transitions are long and often on the time scale of milliseconds.

Lasing can be terminated when the lower lasing level has a longer lifetime than the upper lasing level. This is because after pumping to the upper laser level and lasing to the lower

lasing level, a build-up of ions occurs at the lower laser level. The inversion is reduced and the laser cycle is extinguished until the lower laser level has been sufficiently depopulated. The self terminating nature of the $^4I_{11/2} \rightarrow {}^4I_{13/2}$ transition in Er^{3+}:ZBLAN was the main reason for low power obtained at the 2.75 μm wavelength in the early days of research into these fibre lasers [79, 80]. Lasing on self-terminating transitions was usually associated with pulsed operation since CW operation was not possible. However, in the case of the 2.75 μm Er^{3+}:ZBLAN lasers, operation in CW was possible because of the existence of special spectroscopic mechanisms. These include sufficiently slow spontaneous decay from the upper laser level to the lower one [81, 82], energy-transfer processes [83] and cascade lasing [76].

The long lifetimes of the intermediate excited states caused significant population build-up in those states. The increased population of the higher levels reduced the number of ions in the ground state. This resulted in the saturation of pump absorption, especially at low ion concentrations and small core sizes, all of which manifested in reduced laser efficiency [84].

1.3.3   General spectroscopic challanges in RE doped fibre lasers

Many of the difficulties associated with obtaining long wavelength transitions in RE fibre lasers are associated with the complicated energy levels structure of the dopant. This is especially true for Er^{3+} ions that were used to achieve lasing at 2.75 μm using ZBLAN glass. The 2.75 μm Er^{3+} and 2.9 μm Ho^{3+} transitions have been researched extensively, making them good case studies for the following discussion.

Energy levels with relatively long lifetimes in ZBLAN can give rise to interaction between neighbouring ions in the host [77, 85, 86]. These interactions, shown schematically in Figure 1.5, are dependent on the concentration of the dopant and must be accounted for when designing a fibre laser since some are detrimental to lasing whilst others are beneficial. The ion interactions have been classified in the literature [65] into three main categories: excited-state absorption including upconversion, cross-relaxation and energy-transfer processes. Cross-relaxation and energy-transfer are related to the fabrication issue of ion clustering [87, 88]. A short description of each of these phenomena is presented below.

1.3.3.1   Excited-state absorption and upconversion

Excited-state absorption (ESA) is the result of multiple excitations processes (see Figure 1.5 top left). An ion that has been excited can absorb an additional photon. This
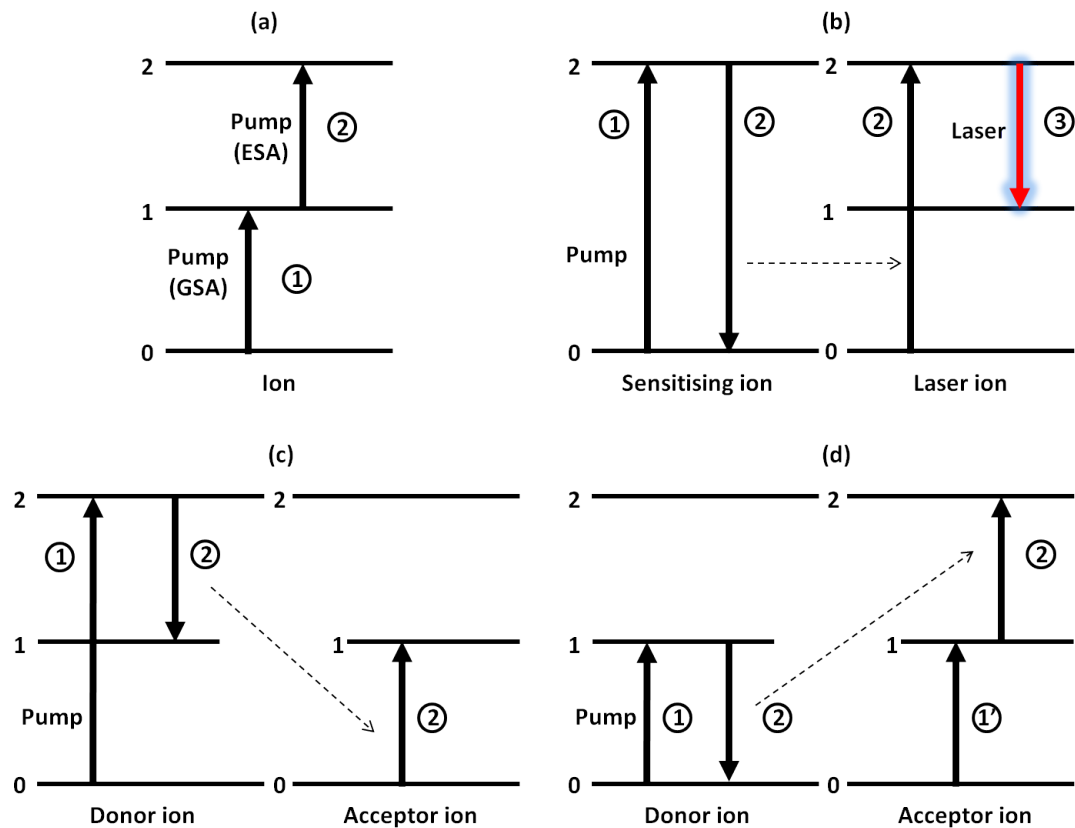
Figure 1.5: Types of energy-transfer processes. (a) Excited-state absorption (ESA); (b) sensitisation of a laser ion by an ion of a different species; (c) cross-relaxation (CR) and (d) energy-transfer upconversion (ETU). Numbers in circles represent the order in which energy is migrating.

additional excitation promotes the ion to a higher energy level. ESA is a linear process which can happen multiple times [89, 90]. With an appropriate pump wavelength, an ion can absorb a few photons consecutively, eventually reaching high energy levels. In an ordinary laser, ESA occurrence is dependent on the availability of appropriate transitions corresponding to the pump wavelength. Long lifetimes of excited states can also promote ESA by increasing the available population of ions in an excited state that are ready to absorb an additional pump photon.

An example of an ESA process is the successive absorption of 974 nm pump photons in Er^{3+} doped laser hosts (Figure 1.6 left). After the initial absorption of a photon, the ion is in the $^4I_{11/2}$ level. From that level, the ion can absorb an additional photon that will promote it to the higher $^4F_{7/2}$ level. This level is thermally coupled to the $^4S_{3/2}/^2H_{11/2}$ levels. These levels decay radiatively via green fluorescence, which is commonly associated with the excitation of Er^{3+} doped materials.

ESA is an important effect that must be taken into account. It can be a nuisance when it depopulates the upper lasing level as in the 2.75 μm laser in Er^{3+} [91, 92]. In some
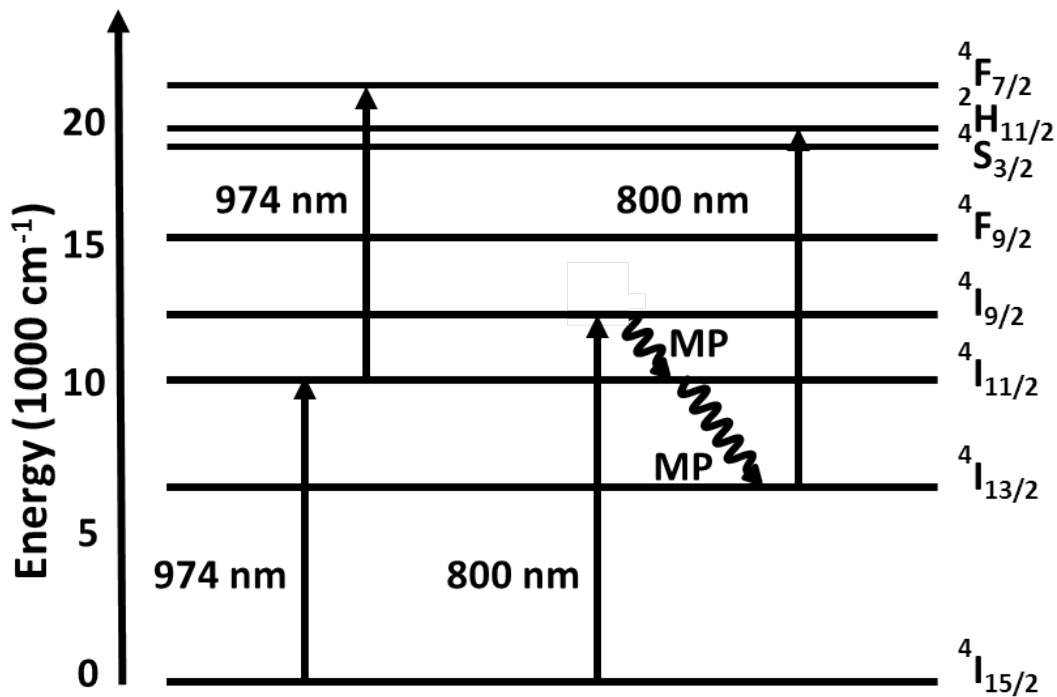
Figure 1.6: Two photon examples of ESA transitions in Er^{3+}:ZBLAN. Straight arrows represent pump photon absorption, curled arrows denote non-radiative multi-phonon decay (MP).

cases ESA even introduces competing laser transitions which saturate the power of the wanted transitions [84]. ESA can be beneficial in some cases, for example upconversion lasers operating in the visible range. Upconversion has been employed to create visible lasers using a wide variety of hosts and the trivalent RE ions [93–95]. The efficiency of the ESA upconversion process is dependent on the host, doping concentration and exact wavelength used [87, 90, 96, 97]. In addition to obtaining ESA using a single pump wavelength, lasers employing two concurrent pump sources operating at different wavelengths have extended the reach of ESA-based up-conversion lasers. Such lasers have been demonstrated in the ultra-violet, blue and green bands [93, 94, 97–103].

1.3.3.2 Energy-transfer, cross-relaxation and energy-transfer upconversion processes

Energy-transfer processes (ET) is the general term used for describing energy exchange interactions between two or more ions. By transferring energy between adjacent ions of similar or different dopant species, ET processes can create a significant population at a higher energy level than the one populated directly by pumping. The total energy in the system must be conserved, although one or two phonons might also be involved.

Phonon-assisted transition allows the total energy to be slightly higher or lower than the combined energy difference of the energy levels alone.

There are two common types of ET between ions: cross-relaxation (CR) and energy-transfer-upconversion (ETU) (see Figure 1.5 (c) and (d), respectively). In CR processes, two ions at different levels exchange energy (the lower one usually at the ground level). The ion at the lower level is excited to a higher level while the other ion, initially in the higher level, is shifted to a lower one. Since the highest excited state in the system is lower than initially, the system is said to have "relaxed." An example of a CR process in Er^{3+}:ZBLAN is the W_{50} process $^2H_{11/2} + ^4I_{15/2} \rightarrow ^4I_{9/2} + ^4I_{13/2}$ shown in Figure 1.7.

ETU between ions of the same species occurs when two ions at the same energy level exchange energy, with one ion being promoted to a higher level while the other one is shifted to the ground state. An example of a common ETU process in Er^{3+}:ZBLAN is the two ion process $^4I_{13/2} + ^4I_{13/2} \rightarrow ^4I_{15/2} + ^4I_{9/2}$. A diagram showing the energy levels changes is displayed in Figure 1.7.
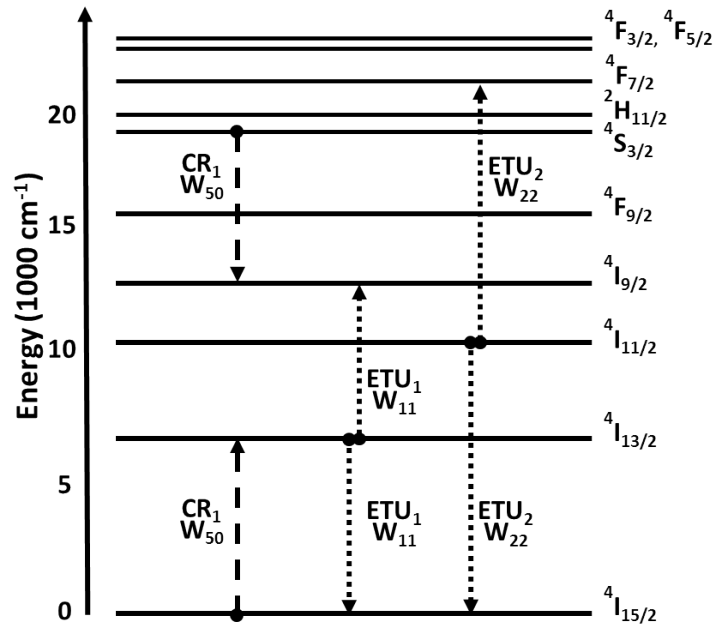
Figure 1.7: Examples of typical cross-relaxation and energy-transfer-upconversion processes in Er^{3+}:ZBLAN. The CR process W_{50} (left) creates two excited ions from one ion in the $^4S_{3/2}/^2H_{11/2}$ and one ion in the ground state $^4I_{15/2}$. The two ETU processes W_{11} (middle) and W_{22} (right) involve two nearby ions which are excited to the same level. One ion relaxes to the ground state while its excitation energy is transferred to the adjacent ion, which is elevated to a higher energy level.

ET processes can occur between different species of dopants as well. One excited dopant can transfer its energy to a different dopant species which has an energy level comparable to the excited level of the first dopant. ET processes are commonly used in lasing cycles

to improve pump absorption and remove lower level bottlenecks [65]. In the case of MIR lasers, the added dopant is often added in a lower concentrations than the main dopant. Pr^{3+} Co-doping in MIR lasers is commonly done to depopulate lower lasing levels in Er^{3+} and Ho^{3+} based lasers [104, 105].

1.3.3.3 Clustering

Clustering is when dopant ions in a host are not dispersed evenly throughout the host material and form small clusters. The clustered ions tend to transfer energy to each other. Two excited ions which are part of a cluster can interact, with one shifted to the ground state, while the other receives the energy lost by the former ion. The energy is eventually dissipated as heat with the excited ion returning to its original energy level. This mechanism is a loss mechanism where pump energy is transformed to heat in the fibre instead of light emission. Clustering is a main reason for reduced efficiency in fibre lasers which use high dopant concentration [87, 88]. The energy transferred between clustered ions effectively allows one ion to relax to the ground level, while the second ion is initially excited to a higher level and then returns to its original excited level. Thus, population inversion is lost without providing any light amplification.

1.4 Rare-earth doped MIR fibre lasers and methods for improving their efficiency

1.4.1 Previous demonstrations of long wavelength transitions

Figure 1.8 depicts the transitions associated with RE doped fibre lasers producing lasing at wavelength > 1.5 μm that were demonstrated to date. All transitions shown in this Figure were demonstrated using ZBLAN glass as a host.

Briarly and France demonstrated in 1988 the first MIR transition in a fibre laser using ZBLAN glass [79]. During the 1990s there was a strong push to increase the power of this long wavelength transition, as well as demonstrate fibre laser operation of even longer electronic transitions based on RE dopants.

Significant work has been done on increasing the output power of the 2.75 μm, $^4I_{11/2} \rightarrow$ $^4I_{13/2}$ transition in Er^{3+}:ZBLAN [71, 84, 106–109]. The maximum power obtained to date is 24 W achieved by Tokita et al. [110], using liquid cooling of an Er^{3+}:ZBLAN glass fibre.
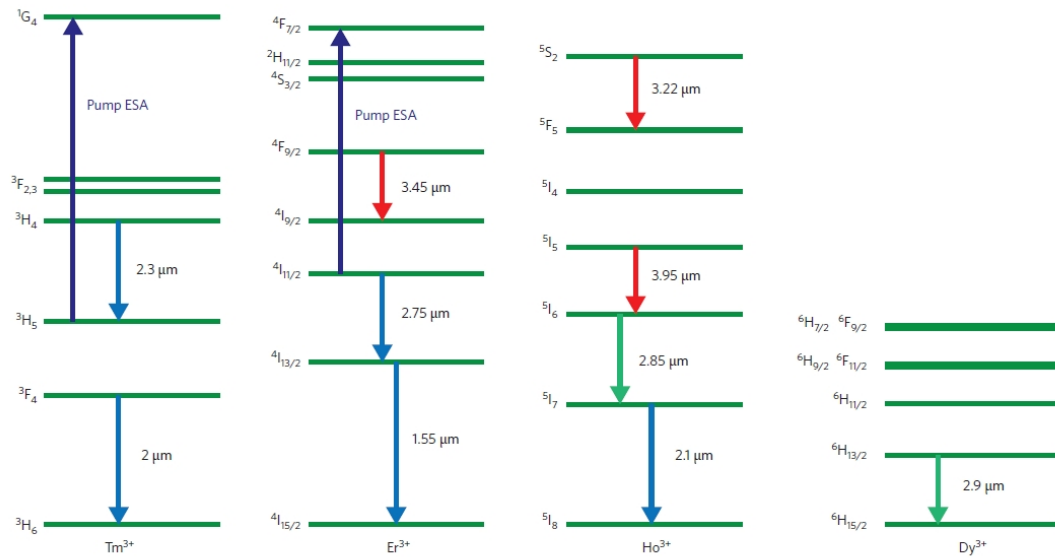
Figure 1.8: Laser transitions of rare-earth ions that produce emission wavelengths longer than 1.5 μm. Figure shows near-infrared (blue arrows), MIR (red arrows) and in-between (green arrows) electronic transitions, together with the primary lasing wavelength from previously demonstrated fibre lasers for each transition. The fluorescence spectra of the $^5I_6 \rightarrow^5 I_7$ transition of Ho^{3+} and the $^6H_{13/2} \rightarrow^6 H_{15/2}$ transition of Dy^{3+} extends across the boundary between the near- and MIR regions. Reprinted by permission from Macmillan Publishers Ltd: Nature Photonics, [1], copyright 2012.

In recent years there has been renewed attention on long-wavelength Ho^{3+}:ZBLAN fibre lasers. Such lasers, operating on the $^5I_6 \rightarrow ^5I_7$ transition, can produce emission on the range 2.8-3.0 μm [111–113]. Higher output powers can be achieved by adding Pr^{3+} ions in small concentration as a sensitiser [108, 114]. The longer wavelength compared with 2.75 μm emission of Er^{3+}:ZBLAN allows for increased absorption by water. Such an increase is a benefit to laser surgery applications.

The published work on transitions longer than 3 μm in RE doped fibre lasers is very limited. To the best of the author's knowledge, all results were demonstrated by one group from the Technischen Universität Braunschweig in Germany during the 1990s. Their initial results are shown in Figure 1.9. The group's first long wavelength transition was demonstrated by Wetenkamp in 1990 using the 2.8-2.9 μm transition in Ho^{3+} [115].

The demonstration of longer transitions followed with the first demonstration of a fibre laser beyond 3 μm operating at 3.5 μm by Többen in 1991 [72]. Following his initial work, Többen was able to demonstrate 8 mW output power with a 2.8% slope efficiency at room temperature and 12 mW under cryogenic cooling [117]. Limited wavelength tuning was also demonstrated using temperature tuning of the fibre laser [118].

Additional work was conducted during the 1990s to expand the number of long wavelength transitions demonstrated. This included the work of Schneider demonstrating
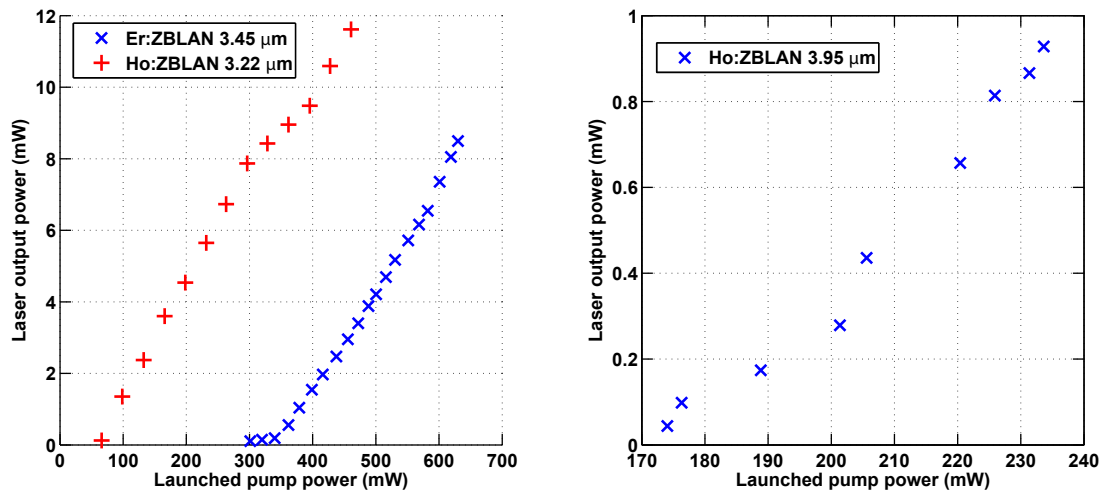
Figure 1.9: Transition longer than 3 μm demonstrated at the Technischen Universität Braunschweig. Left - room temperature Er^{3+}:ZBLAN 3.45 μm demonstrated by Többen [72] and 3.22 μm demonstrated by Carbonier in Ho^{3+}:ZBLAN [116], right - cryogenic 3.95 μm demonstrated by Schneider in Ho^{3+}:ZBLAN [73].

Ho^{3+}:ZBLAN operation using the $^5I_5 \rightarrow {}^5I_6$ transition [73]. It was not possible to operate this fibre laser at room temperature. When operating at liquid nitrogen temperatures, Schneider was able to demonstrate 11 mW of output power with a maximum slope efficiency of 3.7%, [119].

The final long wavelength fibre laser demonstrated by Carbonier of the same group was a room temperature 3.22 μm fibre laser [116]. This laser operated on the $^5S_2 \rightarrow {}^5F_5$ transition in Ho^{3+} and achieved 11 mW with 2.8% slope efficiency.

There has been continuous and significant improvement in the performance of NIR fibre lasers since their inception. In contrast, progress in MIR fibre lasers operating beyond 3 μm stalled after the 1990s with their performance kept well below the current trend line observed in Figure 1.2. This trend, which was added as a guide to the eye, represents a rough guide to the state-of-the-art in RE-doped fibre lasers power as of 2012. Taking into account more recent results would have shifted the trend line higher in the graph. Future improvement will affect it in the same way, until a genuine physical limit will be reached, therefore stopping the march of the trendline upwards. On average, the trend should apply for fibre lasers operating on all wavelengths shown in the graph, including wavelengths longer than 3 μm.

The plateau in the longer than 3 μm wavelengths is the result of discontinued research into RE-doped fibre laser at these wavelengths after the mid-1990s. We can only speculate as to the reason for this halt. One possible reason is that although ZBLAN glass drew much commercial attention by communication companies in the mid-1980s to the 1990s (see for example British Telecom [75, 120]), once the commercial immaturity of the necessary

fluoride glasses was realised in the 1990s, budgets were shifted towards other possible avenues. This shift affected the availability and the commercial incentive to produce high-quality ZBLAN fibres, therefore restricting research only to those few laboratories that could make their own ZBLAN glass fibres (such as Technischen Universität Braunschweig). In addition, the consistent low power and efficiency demonstrated on all longer wavelengths shown in Figure 1.9 might have suggested that such fibre lasers were a scientific dead-end. We therefore suggest that a new approach for the generation of wavelengths longer than $3~\mu m$ in RE doped fibre lasers was needed.

1.4.2 Existing methods for enhancing the power and efficiency of rare-earth doped MIR fibre lasers

We now examine the methods and approaches used to improve the power and efficiency of laser transitions longer than $2.7~\mu m$.

We initially address the choice of host glass. Beyond glass selection, it is imperative to address spectroscopic parameters that facilitate lasing. The most common methods employed in the past are cascade lasing, co-doping and energy recycling.

1.4.2.1 The use of very low phonon energy glasses

In recent years there has been increased focus on generating MIR lasing using chalcogenide glasses that have very low phonon energy [121–124]. Low phonon energy glasses are the key enabler for MIR operation (see section 1.3.2.1). Lowering the phonon energy below the level found in fluoride glasses, such as ZBLAN, improves intrinsic lifetime and can enable lasing on transitions which would otherwise be quenched by multi-phonon processes.

Chalcogenide glasses are based on the chalcogen elements of sulphur, selenium and tellurium, together with other elements from the III-V group, the most common of which are arsenic and germanium. Chalcogenide glasses have lower phonon energies of between 300-450 cm^{-1} for sulfur and selenium based glasses [65], which is lower than ZBLAN. Tellurium based glasses have even lower phonon energies of 150-200 cm^{-1}. This makes them transparent even further into the far infrared region [125]. Thus, they can theoretically support lasing action of much longer wavelengths [126].

Despite their clear theoretical advantage, to the best of the author's knowledge no RE doped chalcogenide fibre laser has been demonstrated at a MIR wavelength to date (2014). Limitations in fibre drawing, difficulties in incorporating RE dopants into the glass matrix and high optical losses due to contaminants have been attributed to this lack of success [121].

1.4.2.2 ESA and cascaded lasing

The long lifetime of some excited states in RE ions doped ZBLAN glass can cause problems. If the lifetime of the lower lasing level is longer than the lifetime of the upper lasing level then bottlenecking in the lower state can prevent operation in CW. This is due to population inversion depletion once lasing commences.

A number of long wavelength transitions suffer from a self-terminating nature, for example the 3.95 μm, $^5I_5 \rightarrow {}^5I_6$ and the 2.9 μm, $^5I_6 \rightarrow {}^5I_7$ transition in Ho^{3+}. However, the best known transition that is impacted by this phenomenon is the 2.75 μm, $^4I_{11/2} \rightarrow {}^4I_{13/2}$ transition in Er^{3+} doped lasers. For example, in low doped Er^{3+}:ZBLAN the upper level $^4I_{11/2}$ has a lifetime of 6.7 ms while the lower level, $^4I_{13/2}$, has a lifetime of 9.5 ms [127]. This typical transition will be used in the coming sections as the case study for improving laser performance.

One way around the bottlenecking problem is to use cascade lasing. This method uses an additional laser transition to empty the lower lasing state and thus avoid bottlenecking.
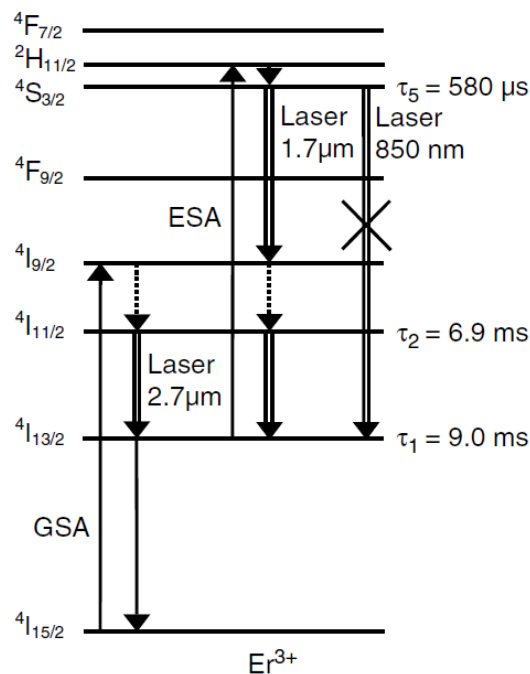
Figure 1.10: Example of bottlenecking avoidance using ESA and cascade lasing. Reproduced from [65] with kind permission from Springer Science and Business Media.

An alternative cure to the bottlenecking problem is to use ESA to deplete the lower lasing level (sometimes in conjunction with cascade lasing). For example, consider Figure 1.10. The ions are first excited to the $^4I_{9/2}$ level, then relax to the $^4I_{11/2}$ level, lase and accumulate in the $^4I_{13/2}$ level. Strong, wavelength-dependent ESA at the pump

wavelength from the $^4I_{13/2}$ to the $^2H_{11/2}$ level depopulates the lower lasing level. However, it can create a population inversion on the transition $^4S_{3/2} \rightarrow {}^4I_{13/2}$ resulting in lasing at 850 nm which terminates the 2.75 μm lasing once again. By inducing a cascade of lasing at 1.7 μm on the $^4S_{3/2} \rightarrow {}^4I_{9/2}$ transition, followed by the desired 2.75 μm lasing on the $^4I_{11/2} \rightarrow {}^4I_{13/2}$ transition, significant power improvement was demonstrated. Using this method it was possible to increase the power from 20 mW with saturated power and efficiency of less than 15% [104], to over 150 mW with 23% efficiency [76].

A similar approach of using a cascaded lasing configuration was used by Schneider in his 3.95 μm fibre laser [119]. In this case, co-lasing at 1.2 μm on the $^5I_6 \rightarrow {}^5I_8$ was used to remove bottlenecking from the $^5I_6$ level, see Figure 1.11. Using cascade lasing at 1.2 μm,
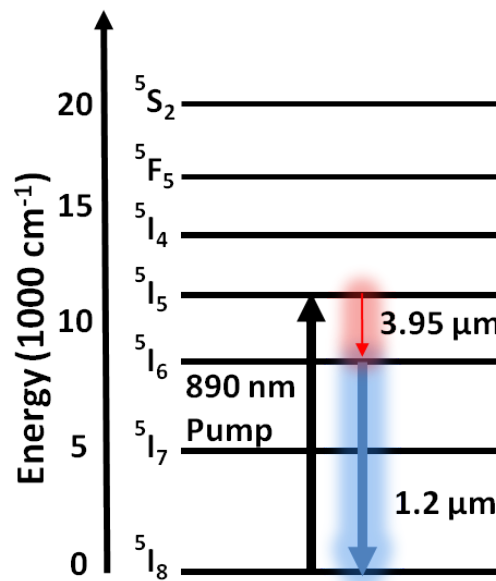
Figure 1.11: Cascade lasing with 3.95 μm using Ho^{3+}:ZBLAN fibre laser as demonstrated in [119]. 1.2 μm lasing removes bottlenecking by depopulating the lower lasing level.

Schneider was able to achieve 11 mW of output power at 3.95 μm together with 70 mW of 1.2 μm power when pumping at 885 nm under cryogenic conditions.

Cascade lasing appears to be the leading method for improving power and efficiency for single-clad, relatively low doping (less than 1 $mol\%$) fibres. When higher doping concentrations are involved, other methods can achieve better results.

1.4.2.3   Co-doping

Laser performance can be improved significantly by adding a second dopant. This applies in cases where the first dopant concentration is higher than 1 $mol\%$ and double-cladding

geometry is used [65]. In high doping concentration and double-clad configuration, the effect of ESA is reduced significantly because of strong ET processes. The population build-up at the lower lasing level is transferred to the second dopant through an ET process and from there to the ground via fast multi-phonon relaxation.

An example of co-doping can be seen in Figure 1.12, which shows the effect of adding Pr^{3+} ions to Er^{3+} ions in ZBLAN glass.
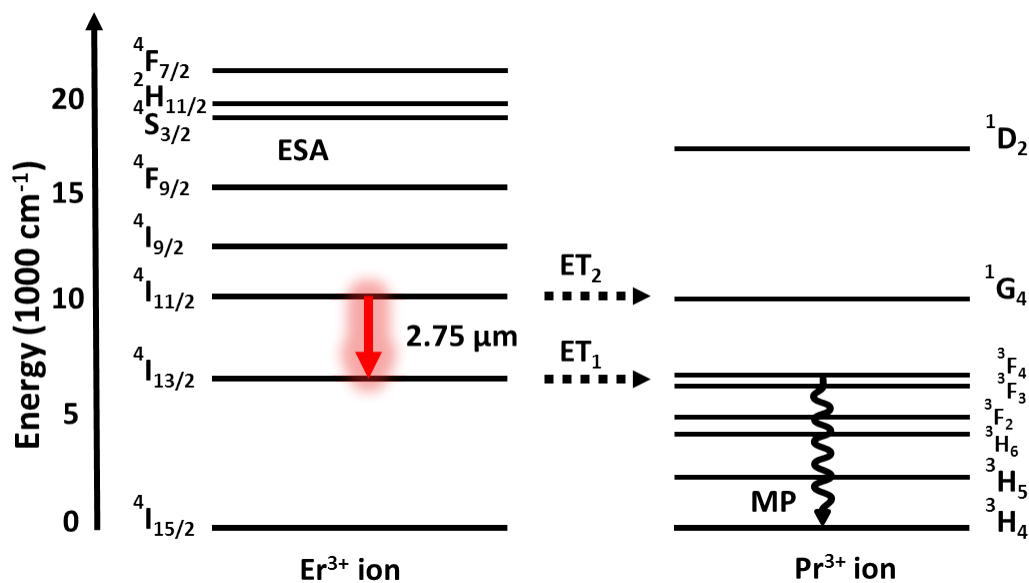
Figure 1.12: Energy level scheme for 2.75 μm lasing using co-doping with Er^{3+} and Pr^{3+} ions [128]. The process ET_1 depopulates the lower lasing level. ET_2 and ESA are both weak and do not reduce the laser efficiency. MP - multi-phonon relaxation.

The addition of the low concentration of Pr^{3+} ions alleviates the self-termination by quenching the lifetime of the lower lasing level via ET process to the Pr^{3+} ions [104, 128–133]. From there, the Pr^{3+} ions relax to the ground via rapid multi-phonon decay.

The co-doping method allowed a significant improvement in laser output power. 1.7 W at 2.75 μm has been demonstrated using 800 nm pumping with 17% slope efficiency [128]. Since ESA does not play a significant role in co-doped, double-clad fibre lasers, it became possible to pump these lasers with a 980 nm pump. Lasers emitting a few watts have been demonstrated with a maximum output of 5.4 W and 21% slope efficiency [134]. Simulated results show that it is possible to achieve about 10 W with slope efficiency close to the Stokes efficiency limit of 29% using Er^{3+}/Pr^{3+} co-doped ZBLAN fibres [134]. The limiting factors are heating of the fibre and more difficult fibre geometries. Further improvement in output power requires operation in the "energy recycling" regime which suffers from these problems to a lesser extent.

1.4.2.4   Energy recycling

In the energy recycling regime, an energy-transfer process is used to increase the population of the upper lasing level while quenching the lifetime of the lower lasing level. A schematic description of this mechanism is shown in Figure 1.13.
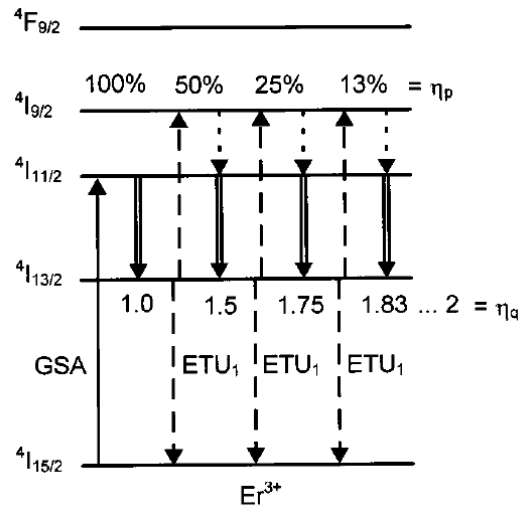
Figure 1.13: Energy recycling mechanism in Er^{3+}:ZBLAN. Recycling of energy occurs between neighbouring ions, in which two ions located in the $^4I_{13/2}$ level cooperate. One relaxes to the ground level while the other is elevated to the $^4I_{9/2}$ level allowing a new lasing cycle to commence. If numerous cycles occur, the quantum efficiency approaches twice the Stokes efficiency limit. Reproduced with permission from [92] © 2001 IEEE.

Since ET processes are dependent on the host and dopant concentration, a carefully chosen host and doping level can alter the cross-section and probabilities of the ESA and CR processes. In this way, it is possible to make the $4I_{11/2} +^4 I_{11/2} \rightarrow {}^4I_{9/2} +^4 I_{15/2}$ CR process, which depletes the lower lasing level, be the dominant depopulation process from the $^4I_{13/2}$ level [135].

ET processes not only depopulate the lower lasing level, but can also transfer a significant fraction of the ions back into the upper lasing level. After excitation, an ion following this process would have produced a laser photon and would have excited another ion to the upper lasing level. At the limit of many repetitions, the laser efficiency can reach twice the Stokes efficiency [114]. Hence, the self-termination issue is resolved and a significant enhancement in laser efficiency is achieved.

This method requires a high concentration of Er^{3+} ions, on the order of 5 $mol\%$ or more. Tokita used this method on a liquid-cooled, singly doped Er^{3+}:ZBLAN laser to obtain 24 W of output power with 13% slope efficiency. Demonstrating higher-than-Stokes efficiency proved to be difficult. Recently, however, an all-fibre design achieved a slope efficiency of 39.5% exceeding the theoretical Stokes efficiency of 34.4% on this transition [136].

1.5 Dual-wavelength pumping approach for lasing in the mid-infrared

In the previous sections, we examined possible approaches for coherent generation of MIR laser light. In the following section a new approach is proposed which uses dual-wavelength pumping (DWP) of fibre lasers to efficiently generate MIR radiation. The approach forms the basis for this research project, the underlying goal of which is to determine whether it is possible to generate MIR laser light inside an optical fibre efficiently using electronic transitions.

The following sections describe the general DWP scheme followed by a more detailed explanation of the DWP method applied to Er^{3+}:ZBLAN fibre lasers. A set of rate equations describing DWP of Er^{3+}:ZBLAN is presented. These equations identify the spectroscopic parameters that are needed to effectively implement the DWP of Er^{+3}:ZBLAN. Some of these parameters have been reported in the literature (see Chapter 2), others have not and they were measured as part of this research in Chapters 3 and 5.

1.5.1 General dual-wavelength pumping scheme

The dual-wavelength pumping scheme for a MIR transition located far above the ground state is illustrated in Figure 1.14. In the standard method of operation (see left of Figure 1.14), ions are excited to the upper laser level using near infrared, or visible pump sources. The laser photon is extracted and the ion is left in an excited state which is often long lived. This ordinary pumping method is subject to two issues. First, the laser has a high quantum defect because the lasing transition is located far above the ground state. Second, the number of ions available for lasing from the ground state is depleted because ions are trapped in long lived excited states post lasing. This means that most of the energy used for pumping is wasted.

In contrast, the DWP method, shown on the right of Figure 1.14, uses bottlenecking to its advantage and reduces the quantum defect by employing two pump sources. The first source, P_1, elevates ions from the ground state to an intermediate level which is meta-stable. A second pump source, P_2, is then utilised to promote the ions from the meta-stable level to the upper lasing level. The laser photon is extracted and the ion returns to the meta-stable energy level. An additional P_2 photon can now repeat the process and elevate the ion again to the upper lasing level. The ions are cycled many times between the meta-stable level and the upper levels before they decay back to the ground state. This mechanism uses a "virtual" ground state at the meta-stable level
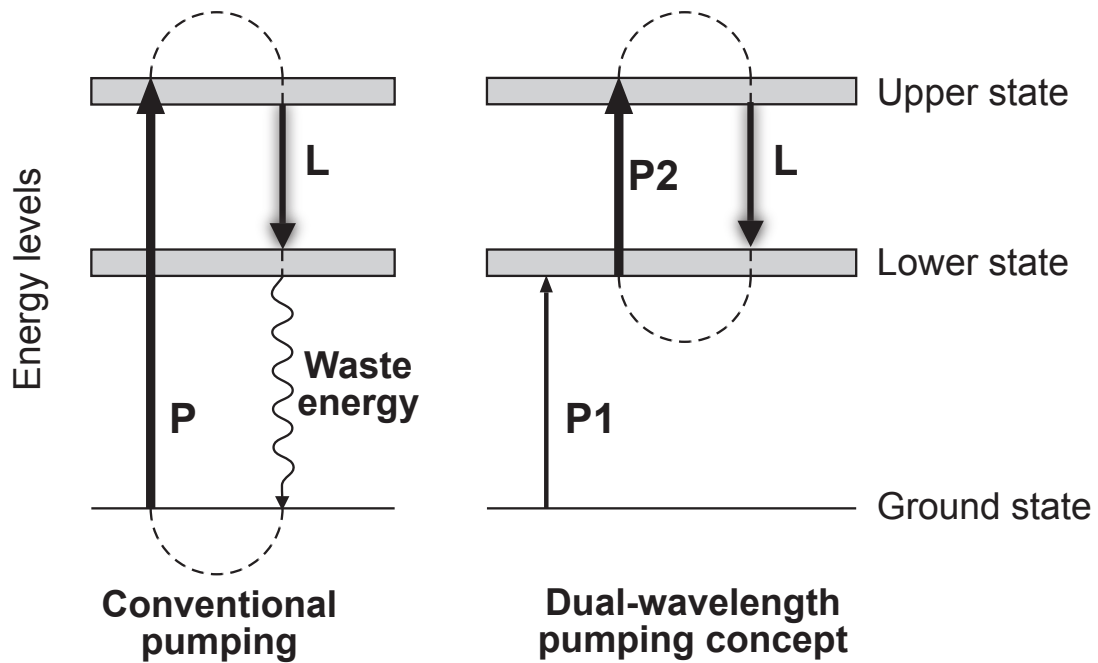
Figure 1.14: Ordinary pumping versus DWP scheme. Energy level schematic for a typical MIR lasing transition. P, P_1 and P_2 - pump absorption, L - laser transition.

and can substantially improve the laser efficiency. The long lifetime of the meta-stable level means that most of the pump power necessary comes from P_2. Some P_1 pump is required to re-populate the atoms that return to the ground state via processes such as spontaneous emission, cross-relaxation and other energy-transfer processes.

1.5.2   Previous demonstrations of dual-wavelength pumping

Dual-wavelength pumping methods have been used to extend the bandwidth of optical communication amplifiers. The telecommunication band is located around 1550 nm, which is where the loss in silica is lowest. In this wavelength region, the waveguide and material dispersions also cancel each other [2]. The throughput of optical fibre systems is getting larger every year, and a wider swath of spectrum is needed to allow more data to be transferred with wavelength-division-multiplexing (WDM) systems. Since all long haul fibre optic systems require amplifiers, a great deal of effort has been put into extending the bandwidth of optical amplifiers [137–139]. One way of achieving this is to use two wavelengths to pump the amplifier [140–143].

Dual-wavelength pumping schemes have been employed in many cases to create upconversion lasers using a wide variety of hosts and trivalent rare-earth ions. Ultra-violet, blue and green lasers have been demonstrated this way [93, 94, 97–103].

Shori [140] proposed using two laser sources to prevent self-terminating a specific MIR transition (see Figure 1.15). In this patent, ESA is used to alleviate self terminating of lasing on the $^4I_{11/2} \rightarrow {}^4I_{13/2}$ transition in Er^{3+}:ZBLAN. The self-terminating nature of this transition is due to the long lifetime of the $^4I_{13/2}$ level compared with $^4I_{11/2}$ level. Shori's solution involves using a first pump source to excite the ions to the top lasing
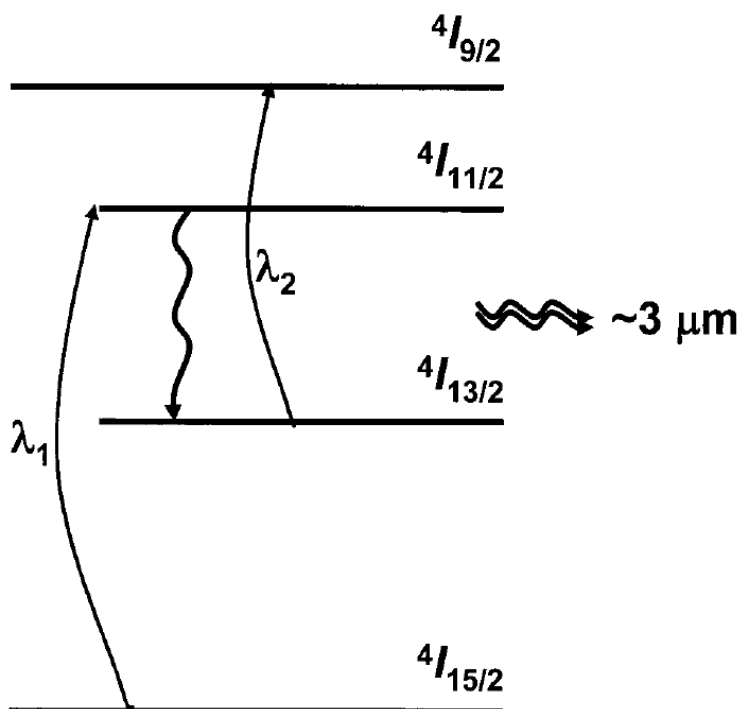
Figure 1.15: Double wavelength pumping for $\sim 2.75~\mu m$ in Er^{3+} doped host. Reproduced from USPTO patent 7,633,990 [140].

level of $^4I_{11/2}$, from which lasing commences. An increasing number of ions settle in the $^4I_{13/2}$ and the original inversion is reversed and lasing ceases. To ameliorate the loss of inversion, a second pump source is used to shift the ions from the $^4I_{13/2}$ level to the $^4I_{9/2}$ level where they rapidly relax to the upper lasing level via multiple phonon relaxation.

To the best of the author's knowledge, Shori's solution was never demonstrated in a scientific or other form of publication beyond the patent and it was not demonstrated in a commercial device. The patent addresses only the 2.75 μm transition of Er^{3+} and does not refer to other lasing transitions or to the general case of improving the efficiency of laser transitions located high above the ground state.

1.5.3 Dual-wavelength pumping on the 3.5 μm transition in Erbium

In our work we implement DWP to achieve efficient lasing on the 3.5 μm MIR transition in Er^{3+}:ZBLAN glass fibre. This method looks similar to the one described in [140], but the mechanism by which it allows lasing and improves efficiency is different.

Figure 1.16 illustrates the energy levels of Er^{3+}:ZBLAN with their corresponding lifetimes. This thesis explores the 3.5 μm lasing on the $^4F_{9/2} \rightarrow ^4I_{9/2}$ transition. The $^4F_{9/2} \rightarrow ^4I_{9/2}$ transition is not self-terminating and as such behaves very differently to the $^4I_{11/2} \rightarrow ^4I_{13/2}$, 2.75 μm transition which was addressed by Shori's method [140].
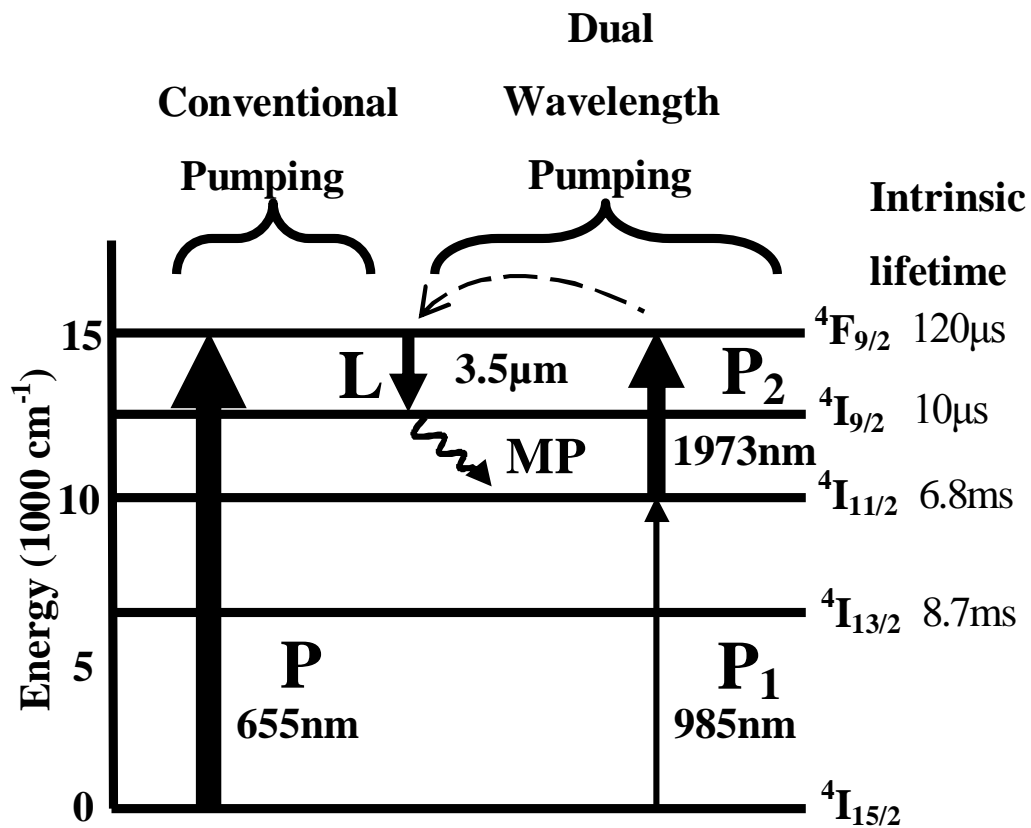
Figure 1.16: Energy level diagram of Er^{3+}:ZBLAN showing the pumping scheme for a typical MIR lasing transition pumped using conventional techniques and the DWP concept. Energy level lifetimes on the right are from [17]. P, P1 and P2, pumps; L, lasing transition; MP, multi-phonon decay. Reproduced with permission from [144].

The conventional scheme to generate 3.5 μm radiation is shown on the left of Figure 1.16 and our method for producing MIR laser radiation on the right. In previous demonstrations of 3.5 μm operation by Többen [117], ions were excited to the upper laser level using visible pump sources. The laser photons were extracted and the ions were left

trapped in the lower, long-lived excited states of $^4I_{11/2}$ and $^4I_{13/2}$. This depleted the number of ions in the ground state and reduced pump light absorption, resulting in reduced efficiency. The significant difference between the energy of the pump and the laser photons meant that considerable energy was wasted.

Többen was able to demonstrate a maximum average output power of 8 mW with a slope efficiency of less than 3% at room temperature. In contrast, our DWP method shown in Figure 1.16 uses two pump lasers. As explained in Chapter 3, our first pump operating at 985 nm (P_1) excites the Er^{3+} ions to the metastable $^4I_{11/2}$ level. A significant population build-up can occur using a relatively low power P_1 pump because this level is long-lived (6.8 ms [133]). The second pump source P_2 excites the ions from the $^4I_{11/2}$ to the upper lasing level, $^4F_{9/2}$. The ions emit laser radiation at 3.5 μm (L) and relax from the lower lasing level $^4I_{9/2}$ to the $^4I_{11/2}$ level via rapid multi-phonon decay (MP). The ions in our DWP laser cycle between the $^4I_{11/2}$ and $^4F_{9/2}$ levels many times, using the "virtual ground" state created in the $^4I_{11/2}$ level.

The maximum theoretical slope efficiency of a 3.5 μm laser using DWP with a fixed P_1 power and a varying P_2 power is 57%. This figure-of-merit is similar to the theoretical Stokes efficiency, which is determined by fixing P_1 power and then taking the ratio of P_2 wavelength (1973 nm) to that of the laser (3.5 μm). This is a significant improvement over the 18% slope efficiency which is the theoretical best case for direct pumping from the ground level to the upper lasing level $^4F_{9/2}$. Although P_1 is not considered when the slope efficiency is calculated, it is still obviously necessary. The maximum optical-to-optical efficiency, which does include the input power of P_1, cannot be determined theoretically without a full numerical analysis.

High power as well as high brightness pump sources at both wavelengths are commercially available off-the-shelf and are significantly less costly than a single pump source for direct pumping to the upper laser level $^4F_{9/2}$ level. ZBLAN is used for this MIR laser because it is a low phonon energy glass, which reduces the rate of non-radiative decay between closely-spaced laser levels. ZBLAN glass is transparent up to 4 μm, can be easily doped with rare-earth ions and fibres drawn from it are available commercially [145].

1.5.4   Rate equations for the 3.5 μm DWP mechanism

To achieve lasing at 3.5 μm, it was necessary to conduct a thorough spectroscopic investigation of the relevant pump parameters, including optimal pump wavelengths, energy level lifetimes and other energy-transfer processes that might affect the proposed laser behaviour.

In order to choose which parameters were required for further investigation, it was beneficial to review the rate equations associated with the proposed 3.5 μm laser system in Er^{3+}:ZBLAN. Once the parameters were determined experimentally, these rate-equations will be used in the future to generate a numerical simulation of the system.

The rate equations shown in Equations 1.2a-1.2g refer to the transitions shown in Figure 1.17 and use similar notations to the one in [114]. A similar figure is provided as a fold-out at the end of this thesis for ease of reference. The system consists of seven
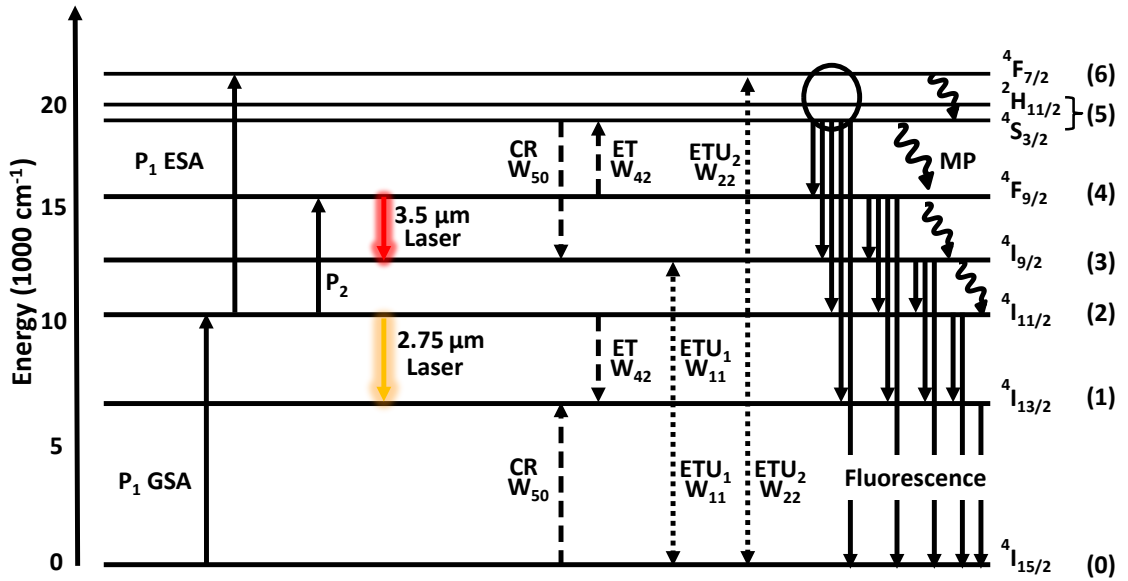
Figure 1.17: Energy levels and spectroscopic processes in Er^{+3}:ZBLAN. $P_{1,2}$ - pump absorption; CR, ET and $ETU_{1,2}$ - cross-relaxation, energy-transfer and energy-transfer-upconversion processes, the indices of W_{ij} indicate the initial levels involved in the process; MP - multi-phonon relaxation. The numbers in brackets to the right represent the number of the rate equation associated with this energy level. Note that $^4S_{3/2}$ and $^2H_{11/2}$ are thermally coupled and share the same rate equation.

coupled equations which describe the temporal evolution of the ion population density of the ground state and the first seven energy levels of Er^{3+}:ZBLAN. We assume that the levels $^4F_{7/2}$, $^2H_{11/2}$ and $^4S_{3/2}$ are thermally coupled and can be treated as one level.

The full set of equations for the ionic population is:

$$dN_6(z)/dt = R_{P_1\,ESA}(z) - \tau_6^{-1}N_6(z) + W_{22}N_2^2(z), \tag{1.2a}$$

$$dN_5(z)/dt = \beta_{65}\tau_6^{-1}N_6(z) - \tau_5^{-1}N_5(z) - W_{50}N_5(z)N_0(z) + W_{42}N_2(z)N_4(z), \tag{1.2b}$$

$$dN_4(z)/dt = R_{P_2}(z) + \beta_{64}\tau_6^{-1}N_6(z) + \beta_{54}\tau_5^{-1}N_5(z) - \tau_4^{-1}N_4(z)$$
$$- W_{42}N_2(z)N_4(z) - R_{SE43}(z), \tag{1.2c}$$

$$dN_3(z)/dt = \Sigma_{i=4...6}[\beta_{i3}\tau_i^{-1}N_i(z)] - \tau_3^{-1}N_3(z) + R_{SE43}(z)$$
$$+ W_{50}N_5(z)N_0(z) + W_{11}N_1^2(z), \tag{1.2d}$$

$$dN_2(z)/dt = R_{P_1\,GSA}(z) - R_{P_1\,ESA}(z) - R_{P_2}(z) + \Sigma_{i=3...6}[\beta_{i2}\tau_i^{-1}N_i(z)] \tag{1.2e}$$
$$- \tau_2^{-1}N_2(z) - 2W_{22}N_2^2(z) - W_{42}N_2(z)N_4(z) - R_{SE21}(z),$$

$$dN_1(z)/dt = \Sigma_{i=2...6}[\beta_{i1}\tau_i^{-1}N_i(z)] - \tau_1^{-1}N_1(z) + W_{50}N_5(z)N_0(z) - 2W_{11}N_1^2(z)$$
$$+ W_{42}N_2(z)N_4(z) + R_{SE21}(z), \tag{1.2f}$$

$$dN_0(z)/dt = \Sigma_{i=1...6}[\beta_{i0}\tau_i^{-1}N_i(z)] - R_{P_1\,GSA}(z) - W_{50}N_5(z)N_0(z) + W_{11}N_1^2(z)$$
$$+ W_{22}N_2^2(z), \tag{1.2g}$$

$$N_{Er} = \Sigma_{i=0...6}N_i(z). \tag{1.2h}$$

In Equations 1.2a-1.2h, N_i is the ion density of the ith energy levels (with N_0 being the ground level $^4I_{15/2}$). $R_{P_1\,GSA}(z)$ and $R_{P_2}(z)$ represent the pump rates of the 985 nm pump and the 1973 nm pump. $R_{P_1\,ESA}(z)$ represent the excited-state absorption rate of pump P_1 on the $^4I_{11/2} \rightarrow {}^4F_{7/2}$ transitions, while $R_{SE43}(z)$ and $R_{SE21}(z)$ are the 3.5 μm and 2.75 μm lasers stimulated emissions, respectively. All the pump rates are dependent on the power of the pumps and on the absorption and emission cross-sections of the relevant transitions. τ_i is the intrinsic lifetime of the ith energy levels, including radiative, as well as multi-phonon relaxation. W_{ij} is a cross-relaxation, energy-transfer or energy-transfer-upconversion process of two ions of levels i and j. β_{ij} is the branching ratio, or the probability of ions to decay from levels i into levels j. N_{Er} is the Er^{3+} ion concentration in the fibre. Only one of the Equations 1.2g and 1.2h is needed to solve the equation set and they are both given here for completeness.

Many of the parameters used in equations 1.2a-1.2g can be found in the literature sources [114, 127, 133, 135, 146, 147]. These include the energy level lifetimes τ_i, branching ratios β_{ij} and numerous rates for energy-transfer-upconversion and cross-relaxation processes W_{ij}.

The pump rates are only partially known and they depend on knowing absorption and emission cross-sections. Adopting the notation used by Pollnau and Jackson [114], the

pump rates along each fibre segment Δl at location z can be characterised by

$$\alpha_1(z, \lambda) = \sigma_{P_1\,GSA}(\lambda)N_0(z) - \sigma_{P_1\,GSA\,em}(\lambda)N_2(z)$$

$$+ \sigma_{P_1\,ESA}(\lambda)N_2(z) - \sigma_{P_1\,ESA\,SE}N_6(z), \tag{1.3a}$$

$$\alpha_2(z, \lambda) = \sigma_{P_2}(\lambda)N_2(z) - \sigma_{P_2\,em}N_4(z), \tag{1.3b}$$

where $\sigma_{P_1\,GSA}$ and $\sigma_{P_1\,ESA}$ represent the ground and excited-state absorption cross-sections for the 985 nm transitions, respectively. $\sigma_{P_1\,GSA\,em}$ and $\sigma_{P_1\,ESA\,em}$ are the emission cross-sections of the inverse process from the ${}^4I_{11/2}$ level to the ground. σ_{P_2} and $\sigma_{P_2\,em}$ are the absorption and emission cross-sections of the 1973 nm pump from the ${}^4I_{11/2}$ level to the ${}^4F_{9/2}$ level and vice verse. Note that the pump rates in Equations 1.3a and 1.3b include the effects of saturation of both pumps and that the cross-sections are wavelength dependent. We can allow for cladding pumping by introducing an effective absorption coefficient in the cladding

$$\alpha_{eff_{1,2}}(z, \lambda) = \alpha_{1,2}\pi r_{core}^2/A_{clad} \tag{1.4}$$

where r_{core} represents the radius of the fibre core and A_{clad} the area of the fibre inner cladding. The pump power launched into every fibre segment $P_{in_{1,2}}(z, \lambda)$ can be found from

$$P_{in_{1,2}}(z, \lambda) = \eta_{in_{1,2}}P_{inc_{1,2}}(\lambda)\prod_{z'=1}^{z-1}\{exp[-\Delta l(z')\alpha_{eff_{1,2}}(z', \lambda)]\}. \tag{1.5}$$

In 1.5, $P_{inc_{1,2}}$ are both pumps power incident on the fibre tip at each wavelength and $\eta_{in_{1,2}}$ are the launch efficiencies. Using the above equations we can find the local pump rate in each fibre segment to be

$$R_{P_1\,GSA/ESA1/ESA2} = [\sigma_{P_1\,GSA/ESA1/ESA2}N_{0,2,3}(z)/\alpha_{eff_1}(z, \lambda)] \tag{1.6a}$$

$$\cdot\{1 - exp[-\Delta l(z)\alpha_{eff_1}(z, \lambda)]\}$$

$$\cdot\frac{\lambda_{p_1}}{hc\Delta l\pi r_{core}^2}P_{in_1}(z, \lambda),$$

$$R_{P_2} = [\sigma_{P_2}N_2(z)/\alpha_{eff_2}(z, \lambda)] \tag{1.6b}$$

$$\cdot\{1 - exp[-\Delta l(z)\alpha_{eff_2}(z, \lambda)]\}$$

$$\cdot\frac{\lambda_{p_2}}{hc\Delta l\pi r_{core}^2}P_{in_2}(z, \lambda).$$

In Equations 1.6a and 1.6b, $\lambda_{p_{1,2}}$ are the pump wavelengths, h is Planck's constant, c is the speed of light in vacuum, and r_{core} is the fibre core radius.

The ground state absorption value of $\sigma_{P_1\,GSA}$ over the entire 970 nm-1000 nm is easily measured using transmission through a sample and using the Beer-Lambert law. Measuring the excited-state absorption cross-section $\sigma_{P_1\,ESA}$ is more involved. Nonetheless,

data are available from measurements by Quimby and Miniscalco [148]. We have so far stipulated in section 1.5.3 that P_1 pump wavelength is 985 nm although bright pump sources are commonly available at 974-976 nm and not 985 nm. In section 3.2 we describe the reasons behind and the implications of using 985 nm as the wavelength for the first pump. In addition, to the best of our knowledge, no measured or calculated value has been presented in the literature for the excited-state absorption cross-section of the transition $^4I_{11/2} \rightarrow {}^4F_{9/2}$ and its wavelength dependency. A substantial part of Chapter 3 will be devoted to determining the optimal P_2 wavelength and the relevant absorption cross-sections.

The stimulated emission rate is given by

$$R_{SE\,43} = [b_4N_4 - (g_4/g_3)b_3N_3]\sigma_{SE}c\phi. \tag{1.7}$$

Here, b_3 and b_4 are the Boltzmann factors for the lower and upper laser levels, g_3 and g_4 are the laser levels degeneracy and ϕ is the photon flux density. Previous work by Többen has shown the shape of the 3.5 μm fluorescence [117], but an emission cross-section, σ_{SE}, of this transition has not been provided. An estimated cross-section based on Többen's data is given in section 2.5, while a value based on our work is provided in section 6.3.2.

The nature of this work is to demonstrate the feasibility of lasing on the 3.5 μm transition and not as a spectroscopy investigation. Nonetheless, a large part of this work involves determining the spectroscopic behaviour of Er^{3+}:ZBLAN. One such observation is the discovery of a previously unknown energy-transfer parameter $W_{42}N_4N_2$ which represents the process $^4F_{9/2} + {}^4I_{11/2} \rightarrow {}^4S_{3/2} + {}^4I_{13/2}$ that is detrimental to lasing at 3.5 μm. This process is discussed in section 5.4.

1.6   Outline of this thesis

In this thesis, we describe the creation of a MIR fibre laser operating at 3.5 μm at room temperature. Chapter 2 details relevant spectroscopic information relating to Er^{3+}:ZBLAN glass that is currently available in literature. Various spectroscopic investigations were conducted during this project and they are detailed in Chapter 3. These include the extraction of cross-section parameters, energy levels and additional parameters which are important to the operation of the 3.5 μm laser and are relevant for future computer simulations of this laser. Chapter 4 describes the pump sources that were built and modified to be used with the 3.5 μm laser, including their construction and characterisation. In Chapter 5, we investigate in detail a population-dependent

lifetime quenching effect of the upper laser level. This effect is shown to be the result of a previously undocumented energy-transfer process; its magnitude is determined as well. The 3.5 μm laser's performance is summarised in Chapter 6. Additional information is derived from the laser's behaviour, including internal resonator losses, emission cross-section and gain. The thesis concludes in Chapter 7 with a brief summary and suggested future work.

Chapter 2

ZBLAN glass spectroscopy - analysis of literature

2.1 Overview

R ARE-EARTH doped fibre lasers in ZBLAN glass have been studied for many years, so a large body of spectroscopic data is available for singly pumped lasers. This chapter explores the literature related to ZBLAN glass and fibres relevant to DWP operation. We start by giving a general overview of the thermo-mechanical properties of ZBLAN glass and its suitability for MIR laser generation. We then examine the ground state absorption of various transitions in bulk ZBLAN glass. A review of the data available in literature regarding non-radiative decay rates in ZBLAN glass is conducted, because non-radiative properties are of the utmost importance when operating in the MIR. Absorption, fluorescence and lifetimes recorded in the literature are then outlined.

2.2 Bulk ZBLAN glass

In this section, we begin with the spectroscopic properties of bulk ZBLAN glass. An overview of its composition and optical properties is detailed and the thermo-mechanical properties of ZBLAN glass are examined.

2.2.1 ZBLAN glass composition

ZBLAN glass is based on fluoride and heavy metals and is the most common fluoride glass used to-date. This glass is named after its constituent ingredients of ZrF_4-BaF_2-LaF_3-AlF_3-NaF. Fluoride glasses were accidentally discovered by Poulain in 1973 [149].

The common, most stable form, first reported by Ohsawa in 1981 [150], has a molar composition of 53% ZrF_4, 20% BaF_2, 4% LaF_3, 3% AlF_3, and 20% NaF.

ZBLAN has good mid-IR transmission, but is relatively difficult to make compared to silica based glasses [57]. High quality glass requires high purity raw materials which are not easily obtained. Common impurities in the raw materials cause significant IR absorption. ZBLAN glass is prone to crystallisation in the glass cooling phase which can be circumvented by rapid fibre drawing and cooling. ZBLAN glass is also hygroscopic. Hence, it must be fabricated and drawn into fibre using a controlled atmosphere and coated while on the drawing tower using UV-curable acrylate coating layers.

ZBLAN fibre is typically fabricated using the preform method where a fibre is drawn from a glass rod at a temperature above the glass softening temperature T_g, but below the glass melting temperature T_m. Various methods have been used to create the initial preforms with rotational casting under reduced pressure providing the lowest losses demonstrated to date of 0.65 dB/km at 2.59 μm [120].

2.2.2   ZBLAN glass optical and mechanical properties

The common composition of ZBLAN glass has good transparency from 300 nm up to 5 μm. The weaker bonds between the heavy metal and fluoride ions and their high reduced mass are associated with this longer wavelength IR edge. This results in the low maximum phonon energy of the glass matrix of ~ 565 cm^{-1} compared with 1100 cm^{-1} for silica glass [57, 151]. The lower bond strength causes some negative effects, including higher glass reactivity and reduced mechanical stability. Therefore, it is necessary to coat ZBLAN glass fibres to protect them and strengthen them for handling.

The minimum loss predicted for ZBLAN glass is less than 0.01 dB/km at 2.5 μm [75], which is significantly lower than the 0.2 dB/km predicted for silica fibres. This low loss and extended IR transmission motivated intense research on ZBLAN glass during the 1980s for use in optical fibre based telecommunication systems. A loss coefficient of 0.65 dB/km has been demonstrated [120], but the typical minimum loss of commercially available fibres is still between 10-100 dB/km.

The refractive index of ZBLAN is lower than the $n = 1.5$ of wavelengths longer than 600 nm, as seen in Figure 2.1. This relatively low index can be modified by the addition or substitution of ions into the glass matrix. PbF_2 and BiF_3 have been added to raise the refractive index of the fibre core, while the addition of AlF_3 or LiF to the fibre cladding reduces its refractive index. Substituting ZrF_4 with HfF_4 has also been shown to reduce

the refractive index. The phonon edge of ZBLAN, which corresponds to the wavelength at which the glass becomes totally opaque at long wavelengths, is also modified by these substitutions. The usual phonon-edge of 5-6 μm can be increased to longer wavelengths using substitution of the ZrF_4 with HfF_4 or ThF_4, which shift the edge to 7 μm and 8 μm respectively [57].
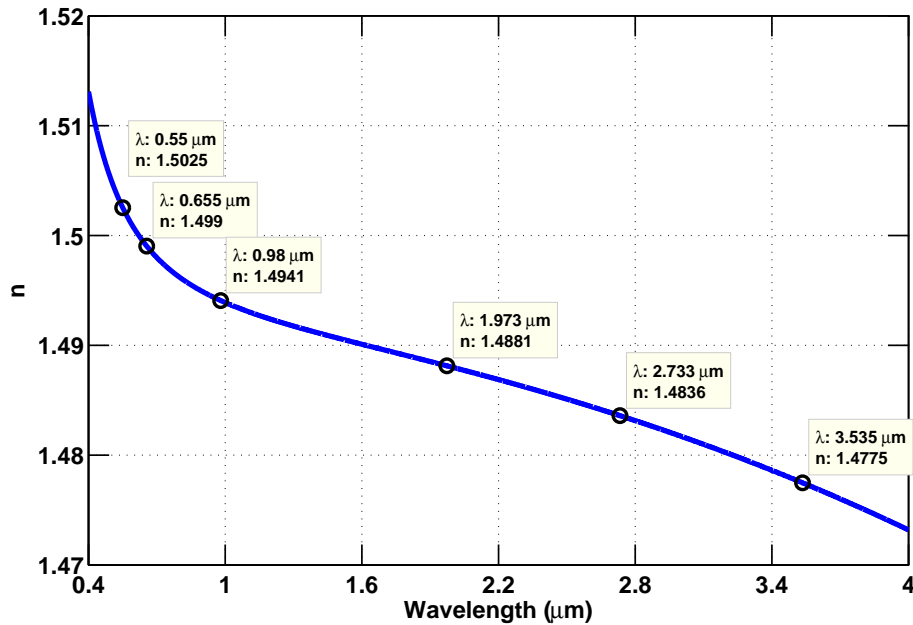
Figure 2.1: ZBLAN refractive index - Sellmeier curve. Curve is based on data from Gan [152].

A comparison between the thermal, mechanical and optical properties of ZBLAN and silica glasses is provided in Table 2.1.

The combination of ZBLAN's low transition temperature combined with its low thermal conductivity makes it difficult to achieve significant output power. Laser power of ~ 300 W has been demonstrated from a single mode Er^{3+} doped silica fibre in the 1.5 μm band [155]. ZBLAN fibre lasers have only demonstrated up to 24 W at 2.75 μm. The optical breakdown damage threshold of ZBLAN glass is about 25 MW/cm^2 [109], which together with thermal restrictions limit the theoretically obtainable laser power at 2.75 μm to the 100 W range [57, 156]. The 2.75 μm wavelength band has similar material losses in commercial fibres as the 3.5 μm band. Prior to our work, only 8 mW of output power at 3.5 μm was demonstrated by Többen in a ZBLAN fibre [117]. There is clearly significant room for increasing the output power of rare-earth doped ZBLAN fibres lasers operating beyond 3 μm.

ZBLAN glass is significantly more brittle and less stable than silica glass. This makes ZBLAN fibres difficult to work with and requires fibres to be coated to increase mechanical

Table 2.1: Properties of ZBLAN and silica glasses, data from [57, 153, 154].

Property	Silica glass	ZBLAN glass
Transmission range ($T > 10\%$) for 1 mm thick sample (μm)	0.16-4.0	0.22-8.0
Transmission range ($T > 90\%$) for 1 m long fibre (μm)	0.38-2.25	0.52-3.94
Source: Silica - [153], ZBLAN - [154]		
Maximum phonon energy (cm^{-1})	1100	565
Transition temperature (°C)	1175	260
Specific heat ($J/(g \cdot K)$)	0.179	0.151
Thermal conductivity ($W/(m \cdot K)$)	1.38	0.628
Coefficient of thermal expansion ($10^{-6}/K$)	0.55	17.2
Density (g/cm^3)	2.20	4.33
Knoop hardness (kg/mm^2)	600	225
Fracture toughness ($MPa \cdot m^{1/2}$)	0.72	0.32
Poisson's ratio	0.17	0.17
Young's modulus (GPa)	70	58.3
Shear's modulus (GPa)	31.2	20.5
Bulk's modulus (GPa)	36.7	47.7
Refractive index (@ 0.589 μm)	1.458	1.499
Abbe number	68	76
Zero dispersion wavelength (μm)	1.3	1.6
Nonlinear index ($10^{-13}\ esu$)	1	0.85
Thermo-optic coefficient ($10^{-6}/K$)	11.9	-14.75

robustness and reduce the risk of breaking while being handled. Nonetheless, ZBLAN glass is currently the most mature fibre technology for mid-IR light delivery and fibre laser operation. Indium fluoride (InF_3) based glass has recently become available commercially but is not quite as mature. Chalcogenide glasses have mostly failed to demonstrate RE-doped laser action beyond the near-IR as a result of high material losses. Two recent demonstrations of Raman based chalcogenide fibre lasers at 3.34 μm [157] and 3.77 μm [29] are notable exceptions.

2.3   Absorption measurements

The spectroscopic investigation of ZBLAN glass begins with a bulk glass absorption measurement. In this measurement, we used a spectrophotometer in the visible to near IR to measure light transmission through the glass. The absorption coefficient of various bands in ZBLAN glass are presented.

2.3.1 Theoretical background of absorption measurement

The absorption of light as it propagates follows the Beer-Lambert law with an exponential reduction inside the material

$$\frac{I_{out}}{I_{in}} = exp(-\alpha(\lambda) \cdot l) = exp(-\sigma_{abs}(\lambda)N_0 \cdot l), \tag{2.1}$$

where I_{out} is the transmitted intensity, I_{in} is the incident intensity, $\alpha(\lambda)$ is the absorption coefficient in cm^{-1}, l is the thickness of the sample in cm, $\sigma_{abs}(\lambda)$ is the absorption cross-section and N_0 is the total dopant ion density in the sample in cm^{-3}. We should note that the $\alpha(\lambda)$ coefficient is dependent on the doping concentration of the sample, whilst $\sigma_{abs}(\lambda)$ is generally not. Equation 2.1 does not take into account Fresnel reflections or scattering and other losses due to the host material.

The glass samples that were measured were not used for fibre drawing, hence results of absorption coefficients were obtained for comparison with literature values only.

The data provided by the spectrophotometer was in absorbance units E, where

$$E = log_{10}\frac{1}{T}, \tag{2.2}$$

where T is the transmitted power through the sample in %. The relation between the absorbance E and the absorption coefficient α is

$$\alpha = \frac{\ln\left(10^{(E-E_0)}\right)}{l}, \tag{2.3}$$

where E_0 is the background loss due to Fresnel reflections, surface and bulk glass scattering and l is the sample thickness. Absorption cross-section σ_{abs} is then found according to

$$\sigma_{abs} = \frac{\alpha}{N_0}. \tag{2.4}$$

In our measurements, the Fresnel reflections and scattering losses were accounted for by normalising all results to an undoped ZBLAN sample, therefore obtaining the value for E_0 as a function of wavelength.

2.3.2 Experimental setup

Absorption of glass samples in the range of 300 nm-3000 nm was measured using an Agilent-Cary 5000 spectrophotometer. A schematic diagram of the device is shown in Figure 2.2. The spectrophotometer consisted of a broadband light source and a grating
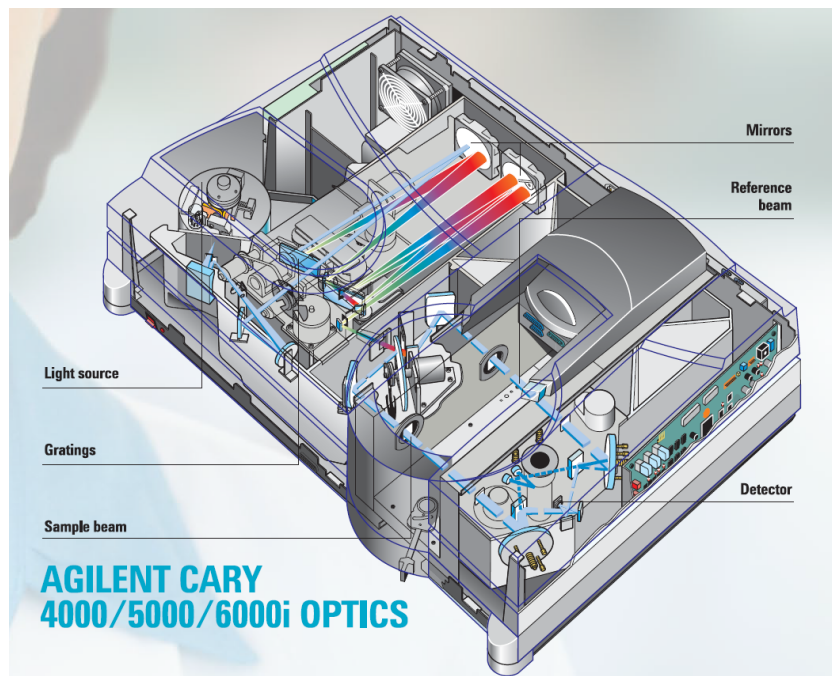
Figure 2.2: Schematic diagram of the Agilent-Cary 5000® spectrophotometer, from [158].

monochromator which enabled the scanning of the incident wavelength. The beam was chopped by a mechanical chopper at a fixed frequency. The light was divided into two paths: a reference beam and the sample beam. Both beams were eventually steered onto a PbS photo detector. The detected signal was demodulated using an internal lock-in amplifier and the results were displayed using dedicated computer software.

2.3.3   Experimental results

We measured one undoped and three different doped Er:ZBLAN samples that were manufactured at the University of Adelaide. The strong absorption of Er^{3+} ions in ZBLAN glass meant that only thin samples of 1 mm thickness were used. Figure 2.3 shows the absorption cross-section of the measured samples. The background loss caused by Fresnel reflection off both glass faces (about 8% in total) and scattering losses from the glass bulk and surfaces were normalised using the scan of the undoped sample.

Absorption cross-sections for all samples were similar, as expected, although small differences were found. These could be attributed to uncertainties in the thickness of the samples ($\pm$0.02 mm due to imperfect parallelism in the hand polished samples) and the ion concentration (estimated to be $\pm$2%). The measured cross-sections were independent of the ion density within the experimental error.

Table 2.2 lists the peak absorption cross-sections for wavelengths longer than 500 nm measured during this work and values from the literature.
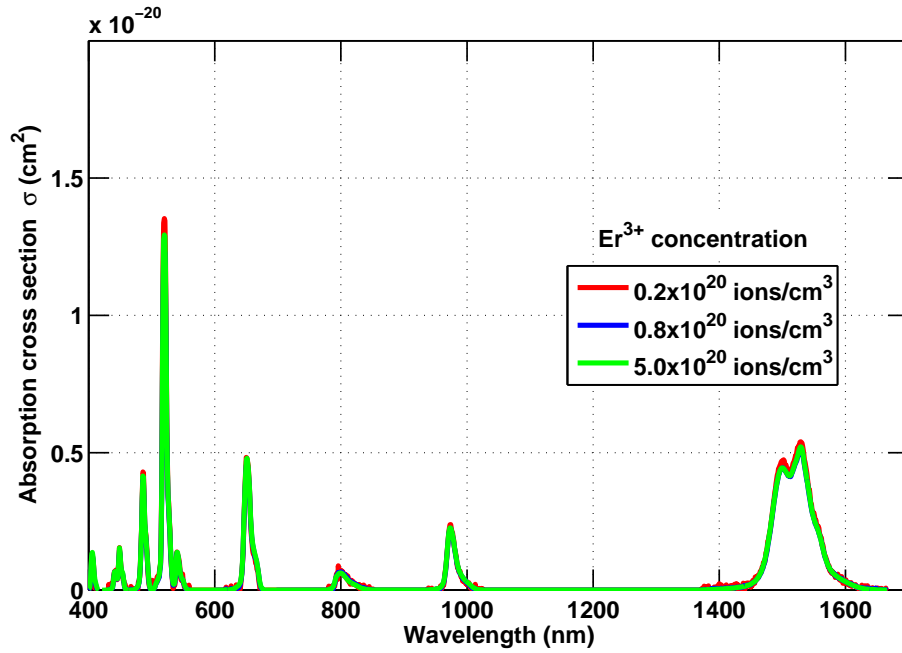
Figure 2.3: Absorption cross-section of bulk glass Er:ZBLAN samples.

Table 2.2: Summary of absorption cross-sections of the first five ground transitions in Er:ZBLAN compared to literature values.

Transition in Er^{3+}:ZBLAN	Peak wavelength (nm)	Cross-section ($\times 10^{-21}$ cm^2)	Reference
$^4I_{15/2} \to {}^4I_{13/2}$	1530	5.23 ± 0.14	This work
		5.27 ± 0.09	[146]
		5.25	[159]
$^4I_{15/2} \to {}^4I_{11/2}$	974	2.29 ± 0.08	This work
		2.35 ± 0.15	[146]
		2.2	[148]
$^4I_{15/2} \to {}^4I_{9/2}$	800	0.67 ± 0.04	This work
		0.69 ± 0.01	[146]
		0.67	[91]
$^4I_{15/2} \to {}^4F_{9/2}$	651	4.68 ± 0.15	This work
		5.0 ± 0.3	[146]
		4.8	[159]
$^4I_{15/2} \to$ $^4S_{3/2}/^2H_{11/2}$	520	12.9 ± 0.6	This work
		13.3 ± 0.4	[146]
		12.8	[159]

2.4   Fluorescence lifetime

An additional spectroscopic property of ZBLAN glass needed for the characterization of the host glass is the lifetime of excited states and the rate at which multi-phonon decay depopulates them. It was initially planned to measure the lifetimes of excited states in bulk glass. However, lack of a suitable source that could pump directly into $^4I_{9/2}$ (800 nm) and $^4F_{9/2}$ (655 nm) required us to use data from the literature instead, which is presented in the coming section. We initially describe the Judd-Ofelt method, which enables obtaining the radiative lifetimes of energy levels by measuring their absorption spectra. By comparing literature values of the calculated radiative lifetimes to measured lifetimes from various literature sources, we obtain the non-radiative decay rates applicable to ZBLAN glass. Later in this work, it became necessary to measure the lifetimes of the excited states of a doped fibre while it was being pumped. This latter approach is discussed in section 5.3.

2.4.1   Judd-Ofelt analysis and energy levels lifetime

It is possible to calculate the theoretical emission properties of different energy levels of Er^{3+} ions in ZBLAN glass using measured absorption cross-sections values. This analysis is common for the characterisation of new laser materials by examining their luminescence properties. This technique is named after Judd and Ofelt who described it independently for the first time [160, 161]. A brief background for the Judd-Ofelt analysis is presented below.

The Judd-Ofelt analysis compares measured absorption dipole oscillator strength P_{exp} and the theoretical electric P_{ed} and magnetic P_{md} absorption dipole oscillators strength

$$P_{exp} = P_{ed} + P_{md}. \tag{2.5}$$

The measured absorption oscillator strength P_{exp} is derived from the area under the absorption cross-section curve for each absorption band, which in the common CGS representation is

$$P_{exp} = \frac{m_e c^2}{\pi e^2} \frac{1}{\lambda_b^2} \int \sigma_{abs} d\lambda, \tag{2.6}$$

where m_e is the electron mass, c is the speed of light, e is the electron charge (in esu) and λ_b is the absorption band barycentre defined using the absorbance E by

$$\lambda_b = \frac{\int E\lambda d\lambda}{\int E d\lambda}. \tag{2.7}$$

The theoretical electric and magnetics dipole oscillator strengths are

$$P_{ed} = \frac{8\pi^2 m_e c}{3h} \frac{1}{(2J+1)} \frac{1}{\lambda_b} \hat{n} \sum \Omega_t \cdot \left\| U^{(t)} \right\|^2 \tag{2.8}$$

$$P_{md} = n \cdot P'_{md} = n \cdot \left(\frac{h}{6 m_e c} \frac{1}{(2J+1)} \frac{1}{\lambda_b} LS \right) \tag{2.9}$$

where h is Plank's constant, J is the total angular momentum quantum number of the ground state (15/2 for the case of Er^{3+}) and $\hat{n} = (n^2 + 2)^2/9n$ is a parameter based on the host refractive index at the specific wavelength band barycentre. Ω_t is three host dependent Judd-Ofelt parameters determined by solving Equation 2.5 which equates the experimentally found oscillator strength (Equation 2.6) and the theoretically calculated one (Equations 2.8 and 2.9). $\left\| U^{(t)} \right\|^2$ and LS are matrix parameters which are independent of the host. The $\left\| U^{(t)} \right\|^2$ matrix contains parameters which are associated with all possible ground, as well as excited state transitions $i \rightarrow j$. Values for $\left\| U^{(t)} \right\|^2$ and LS elements can be found in the literature, with data for Er^{3+} ions found for example in [146, 162]. To calculate the three Ω_t parameters, the absorption spectra of three different transitions must be obtained. Increasing the number of spectra used improves the accuracy of the fitted Ω_t parameters.

Once the Ω_t parameters have been calculated, they can be used to find the theoretical radiative decay rates. These rates are due to spontaneous emissions from each energy level using the appropriate $\left\| U^{(t)} \right\|^2$ following

$$A_{ed} = \frac{64\pi^4}{3h} \frac{\tilde{\nu}_b^3}{2J+1} n^2 \hat{n} e^2 \sum_{t=2,4,6} \Omega_t \cdot \left\| U^{(t)} \right\|^2 \tag{2.10}$$

$$A_{md} = \frac{8\pi^2 e^2 \tilde{\nu}_b^2 n^3}{m_e c \hat{n}} P_{md}, \tag{2.11}$$

where $\tilde{\nu}_b$ is the absorption spectra wavenumber barycentre with cm^{-1} units. The total decay rate is the sum of the electric and magnetic dipole rates, $A = A_{ed} + A_{md}$. The radiative lifetime τ_{r_i} of an energy level i is the inverse of the sum over all radiative decay rates from the ith level, A_i

$$\tau_{r_i} = \frac{1}{\sum_j A_{ij}} = \frac{1}{A_i}, \tag{2.12}$$

with A_{ij} being the radiative decay rate from energy level i to a lower level j. The branching ratio β_{ij}, or percentage of the radiative decay from level i to a lower level j compared with the total decay rate is defined by

$$\beta_{ij} = \tau_{r_i} A_{ij}. \tag{2.13}$$

The theoretical lifetimes (which are usually referred to as "radiative lifetime") of the energy levels of Er^{3+} ions in ZBLAN glass can be derived using the equations above. Judd-Ofelt analysis has been presented in literature many times before for bulk Er:ZBLAN glass drawn into fibre, for example [147] and also when used for fibre lasers [127, 146]. Since our glass samples were not drawn into fibres, we chose to use literature values of the Judd-Ofelt parameters calculated by Caspary [146] for the seven lowest energy levels of Er^{3+}:ZBLAN. These are shown in table 2.3. The table includes the calculated energy gap k_{calc} and wavelength λ_{calc}, reduced matrix elements $\left\|U^{(t)}\right\|^2$, magnetic dipole contribution $\left\|M/\beta_m\right\|^2$, electric ($A_{ed}$) and magnetic ($A_{md}$) dipole transition rates and the branching ratios associates with each of the first seven energy levels and its transitions to lower laying levels. The dataset presented by Caspary was chosen for its rigour and completeness and is used throughout this thesis as the basis for theoretical radiative lifetime values.

In the next section, we combine the calculated and measured literature lifetime data to find consistent non-radiative decay values for Er^{3+}:ZBLAN.

2.4.2 Analysis of radiative and non-radiative lifetime data from literature

Energy level lifetimes are one of the properties calculated using Judd-Ofelt analysis. The results obtained are labeled "radiative" lifetimes since they do not take into account non-radiative processes such as multi-phonon decay and other energy-transfer processes. The lifetime observed in measurement, or "intrinsic" lifetime, can only be determined experimentally.

The intrinsic lifetime is the result of a combination between the radiative lifetime. Any other non-radiative decay effect and its measurement is described later in this section. The low phonon-energy of ZBLAN glass causes the effect of multi-phonon decay to be very noticeable in reducing the lifetime of many energy levels compared with the calculated radiative lifetime. This is in contrast to other gain media with higher phonon-energy where transitions that are affected by multi-phonon decay are depopulated very rapidly and thus emit almost no fluorescence. The lifetime of energy levels not affected by multi-phonon decay in the same gain media will be similar to the calculated radiative lifetime.

To obtain separate values for the non-radiative decay rates, it is necessary to perform direct measurement of the decay lifetime of excited states and compare it to calculated radiative decay rates. We did not have a suitable source for such a measurement

Table 2.3: Judd-Ofelt parameters ($\left\|U^{(t)}\right\|^2$), electric (A_{ed}) and magnetic (A_{md}) dipole decay rates and branching ratios (β) of Er^{3+}:ZBLAN; reproduced from Caspary [146]. k_{calc} and λ_{calc} represent the calculated wavenumber and wavelength respectively of the line centre of the transition obtained from the Judd-Ofelt fit.

final	k_{calc} cm^{-1}	λ_{calc} nm	$|U^{(2)}|^2$	$|U^{(4)}|^2$	$|U^{(6)}|^2$	$|M/\beta_m|^2$	A_{ed} s^{-1}	A_{md} s^{-1}	β
		initial: $^4F_{7/2}$						$\tau = 0.34\,ms$	
$^2H^{(2)}_{11/2}$	1330	7521	0.1246	0.0158	0.3980	0.0000	0	0	0.000
$^4S_{3/2}$	2083	4800	0.0001	0.0052	0.0000	0.0000	0	0	0.000
$^4F_{9/2}$	5232	1911	0.0120	0.0360	0.0130	6.4133	4	10	0.005
$^4I_{9/2}$	8055	1242	0.0159	0.0959	0.4300	1.8014	99	11	0.037
$^4I_{11/2}$	10301	971	0.0034	0.2660	0.1541	0.0000	174	0	0.059
$^4I_{13/2}$	13952	717	0.0000	0.3383	0.0001	0.0000	370	0	0.125
$^4I_{15/2}$	20487	488	0.0000	0.1467	0.6283	0.0000	2301	0	0.775
		initial: $^2H^{(2)}_{11/2}$						$\tau = 0.26\,ms$	
$^4S_{3/2}$	754	–	0.0000	0.2000	0.0096	0.0000	0	0	0.000
$^4F_{9/2}$	3902	2562	0.3683	0.0228	0.0017	0.2819	12	0	0.003
$^4I_{9/2}$	6725	1487	0.2021	0.0661	0.2844	0.2632	56	1	0.015
$^4I_{11/2}$	8971	1115	0.0356	0.1383	0.0370	1.3507	46	7	0.014
$^4I_{13/2}$	12622	792	0.0230	0.0607	0.0523	3.7573	80	58	0.036
$^4I_{15/2}$	19158	522	0.7091	0.4106	0.0934	0.0000	3625	0	0.933
		initial: $^4S_{3/2}$						$\tau = 0.73\,ms$	
$^4F_{9/2}$	3149	3176	0.0000	0.0002	0.0254	0.0000	1	0	0.000
$^4I_{9/2}$	5971	1675	0.0000	0.0756	0.2539	0.0000	47	0	0.035
$^4I_{11/2}$	8217	1217	0.0000	0.0049	0.0783	0.0000	30	0	0.022
$^4I_{13/2}$	11868	843	0.0000	0.0000	0.3403	0.0000	369	0	0.271
$^4I_{15/2}$	18404	543	0.0000	0.0000	0.2233	0.0000	915	0	0.672
		initial: $^4F_{9/2}$						$\tau = 0.86\,ms$	
$^4I_{9/2}$	2823	3543	0.1256	0.0060	0.0249	11.5670	2	2	0.004
$^4I_{11/2}$	5069	1973	0.0709	0.0106	1.2752	4.8271	49	6	0.047
$^4I_{13/2}$	8720	1147	0.0105	0.1536	0.0775	0.0000	50	0	0.043
$^4I_{15/2}$	15255	656	0.0000	0.5431	0.4637	0.0000	1053	0	0.906
		initial: $^4I_{9/2}$						$\tau = 6.78\,ms$	
$^4I_{11/2}$	2246	4452	0.0026	0.0681	0.1379	10.6725	1	1	0.011
$^4I_{13/2}$	5897	1696	0.0004	0.0099	0.7159	0.0000	38	0	0.260
$^4I_{15/2}$	12432	804	0.0000	0.1670	0.0090	0.0000	108	0	0.729
		initial: $^4I_{11/2}$						$\tau = 7.87\,ms$	
$^4I_{13/2}$	3651	2739	0.0332	0.1705	1.0886	20.7669	14	8	0.171
$^4I_{15/2}$	10186	982	0.0279	0.0003	0.3937	0.0000	105	0	0.829
		initial: $^4I_{13/2}$						$\tau = 8.52\,ms$	
$^4I_{15/2}$	6535	1530	0.0195	0.1173	1.4328	18.8413	83	34	1.000

therefore we conducted a literature study. Published data of lifetimes in Er:ZBLAN mostly concentrated on the levels associated with the 2.75 μm lasing transition, namely $^4I_{13/2}$, $^4I_{11/2}$ and $^4S_{3/2}$, see [127, 135, 146, 147, 163]. The latter energy level, although not directly involved with the lasing action, is populated by excited-state absorption of 974 nm pump from $^4I_{11/2}$. Our DWP scheme requires knowledge of the lifetime properties of $^4I_{9/2}$ and $^4F_{9/2}$ levels as well.

Several publications detail investigation of the lifetimes of the $^4I_{11/2}$, $^4I_{9/2}$ and $^4F_{9/2}$ levels in Er:ZBLAN with direct pumping [135, 147, 159, 163]. Unfortunately, none of those sources contained a full Judd-Ofelt analysis which was accompanied with measured lifetimes of the levels relevant to our work. We therefore conducted a study of available literature data and combined results from those multiple sources. The end goal of this investigation was to reach a better understanding of the expected measured lifetime and non-radiative decay rates associated with those energy levels.

A typical setup for lifetime measurements (see Figure 2.4) uses excitation by a short pulse duration source, usually an optical parametric oscillator. These sources can
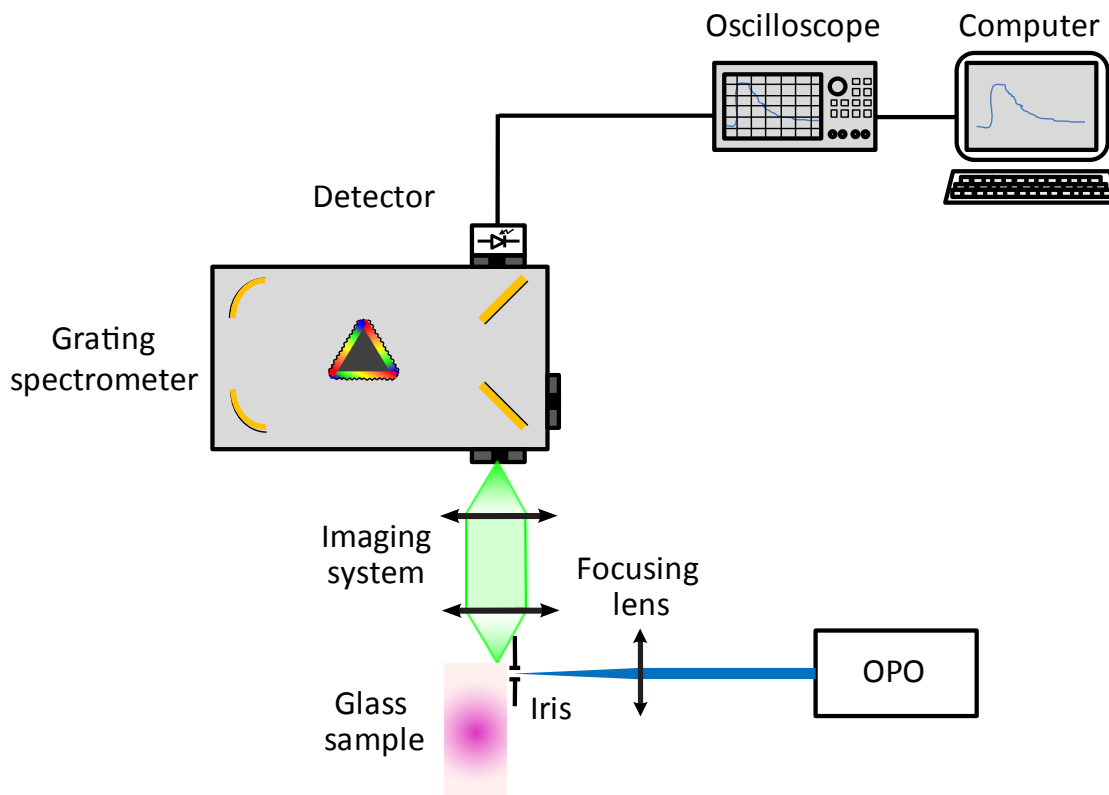
Figure 2.4: Schematics of a typical bulk glass lifetime measurement setup.

provide short pulses on the order of hundreds of femto-seconds to a few nano-seconds, which are much shorter than the intrinsic lifetime of the levels investigated. The tunable source beam is focused onto the glass sample and fluorescence is collected through a

spectrometer used for wavelength discrimination onto a fast detector. Radiation trapping is a phenomenon that increases the observed lifetime of the excited level. It is caused by repeated re-absorption and fluorescing cycles by neighbouring ions resulting in an increase in the observed fluorescence lifetime from the sample. Minimisation of this effect is achieved by collecting the fluorescence from the edge of the sample or by using a pinhole on the surface of the sample [164].

Samples with low doping are usually used when intrinsic lifetimes are measured for the purpose of obtaining multi-phonon rates. This is done to minimise energy-transfer (ET) and cross-relaxation (CR) processes, which can dominate the temporal behaviour when high doping concentrations are concerned. The collection of data concerning ET and CR effects is also of interest and most literature presents lifetime information for Er^{3+}:ZBLAN as a function of doping [77, 135, 159, 163].

Consider an energy level N_1 that has reached a steady state population when pumped with a constant pump power. If the pumping is abruptly stopped and the level is only depopulated by a radiative process with a rate A_r and a non-radiative process ω_{nr}, it will follow a rate equation of the form:

$$\frac{dN_1(t)}{dt} = -(A_r + \omega_{nr})N(t). \tag{2.14}$$

Equation 2.14 has a solution in the form of a product of two exponential decays, one radiative with a time constant τ_r and another non-radiative with a different time constant τ_{nr}

$$N(t) = N_1(0)e^{-t\left(\frac{1}{\tau_r} + \frac{1}{\tau_{nr}}\right)}, \tag{2.15}$$

where $N_1(0)$ is the population when pumping has stopped.

Once the measured lifetime τ_m of an energy level has been found experimentally the non-radiative decay rate due to multi-phonon decay (A_{nr}) can be determined using the radiative rate A_r. A_r is the sum of the calculated electric and magnetic dipole radiative rates taken from Table 2.3

$$A_r = A_{ed} + A_{md}, \tag{2.16}$$

and while using the relation $A = 1/\tau$ according to

$$\frac{1}{\tau_{nr}} = \frac{1}{\tau_m} - \frac{1}{\tau_r}, \tag{2.17}$$

or in the form of decay rates

$$A_{nr} = A_m - A_r. \tag{2.18}$$

Table 2.4 contains a comparison between different lifetime values obtained from the literature. Where the source provided both intrinsic and radiative lifetimes, we calculated the multi-phonon rates and added them to a separate column in Table 2.4. The commonly cited work of Shinn et al. [151] is not included because of the slightly different glass used.

Table 2.4: Literature values of intrinsic (τ_m) and radiative (τ_r) lifetime results for different energy levels in Er^{3+}:ZBLAN. Non-radiative rates are calculated in the cases where both radiative and measured lifetimes were given in the data source. Lifetimes data are for room temperature and the following doping concentrations: [127, 146, 163] - 0.1 $mol\%$, [135] - 0.2 $mol\%$ [147] - 0.5 $mol\%$

Energy level	Energy gap to next lower level (cm^{-1})	Radiative lifetime (τ_r), based on Judd-Ofelt analysis	Measured (intrinsic) lifetime (τ_m)	Calculated non-radiative rate to next level (sec^{-1})	Data source
$^4I_{13/2}$	6535	8.52 ms			[146]
		9.52 ms	8.69 ms	Uncertainty	[127]
	$\rightarrow {}^4I_{15/2}$	9.8 ms	9.5 ms	too high,	[135]
		7.1 ms	16.2 ms	thus not calculated	[147]
$^4I_{11/2}$	3651	7.87 ms			[146]
		8.69 ms	6.71 ms	34	[127]
	$\rightarrow {}^4I_{13/2}$	8.7 ms	7.7 ms	8	[135]
		7.5 ms	7.32 ms	3.6	[147]
$^4I_{9/2}$	2246	6.78 ms			[146]
		6.5 ms	7.9 μs	125,000	[135]
	$\rightarrow {}^4I_{11/2}$		10 μs		[163]
$^4F_{9/2}$	2823	0.86 ms			[146]
			0.59 ms		[127]
	$\rightarrow {}^4I_{9/2}$	0.92 ms	163 μs	4565	[135]
		0.936 ms	52 μs	18,200	[147]
			230 μs		[163]
			148 μs		This work
$^4S_{3/2}$	3149	0.73 ms			[146]
		0.70 ms	0.57 ms	325	[127]
	$\rightarrow {}^4F_{9/2}$	0.74 ms	0.53 ms	533	[135]
		0.745 ms	0.354 ms	1480	[147]
			0.56 ms		[163]

The calculated radiative lifetimes in table 2.4 are fairly consistent, with only slight variations between literature sources. In contrast, the measured lifetimes exhibited significant variations between sources. The observable different values obtained by Zou

and Izumitani in [147], especially for the case of $^4I_{13/2}$, were somewhat difficult to explain. Even their higher doping concentration of 0.5 $mol\%$ Er^{3+} ions should not have made such a large difference. Their indirect method of populating some of those levels may have caused the increased lifetime of $^4I_{13/2}$. Large variations in the measured lifetime of the $^4F_{9/2}$ level between the different sources were also of interest. An especially long $^4F_{9/2}$ lifetime observed by Wetenkamp in [127] was also difficult to explain. Other sources and our own investigations of $^4F_{9/2}$ lifetime inside a ZBLAN fibre, described in section 5.3, point to a much shorter lifetime of less than 200 μs. Using the average values of each level lifetime and excluding the outliers, we can construct an averaged estimate for the non-radiative rate in ZBLAN glass, summarised in Table 2.5.

Table 2.5: Average non-radiative decay rates in Er:ZBLAN, derived from literature values shown in table 2.4 with outliers excluded.

Transition	Energy gap to underlying level (cm^{-1})	Average radiative lifetime to ground $^4I_{15/2}$ (τ_r)	Average measured lifetime to ground $^4I_{15/2}$ (τ_m)	Average NR rate (A_{nr}) (s^{-1})
$^4I_{13/2} \rightarrow {}^4I_{15/2}$	6535	9.28 ms	9.1 ms	2
$^4I_{11/2} \rightarrow {}^4I_{13/2}$	3651	8.14 ms	7.32 ms	14
$^4I_{9/2} \rightarrow {}^4I_{11/2}$	2246	6.64 ms	9.0 μs	111,000
$^4F_{9/2} \rightarrow {}^4I_{9/2}$	2823	0.91 ms	180 μs	4,457
$^4S_{3/2} \rightarrow {}^4F_{9/2}$	3149	0.73 ms	0.55 ms	448

The values in table 2.5 enabled us to find an average trend for multi-phonon decay in ZBLAN glass. An exponential model for the multi-phonon decay rate can be found based on a crystal model applied to glasses by Layne et al. [59]

$$W_{mp} = K \left(n(T) + 1 \right)^p exp(-\alpha'' \Delta E),$$
(2.19)

where K and α'' are host dependent constants, $n(T)$ is the occupation of the relevant level, p is the number of phonons involved in the transition and ΔE is the energy gap bridged. This equation is often simplified for room temperature values using

$$W_{mp} = C exp(-\alpha' \Delta E),$$
(2.20)

where C and α' are material and temperature dependent coefficient which are determined experimentally, while ΔE is the energy gap between adjacent energy levels. For a good fit of the parameters, it is necessary to use various dopant ions to be able to measure different energy gaps. In addition, the samples used must have low doping concentrations to avoid the influence of energy-transfer processes which are commonplace in higher doping concentrations.

Figure 2.5 places the average multi-phonon rates summarised in Table 2.5 against a variety of different ZBLAN glass multi-phonon rate models used in literature. In this case,
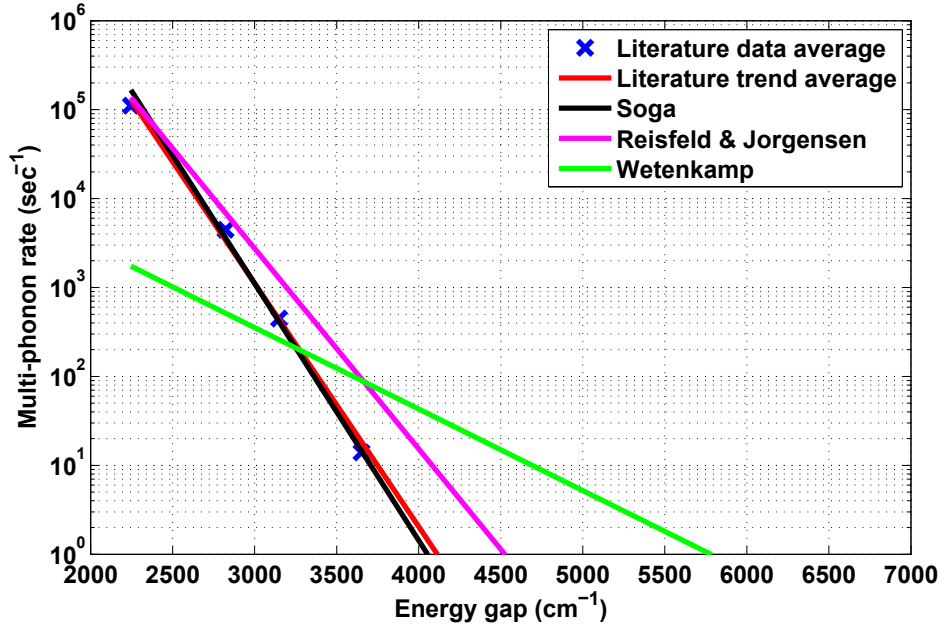
Figure 2.5: Comparison of different multi-phonon rate models at room temperature from literature. Red - average trend from table 2.5, black - Soga et al. [165], magenta - Reisfeld and Jorgensen [166] and green - Wetenkamp [127].

our average fit (red in Figure 2.5) with values of $\alpha' = 0.0063\,cm^{-1}$ and $C = 1.8 \times 10^{11}\,s^{-1}$ was very close to the fit found by Soga et al. [165] which used $\alpha' = 0.00665\,cm^{-1}$ and $C = 5.11 \times 10^{11}\,s^{-1}$. These values are very far from the commonly used values obtained by Wetenkamp [127] with $\alpha' = 0.0021\,cm^{-1}$ and $C = 1.99 \times 10^5\,s^{-1}$, depicted in green in Figure 2.5.

ZBLAN glass with its heavy elements and weak bonds has a comparatively low maximum phonon energy of $\approx 565\,cm^{-1}$ compared with the silica glass value of $\approx 1100\,cm^{-1}$. This enables ZBLAN fibres to be transparent up to about 4 μm in contrast with 2.5 μm for silica (see Table 2.1). A comparison of literature values of multi-phonon decay rates of various glass families is shown in Figure 2.6.

The curves in Figure 2.5 demonstrate the strong dependency of the multi-phonon decay rate on the energy gap between adjacent levels. The number of phonons that the glass matrix can support also depends on the material temperature. A higher temperature increases the number of phonons available according to a Boltzmann-like distribution. Such behaviour raises the multi-phonon decay rate at temperatures considerably higher than absolute zero. Following theoretical work by Riseberg and Moos
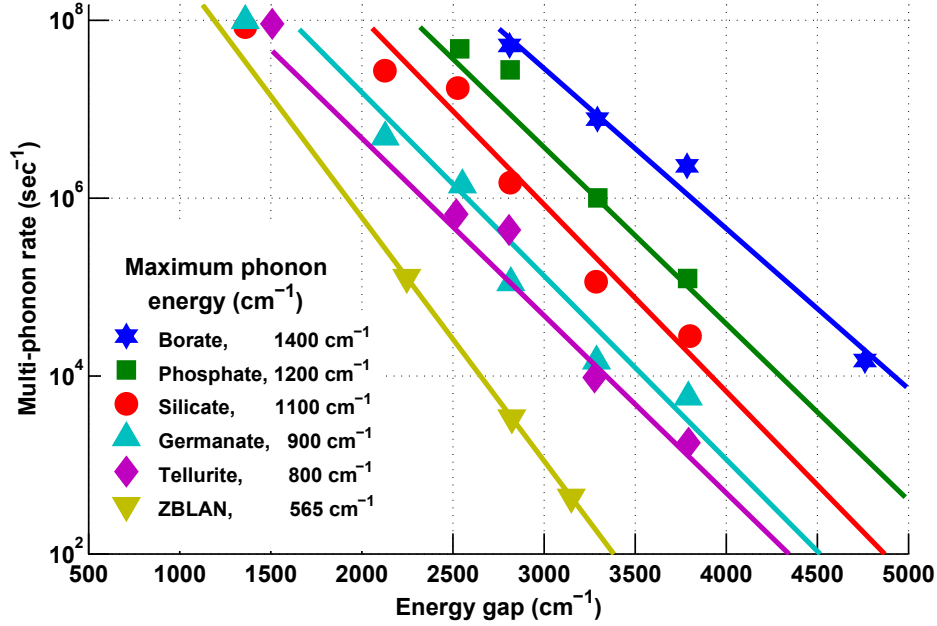
Figure 2.6: Comparison of multi-phonon rates for different glass families as a function of energy gap between levels. Adapted from Layne [59] with the addition of ZBLAN information from this section. Maximum phonon energy for each glass family is displayed as well.

[167] and experiments by Layne et al. [59], Equation 2.19 can be expanded to include the temperature dependency of the multi-phonon decay rate in glass

$$W_p = C \left[\frac{1}{e^{\hbar\nu/k_B T} - 1} + 1 \right]^p e^{-\alpha\Delta E}. \tag{2.21}$$

Here, $\hbar\omega$ is a single frequency equivalent to the maximum phonon energy supported by the glass matrix, k_B is Boltzmann's constant and T the temperature in Kelvin. We assumed an integer number of phonons of the maximum energy are involved in the decay. This approach has been verified experimentally both in crystals [167, 168] and in glasses [59]. It is therefore instructive to see the predicted multi-phonon decay rate change as a function of temperature for the required laser transition $^4F_{9/2} \rightarrow {}^4I_{9/2}$ and the transition below it $^4I_{9/2} \rightarrow {}^4I_{11/2}$. Both transitions are shown in Figure 2.7. We can see that for the lasing transition with an energy gap of 2823 cm^{-1}, the calculated change in decay rate for a $50°K$ increase in fibre temperature from room temperature is only about 20%. This behaviour will be discussed further in section 5.3.

The importance of finding the correct multi-phonon values lies in applying those values in future numerical rate-equation analysis that will be used to simulate the DWP laser.
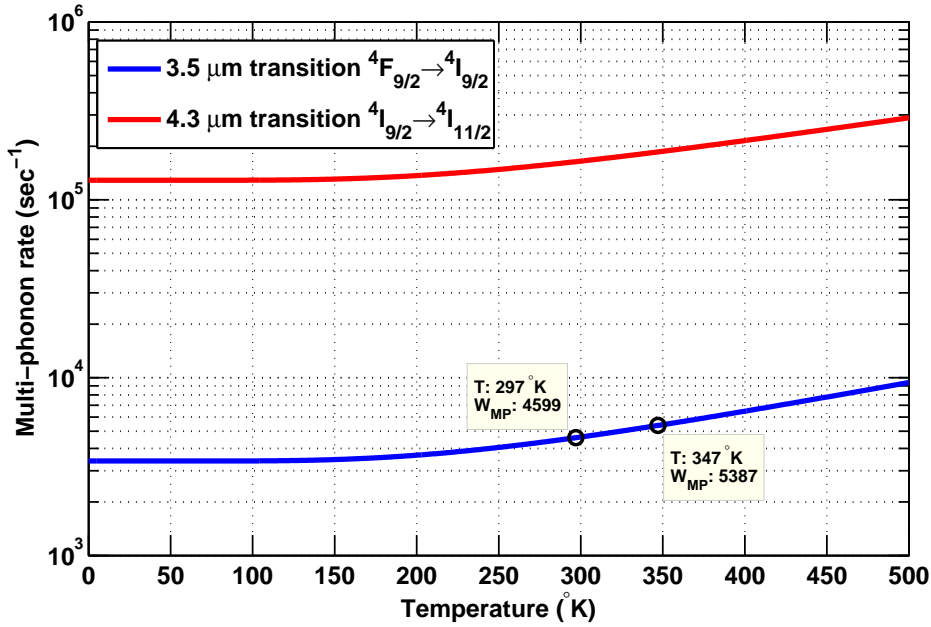
Figure 2.7: Calculated multi-phonon rate change with temperature for two ZBLAN glass transitions: the lasing transition $^4F_{9/2} \to {}^4I_{9/2}$ and the transition underneath it $^4I_{9/2} \to {}^4I_{11/2}$.

2.4.3   Energy-transfer and cross-relaxation processes

Er^{3+} ions can support numerous cross-relaxation (CR) and energy-transfer (ET) processes. The abundance of these processes is the result of the large number of energy levels accessible to the Er^{3+} ion. This can effectively redistribute energy between neighbouring ions using phonon-assisted ET processes. Determining the CR and ET processes macro-parameters was of significant importance for understanding the spectroscopic behaviour of Er^{3+}:ZBLAN. An example can be found in Pollnau and Jackson's work predicting a significant increase in laser efficiency of the $^4I_{11/2} \to {}^4I_{13/2}$, 2.75 μm transition. This is because of the increased rate f the $^4I_{13/2} +^4 I_{13/2} \to {}^4I_{9/2} + {}^4I_{15/2}$ ET process at high doping concentration, which removes a bottleneck in the lower lasing level and improves laser efficiency [114] (See also section 1.4.2.4). Their work showed that it is theoretically possible to exceed the Stokes efficiency from this transition. Recent work by Faucher et al. [136] demonstrated such behaviour for the first time.

We saw in Equation 2.15 that when there are no CR or ET processes, the fluorescence from an energy level after its direct excitation follows an exponential decay. When CR and ET processes are present the fluorescence decay behaviour becomes more complicated. The most common approach for measuring the CR and ET rate parameters involves observing changes in the shape and time constants of fluorescence decay after direct excitation of an energy level [77, 169].

CR processes, which involve energy sharing of ions from different levels, maintain an exponential decay of the fluorescence. An example can be found in a process that involves the ground state, N_0 and an additional energy level N. In this case, the rate equation for the population density of N after the pumping has ceased is

$$\frac{dN(t)}{dt} = -(A_{int})N(t) - WN_0(t)N(t), \tag{2.22}$$

where $A_{int} = 1/\tau_{int}$ is the intrinsic decay rate of the energy level including multi-phonon decay, W is the rate coefficient for the CR process involved and $N_0(t)$ is the ground state ion density. $N_0(t) \approx N_0(0) \approx C$ under the assumption of small perturbation to the ground state. Therefore, Equation 2.22 can be simplified to

$$\frac{dN(t)}{dt} = -\frac{N(t)}{\tau_{int}} - W_{CR}N_0N(t), \tag{2.23}$$

which has a solution following an exponential decay of the form

$$N(t) = N(0)\exp-(\frac{1}{\tau_{int}} + W_{CR}N_0). \tag{2.24}$$

The CR process most researched in relation to the 2.75 μm lasing in Er^{3+}:ZBLAN was the process $^2H_{11/2} + ^4I_{15/2} \rightarrow ^4I_{9/2} + ^4I_{13/2}$, denoted by W_{50}. This process is dependent on the total ion population, or ground level population prior to pumping - N_0. Therefore, by pumping directly into the $^4S_{3/2}/^2H_{11/2}$ level and measuring the lifetime of samples with different dopant concentrations, the CR rate was found using

$$\frac{1}{\tau_{5_{eff}}} = \frac{1}{\tau_{5_{int}}} + W_{50}N_0, \tag{2.25}$$

where $\tau_{5_{eff}}$ denotes the effective fluorescence lifetime wherein $\tau_{5_{int}}$ was the intrinsic lifetime of the $^4S_{3/2}/^2H_{11/2}$ levels at very low doping concentration. The parameter values found by Golding in [77] for different Er^{3+} doping concentrations are shown in Table 2.6.

ET processes involving two ions from the same levels cause the fluorescence decay rate to change to a non-exponential one. This follows from the rate equation generally associated with such a case

$$\frac{dN(t)}{dt} = -\frac{N(t)}{\tau_{int}} - W_{ETU}N^2(t). \tag{2.26}$$

This rate equation has a non-exponential decay solution of the form

$$\frac{N_0}{N(t)}exp(-t/\tau) - 1 = 2W_{ETU}N_0\tau[1 - exp(-t/\tau)]. \tag{2.27}$$

This equation can be applied to the W_{11} or W_{22} processes in Er^{3+}:ZBLAN, which depopulate the $^4I_{11/2}$ or $^4I_{13/2}$ levels. W_{ETU} represents the rate of W_{11} or W_{22} ETU processes. Golding et al. showed that upon direct excitation of the $^4I_{11/2}$ and $^4I_{13/2}$ levels, the fluorescence did not decay exponentially either. The initial few ms exhibited a fast, non-exponential decay, which was dependent on the initial excitation energy used. After the rapidly-decaying component had subsided, the fluorescence decay reverted to an ordinary exponential decay form independent from the initial population density. Golding et al. attributed the fast decays to the two aforementioned energy-transfer upconversion (ETU) processes of the forms $^4I_{13/2} +^4 I_{13/2} \rightarrow\ ^4I_{9/2} + ^4I_{15/2}$ and $^4I_{11/2} +^4 I_{11/2} \rightarrow\ ^4F_{7/2} + ^4I_{15/2}$ denoted by W_{11} and W_{22}, respectively. The W_{11} and W_{22} rate parameters were found by finding the slope of the curve which corresponds to $2W_{ETU}N_0\tau$ at time $t = 0$ since this is when the ETU process is most prominent.

The ETU parameters, which were measured in bulk ZBLAN glass by Golding et al. [77], are on the order of 10^{-17} cm^3/s and are referred to in this work as the "strongly interacting" (SI) parameters. These values were used extensively in the literature until recently when a new, "weakly interacting" (WI) approach was introduced by Gorjan et al. [86] and later extended by Li and Jackson [170]. The WI approach asserts that CR and ETU processes are considerably weaker in ZBLAN fibres than in bulk glass, with values on the order of 5×10^{-19} cm^3/s. The WI-based CR and ETU parameter values were found numerically by Gorjan et al. when fitting experimental data to a set of rate-equations. Both approaches are currently in use and values of CR and ETU parameters for both are presented in Table 2.6.

Table 2.6: Macroscopic CR and ETU parameters in Er^{3+}:ZBLAN for different doping concentrations. Ordinary parameters from Golding et al. [77] are denoted "SI" for "strongly interacting" while "weakly interacting" parameters are in the "WI" row and are based on data from Li and Jackson [170]. Macroscopic CR and ETU parameters for Er^{3+} concentrations relevant to this work, which fall in between values found in literature, were interpolated (*) or extrapolated (‡) according to the curves provided in [77, 170].

	Parameter	Value						
	Er^{3+} mol %	0.25	1	1.25	1.7	4	5.00	8.75
	Er^{3+} $\times 10^{20}$ $ions/cm^3$	0.4	1.6	2	2.7	6.4	8	14
SI	CR W_{50}	0.6	0.48*	0.6	0.8*	1.9*	2.4	3.3
	ETU W_{11} $\times 10^{-17}$ cm^3/s		1.3‡	1.3	1.4*	2.2*	2.8	6.7
	ETU W_{22}		0.16‡	0.2	0.3*	0.8*	1.0	1.9
WI	CR W_{50}		0.1‡	0.12‡	0.17‡	0.38	0.46*	0.6
	ETU W_{11} $\times 10^{-18}$ cm^3/s		0.4‡	0.4‡	0.4‡	0.6	0.8*	1.8
	ETU W_{22}		0.08‡	0.09‡	0.1‡	0.2	0.26*	0.43

Recent numerical analysis based on the WI approach has been more successful in reproducing experimental results that could not be explained using SI-based numerical analysis in ZBLAN fibre lasers [86, 170–172]. However, no physical mechanism has been identified so far to explain the discrepancy between the SI results in bulk glass and WI simulated values in fibres. During our spectroscopic investigations, both sets of parameters were used where applicable with the results compared, see for example section 5.4.3.

Beyond the processes recognised by Golding et al., there are numerous possible spectroscopic processes available in Er^{3+}:ZBLAN, most of them are less known. Many of those processes were investigated independently by Bogdanov [135]. In his work, Bogdanov showed that beyond the common two ions processes, there was room to include three ions processes that could influence behaviour to some extent (see examples in Figure 2.8).

Bogdanov demonstrated that by including three ion interactions, it was possible to achieve better consistency between simulated and measured fluorescence rise and fall waveforms. Three-ion interactions were shown to be particularly important at high Er^{3+} concentrations over 6 mol% and when observing fluorescence rise and decay waveforms of levels under non-direct pumping conditions [85, 135, 173].
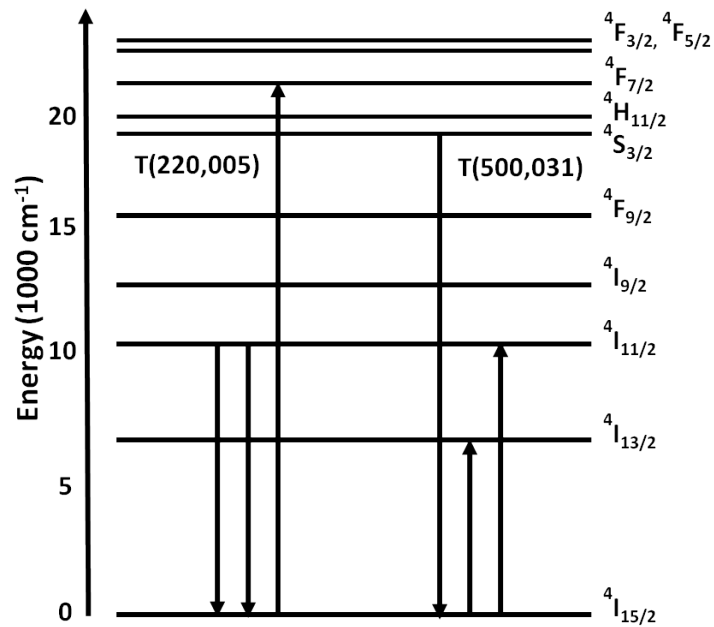
Figure 2.8: Three ion energy-transfer process based on the work of Bogdanov [85]. The transition notation is based on [169]. It describes the energy levels of the donor ions on the left and the accepting ions on the right. The T(220,005) requires the emission of a phonon to conserve energy.

Three ion processes appeared to have relatively small cross-sections. This made them more relevant for higher doping of Er^{3+} ions, where the interaction between neighbouring

ions was more likely. Additional two and three ion processes were also described in [135, 173] but their influence was negligible in a low doping regime such as in our work. Current literature tends to only use two ion interaction processes and good agreement with experimental results is achieved (see [86, 174]). We therefore decided to exclude three ion interactions from the scope of this work.

2.5 Emission cross-sections in Er^{3+}:ZBLAN

The magnitude of the emission cross-sections of laser transitions determine the gain of a specific transition. The spectroscopic investigation of many glass samples culminates in obtaining the emission cross-section after measuring absorption cross-sections and energy level lifetimes. These two are needed in order to obtain the emission cross-section which is difficult to determine directly.

Direct measurement of emission cross-sections requires a careful unbiased collection of all photons emitted isotropically over a certain wavelength. Since this is often very difficult to achieve, two common alternatives have been employed to determining the emission cross-section. The McCumber relation is a method based on the absorption cross-section of the same transition which has a reciprocal relation to the emission cross-section. The Fuchtbauer-Ladenburg method normalises the fluorescence curve obtained from the relevant transition to obtain the emission cross-section by using the radiative lifetime as a base for the normalisation.

The McCumber relation [175] links the emission $\sigma_e(\lambda)$ and absorption $\sigma_{abs}(\lambda)$ cross-section

$$\sigma_e(\lambda) = \sigma_{abs}(\lambda) exp\left(\frac{\epsilon - h\nu}{k_B T}\right), \qquad (2.28)$$

k_B is Boltzman's constant, T the absolute temperature and ϵ is the net free energy difference between the two manifolds involved and is related to their partition functions at the calculated temperature.

We can find $exp(\epsilon/k_B T)$ based on the ratio between the partition functions of the lower and upper manifolds N_l and N_u

$$exp\left(\frac{\epsilon}{k_B T}\right) = \frac{N_l}{N_u} = \frac{1 + \sum_{j=2}^{C_s} exp(-E_{1j}/k_B T)}{exp(-E_{s0}/k_B T)\left[1 + \sum_{j=2}^{C_s} exp(-E_{2j}/k_B T)\right]}. \qquad (2.29)$$

Here C_s is the number of Stark levels in manifold s. This number is equivalent to $2J_s + 1$ and $J + 1/2$ for manifolds with even or odd number quantum number J, respectively. E_0

is the separation between the lowest Stark levels of the two manifolds and E_{ij} is the energy difference between each Stark level to the lowest Stark level of the same manifold.

Equation 2.28 is generally applicable to crystal and glass hosts. The theory assumes that the thermal redistribution of population between Stark levels is much faster than the lifetime of the level. It also operates under the assumption of individual Stark levels' width being small compared with $k_B T$ [176]. The latter assumption is not always true, yet the McCumber relation has been shown to work well under most room-temperature conditions with only small deviations in special cases [177].

An important parameter for future numerical study of a DWP system is the emission cross-section of the 3.5 μm transition. One way of obtaining this value is by applying the McCumber relation on the absorption cross-section of the $^4I_{9/2} \rightarrow {}^4F_{9/2}$. Despite the large body of research relating to Er^{3+}:ZBLAN, the author did not find a literature value for the 3.5 μm transition absorption cross-section. We did not have suitable equipment to allow us to determine the ESA cross-section directly. We therefore used the Fuchtbauer-Ladenburg method to determine the emission cross-section. This method is an extension of the Einstein A and B coefficient for a wideband emission [178]. The Fuchtbauer-Ladenburg method enables the normalising of the integral of the fluorescence collected to the radiative lifetime τ_r of the transition.

Using the measured fluorescence lineshape $\sigma_e(\lambda)$ with respect to wavelength or in CGS units $\sigma_e(\nu)$ as a function of frequency ν, the speed of light c and the average refractive index n, we can use [179]

$$\frac{1}{\tau_r} = 8\pi n^2 c \int \frac{\sigma_e(\lambda)}{\lambda^4} d\lambda \tag{2.30}$$

$$= \frac{8\pi n^2}{c} \int \nu^2 \sigma_e(\nu) d\nu, \tag{2.31}$$

which allows for directly equating the integrated lineshape to the radiative lifetime.

When non-radiative decay mechanisms are prevalent, it is necessary to introduce the relevant radiative branching ratio. The radiative lifetime and branching ratio can be found using Judd-Ofelt analysis. The term τ_r^{-1} will therefore change in our case to

$$\frac{1}{\tau_r} = A_r \cdot \beta_{43} = A_{43}, \tag{2.32}$$

with A_r being the total radiative rate, β_{43} the radiative branching ratio of the $^4F_{9/2} \rightarrow {}^4I_{9/2}$ transition and A_{43} the corresponding radiative rate for the 3.5 μm fluorescence. Figure 2.9 depicts the emission cross-section of the $^4F_{9/2} \rightarrow {}^4I_{9/2}$ transition based on the fluorescence data provided by Többen [117] and literature values of radiative lifetime
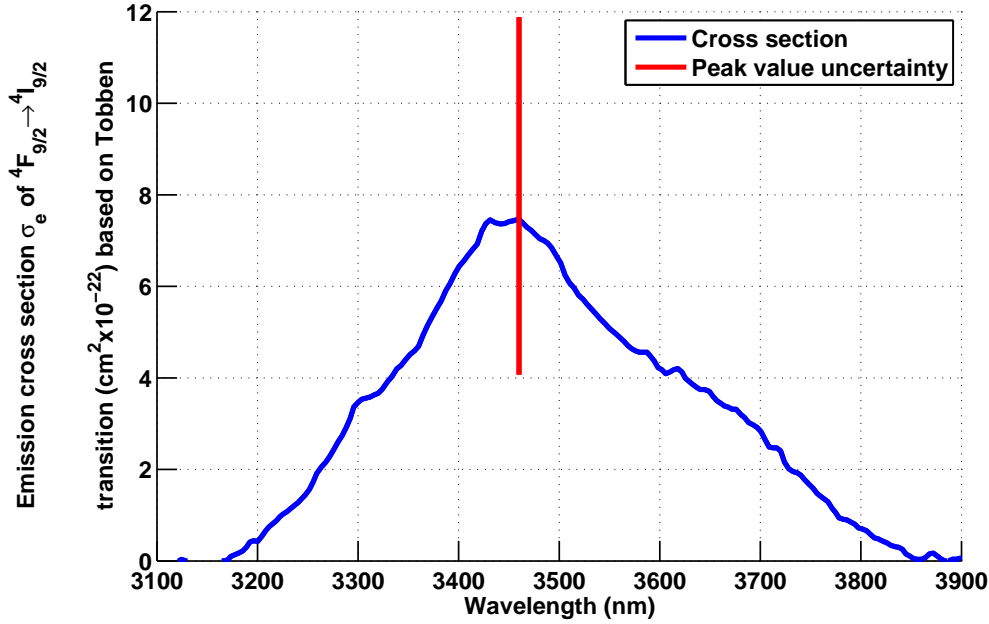
Figure 2.9: Emission cross-section of the $^4F_{9/2} \to {}^4I_{9/2}$, 3.5 μm transition based on fluorescence data from Többen [117]. Cross-section is calculated using the Fuchtbauer-Ladenburg method and radiative lifetime of 0.81 ms from Többen [180]. The vertical red line represents the uncertainty in the cross-section peak value. This uncertainty is based on the literature variations in the calculated radiative branching ratios of the $^4F_{9/2} \to {}^4I_{9/2}$ transition.

of the transition [146]. The peak of the cross-section was normalised using Equation 2.30 which equates the inverse of the radiative lifetime of the level to the integral over the fluorescence lineshape. These literature values were obtained using Judd-Oflet analysis. One problem arising with literature values is that the branching ratio (β_{43}) associated with the $^4F_{9/2} \to {}^4I_{9/2}$ transition varies significantly between publications. The branching ratio fraction is rather small; β_{43} values vary between $\beta = 0.001$ [151] and $\beta = 0.0034$ [146]. The significant variation in β_{43} values result in an estimated peak cross-section value of $7.5 \times 10^{-22}\ cm^2$. The full range of possible cross-sections, however, is on the order of 50% uncertainty with values ranging between $4 - 12 \times 10^{-22}\ cm^2$. The large variations in the branching ratio between different literature sources are probably the result of the branching-ratio value being so small. Uncertainties in determining the Judd-Ofelt parameters in conjunction with slight variations in glass composition are likely to have resulted in the aforementioned differences. These differences result in large uncertainty in the calculated cross-section. In our future numerical work, a more precise value could be found by fitting simulated data to experimental results by varying the peak emission cross-section value.

2.6 Summary

In this chapter we examined the available literature data concerning Er^{3+}:ZBLAN, which is relevant to our DWP laser investigation. We started by reviewing mechanical and thermal parameters of bulk ZBLAN glass including the damage threshold and the Sellmeier curve of ZBLAN refractive index.

We continued with literature data available on the absorption cross-section of various transitions associated with Er^{3+} doping of ZBLAN glass. We compared those literature data to our own measurements conducted on in-house made bulk ZBLAN samples.

The importance of absorption measurements was presented in lieu of the Judd-Ofelt analysis that can determine oscillator strength of various transitions. Literature values were presented including radiative probabilities and branching ratios associated with the transitions relevant to the 3.5 μm laser and the DWP method.

By using values from various literature sources, we were able to conduct a literature study of the non-radiative multi-phonon decay rates in ZBLAN glass. Calculated data was also presented for the multi-phonon rate variation with temperature. We found that by using $\alpha' = 0.0063 \ cm^{-1}$ and $C = 1.8 \times 10^{11} \ s^{-1}$ as the parameters for the non-radiative fit in Equation 2.20, we were able to consistently fit the average lifetimes values found in literature. Non-radiative parameters related to CR and ET processes were also presented for both the "strongly interacting" and "weakly interacting" cases. CR and ETU parameters were also discussed in light of their importance to the complicated spectroscopic behaviour of Er^{3+}:ZBLAN glass.

Employing the Fuchtbauer-Ladenburg method enabled us to calculate the emission cross-section of the $^4F_{9/2} \rightarrow {}^4I_{9/2}$, 3.5 μm transition to be $7.5^{+4.5}_{-3.5} \times 10^{-22} \ cm^2$. This was based on literature data of fluorescence line shape from the first laser to operate on this transition as well as radiative lifetime data from literature. This value will be compared later to the value found in Chapter 6.

This chapter aims to create a coherent picture of spectroscopic data, which is available from the literature and is relevant for Er^{3+}:ZBLAN in the context of DWP operation. The parameters found in this chapter, together with parameters found experimentally in Chapters 3, 5, 6 will be used in future numerical analysis based on rate equation. Such a model will enable an efficient investigation of the DWP laser system, by exploring different fibre parameters, such as doping, geometry and pump configurations, before committing to costly experimental investigation of the more promising designs. In Chapter 3, we investigate parameters relevant to DWP which are not available from the literature.

Chapter 3

Pump sources spectroscopy

3.1 Overview

IN this chapter, we present the spectroscopic investigations that were conducted to determine the optimum pump wavelengths for our 3.5 μm DWP laser system.

First, analysis is presented of data from the literature regarding the optimal wavelength for the first pump source. The role of this pump is to excite ions from the $^4I_{15/2}$ level to the $^4I_{11/2}$ level by ground state absorption (GSA). Experimental data is presented to support the choice of the first pump wavelength.

Secondly, an investigation of the optimal wavelength for the second pump, which excites ions from the $^4I_{11/2}$ state to the $^4F_{9/2}$ state by excited-state absorption (ESA), is presented. Two pump-probe experiments were conducted. The first determined the lineshape and hence the optimal wavelength for highest absorption. The second calibrated this data to convert the lineshape to a wavelength dependent cross-section.

3.2 Evaluation of first pump wavelength

The absorption band of the $^4I_{15/2} \rightarrow {}^4I_{11/2}$ transition is strongest at 973 nm and has a linewidth of 20 nm (see section 2.3.3). The success of the erbium doped fibre amplifier (EDFA) used in the optical fibre telecommunication industry created a strong commercial incentive for brighter sources in this band. The availability of such sources is continuously improving and it is now possible to purchase off-the-shelf a 700 mW fibre-coupled, single transverse mode source [181].

The existence of a strong absorption peak in Er^{3+}:ZBLAN at 974 nm does not mean it is the optimal wavelength for pumping into this level. Numerous investigations of ESA and

the effects of slight wavelength tuning of the pump have been published [114, 170]. These investigations have had two different motivations. The first is reducing the amount of ESA upconversion on the $^4I_{11/2} \rightarrow {}^4F_{7/2}$ transition. Spontaneous decay after this transition is associated with bright green coloured fluorescence. ESA results in ions lost from the top lasing levels and subsequent decays, which generate heat in the fibre and therefore reduce the amplification achieved by EDFAs [82, 148, 182]. The second motivation is enhancing the green or other visible fluorescence colours using an upconversion mechanism. The aim of this approach is to achieve a visible colour laser, mostly for coloured display purposes using easily-available IR wavelength pump sources [183].

3.2.1 Choice of first pump wavelength - data from literature

Quimby et al. presented a comparison of measured GSA and ESA cross-sections of the 980 nm band [148] (see Figure 3.1). These ESA values were found by measuring the
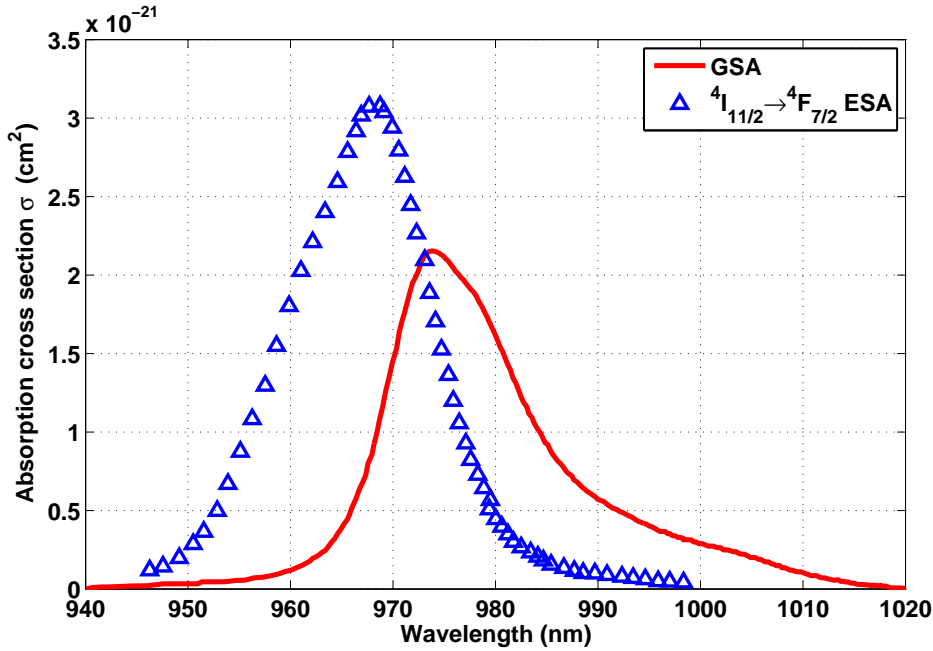
Figure 3.1: Cross-sections of GSA (red) and ESA (blue) in Er^{3+}:ZBLAN at the 980 nm band, from Quimby and Miniscalco [148]. Red line - GSA cross-section ($^4I_{15/2} \rightarrow {}^4F_{9/2}$), blue triangles - first ESA transition evaluated by comparing green fluorescence intensity.

relative fluorescence from the $^4S_{3/2}/{}^2H_{11/2}$ levels (which fluoresce in green) as a function of the pump source $I_p(\lambda)$ power and wavelength. In their experiment, the number of photons from the $^4S_{3/2}/{}^2H_{11/2}$ levels was proportional to $(W_{P_{GSA}} \cdot \tau_{2\,eff})(W_{P_{ESA}} \cdot \tau_{5\,eff})$. $W_{P_{GSA/ESA}}$ are the GSA and ESA pump rates found by

$$W_{P_{GSA}}(\lambda) = \frac{I_p(\lambda)\sigma_{GSA}(\lambda) \cdot \lambda}{hc}, \tag{3.1}$$

with $\sigma_{GSA/ESA}$ the ground and excited-state absorption cross-sections, respectively. $\tau_{2\,eff}$ and $\tau_{5\,eff}$ are the intrinsic lifetimes of the $^4I_{11/2}$ and $^4S_{3/2}$ levels. Their measured signal $S(\lambda)$ from the green fluorescence was proportional to the pump power P, wavelength and cross-sections according to

$$S(\lambda) \propto P^2(\lambda)\lambda^2\sigma_{GSA}(\lambda)\sigma_{ESA}(\lambda). \tag{3.2}$$

In deriving Equation 3.2, Quimby and Miniscalco assumed negligible depletion of the ground state and effectively no energy-transfer processes affecting the population of the $^4I_{11/2}$ or $^4S_{3/2}$ levels. These assumptions seem appropriate under the low doping, low brightness conditions of their experiments.

By changing the wavelength of their pump source, the relative lineshape of the ESA curve was obtained. The absolute cross-section was determined by equating the integral of the experimentally obtained ESA curve to the calculated oscillator strength, found using Judd-Ofelt analysis. A similar procedure was described in more detail in section 2.4.1 of this work.

In a paper describing the dependence of 2.75 μm lasing on different factors [82], Frerichs determined that the optimal pump wavelength of operation for this lasing transition is 982 nm. At this wavelength, the ESA cross-section is about 10% of its peak value and only 20% of the GSA cross-section, while the GSA maintains 60% of its peak value.

The data in Figure 3.1 suggest that ESA upconversion effects can be minimised by using a longer wavelength of operation for the first pump. The most common commercially available pump diodes operate at 974 nm, corresponding to the peak of the GSA absorption band. At this wavelength, the ESA cross-section is about 70% of its maximum value and has almost equal magnitude to the GSA cross-section. The wavelength that was eventually chosen was 985 nm. At this wavelength, the GSA cross-section is $\sigma_{GSA} = 0.93 \times 10^{-21}\ cm^2$, which is 43% of its peak value. At the same time, the ESA cross-section is only 5% of its maximal value. Moreover, since the expected pump power required for our DWP laser was significantly higher than in Frerichs' case, it was decided to err on the side of a longer wavelength.

High-brightness diodes are commercially available with wavelengths ranging between 972 nm to 978 nm and by special order up to 980 nm. Therefore we could not obtain a diode that was designed to operate at 985 nm. We tried and were successful in converting a commercially available 974 nm diode (a 300 mW, Thorlabs PL980P330J) to operate at 985 nm. This was achieved by replacing the diode's external 974 nm fibre Bragg grating (FBG) with a 985 nm FBG. This was done by cleaving off the original FBG and splicing

another FBG centred at 985 nm with low peak reflectivity of 9% (sourced from O/E Land p/n 98-008-5-5503). The external FBGs in these diodes provide the feedback for wavelength stabilisation (see section 4.2.1 for more details). Although the diode operated at 985 nm, it was necessary to maintain good temperature control to ensure operation only at 985 nm. In addition, the maximum power available by the diode was reduced by about 20%.

Our initial decision to use 985 nm as the first pump wavelength was later supported by numerical and experimental data. Theoretical thermal analysis discussed in Appendix E determined that operating under 985 nm pump would result in about a 5°C increase in temperature compared with about 30°C for a 974 nm pump. Results presented in section 5.3 showed 15% less lifetime quenching of the upper laser level using 985 nm over 974 nm. This trend was maintained in our laser results, which are presented in Chapter 6. In the case of laser operation, maximum power was obtained using 985 nm as the first pump while shifting to 974 nm resulted in the laser ceasing operation completely in most cases.

3.3   Excited-state absorption analysis of second pump wavelength

The role of the second pump source in our DWP system is to excite ions from the "virtual ground state" ($^4I_{11/2}$) to the upper laser level $^4F_{9/2}$. To achieve this efficiently, it was necessary to identify the optimal wavelength for the second pump.

Calculated data from Caspary [146] suggested a zero-phonon transition wavelength of 1973 nm on the $^4F_{9/2} \to {}^4I_{9/2}$ transition. However, to the best of our knowledge, the $^4I_{11/2} \to {}^4F_{9/2}$ ESA cross-section has not been measured before. We therefore used excited state spectroscopy to determine the optimal pump wavelength.

A set of experimental measurements was conducted to find the wavelength with the highest absorption cross-section for the $^4I_{11/2} \to {}^4F_{9/2}$ transition. Six sets of pump-probe experiments were conducted to measure this cross-section. Two additional sets of experiments were then performed to verify the viability of the DWP method. While a theoretical background and detailed rationale for conducting each experiment is provided in sections 3.3.1-3.3.3, a brief description of the experiments is presented here:

1. The lineshape and peak absorption wavelength of the second pump operating on the $^4I_{11/2} \to {}^4F_{9/2}$ transition were determined and are discussed in section 3.3.1

and presented briefly in items 2b and 2c below. This section also contains a detailed description of the basic experimental setup used in experimental stage 1. In this measurement, two light sources were launched into a ZBLAN fibre. The first was a 974 nm diode and the second source was a broadband supercontinuum laser source (SCS). Note that all experiments in this chapter were conducted prior to realising the importance of shifting the first pump wavelength to 985 nm. The 974 nm diode excited ions from the ground state and created a population at the $^4I_{11/2}$ level. The SCS source excited ions further to levels higher than $^4I_{11/2}$ according the ESA cross-sections from this level at various wavelengths. The broadband ESA spectra obtained with the SCS beam was recorded and provided a relative ESA transition lineshape. The peak of the ESA transition was determined to be at 1973 nm, although an absolute cross-section was only determined in the next set of experiments.

2. The ESA lineshape found in section 3.3.1 was calibrated to an absolute cross-section value using the set of experiments detailed in section 3.3.2. The theoretical background on which the measurements were based is also provided in this section. The calibration process was performed in three stages:

   (a) Two preliminary pump-probe experiments were performed and are described in section 3.3.2.2:

      i. A broadband scan between 1500 nm and 2200 nm verified that there were no additional ESA transitions in the vicinity of the 1973 nm ESA band. If additional ESA transitions were to be found, they would have had an impact on the additional measurements planned. This measurement was conducted using the 974 nm pump and the SCS beam filtered to transmit wavelengths longer than 1500 nm. The scan showed that there were no additional ESA transitions that could affect the next stages.

      ii. A second pump-probe experiment using the 974 nm pump with the SCS beam filtered to only transmit around 800 nm was performed next. The purpose of this measurement was to determine the wavelength least affected by ESA, while still having strong GSA at the 800 nm band. The wavelength with the least ESA and maximum GSA at the 800 nm band was found to be 797 nm. This wavelength was used as the probe wavelength in the next experiment (see stage 2b). The GSA and ESA cross-sections at 797 nm were later used in obtaining the average population of the $^4I_{11/2}$ level in the fibre.

   (b) A third pump-probe experiment used the wavelength found in stage 2(a)ii as the probe wavelength in conjunction with the 974 nm pump. This experiment

is described in section 3.3.2.3. In this measurement, we recorded the change in 797 nm probe transmission through the fibre as a function of the 974 nm pump power. This provided an absolute average value for the change in the ground population of the fibre. This change in transmission was the result of "bleaching of the ground state" $^4I_{15/2}$. This term is used throughout this work to mean a significant reduction in the population of the state ($^4I_{15/2}$ in this case) because of high pump intensity. In addition, the reduced population at this state results in less pump power being absorbed as well. The relative change in 797 nm transmission allowed the population of the $^4I_{11/2}$ level to be determined under varying 974 nm pump conditions.

(c) The final pump-probe experiment is described in section 3.3.2.3. In this experiment, we maintained the same setup as in stage 2b, but with the SCS beam transmission changed to around the 1970 nm band instead of 800 nm band. Since the population of the $^4I_{11/2}$ level was determined in the previous experiment, it was possible to infer the absolute cross-section. The peak value of the ESA cross-section of the 1970 nm band, was found from the relative change in its transmission under varying 974 nm pump conditions.

3. The last set of measurements, described in section 3.3.3, provided an independent evaluation of the DWP method viability by observing the 657 nm and 3.5 μm fluorescence. The upper laser level, $^4F_{9/2}$, fluoresces mostly to the ground by emitting at the 657 nm band (see Figure 3.2). Therefore, observing a an order of magnitude increase in the fluorescence at 657 nm was a good indication of efficient filling of the $^4F_{9/2}$ level. Under 974 nm pumping, the 3.5 μm fluorescence was undetectable with our equipment. Once a significant population was built at the $^4F_{9/2}$ level, however, the likelihood of observing 3.5 μm photons increased significantly. In these observations, we used the 974 nm pump together with a more powerful source than the SCS. Due to equipment limitations at this stage, we could not use a 1973 nm source but a non-optimal laser operating at 1910 nm. Nevertheless, we observed both a strong increase in the 657 nm band fluorescence and experienced our first observation of 3.5 μm fluorescence under DWP conditions.

These experiments allowed us to find the optimal wavelength, infer its cross-section and verify that the DWP method could indeed build a significant population at the $^4F_{9/2}$ level.

3.3.1   Measurement of peak absorption wavelength

Our first task was to establish the width of the $^4I_{11/2} \rightarrow {}^4F_{9/2}$ transition at around 1973 nm and its peak absorption wavelength. Figure 3.2 shows the first eight energy

levels of Er^{3+} doped ZBLAN glass. According to the energy level diagram and the
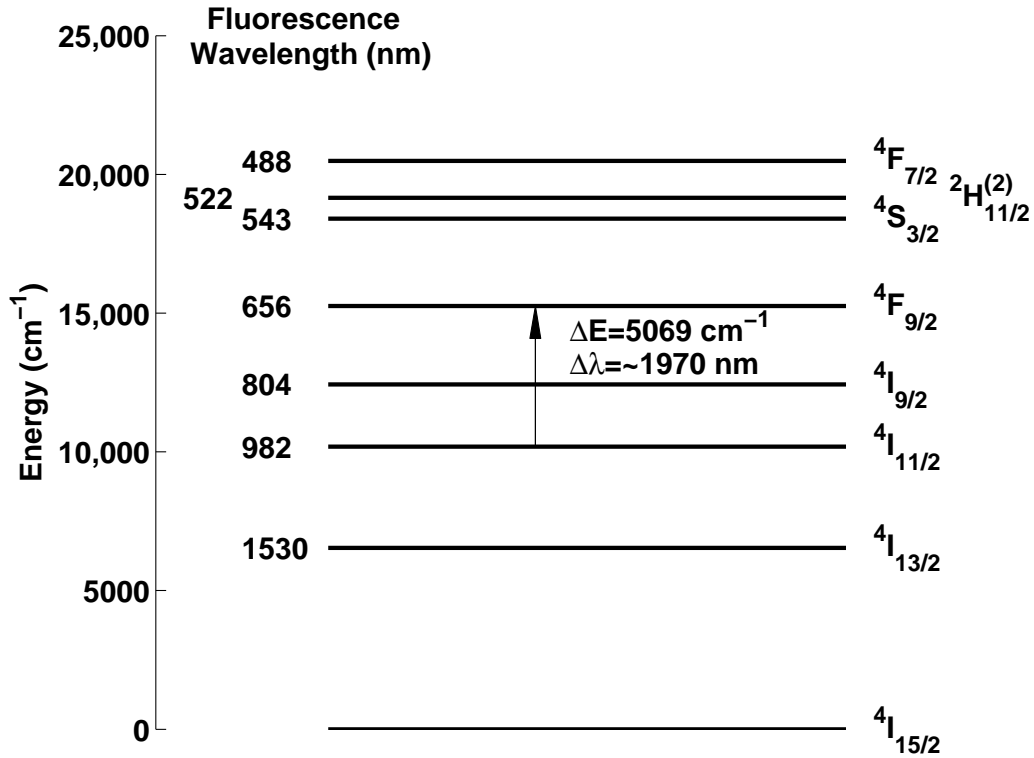
Figure 3.2: Energy levels diagram of Er^{3+} doped ZBLAN glass. Wavelengths and energy of excited states from Caspary [146].

spectroscopic data available from Caspary [146], the $^4I_{11/2} \rightarrow {}^4F_{9/2}$ transition is centred around 1970 nm. No other GSA or ESA transitions correspond to the same wavelength band, according to [146], which enabled us to do a simplified pump-probe measurement with little interference from other transitions.

In the following experiment, we determined the lineshape and peak absorption wavelength the $^4I_{11/2} \rightarrow {}^4F_{9/2}$ ESA transition. This was done by launching into an Er^{3+}:ZBLAN fibre the light from a 974 nm diode and a broadband SCS. The 974 nm diode excited ions from the ground state and created a population at the $^4I_{11/2}$ level. The broadband SCS source excited ions further to levels higher than the $^4I_{11/2}$ level according to the ESA cross-sections from the $^4I_{11/2}$ level at various wavelengths. By undergoing an ESA transition, the ions absorbed certain wavelength bands of the SCS light. Therefore, by recording the difference in transmission of the SCS through the fibre with and without the 974 nm pump, a relative ESA transition lineshape was obtained.

3.3.1.1   Experimental setup using in-fibre pump-probe

Determining the optimal ESA wavelength in a fibre has two major advantages: first, the increased interaction length facilitates the detection of even small absorption cross-sections, secondly, the fibre ensures good overlap between both pump and probe beams. For the fibre experiments, we used the commercially available FiberLabs ZSF, Er^{3+} doped ZBLAN fibre. The fibre had a 3.6 μm core with an NA = 0.28 and 125 μm diameter cladding surrounded by polymer coating with 250 μm diameter. The doping concentration was 8×10^{19} $ions/cm^3$ (approximately 5,000 ppm, or 0.5 mol%), which is considered low doping for an Er:ZBLAN fibre.

The experimental setup for the fibre based pump-probe experiment is shown in Figure 3.3. In this measurement, both the pump and probe beams were launched into the fibre
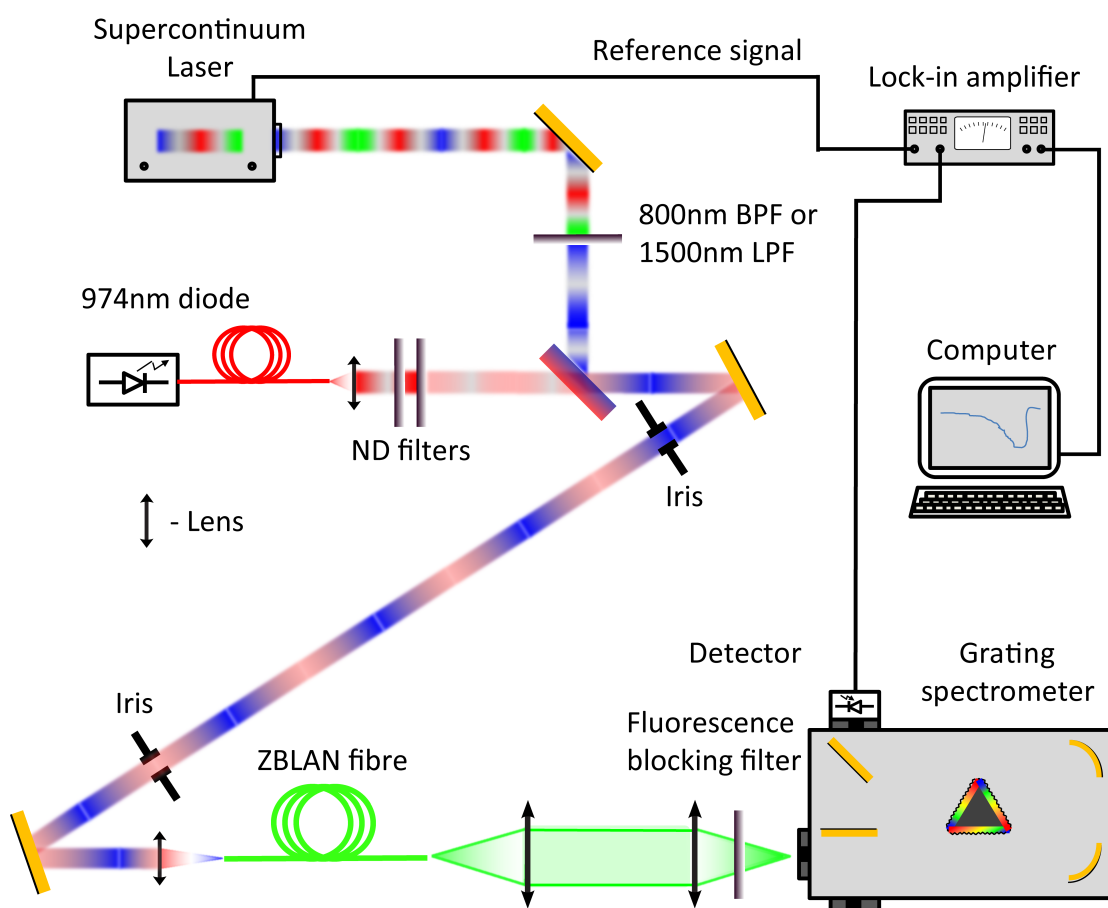
Figure 3.3: Experimental setup for in-fibre pump-probe measurement for determining $^4I_{11/2} \to {}^4F_{9/2}$ transition cross-section. BPF - bandpass filter, LPF - longpass filter.

from the same direction. The same setup was later used with some modifications for measuring the $^4I_{11/2} \to {}^4F_{9/2}$ transition cross-section and verifying the DWP method.

The pump beam was a 330 mW, 974 nm single mode, fibre-coupled laser diode (Thorlabs PL980P330J). The 974 nm beam was collimated using an $f = 6.15$ mm aspheric lens

(Thorlabs C170-TME-B). Some measurements also required neutral density filters to reduce the power of the beam while maintaining a constant current for the 974 nm laser diode. This was necessary to maintain a fixed temperature of the diode to improve both power and wavelength stability.

The collimated probe beam was generated by an SCS (Koheras SuprK compact). This was a spatially coherent, broadband light source, generating continuous broadband emission from ~ 500 nm to ~ 2400 nm. The SCS spectral power density was about 0.01 mW/nm around the 1970 nm band. The single transverse mode of the SCS output enabled easy alignment and focusing using a single lens. The SCS was internally pulsed with a pulse width of ~ 1 ns and a repetition frequency of 22.6 kHz. The TTL output from SCS source was used to synchronise the lock-in amplifier (LIA). Various filters were used to allow only a certain band of the SCS to be incident on the ZBLAN fibre. An 800 ± 20 nm bandpass filter and a longpass 1500 nm filter were two examples of filters used depending on the measurement conducted.

The SCS beam traversed the optical table by a double periscope setup and turning mirrors. The beam from the SCS was then combined with the 974 nm beam on a $45°$ dichroic mirror (CVI SWP-45-Ru1960-Tu980-PW-1025-C). The dichroic mirror reflected the wavelength range of 1500-2400 nm (as well as a low level residual reflection at 630-700 nm) while it transmitted the 974 nm beam. Co-alignment of both beams was achieved using two pinholes.

The beams were then launched through an AR coated $f = 1.49$ mm aspheric lens (Thorlabs C710-TME-C) into the ZBLAN fibre. Co-alignment was more difficult than expected due to the need to align the waists of the two beams very precisely in three dimensions into a 3.6 μm core. Moreover, the chromatic dispersion of the launching asphere resulted in large variations in launch efficiency at the different wavelengths used. This was especially noticeable when launching the 974 nm pump and the broadband SCS beam around 1900 nm band. The launching conditions were thus a trade-off between launched pump and probe power. A better future approach for such an experiment would be to use reflective focusing optics, such as off-axis parabolic mirrors. These, however, were not available at the time. The relative nature of the pump-probe experiment made this a signal-to-noise issue and not a fundamental problem. This is because in the measurement we conducted a spectral scan of the SCS beam transmitted through the fibre followed by a repeated scan with the 974 nm pump turned on. Therefore beam launching conditions remained the same in both cases. This meant that the trade-off in launching conditions resulted in changes to the minimum resolvable difference measured with the transmitted broadband probe beam.

The combined beams were launched into the fibre. The SCS beam, which was filtered to transmit the 800 nm or 1970 nm bands, interacted with the Er^{3+} ions by GSA and ESA transitions when the 974 nm pump was unblocked by the chopper and then emerged from the other end. Light emerging from the fibre was collimated by an uncoated, $f = 20~mm$, CaF_2 lens. The beam was then filtered by either 1550 nm or 1150 nm longpass filters (Thorlabs FEL1500 and FEL1150, respectively). The filters were used to remove short wavelength fluorescence emerging through the grating spectrometer higher orders. Following the filters, the light was focused into the spectrometer using an additional CaF_2 lens with f=150 mm. The focal length of the lens was chosen based on the beam diameter to closely match the f-number of the spectrometer.

We used a $^1/_2~m$ triple grating spectrometer (Princeton Instrument, Acton 2570i). The light diffracted by the grating was detected using three different detectors, two of which could be mounted simultaneously on the two output ports of the spectrometer. The two detectors could only be used sequentially, though, since the spectrometer required flipping an internal mirror to select the output port. Visible and near-IR wavelengths were detected using a silicon photo-diode biased detector (Horiba DSS S-025-TE2-H). The 1970 nm band light was detected by an extended InGaAs biased photodiode detector (Thorlabs DET10D). To observe the 2.75 μm and 3.5 μm radiation coming out of the fibre, a liquid nitrogen cooled amplified InSb photodiode was used (Judson J10D-M204-R01M-60). The signal from the detector was fed into a LIA (Stanford Research System SRS830) for amplification and demodulation at the SCS frequency. The signal from the LIA was then transmitted through an additional amplifier and was logged by computerised acquisition and control system (Princeton Instruments, SpectraHub).

3.3.1.2   ESA preliminary results

Initial wideband, low resolution (6 nm) results of the change in transmitted probe beam spectrum are presented in Figure 3.4. The curves represent the change in the transmission of the probe beam when there was no pump power present and with three different levels of incident 974 nm pump power. The fibre length used in these experiments was 134 mm and the detector used was the extended InGaAs photo-diode.

A higher resolution (1 nm) scan showed a wide absorption band stretching between 1900 nm and 2020 nm, with its peak centred at 1973 nm (see Figure 3.5). The depth of the absorption band was strongly dependent on the level of the 974 nm power launched into the fibre.

The results shown in Figures 3.4 and 3.5 were obtained with sub-optimal alignment of both beams into the fibre, which allowed us to observe the continuous change in the
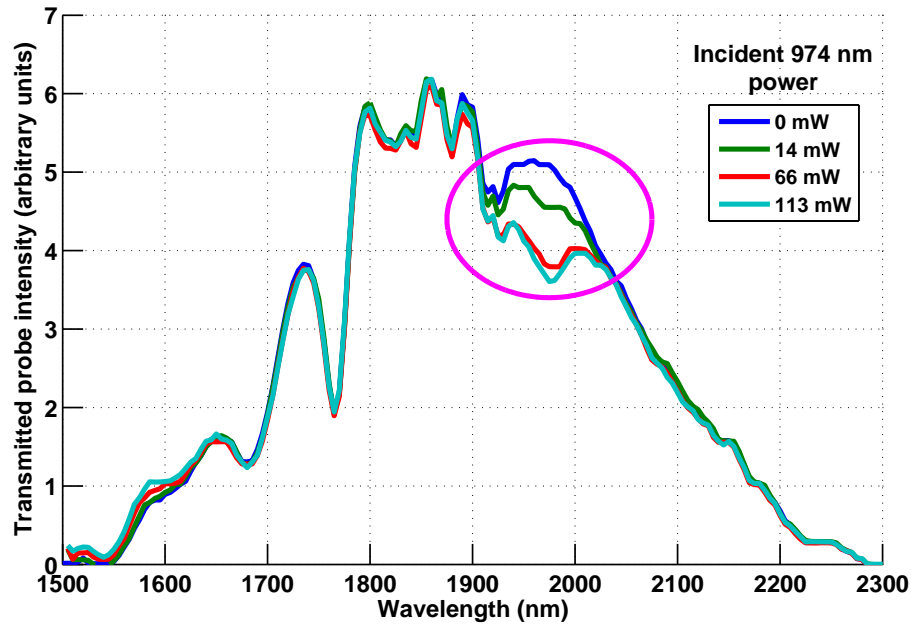
Figure 3.4: Initial broadband transmission scan showing $^4I_{11/2} \to {}^4F_{9/2}$ ESA. The ellipse encompasses the ESA region of the 1973 nm absorption maximum. On the left side of the curves, we see hints of weak stimulated emission around the 1550 nm band. Resolution of measurement is 6 nm.
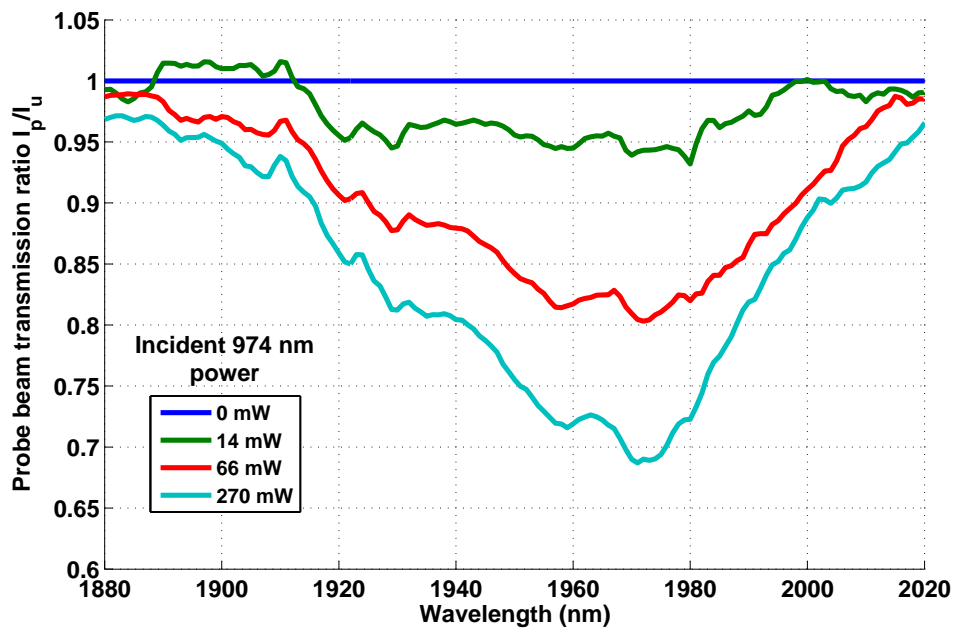
Figure 3.5: Higher resolution scan of changes in 1970 nm band absorption at different 974 nm pump powers. Resolution of measurement is 1 nm.

probe beam transmission with varying pump power. Once alignment was optimised, a strong saturation of the absorption occurred at a level similar to the one shown with the 270 mW curves in Figures 3.4 and 3.5. The saturation effects became apparent immediately after the 974 nm pump diode reached threshold with an output of a few mW. The absorption band became completely saturated at about 15 mW of incident 974 nm power, which was very close to the threshold of the diode and was $\sim 5\%$ of the maximum available power.

The change in transmission was assumed to be the same as the absorption ESA profile, therefore the curves found in Figure 3.5 were used to obtain the lineshape of the $^4I_{11/2} \rightarrow {}^4F_{9/2}$ transition (see Figure 3.6).
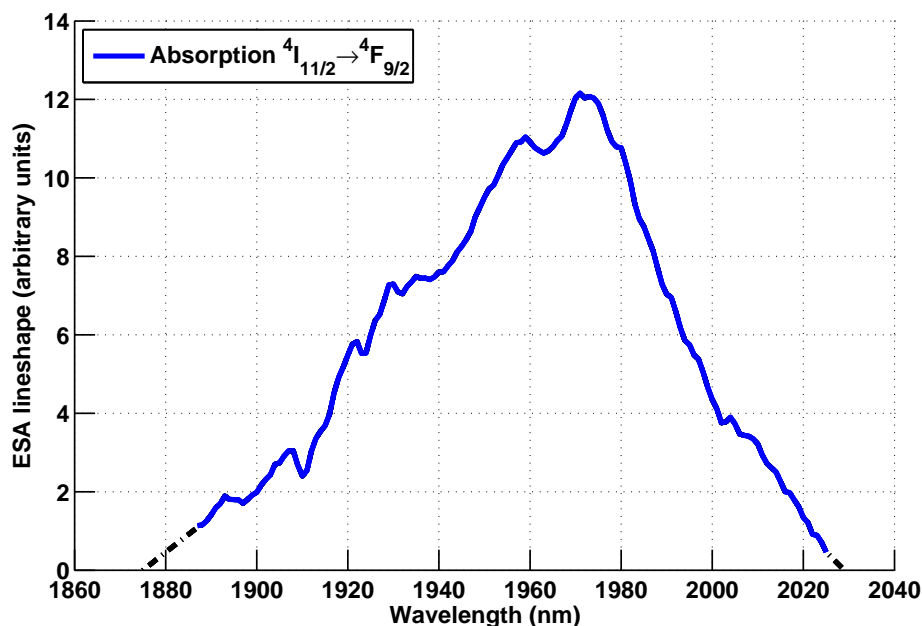
Figure 3.6: Absorption lineshape of the $^4I_{11/2} \rightarrow {}^4F_{9/2}$ transition. The dashed line at the wings of the curve represents extrapolation of the measured absorption data.

3.3.2   Calibration of absorption spectra

The absorption lineshape obtained was only a relative one and, since the measurement in section 3.3.1.2 did not provide us with an absolute cross-section. In our next set of experiments, we calibrated the ESA absorption spectrum using a pump-probe experiment. To do this, we needed to determine the value at the peak absorption. This required us to know the average population density along the fibre of the $^4I_{11/2}$ level when the ESA measurement was performed based on an equation similar to the Beer-Lambert law. In the following section, we theoretically derive the equations necessary to determine the $^4I_{11/2}$ population and the 1973 nm ESA cross-section.

3.3.2.1   Theoretical background of pump-probe technique

To measure the ESA cross-section, two light sources are needed. The first is a narrow-band pump source, which excites ions from the ground state to an elevated state. This source operates in CW or is pulsed or mechanically chopped at low frequency. A second broadband and usually weak probe source is used to observe the ESA spectrum. The second source can operate in either CW or be pulsed at higher frequency. The absorption spectrum of the second source depends on the GSA, ESA and SE properties of the material under test.

If the probe beam is sufficiently weak as to not perturb the ground state population significantly, the transmission of the probe beam I_u through the medium when the pump is off is described by

$$I_u = I_0 exp(-N_{Er}\sigma_{GSA}l), \tag{3.3}$$

where I_0 is the launched beam intensity, N_{Er} is the total ion population density, σ_{GSA} is the ground-state absorption cross-section and l is the fibre length. This expression does not include Fresnel reflection off the input and output facets nor background losses, which are later cancelled out by the relative nature of the measurement.

When the pump beam is turned on, the transmitted probe beam intensity I_p is changed to [184]

$$I_p = I_0 exp(-l\{N_g\sigma_{GSA} + \sum_i [N_i\sigma_{ESA}(i)] - \sum_i [N_i\sigma_{SE}(i)]\}), \tag{3.4}$$

where N_g is the population density of the ground state when the pump is on and N_i is the population density of the excited level i with its appropriate ESA cross-section $\sigma_{ESA}(i)$ and stimulated emission cross-section $\sigma_{SE}(i)$. If we divide 3.4 by 3.3 and rearrange using $N_{Er} = N_g + N_e$, we arrive at

$$\frac{1}{N_e l} \ln\left(\frac{I_p}{I_u}\right) = \sigma_{GSA} + \sum_i \frac{N_i}{N_e} \left[\sigma_{SE}(i) - \sigma_{ESA}(i)\right]. \tag{3.5}$$

In Equation 3.5, we defined $N_e = \sum_i N_i$ as the total population density of all excited states.

When operating under steady-state conditions, it was possible to estimate the total excited ions population N_e by observing the ratio $\frac{I_p}{I_u}$ at wavelengths where there are no ESA and SE processes. This is either because the relevant ion populations are very small or because the cross-sections are negligible. In this case, the terms in the summation on the right-hand side of Equation 3.5 can be neglected and this equation can be simplified to

$$N_e = \frac{1}{\sigma_{GSA}l} \ln\left(\frac{I_p}{I_u}\right). \tag{3.6}$$

In the case where only one ESA process is dominant and there are no GSA or SE processes, the ESA cross-section can be determined by simplifying Equation 3.5 to

$$\sigma_{ESA}(i) = \frac{1}{N_i l} \ln \left(\frac{I_p}{I_u} \right).$$

(3.7)

The population of the excited state follows Beer-Lambert law.

We were able to determine the $^4I_{11/2}$ level population density by employing a pump source at 974 nm and a probe beam at the 800 nm band. This was done by observing the changes in absorption of the 800 nm pump with and without the 974 nm pump due to bleaching of the ground state. Once the $^4I_{11/2}$ population was found, it was possible to calculate the cross-section of the 1970 nm transition, $\sigma_{1970\ nm}$, using the following method.

The change in the ground population ΔN_{ground} due to the 974 nm pump is

$$\Delta N_g = N_{ground\ with\ pump} - N_{ground} = -N_e$$
$$= -(N_{^4I_{13/2}} + N_{^4I_{11/2}} + N_{^4I_{9/2}} + N_{Higher}),$$

(3.8)

where N_{Higher} is the population of all other excited states.

The total power of the SCS over the entire 800 nm band (about 0.2 mW incident excluding launch efficiency) was significantly lower than the 974 nm light incident on the fibre. The intrinsic lifetime of the $^4I_{9/2}$ state is three orders of magnitude shorter than the lifetimes of the $^4I_{11/2}$ and $^4I_{13/2}$ levels (see Table 2.5). This means the population of the $^4I_{9/2}$ state was negligible compared with $^4I_{11/2}$ and $^4I_{13/2}$. Hence we could neglect the term for $N_{^4I_{9/2}}$ from Equation 3.8.

The population of higher excited states, N_{Higher}, was small because of the combination of low pump power, low doping concentration and the short lifetimes of levels above $^4I_{11/2}$. Pollnau et al. showed numerically [91], in a case similar to ours with CW 974 nm pumping that less than 1% of the population occupied levels above $^4I_{11/2}$. Hence, we disregard the N_{Higher} term in Equation 3.8. We therefore only maintained the following terms

$$\Delta N_g = -N_e = -(N_{^4I_{13/2}} + N_{^4I_{11/2}}).$$

(3.9)

In [91], Pollnau et al. also derived the ratio of population of the $^4I_{13/2}$ and $^4I_{11/2}$ levels to the total excited population. The ratio was calculated numerically using a system of rate equations taking into account the $^4I_{15/2}$, $^4I_{13/2}$ and $^4I_{11/2}$ levels, as well as the ESA populated $^4S_{3/2}$ level. Pollnu et al. found that the population of the levels was

dominated by the ratio of lifetimes of the energy levels. According to their calculations, the lifetimes of the levels dominated the dynamics at up to almost 4 $mol\%$ doping of Er^{3+} ions [77, 135], which is considerably higher than the doping used in the fibre in our experiment (0.5 $mol\%$). We can therefore use the excited population ratio found by Pollnau of 33% and 66% for the $^4I_{13/2}$ and $^4I_{11/2}$ levels' occupation, respectively. Using these results together with Equation 3.9, we assume

$$N_{^4I_{11/2}} \simeq -\frac{2}{3}(\Delta N_g).$$

(3.10)

We can find an expression for the transmission of the 800 nm band light with and without pumping at 974 nm by applying Equation 3.5 without SE terms. If we now use the value of $N_{^4I_{11/2}}$ according to Equation 3.10 together with the population ratio $N_{^4I_{13/2}} = \frac{1}{2}N_{^4I_{11/2}}$ from [91] and substitute Equation 3.10 into Equation 3.5, we can show that

$$\ln\left(\frac{I_{out800nm\,pump}(\lambda_1)}{I_{out\,800nm}(\lambda_1)}\right) =$$
$$= \left[-\sigma_{GSA}(\lambda_1)\Delta N_{ground} - \sigma_{ESA_{^4I_{13/2}}}(\lambda_1)N_{^4I_{13/2}} - \sigma_{ESA_{^4I_{11/2}}}(\lambda_1)N_{^4I_{11/2}}\right]\cdot l \quad (3.11)$$
$$= N_{^4I_{11/2}}\cdot l\left[1\frac{1}{2}\sigma_{800nm}(\lambda_1) - \frac{1}{2}\sigma_{ESA_{^4I_{13/2}}}(\lambda_1) - \sigma_{ESA_{^4I_{11/2}}}(\lambda_1)\right],$$

where $I_{out800nm\,pump}(\lambda_1)$ and $I_{out800nm}(\lambda_1)$ are the terms for the transmitted 800 nm band light at a specific wavelength λ_1 with and without the 974 nm pump, respectively. Equation 3.11 can be rearranged to reach the final expression for $N_{^4I_{11/2}}$,

$$N_{^4I_{11/2}} = \ln\left(\frac{I_{out\,800nm\,pump}(\lambda_1)}{I_{out\,800nm}(\lambda_1)}\right)\cdot\frac{1}{1\frac{1}{2}\sigma_{GSA}(\lambda_1) - \frac{1}{2}\sigma_{ESA_{^4I_{13/2}}}(\lambda_1) - \sigma_{ESA_{^4I_{11/2}}}(\lambda_1)}\cdot\frac{1}{l}.$$

(3.12)

To determine the population of the $^4I_{11/2}$, it was necessary to know the GSA and ESA cross-sections for specific wavelengths. These values were found using the data provided by Pollnau et al. [91]. To maximise the signal-to-noise, it was important to conduct the calculations at a wavelength within the 800 nm band where GSA is dominant.

We could then determine the ESA cross-section of the $^4I_{11/2} \rightarrow {}^4F_{9/2}$ transition. We saw in Equation 3.7 that if there are no GSA and SE transitions and there is only one ESA transition involved, then the absorption of the probe beam follows Beer-Lambert law. Pumping with 974 nm generated only a very small population at the $^4F_{9/2}$ level. This population is the result of non-radiative decay from the $^4S_{3/2}/{}^2H_{11/2}$ levels, which is assumed to be very small. Thus, SE caused by the passage of the 1970 nm band weak probe beam was assumed to be negligible. In addition, there were no ground-state absorption transitions associated with the 1970 nm band and the only ESA transition

available at this band was the $^4I_{11/2} \rightarrow {}^4F_{9/2}$. In that case, once the $^4I_{11/2}$ level population density was known, it was possible to evaluate the 1970 nm band ESA cross-section at a specific wavelength, $\sigma_{ESA\,1970nm}(\lambda_2)$, by measuring the ratio between the pumped ($I_{1973nm\,with\,pump}(\lambda_2)$) and unpumped ($I_{1973nm}(\lambda_2)$) transmissions of the 1970 nm band light using

$$\sigma_{ESA\,1970nm}(\lambda_2) = -\frac{1}{N_{^4I_{11/2}}l} \ln\left(\frac{I_{1973nm\,with\,pump}(\lambda_2)}{I_{1973nm}(\lambda_2)}\right). \qquad (3.13)$$

By combining Equation 3.13 and 3.12, we reached the final form of the 1970 nm cross-section as a function of transmitted 1970 nm power and 800 nm power when the 974 nm pump is on

$$\sigma_{ESA\,1970nm}(\lambda_2) = -\frac{1\frac{1}{2}\sigma_{800nm}(\lambda_1) + \frac{1}{2}\sigma_{ESA_{^4I_{13/2}}}(\lambda_1) + \sigma_{ESA_{^4I_{11/2}}}(\lambda_1)}{\ln\left(\frac{I_{out\,800nm\,pump}(\lambda_1)}{I_{out\,800nm}(\lambda_1)}\right)}$$
$$\times \ln\left(\frac{I_{1973nm\,with\,pump}(\lambda_2)}{I_{1973nm}(\lambda_2)}\right). \qquad (3.14)$$

In the above derivation, all population densities are assumed to be the average values over the entire fibre length. The exponential absorption profile of the pump means that the local ion density at each position along the fibre is different. Under the assumptions of negligible effect of CR and ETU processes and negligible loss in the fibre, the average ion densities are independent of the local population and depend only on the total pump power absorbed. These assumptions are thus expected to be valid in our case since the fibre used had low doping concentration and the pump power used was low, both minimising the effects of CR and ETU processes.

The derivation by Pollnau et al. in [91] assumed that bleaching of the ground state was very limited. In their case, less than 15% of the population was in an excited state. In our case, due to the small core of the fibre, a large fraction of the population could be excited. Thus, in order to maintain the validity of the above derivation, it was necessary to reduce the pump power to as low levels as possible. The calculated $\sigma_{ESA\,1973nm}(\lambda_2)$ value was not accurate when using high 974 nm pump power which excited a significant fraction of the ion population.

Since a pump-probe measurement is oriented towards detecting changes and not absolute intensity of the probe beam, the change in readings can have positive or negative values. ESA transitions reduce the amount of probe beam transmitted and are thus manifested as a negative change in signal. SE, which increases the amount of transmitted light under pumping conditions, would show as a positive change, or increased signal. In the case of

GSA transitions, when the sample is pumped there is a smaller population that is able to absorb the probe wavelengths associated with GSA, resulting in bleaching of the ground state, which in turn reduces the pump absorption. The bleaching term is represented by the first term on the right-hand side of Equation 3.5. Since more of the probe beam intensity is transmitted, $I_p - I_u$ is positive, resulting in a total positive change in signal as well.

Following the above derivation, the cross-section of the $^4F_{9/2} \rightarrow {}^4I_{9/2}$ transition was found following a three stage approach. First, it was necessary to determine the changes in the $^4I_{15/2}$ ground state population under 974 nm pumping to later be able to calculate the transmission of the 1973 nm band. The change in the ground state under 974 nm pump was found using a pump-probe measurement, which involved pumping at 974 nm and using a probe beam within the 800 nm band. This measurement required two preliminary stages, which are described in sections 3.3.2.2.2 and 3.3.2.2.3, in which we determined whether there were more than one ESA possible at the 1973 nm band and which wavelength around 800 nm was the most suitable as a probe wavelength for the main experiment. In the next stages, described in section 3.3.2.3, we found the population of the $^4I_{11/2}$ level under different 974 nm pump conditions using changes in the transmission of the 800 nm band. Finally, we determined the ESA cross-section of the 1973 nm band by observing the changes in transmission of a broadband 1970 nm beam using the same experimental setup and 974 nm pump conditions.

3.3.2.2 Preliminary experiments to determine the existence of additional ESA transitions at the 1970 nm band and to find the optimal 800 nm band wavelength for measuring bleaching of the ground state

In deriving Equation 3.13, we assumed that there was only a single ESA transition at the 1970 nm band. This allowed us to use Equation 3.7, which is essentially Beer-Lambert law applied to a single ESA transition. The work of Caspary [146] showed theoretically that there were no ESA transitions centred around the 1970 nm band except the $^4I_{11/2} \rightarrow {}^4F_{9/2}$ transition. Piatkowski and Mackowski published in [185, 186] an experimental and theoretical analysis of ESA transitions in Er^{3+}:ZBLAN for the first five energy levels. No results were published, however, for ESA transition longer than 1800 nm including the $^4I_{11/2} \rightarrow {}^4F_{9/2}$ transition. To the best of our knowledge, until our work there was no experimental verification that the 1970 nm band was not covered by the wings of another ESA transition. Therefore, we conducted the first preliminary experiment to verify that the 1970 nm ESA transition stands on its own.

To find the ground state bleaching under 974 *nm* pump, we observed the transmission of 800 *nm* band light through the fibre. The 800 *nm* band was found using a pump-probe measurement, which involved pumping at 974 *nm* and using a probe beam within the 800 *nm* band. The 800 *nm* band is covered by a GSA transition and two ESA transitions [91]. To maximise the signal-to-noise in this experiment, it was necessary to determine which wavelength was mostly dominated by GSA in contrast to ESA. The wavelength found was later used for our bleaching of the ground experiment.

3.3.2.2.1   Preliminary experimental setup

In the preliminary experiments, we used a pump-probe experimental setup comprising of two LIAs in a double-modulation configuration. The setup was similar to the ones in the works of Pollnau et al. and De-Sousa et al. in [91] and [187], respectively. This setup added to that shown in Figure 3.3 a second LIA and a mechanical chopper modulating the pump beam. A schematic of the preliminary experimental setup is shown in Figure 3.7.
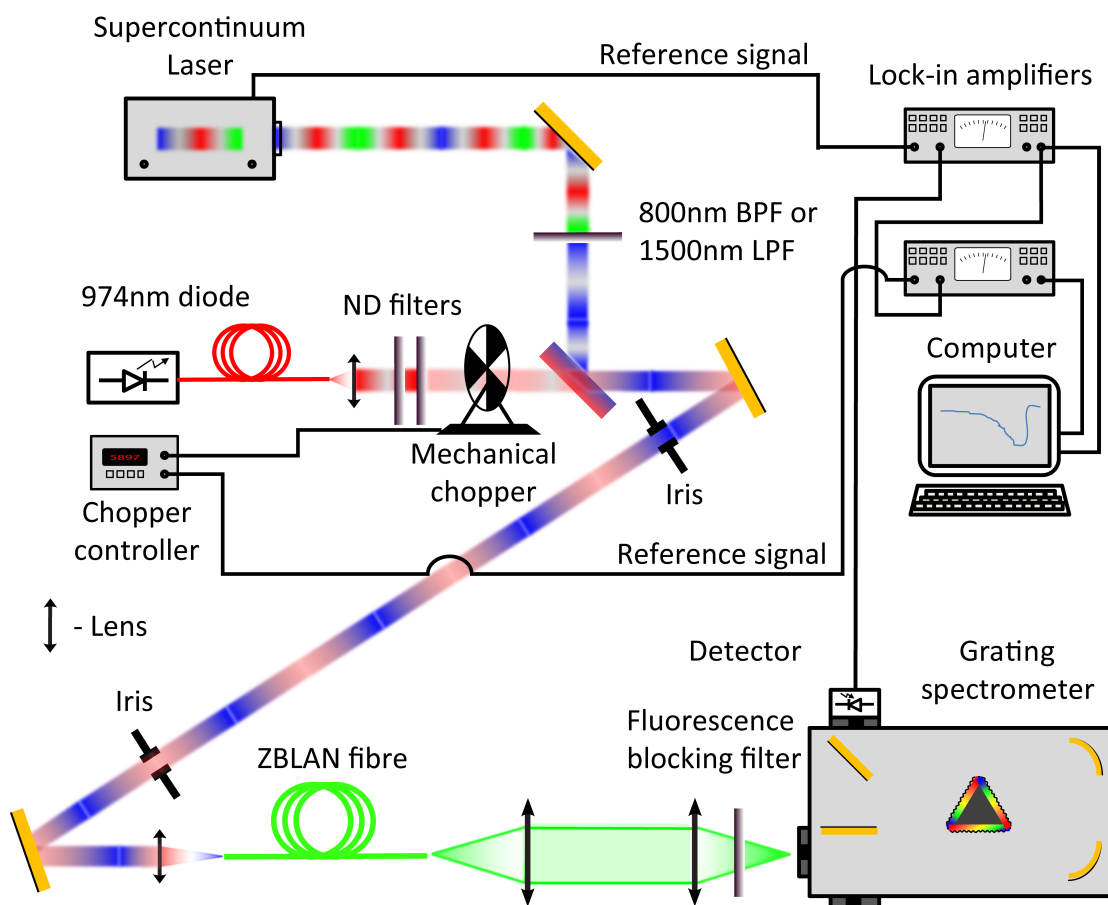
Figure 3.7: Experimental setup for in-fibre pump-probe using double modulation. BPF - bandpass filter, LPF - longpass filter.

The double-modulation configuration followed the same mathematical behaviour of the simple pump-probe technique defined in Equation 3.5. The difference between the two

techniques arises from the number of scans necessary to obtain the reading of $\ln\left(I_p/I_u\right)$ on the left-hand side of Equation 3.5. In the simple configuration, it was necessary to run two scans: one with the pump off and another with the pump on. The natural logarithm was then calculated off-line. In the double modulation experiment, the logarithm could be obtained directly because of the following approximation, which was valid under the assumption of a weak pump and probe beams

$$\ln\left(\frac{I_p}{I_u}\right) = \ln\left(1 + \frac{I_p - I_u}{I_u}\right) = \ln\left(1 + \frac{\Delta I}{I_u}\right) \approx \frac{\Delta I}{I_u} \approx \frac{\Delta I}{I}. \qquad (3.15)$$

ΔI here is the difference in the measured intensity with the pump on and off. The second to last assignment in Equation 3.15 was valid when the weak probe beam only caused minor perturbation to the ground state, while the last assignment holds for low pump powers that did not alter the transmitted probe I significantly, therefore $I_p \approx I_u \approx I$. In the measurement, the output signal of the first LIA was filtered with a relatively wideband filter. This made the output contain both a signal modulated by the probe beam and an additional signal, which was proportional to the probe beam intensity modulated by the pump beam frequency (see Figure 3.8). The additional signal, which was proportional to the difference between the pumped and unpumped cases $I_p - I_u$, was isolated as the output signal of the second LIA. The two LIA outputs were divided using software and the resulting signal, which was proportional to $\Delta I/I$, was found. The proportion factor would be the amplification factor of the first LIA.

For the system to operate properly, a few requirements had to be met:

1. A two-slot mechanical chopper (Thorlabs MC1000A system) was added to modulate the pump beam. The chopper had to operate at a slow enough frequency to allow the excited states sufficient time to stabilise. This required using three to five lifetimes of the excited state for full stabilisation. In the following experiments, the $^4I_{11/2}$ level lifetime was on the order of 7 ms, so an exposure time of 21 ms or longer was necessary for a steady state. The corresponding frequency of this exposure time was 23 Hz when operating at 50% duty-cycle. We operated at frequencies ranging from 41.6 Hz (in cases where 90% stabilisation, equivalent to 1.5 lifetimes, was sufficient for qualitative measurements) to 10 Hz for the quantitative measurements.

2. The bandwidth of the internal filter of the first LIA had to be relatively wide with a corresponding integration time of just 1 ms. Such fast integration time was based on the SCS reference frequency of 22.6 kHz. This short integration time ensured that the first LIA's filter did not remove the $\nu_{probe} - \nu_{pump}$ and $\nu_{probe} + \nu_{pump}$ signals when demodulating the incoming signal, as shown in Figure 3.8. In this
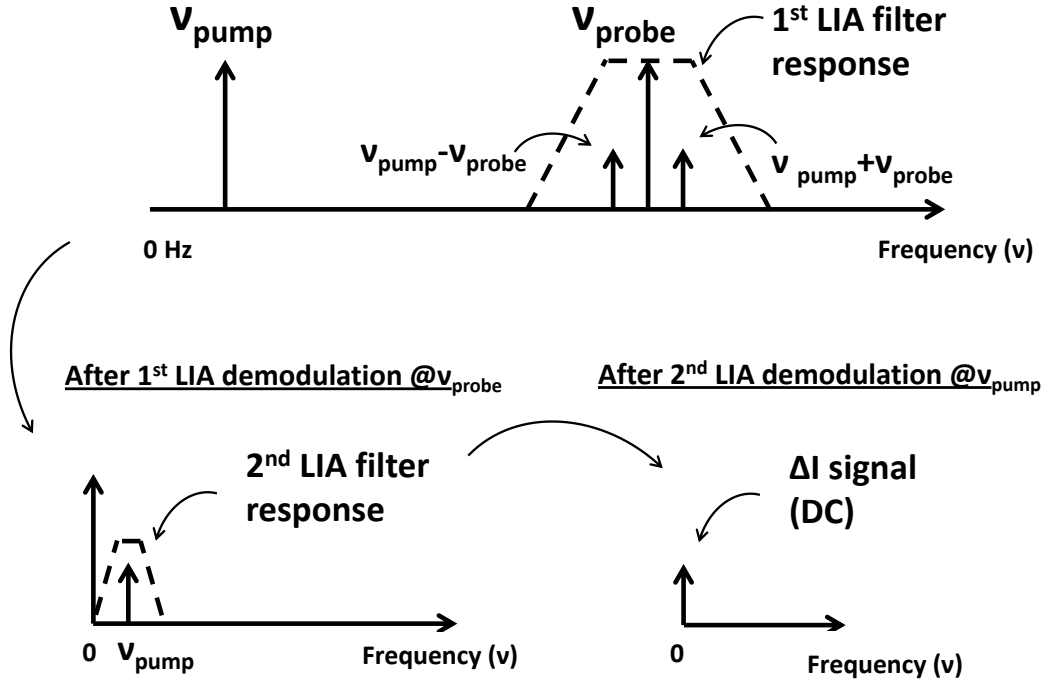
Figure 3.8: Principles of operation of double modulation pump-probe measurement. The initial signal was generated from the transmitted probe beam, which was modulated by the pump frequency. Therefore, it contained a fundamental frequency at ν_{probe} and two side-lobes at $\nu_{probe} - \nu_{pump}$ and $\nu_{probe} + \nu_{pump}$. After applying the first LIA filter, the signal was folded around zero frequency with the remaining signal at ν_{pump}. Applying the second LIA filtering isolated the signal, which was proportional to $I_p - I_u$ and brought it to DC (0 Hz).

fashion, the signals were able to be carried through to the LIA output and then be demodulated further in the second LIA.

3. The second LIA required a narrow filter corresponding to a longer integration time. In our setup, this filter was set to between 100 ms and 1 s of integration time, depending on the slow chopper frequency used while using 24 $dB/Octave$ roll off. The output of the second LIA was a DC signal proportional to the difference $I_p - I_u$.

The first LIA (Stanford Research SRS830) used the SCS TTL output frequency as its reference. This LIA used the signal from the detector on the output slit of the spectrometer to measure the transmitted probe power levels through the sample I. The second LIA used the probe beam chopper as its reference and was fed by the demodulated output of the first LIA. Our second LIA (Stanford Research SRS850) effectively measured the difference, ΔI, of the transmission of the sample with the pump beam in the on and

off states, respectively. The two LIA outputs were then divided using the software and the resulting $\Delta I / I$ signal was proportional to the sum of the GSA/ESA/SE transitions, as described in section 3.3.2.1.

3.3.2.2.2   Results of wideband scan of the 1970 nm band for identifying additional ESA transitions

The results of the wideband ESA verification measurement are shown in Figure 3.9. The 1970 nm ESA transition can be seen clearly, while no additional, neighbouring ESA transitions were observed. This scan confirmed our assumption of a single ESA transition at the 1970 nm band, thus validating the usage of Equation 3.7 in our derivation at section 3.3.2.1.

ESA and SE bands, which were further removed from the 1970 nm band, were identified. The negative shallow feature at 1620-1720 nm was the result of ESA on the $^4I_{13/2} \rightarrow {}^4I_{9/2}$ transition. The strong positive lines close to 1550 nm and shorter were the result of the $^4I_{15/2} \rightarrow {}^4I_{13/2}$ GSA transition combined with SE on the $^2H_{11/2} \rightarrow {}^4I_{9/2}$ transition. This SE transition starts at 1470 nm but the short edge was not measured in this scan, shown in Figure 3.9, because of the 1500 nm longpass filter used to eliminate second order shorter wavelengths from coming through the spectrometer.
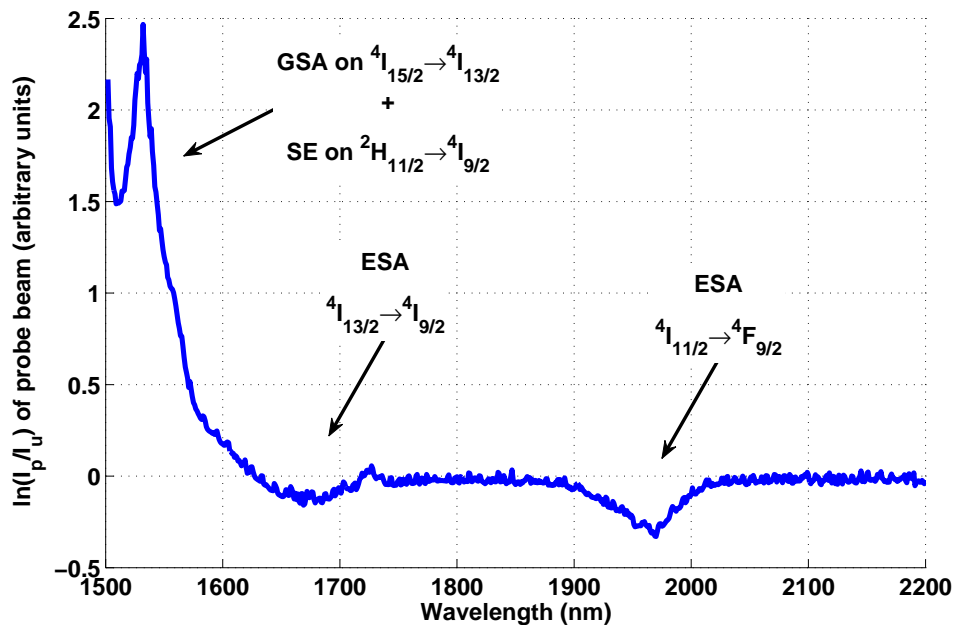
Figure 3.9: Wideband pump-probe scan. The scan starts at 1500 nm since it was necessary to use a 1500 nm longpass filter to block higher diffractions orders from showing on the spectrometer scan.

3.3.2.2.3   Results of the narrow-band scan of the 800 *nm* band

The results of the second preliminary experiment are shown in Figure 3.10. This scan helped to determine the peak GSA wavelength at the 800 *nm* band to be used in the bleaching of the ground experiment.
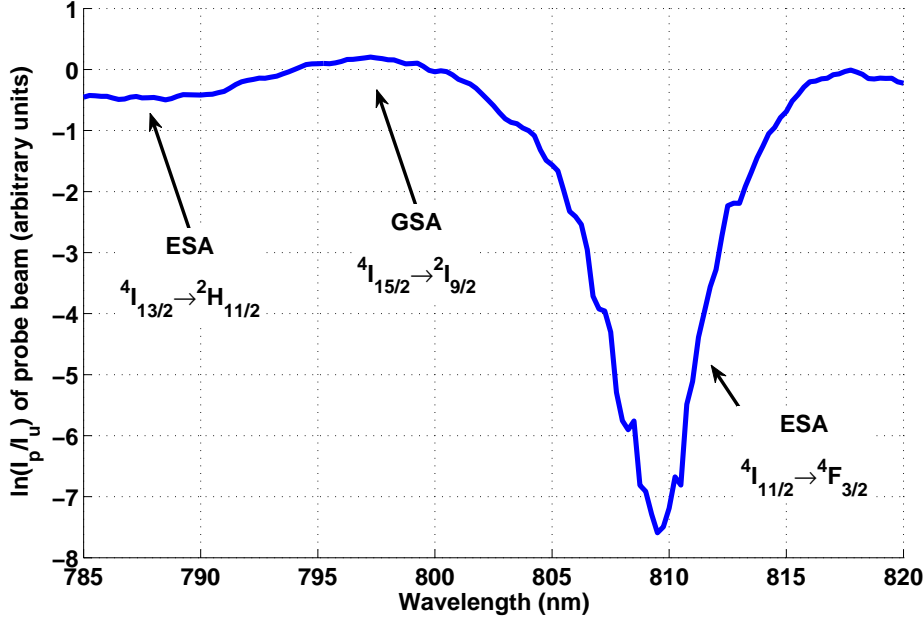
Figure 3.10: Pump-probe scan for determining 800 *nm* wavelength. The only region with dominant GSA is at 797.25 *nm*.

From Equation 3.5, we see that when there is negligible SE with GSA and multiple ESA present, the logarithm of the ratio between the pumped and unpumped follows

$$\frac{1}{l}\ln\left(\frac{I_p}{I_u}\right) = n_e\sigma_{GSA} - \sum_i N_e\sigma_{ESA}(i). \tag{3.16}$$

We can therefore see that the signal will only be positive if GSA is dominant. The scan showed that ESA transitions were common at the 800 *nm* band. Figure 3.10 also shows that GSA is the dominant effect around the wavelength of 797.25 *nm*. This result reaffirmed the results of Pollnau et al. in [91] where GSA and ESA cross-section curves are compared. The peak of the $^4I_{15/2} \to^4 I_{9/2}$ GSA transition was very close to 797.25 *nm*, while being coincidentally at the intersection point of both $^4I_{13/2} \to^2 H_{11/2}$ and $^4I_{11/2} \to^4 F_{3/2}$ ESA transition cross-section curves. By using this wavelength, we were able to obtain the highest signal-to-noise and be least affected by ESA at the 800 *nm* band.

3.3.2.3   Measurement of the average $^4I_{11/2}$ population density and the 1970 nm-band cross-section

The preliminary experiments verified the necessary assumptions of our derivation in section 3.3.2.1. We therefore continued with two consecutive experiments to find the average $^4I_{11/2}$ population density along the fibre which allowed us to measure the 1973 nm, ESA cross-section.

In the first experiment, we determined the average population density of the $^4I_{11/2}$ level as a function of pump power using Equation 3.12. This was done by observing the changes in the transmitted 797 nm light under varying 974 nm pump power. The transmission ratio, together with GSA and ESA cross-sections at 797 nm from [91] ($\sigma_{GSA} = 6.7 \times 10^{-22}\, cm^2$, $\sigma_{ESA_{4_{I_{13/2}}}} = 11.6 \times 10^{-22}\, cm^2$ and $\sigma_{ESA_{4_{I_{11/2}}}} = 1.5 \times 10^{-22}\, cm^2$), were substituted into Equation 3.12 and provided the average ion density.

We then immediately switched to the second experiment, which used the same setup. This maintained the same 974 nm launching condition, therefore obtaining the same $^4I_{11/2}$ level population density and bleaching of the ground state. We then observed the changes in the transmitted 1973 nm intensity under varying 974 nm pump power. The transmission ratio, and the previously calculated average ion density were substituted into Equation 3.13, providing us with the ESA cross-section.

3.3.2.3.1   Experimental setup for measuring the average $^4I_{11/2}$ population density and the 1970 nm-band cross-section

The two experiments used an experimental setup very similar to the one described in section 3.3.1.1 and shown in Figure 3.3. Some slight variations are described below.

We originally used a 1500 nm longpass filter in the setup which was replaced by an 800 nm bandpass filter for this experiment. An 800 nm filter was used for the first stage of the experiment while the 1500 longpass filter was used for the second part.

A 65 cm long fibre was used. This was done to achieve stronger absorption observed from the light traversing the fibre. The 800 nm filtered SCS beam was detected by an amplified Si based photodiode (Horiba DSS S-025-TE2-H) with its signal delivered to the LIA. The wavelengths around 1973 nm were detected by an extended InGaAs biased photodiode detector (Thorlabs DET10D). The measurement procedure used the following methodology:

1. Transmission measurement of 797.25 nm at the peak GSA was performed. The 974 nm power level incident on the fibre was varied. This was done while keeping the 974 nm diode power level fixed using neutral density (ND) filters on the 974 nm pump arm. This prevented changes in diode wavelengths when changing pump power and improved power stability by operating the diode high above its threshold. It also enabled obtaining low incident power, which was needed for operation within the validity of our derivation in section 3.3.2.1.

2. $N_{^4I_{11/2}}$ was calculated by comparing the transmission of 800 nm light with and without 974 nm pumping. Separate spectra were taken for each case, i.e. we did not use double modulation. Two operational power levels of the 974 nm diode were used, 13.5 mW and 270 mW. These levels were obtained by attenuating the beam using a set of ND filters with optical densities ranging from 2.5 to 0.2. Stable readings with incident 974 nm pump power as low as 0.5 mW were taken. To further increase the precision and average the noise from the SCS source, averaging of multiple scans was performed at each power level.

3. Measurement of ESA was performed at the 1970 nm band while using the same setup and 974 nm power levels as in step 2. For this measurement, the 800 nm filter was removed and replaced with the 1500 nm longpass filter. The silicon photo-diode used for detecting the 800 nm band was swapped with the extended InGaAs photo-diode capable of detecting the 1970 nm band.

4. Peak σ_{1970nm} was deduced from the transmission ratio of the 1973 nm light with and without the 974 nm pump and the $N_{^4I_{11/2}}$ population using Equations 3.12 and 3.13. The 1970 nm ESA lineshape from Figure 3.6 was then normalised to absolute values.

3.3.2.3.2   Results and analysis of the average $^4I_{11/2}$ population density and the 1970 nm-band cross-section measurements

The results of the average ion density and cross-section measurements are shown in Figures 3.11 and 3.12, respectively.   The $^4I_{11/2}$ level ion density averaged over the fibre is seen in Figure 3.11. The results indicated that bleaching of the ground and 974 nm pump saturation started occurring at 25 mW of incident power. The measured $N_{^4I_{11/2}}$ population density at this power level was 1.2×10^{19} $ions/cm^3$. Combining this result with the expected population density of $^4I_{13/2}$ of half the aforementioned value, we reached a total excited population of about 1.8×10^{18} $ions/cm^3$. This population was equivalent to about 23% of the total ion population. As the data in Figure 3.11 shows, the excited $^4I_{11/2}$ population was about twice that value when using 270 mW of incident power, reaching close to half the total excited ion population. This number is indicative
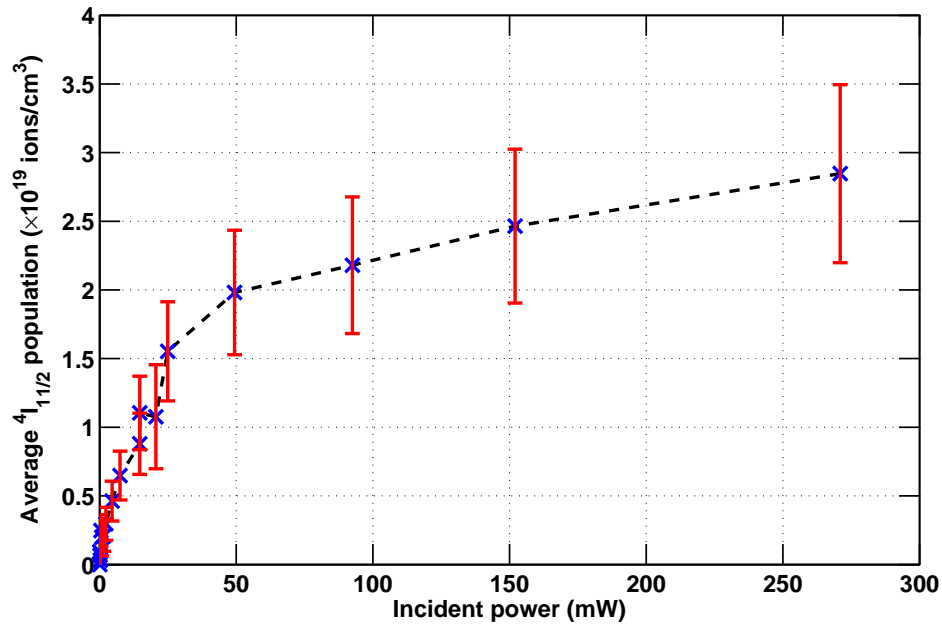
Figure 3.11: Measured $N_{4_{I_{11/2}}}$ population averaged over the fibre as a function of incident 974 nm pump. To achieve the various power levels, a single incident power at 974 nm was used while being attenuated with neutral density filters. A FiberLabs ZSF fibre with 3.6 μm core and 5000 ppm Er^{3+} concentration was used. For incident power levels of up to 4 mW, an attenuated beam of 13.5 mW was used, while all other results used an attenuated beam of 270 mW. The line in the graph is added as a guide to the eye.
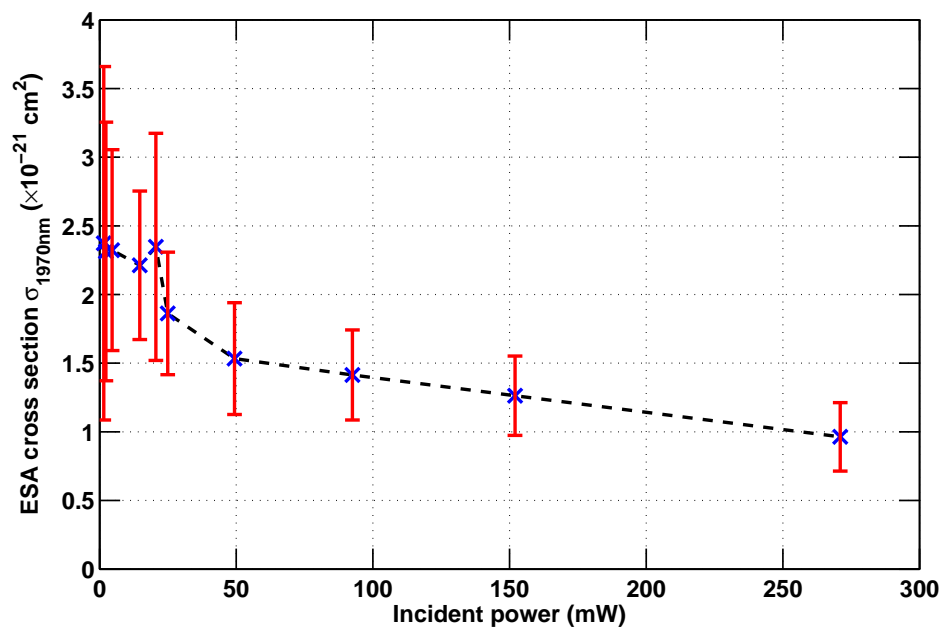
Figure 3.12: Derived σ_{1973nm} ESA cross-section as a function of incident 974 nm pump. Power levels change was obtained in a similar fashion to Figure 3.11.The line in the graph is added as a guide to the eye.

only, however, since at these population levels the underlying assumption of the rate equation model used for deriving the population did not hold [91]. This is because the derivation by Pollnau et al. assumed no significant bleaching of the ground nor any pump absorption saturation, both of which were clearly present at high pump power in our case. By pump absorption saturation we mean lower absorption of the pump because of reduced population density at the lower level or due to SE from the level pumped to, in case it does not decay sufficiently fast. Strong saturation of the $^4I_{11/2}$ level would have increased the population of higher levels due to both ESA and energy-transfer processes, thus invalidating the simplified assumptions in the numerical model by Pollnau et al.

Figure 3.12 transformed the $N_{4_{I_{11/2}}}$ population into 1973 nm ESA cross-section values according to Equation 3.14. This was done using additional SCS transmission measurement with the 974 nm pump in the on and off states. Although the 800 nm filter was replaced with the 1500 nm longpass filter, all other experimental conditions were maintained.

A consistent cross-section was maintained at low incident 974 nm power. An average of $\sigma_{1973nm} = 2.3 \pm 0.8 \times 10^{-21}\ cm^2$ was obtained for the first five data points. The relatively high uncertainty at the low power data arises from the lower signal-to-noise and instabilities of the SCS source. At higher incident 974 nm power, we see a steady decline in the calculated cross-section, which is likely the result of our calculation assumptions, which were based on the model by Pollnau et al., not being valid any more as explained above. Using the average value of $\sigma_{1973nm} = 2.3 \times 10^{-21}\ cm^2$, we were able to normalise the ESA absorption according to the lineshape in Figure 3.6 and obtain an absolute ESA cross-section, which can be seen in Figure 3.13.

Once the ESA absorption cross-section was known, we could infer the emission cross-section of the $^4F_{9/2} \rightarrow ^4I_{11/2}$ transition, which was superimposed on Figure 3.13. This was done by applying the McCumber relation presented in Equation 2.28 in section 2.5. By using Equation 2.28 together with the absorption cross-section found here and the energy of the appropriate Stark levels found in [188], we arrived at a peak emission cross-section of $\sigma_e = 2.6 \pm 0.9 \times 10^{-21}\ cm^2$ with the wavelength dependency shown in Figure 3.13. The McCumber method is common for obtaining emission cross-sections based on experimental values of GSA transitions' cross-section. Quimby and Zheng showed that this method is applicable for obtaining ESA and SE spectra while finding their absolute values as well [189].

In conclusion, we obtained the population of both $^4I_{11/2}$ and $^4I_{13/2}$ under 974 nm pump conditions with an 800 nm band probe beam. ESA of the $^4I_{11/2} \rightarrow^4 F_{9/2}$ transition was evaluated by combining this data with the relative transmission of the 1970 nm band under 974 nm pumping. The value obtained of $\sigma_{1973nm} = 2.3 \pm 0.8 \times 10^{-21}\ cm^2$ is the first experimental value obtained for this ESA transition.
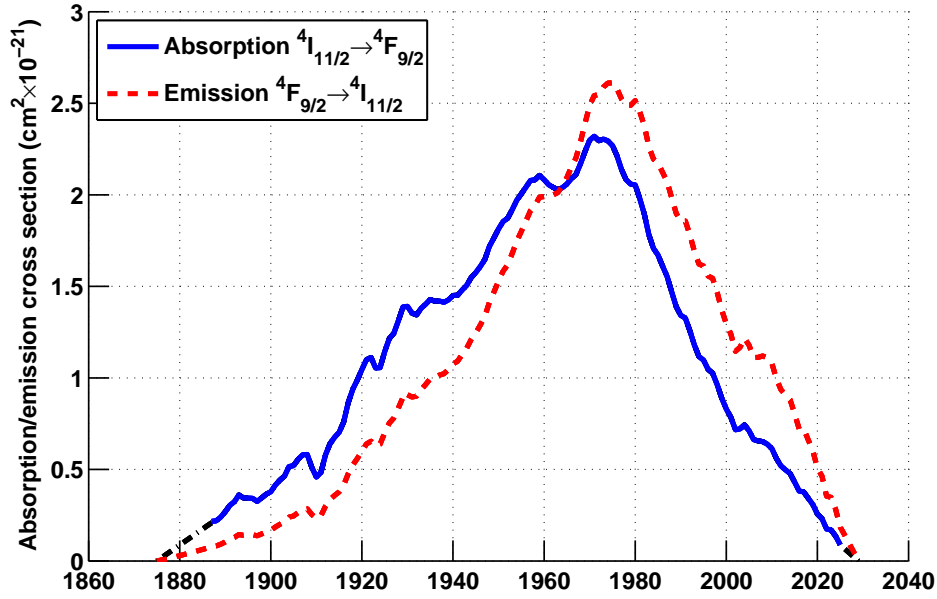
Figure 3.13: ESA cross-section of the $^4I_{11/2} \to {}^4F_{9/2}$ transition based on measurement of bleaching of the ground. The black dot-dashed line represents extrapolation of the measured absorption data. Peak absorption cross-section value is $\sigma_{1973nm\ abs} = 2.3 \pm 0.8 \times 10^{-21}\ cm^2$ and emission peak value is $\sigma_{1973nm\ em} = 2.6 \pm 0.9 \times 10^{-21}\ cm^2$.

3.3.3   Independent confirmation of DWP mechanism

Before lasing was achieved (see Chapter 6), it was desirable to have an independent confirmation that the observed 1973 nm band ESA was the result of the absorption of the probe beam due to DWP and not an artefact of the measurement caused by heating or misalignment. Three different methods were tried.

We first tried to observe the 1970 nm fluorescence on the $^4F_{9/2} \to {}^4I_{11/2}$ transition. Such fluorescence would have been the result of the increased population of the $^4F_{9/2}$ level. We were unsuccessful, however, as this weak fluorescence was obscured by the broadband SCS beam when we observed the light coming out of the fibre. Looking at the fluorescence through the side of the fibre was not possible, due to the absorption of 1970 nm light by its coating and its mechanical fragility, which prevented stripping it far from the tip and thus observing with low level of scattered pump light.

The second approach, described in section 3.3.3.1, was based on observing the 657 nm fluorescence from $^4F_{9/2}$ to the ground state. At this stage, however, it was realised that a second pump source more powerful than the SCS was needed. We constructed such a source based on a Tm^{3+} doped silica fibre (see Appendix C.1). Using this source, operating in conjunction with the previously used 974 nm pump diode, it was possible

to increase the population of the $^4F_{9/2}$ level dramatically. We observed a significant increase in the fluorescence of the 657 nm due to the DWP mechanism.

In the last method tried, we observed 3.5 μm fluorescence from the $^4F_{9/2}$ level that was populated using the DWP mechanism (see section C.2.1). This was the first time we observed this fluorescence. Fluorescence at 3.5 μm was a good indicator for $^4F_{9/2}$ population build up and thus validated the DWP mechanism. This is because the $^4F_{9/2}$ population under sole 974 nm pumping was very small (although weak fluorescence at 657 nm was observable with very low signal to noise). Moreover, the very small branching ratio of the $^4F_{9/2} \rightarrow {}^4I_{9/2}$ transition combined with its preferred non-radiate depopulation mechanism quickly quenches this level. Therefore, without strong population build-up at the $^4F_{9/2}$ level, 3.5 μm fluorescence would have been undetectable by our instruments. Obtaining significant 3.5 μm fluorescence emanating from the $^4F_{9/2} \rightarrow {}^4I_{9/2}$ transition was a necessary precursor to obtain laser action on this transition. The results obtained with the new second pump source provided an incentive to move towards building a full DWP system.

3.3.3.1   Observation of increase in 657 nm band fluorescence from the $^4F_{9/2}$ level using DWP

The objective of this experiment was observing increased 657 nm fluorescence from the $^4F_{9/2}$ level under DWP conditions. The intensity of fluorescence on both the $^4F_{9/2} \rightarrow {}^4I_{15/2}$ transition to the ground and $^4F_{9/2} \rightarrow {}^4I_{9/2}$ laser transition were dependent on the population of the $^4F_{9/2}$ level. Therefore, observing a significantly stronger 657 nm fluorescence from the $^4F_{9/2}$ level would be an indication of the levels' increased population.

Using the SCS in DWP configuration created a relatively small population density at the $^4F_{9/2}$ level because of the low spectral power density available from the SCS at the 1970 nm band (≈ 0.01 mW/nm [190]). Observation of a significant population build-up necessitated using a more powerful second pump source. We constructed such a source based on a Tm^{3+} doped silica fibre (TFL), replicating the design of Wu et al. [191]. This source, which had three orders of magnitude improvement in spectral power density, operating in conjunction with the previously used 974 nm pump diode, increased the population of the $^4F_{9/2}$ level dramatically. We therefore observed a significant increase in the fluorescence of the 657 nm due to the DWP mechanism.

The experimental setup for observing the increase in the 657 nm fluorescence experiment is shown in Figure 3.14. This setup had the following modifications from the setup used for the pump-probe measurements shown in Figure 3.3:
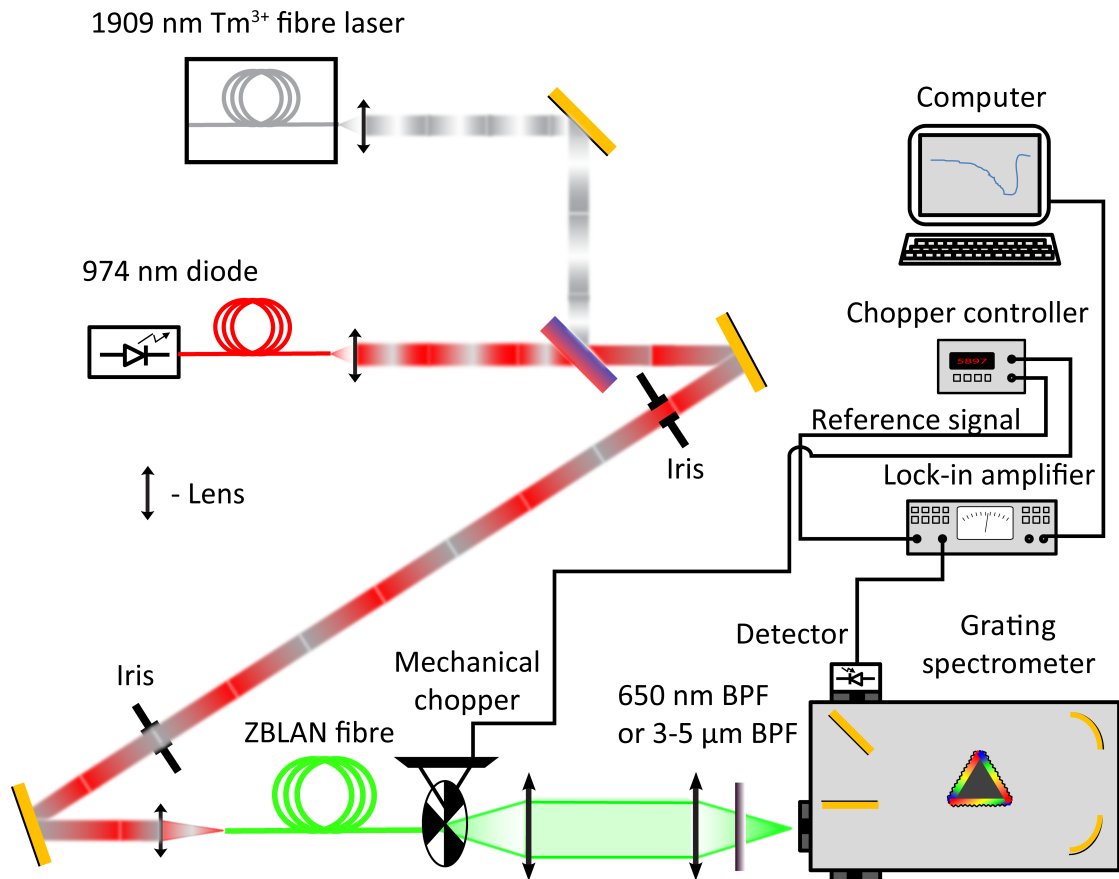
Figure 3.14: Experimental setup for observing increased 657 nm fluorescence and 3.5 μm fluorescence. To switch between detecting 657 nm and 3.5 μm, we replaced the 650 nm bandpass with a 3-5 μm bandpass filter and the detector was changed from a Si photo-diode based detector to an InSb photo detector.

1. The Er:ZBLAN fibre length was changed to 173 mm to allow for increased absorption of the second pump.

2. The wideband, low power SCS probe beam was replaced with the output fibre from the TFL. This fibre laser emitted up to 350 mW at 1909 nm when operated in CW.

3. A mechanical chopper (Thorlabs MC1000) operating with a 10 slots blade at up to 1 kHz was used on the fluorescence emerging from the ZBLAN fibre to improve the signal-to-noise while using a LIA.

4. The 1550 nm longpass filter originally used after the ZBLAN fibre was replaced with a bandpass filter centred at 650 nm and 40 nm wide (Thorlabs FBH650-40 denoted as BPF in Figure 3.14).

5. A Si photo-diode (Horiba DSS S-025-TE2-H) replaced the extended InGaAs detector.

Schematics and other operational details of this replicated TFL are described in detail in Appendix C. The fibre laser operated in CW mode and produced between 200 and 350 mW at 1909 nm, depending on the cooling method used. As evident from Figure 3.13, operation at 1909 nm was not ideal as it was far into the short wing of the $^4I_{11/2} \to {}^4F_{9/2}$ ESA transition. The absorption cross-section was approximately six times lower than the peak absorption possible around 1973 nm. Component constraints did not allow changing the wavelength, thus we used this laser.

The 657 nm fluorescence level was recorded as a function of incident 1909 nm TFL power, as seen in Figure 3.15. Baseline 657 nm fluorescence was taken with the fibre
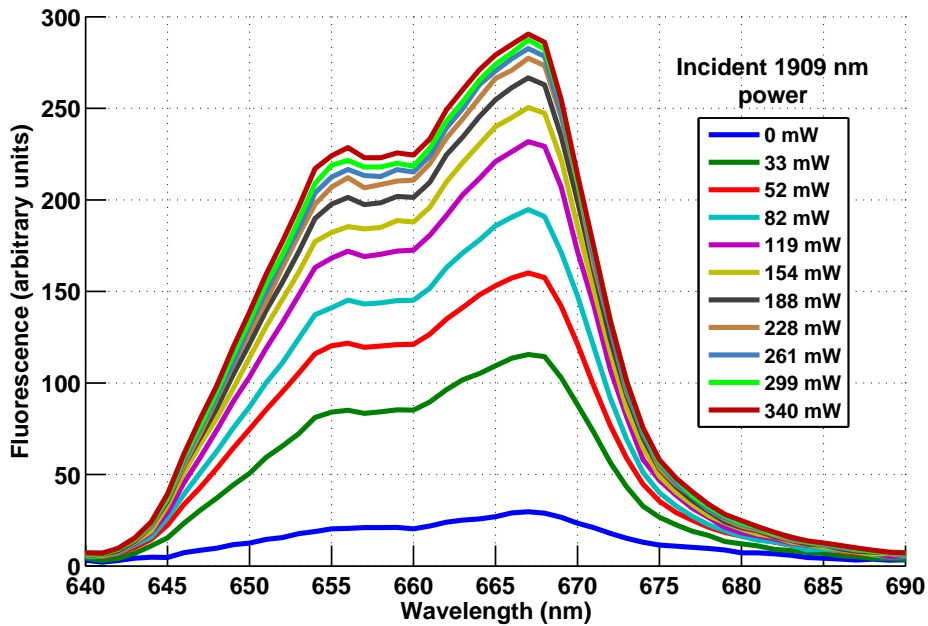
Figure 3.15: 657 nm fluorescence level when DWP. 974 nm incident power is 14 mW with the 1909 nm incident power varying.

laser off while the 974 nm pump operating at 14 mW of incident power. Some 657 nm fluorescence was observed due to the $^4I_{11/2} \to {}^4F_{7/2}$ ESA relaxation to the $^4F_{9/2}$ level. From there, ions which relax radiatively did so, mostly by 657 nm fluorescence according to the branching ratio. The 974 nm pump was kept at the 14 mW level, while additional measurements were conducted with varying levels of incident 1909 nm TFL power. A linear increase in the fluorescence power was observed at incident power of up to 120 mW of the TFL. Beyond that power, saturation effects were observed likely as a result of saturation of the 1909 nm pump absorption. The eight fold increase in 657 nm

fluorescence was a clear indication of a more significant population of the $^4F_{9/2}$ level due to the DWP mechanism.

3.3.3.2   Observation of 3.5 μm fluorescence

The strong increase in 657 nm fluorescence while pumping with the 1909 nm TFL encouraged us to search for 3.5 μm fluorescence as well. Because of the very low branching of the $^4F_{9/2} \rightarrow {}^4I_{9/2}$ transition, 3.5 μm fluorescence is very weak. To observe this fluorescence, it was necessary to significantly increase the population of the $^4F_{9/2}$ level. We therefore used the same setup used for observing the increase in 657 nm. In the previous measurement, we used a rather low incident 974 nm pump power so we could observe the linear behaviour at low pump. In this experiment, we used all the power that was available to us to generate maximum 3.5 μm fluorescence, which was otherwise too feeble to observe.

To observe the 3.5 μm fluorescence, we used the same experimental setup as the one used for observing the 657 nm fluorescence (see Figure 3.14), with two minor modifications. The Si photo-diode detector at the spectrometer output was replaced by a liquid nitrogen cooled InSb detector (Judson J10D-M204-R01M-60) and the 650 nm BPF was replaced with a 3-5 μm BPF (Spectrogon BBP-3000-5000nm).

Operating at 290 mW and 325 mW of incident 974 nm and 1909 nm, respectively, we observed a broad fluorescence lineshape centred at 3470 nm (see Figure 3.16). The fluorescence intensity in the figure is normalised to the 3.5 μm fluorescence reported by Többen [117] superimposed as a reference. This 3.5 μm band fluorescence was the first indication that it was possible to generate some observable fluorescence on the $^4F_{9/2} \rightarrow {}^4I_{9/2}$ transition.

The distinct feature at 3810 nm was verified to be the result of a second order of the 1909 nm pump that was able to pass through the spectrometer and the 3-5 μm BPF. The fluorescence had a very broad nature starting at 3100 nm and ending at over 3850 nm with its peak at 3470 nm. This peak value was slightly shorter than the 3545 nm predicted by Caspary [146]. The shape of the fluorescence curve matched well the fluorescence shape obtained by Többen in [117], although it appeared slightly broader, possibly due to noise in our measurement. Later in this work, after the proper pump sources were constructed, slightly different fluorescence curve shapes were encountered (as described in Chapters 5 and 6). Those 3.5 μm fluorescence curves were taken from different fibres made by different manufacturers and with various doping concentrations, which may explain the slight shape differences.
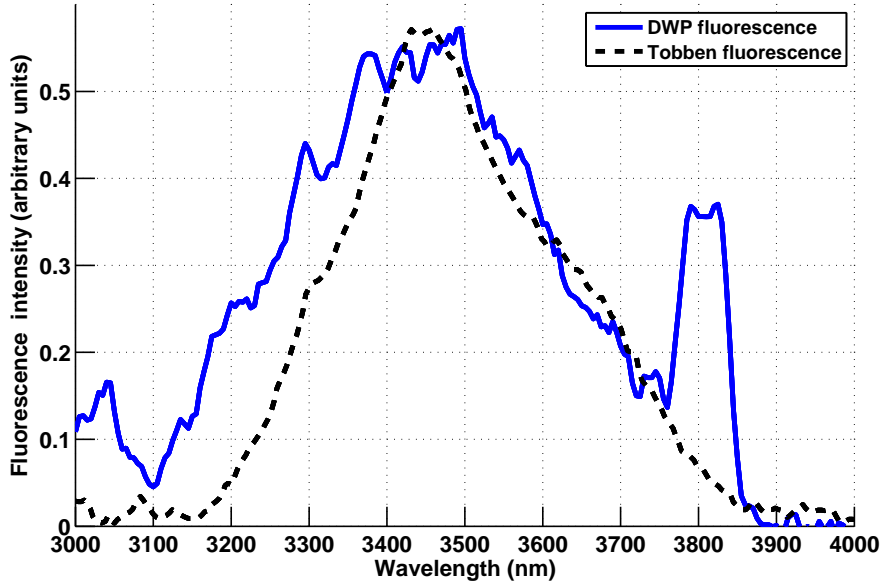
Figure 3.16: First observation of 3.5 μm fluorescence obtained in ZBLAN fibre using DWP method. The 974 nm diode operated at 290 mW incident power while the 1909 nm fibre laser incident power was 325 mW. Approximately 30 mW of 1909 nm pump power was absorbed in the fibre. The distinctive feature at 3820 nm is the result of stray light from the 1909 nm source passing through the 3-5 μm BPF. Additional filtering of the 1909 nm light dropped the 3.5 μm signal level to the noise level and thus it was not used.

This newly observed fluorescence was an additional confirmation that the 3.5 μm fluorescence could be obtained using the DWP method. The poor matching between the 1909 nm pump source and the optimal wavelength of 1973 nm meant that improved pump sources were necessary to achieve lasing.

3.4 Conclusions

At the beginning of this chapter, we presented a brief overview of available literature data regarding the optimal wavelength for the first pump. It was found that operating at the vicinity of 985 nm would have several advantages. Those included a more even pump absorption for both pumps while maintaining low ESA levels for the first pump.

By using the broadband SCS and a 974 nm diode, in a pump-probe configuration we found the optimal second pump wavelength to be 1972 ± 2 nm. In addition, we were able to derive the population of both $^4I_{11/2}$ and $^4I_{13/2}$ under 974 nm pump conditions. This was achieved by observing the changes in the absorption of an 800 nm beam launched into the ZBLAN fibre while co-pumping with the 974 nm pump. ESA cross-section of
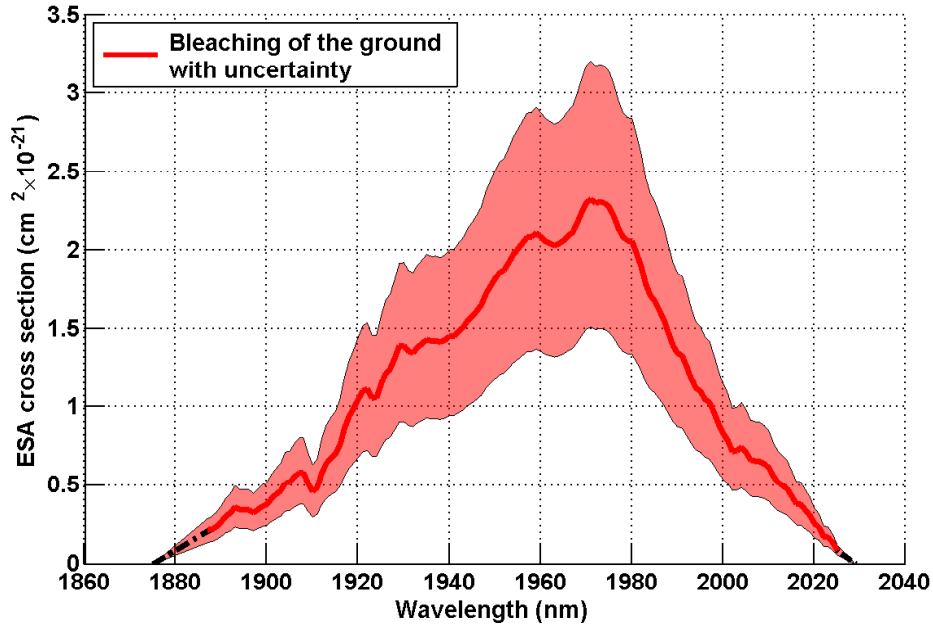
Figure 3.17: 1973 nm ESA with uncertainty. The dark red line represent the values obtained using bleaching of the ground measurement (section 3.3.2.3.2). The shaded red area represents the uncertainty in the cross-section, which is assumed to scale in a similar fashion to the peak value uncertainty for all wavelengths.

the $^4I_{11/2} \rightarrow ^4 F_{9/2}$ transition, seen in Figure 3.17, was evaluated with a value obtained of $\sigma_{1973nm} = 2.3 \pm 0.8 \times 10^{-21} \ cm^2$. This method is the first experimentally obtained value for this ESA transition.

We constructed a preliminary DWP setup, which included a 974 nm diode and a 1909 nm TFL. We conducted two measurements with this setup. The first observed an increase in the 657 nm fluorescence when DWP. The second measurement obtained our first 3.5 μm fluorescence observed with DWP. Both showed that the DWP method can be applied to create a significant population at the $^4F_{9/2}$ level, a necessary precursor for 3.5 μm lasing.

The results obtained in this chapter were utilised to create the first 3.5 μm DWP laser (as described in Chapter 6). These results will be used in future numerical analysis of the DWP system.

Chapter 4

Pump sources

4.1 Overview

IN this chapter we discuss the pump sources used throughout this work. First we describe the construction and characterisation of the source used to promote Er^{3+} ions from the ground state ($^4I_{15/2}$) to the "virtual ground" state ($^4I_{11/2}$). We include descriptions of commercial sources that were sometimes modified to achieve a different wavelength than that for which they were designed.

A second pump source for elevating ions from the $^4I_{11/2}$ state to the $^4F_{9/2}$ state was also needed. The optimal wavelength for this transition is 1973 nm (see section 3.3.2). At the beginning of this research, affordable sources with good beam quality were not commercially available and therefore we needed to build them. Three different variants were developed during this work. The first two are described in Appendix C while the final version used in the 3.5 μm laser experiments is described in this chapter.

Most of the experimental work described in this thesis was conducted using a single-clad Er^{3+}:ZBLAN fibre (except in some parts of Chapter 5). When using such a fibre, it was necessary to launch the pump beam into fibre cores with diameters ranging from 3.6 to 10 μm. The combination of the numerical aperture of these fibres (NA = 0.12 and 0.15, respectively) with their core size resulted in supporting only a small number of guided modes at the 980 nm band and a single mode or four modes at 1973 nm (depending on manufacturing tolerances). Achieving good launch efficiency of both pump beams into these fibres required both pump sources to have excellent beam quality, therefore predominately coupling to the fundamental transverse mode of the fibre. Fibre-coupled sources which supported only a single transverse mode were thus used when core pumping fibres in this work.

4.2   First pump source

Commercial solid-state sources relevant to pumping of Er^{3+} ions are currently available from 970 nm to 980 nm. They are available as fibre-coupled sources in either a single transverse mode, or highly multi-mode, high power, low brightness source. The wavelength bands commonly used for telecom applications is 974-976 nm. These wavelengths correspond to the peak of the absorption of Er^{3+} and Yb^{3+} ions. Both are available with fibre-coupled outputs, allowing for easier integration into existing setups. High brightness, single transverse mode sources are often used in telecom amplifiers. High power, low brightness sources are mostly used for 1550 nm fibre lasers that employ a double-clad fibre geometry.

The peak absorption of the $^4I_{15/2} \rightarrow {}^4I_{11/2}$ ground state absorption (GSA) transition in ZBLAN glass is 974 nm (see section 2.3). This wavelength is similar to the GSA in Er^{3+} doped silica glass and hence a large selection of sources are commercially available. This is because the 974 nm band is used as the pump wavelength of choice for optical amplifiers in the telecom industry.

4.2.1   High-brightness, single transverse mode source

Experiments that used core pumping at the 980 nm band required a high brightness diode with excellent beam quality. For these experiments, a fibre-coupled, 974 nm, single transverse mode, 330 mW un-polarised source was used (Thorlabs PL980P330J). The pigtail fibre attached to the diode was a HI1060 single mode fibre with a 5.9 μm mode-field diameter. To maintain excellent beam quality out of the fibre, the beam was collimated for different experiments using various aspheric lenses. The most common one was a Thorlabs C170-TME-C with a focal length of $f = 6.213$ mm at 980 nm.

The high-brightness diode was designed to operate with a bandwidth of less than 1 nm. To achieve this narrow band and maintain wavelength stability against changing temperature, an external fibre Bragg grating (FBG) with 9% reflectivity was spliced by the manufacturer onto the pigtail fibre of the diode.

In section 3.2 we found that it is preferential to use a pump operating at 985 nm over 974 nm. This is because pumping at 985 nm results in a higher population in the $^4I_{11/2}$ level. In addition, the $^4I_{11/2}$ population is more evenly distributed along the fibre. Both of these properties improve the absorption of the second, 1973 nm pump. Further, a significantly smaller fraction of the pump power results in excited state absorption
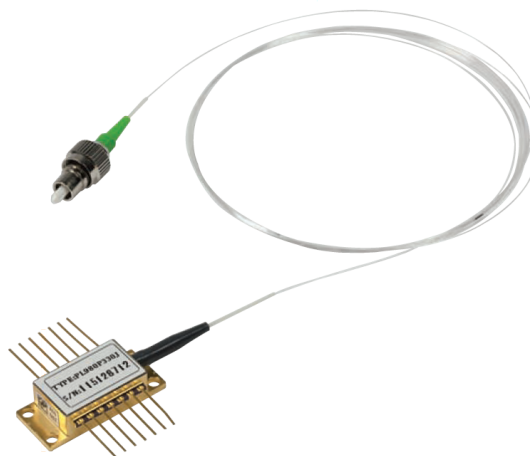
Figure 4.1: 974 nm fibre-coupled single transversal mode diode

(ESA), which can substantially reduce the thermal load in the fibre core (described in Appendix E).

Fibre-coupled, solid-state pump sources at 985 nm are non-standard and to the best of our knowledge are not available off-the-shelf. Therefore, to allow operation at 985 nm, the external FBG was removed and a different FBG at a wavelength of 985.23 nm (O/E land 98-008-5-5503) was spliced in its place.

Figure 4.2 shows the spectrum of the fibre-coupled diode as a function of the diode junction temperature after removing the original 974 nm FBG, but prior to splicing the new FBG. The temperature was determined by monitoring the voltage of the internal thermistor of the diode. The wavelength was measured by collecting light reflected off a lens using a large core, high numerical aperture fibre that was fed into an optical spectrum analyser (Yokogawa ANDO AQ6315E). The figure shows that the peak wavelength red-shifted as the temperature of the diode increased. To obtain power at a wavelength close to 985 nm, it was necessary to operate the diode at high temperature that exceeds 40°C. Figure 4.2 demonstrates that without an FBG, the peak output was at 985 nm only when the diode temperature was increased to 51°C. The high-brightness diode was able to operate at 974 nm with its original FBG, at 985 nm and 974 nm with the new FBG and in-between these wavelengths without the FBG. We shall therefore refer to this diode as the 980 nm diode. When the wavelength of operation is of importance to the discussion, it will shall refer to the wavelength explicitly.

The spectral behaviour of the diode with the 980 nm FBG spliced onto it is shown in Figure 4.3. Multiple features appear if the diode temperature is too cold. When the diode temperature was increased to above 30°C, a more pronounced and stable 985 nm line appeared.
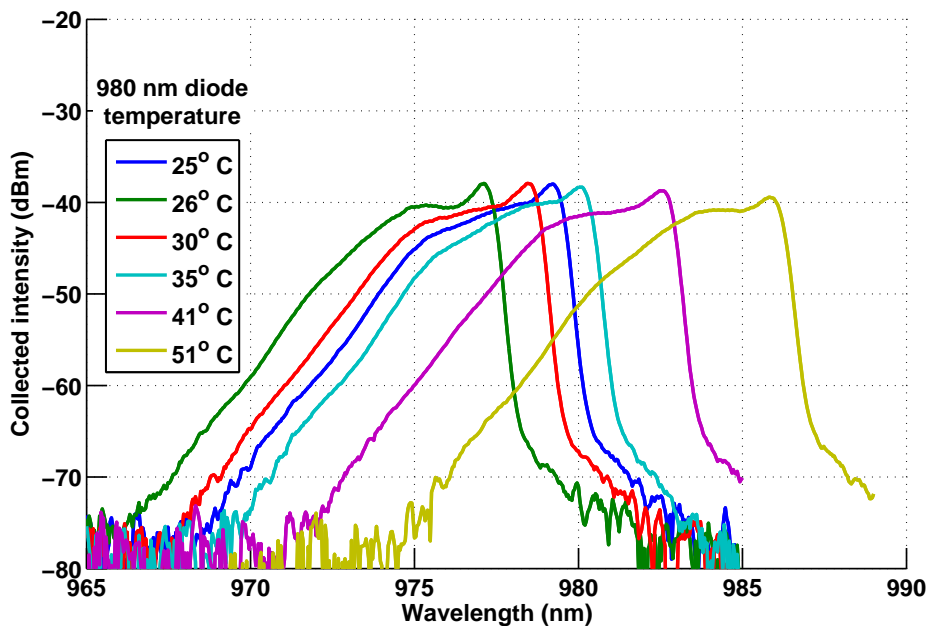
Figure 4.2: 980 nm diode wavelength change with temperature without FBG. Diode operating at its maximum supply current of 700 mA. Temperature reading is based on the diode's internal thermistor resistance. Note that measured power (in dBm - 10-based logarithmic scale relative to 1 mW) is small since the light was collected off a reflection of a lens in the path of the beam.
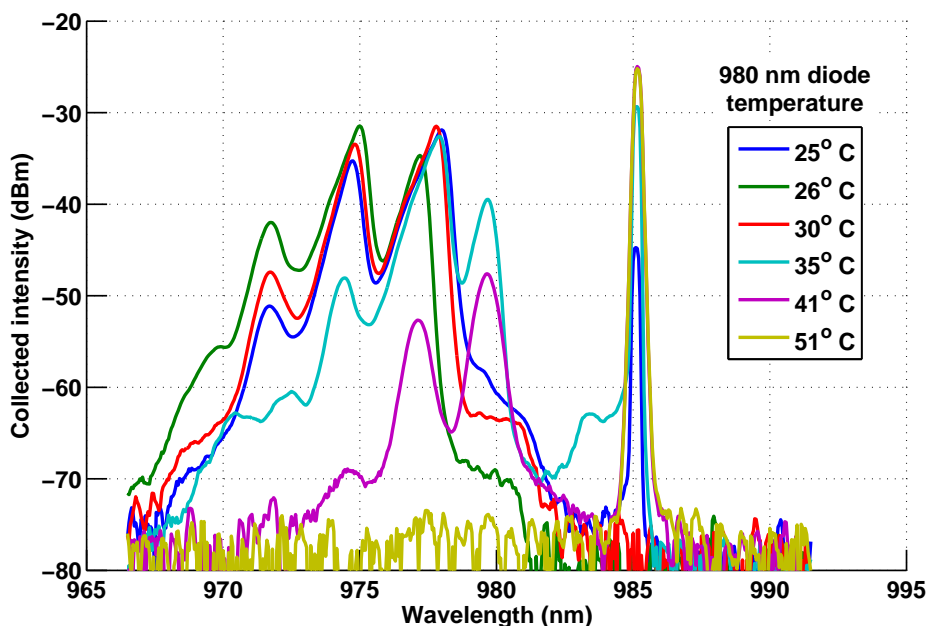
Figure 4.3: 980 nm diode spectral purity as a function of temperature with 985 nm FBG. Diode operating at its maximum supply current of 700 mA. Temperature reading is based on the diode internal thermistor resistance. Note that measured power (in dBm - logarithmic scale relative to 1 mW) is small since the light was collected off a reflection of a lens in the path of the beam.

At lower temperatures, the diode would operate predominantly on two lines: 975 nm and 978 nm. A suitable combination of current and temperature made it possible to operate the diode with the bulk of its output power concentrated at the 974 nm line only. This was used to study the difference between pumping with 974 nm or 985 nm as described in Chapter 5.

The high temperature needed to ensure stable operation at 985 nm reduced the efficiency of the diode. Figure 4.4 compares the output power exiting the fibre of the diode with its
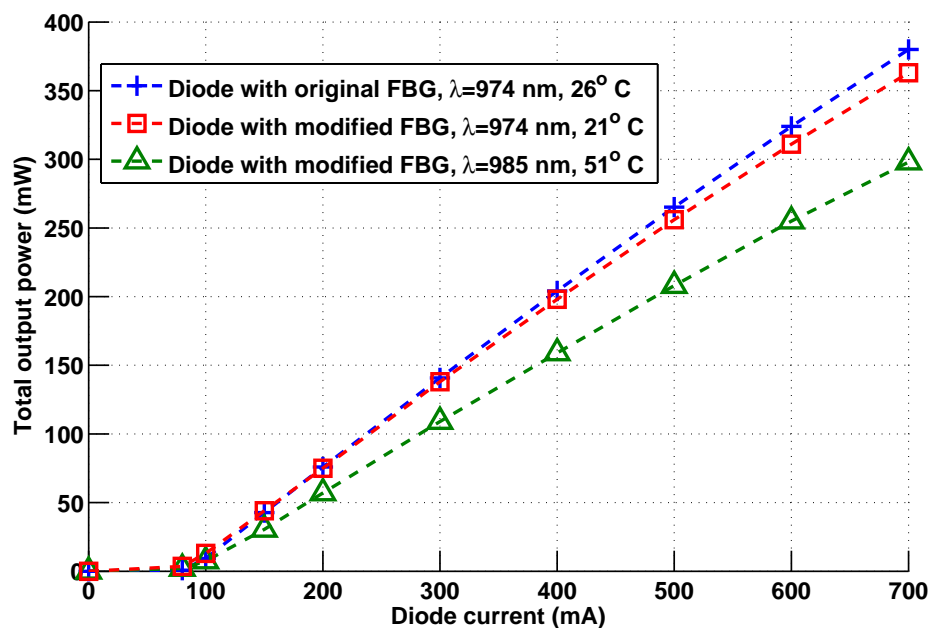
Figure 4.4: 980 nm high-brightness diode output power comparison between original, 974 nm FBG and spliced 985 nm FBG. The wavelengths in the legend are the ones containing over 95% of the power of the diode while operating at the stated temperature. Therefore, at 21°C, the diode with the modified 985 nm FBG maintained operation at the peak of its gain, which was 974 nm. To ensure stable, narrow-line operation at 985 nm for all power levels, it was necessary to raise the temperature of the diode to 51°C.

original 974 nm FBG to the power with the spliced 985 nm FBG. When the diode with the modified FBG was operated close to room temperature, it preferentially operated on the 974 nm and 978 nm lines. The diode with the modified FBG delivered a maximum of 363 mW at 974 nm while operating at the slightly lower temperature of 21°C. This was only a 4.5% reduction in the output power compared with the diode in its original configuration. To ensure stable, narrow-line 985 nm operation at all power levels, it was necessary to operate the diode at 51°C. This relatively high operation temperature decreased its maximum output power to 298 mW, a 21% reduction in the maximum power compared with the original configuration.

The lower power available at 985 nm would affect our 3.5 μm laser performance in Chapter 6 by creating a slightly smaller population at the $^4I_{11/2}$ state. However, it was very difficult to obtain lasing while operating with the first pump operating at 974 nm. Therefore, until higher brightness sources become available, this degradation had to be tolerated.

4.2.2   High-power, low brightness, 974 nm source

Some of the experiments in this work were conducted using a double-clad ZBLAN fibre. These experiments, which used the double-clad, ZDF fibre from FiberLabs, are described in Chapter 5. This fibre was pumped by a high-power, low-brightness, 974 nm diode because light from the diode could be easily coupled to the 300 μm inner cladding of the fibre. This diode was used in our initial lasing trials prior to our realisation that 985 nm is better suited for DWP purposes (see section 3.2). The diode was used after we gained this understanding during the upper laser level lifetime quenching investigations, which are described in section 5.3. It was not possible to temperature-tune the wavelength of this diode to 985 nm because of the high temperature it would have necessitated. However, in the future we expect to be able to procure similar diodes that operate closer to 980 nm and will enable wavelength tuning close to 985 nm.

The advantages of clad-pumping over core pumping include a longer interaction length, allowing for higher overall gain. In addition, a more even, almost linear excitation of the ions is achieved in the fibre core. A further advantage is the thermal load per unit length is significantly reduced, which means less demanding thermal management requirements in possible future applications.

The high-power, low-brightness source we used was a 30 W, fibre-coupled, 974 nm laser diode (LIMO HLU30F200-980, see Figure 4.5). This multi-mode diode was coupled into a 200 μm, multi-mode delivery fibre. The output from the delivery fibre was collimated using a fast aspheric lens (Thorlabs AL2520 with focal length $f = 20$ mm and numerical aperture NA = 0.54) and later focused into the ZBLAN fibre.

The output power of the LIMO diode as a function of the driving current is shown in Figure 4.6. Wavelength tuning of the LIMO diode was not attempted as its specifications would require temperature of operation exceeding 70°C.

Figure 4.5: High-power, low-brightness, 974 nm laser diode source LIMO HLU30F200-980
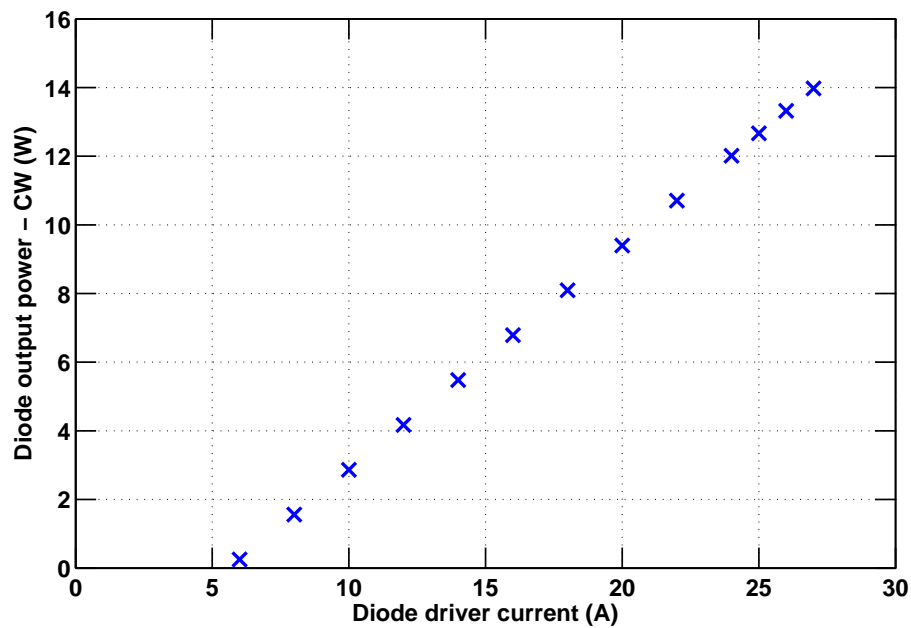
Figure 4.6: LIMO 974 nm high-power low-brightness diode output power as a function of driver current.

4.3 Second pump sources using Tm^{3+}:silica fibre lasers

Three versions of the second, 1973 nm pump source were built. All versions used Tm^{3+} doped silica to make thulium-based fibre lasers (TFL). The first two versions were based on a 1550 nm in-band pumped gain switched design that were operated in CW instead of pulsed operation. The third version used a simple 790 nm pumped, double clad, Tm^{3+} doped silica fibre. This version was the one used for obtaining 3.5 μm lasing using DWP. We used the two gain switched versions initially due to their availability. Details of the construction and performance of these preliminary in-band TFL sources are provided in Appendix C. The final TFL version was constructed to simplify operation. Its design and operational details are provided in this section.

4.3.1 Simplified TFL based on 790 nm pumped double-clad fibre

Details of this TFL laser are shown schematically in Figure 4.7. It was designed and built when a 790 nm high-power fibre-coupled laser diode became available to us. This variant significantly simplified construction and allowed higher CW output power levels to be achieved. This TFL comprised of pump diode segment and a laser resonator.
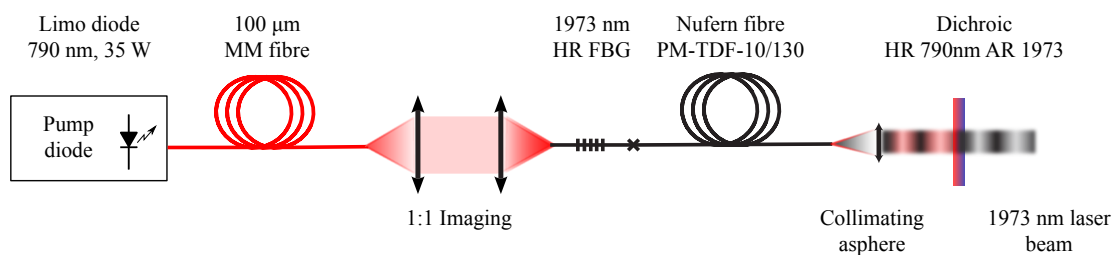
Figure 4.7: Schematic of 790 nm pumped Tm^{3+} fibre laser.

The pump source was a 790 nm fibre-coupled, high-power, low brightness diode (LIMO 35-F100-DL790). The fibre of this diode was well matched to the 125 μm diameter, double-clad fibre because its delivery fibre was 100 μm in diameter. Since the reinforced delivery fibre could not be spliced, the 790 nm beam was imaged into the next fibre.

The pump light was launched into the next fibre using a set of two aspheric lenses (Thorlabs C230-TME-B) for a 1:1 imaging. This fibre contained a narrow-band, 1973 nm, highly-reflective FBG (Teraxion PWS-HPR-1970-1.6-99.5-PM10/130-0-1) acting as the back resonator mirror. The FBG was spliced to 2.5 m of active Tm^{3+} doped silica fibre (Nufern PM-TDF-10/130). This fibre had a 130 μm inner cladding and a core diameter of 10 μm with a numerical aperture of NA = 0.15, which made this fibre single mode at the wavelength of 1973 nm. The 2.5 m of fibre that was available achieved 75% pump absorption. The other end of the resonator was completed by the Fresnel reflection from the straight cleaved end of the fibre.

The output beam of this TFL was collimated using an aspheric lens (Thorlabs C560-TME-C). The 790 nm pump power emerging from the Tm^{3+} doped fibre was reflected back into the resonator using a dichroic mirror. This mirror had a highly reflective coating at 790 nm which was also anti-reflective at 1973 nm. The addition of the dichroic mirror improved the laser output power by 10%. This TFL reached threshold at 1.72 W of incident 790 nm pump and it was operated to a maximum power of 5 W, with a slope efficiency of 25.7% (see Figure 4.8). These results are comparable to early results from Tm^{3+}-doped double clad silica fibres [192] that were limited by the 39% Stokes efficiency of this transition. Slope efficiency could be improved significantly in highly doped and specialised fibres due to the CR process $^3F_4 + ^3H_6 \rightarrow ^3H_4 + ^3H_4$ (see

for example [193, 194]). This process should enable reaching close to twice the Stokes efficiency. We did not have longer lengths of Tm^{3+}-doped that could achieve higher pump absorption and since this power level was deemed sufficient for our DWP application, we did not pursue higher output power.
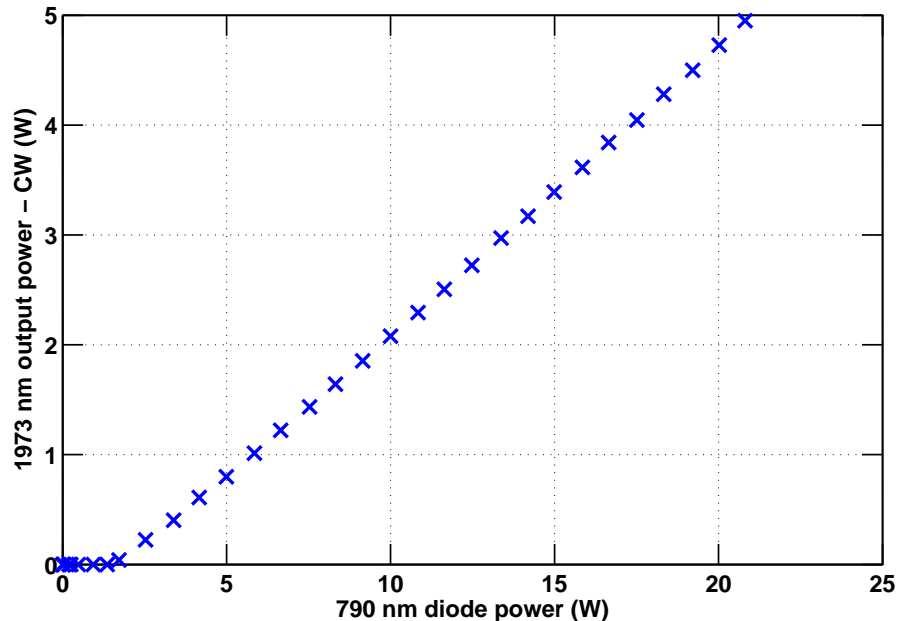
Figure 4.8: Power output of the 790 nm pumped Tm^{3+} fibre laser.

Over 75% of the power emitted by this laser was incident on the ZBLAN fibre when dual-wavelength pumping (DWP). This pump source was used to demonstrate 3.5 μm lasing with the DWP scheme. With over 3.5 W of incident power, there was no need for additional improvement in the power of our second pump source, since the 3.5 μm laser power was limited by the brightness of our first pump source (see section 6.4.3).

4.4   Conclusions

In this chapter, we describe the various pump sources used with our investigations of the DWP scheme. We start by presenting the commercial sources used as the first pump for elevating ions from the ground state ($^4I_{15/2}$) to the meta-stable level ($^4I_{11/2}$). We then describe the final variant of TFL used as the second pump source. This pump source was used to elevate the ions from the "virtual ground" state ($^4I_{11/2}$) to the upper laser level ($^4F_{9/2}$). This TFL variant was used for demonstrating the 3.5 μm lasing in Chapter 6. A design which would allow future gain switching of the 3.5 μm laser and obtaining high peak power is presented in Appendix C.

In the next chapter, we examine a few parameters important for the eventual demonstration of 3.5 μm lasing using the DWP method.

Chapter 5

The challenges of using Er^{3+}:ZBLAN based fibres

5.1 Overview

D EVELOPING a 3.5 μm fibre laser was more difficult than originally expected. The four-level nature of this transition should allow lasing with a relatively modest amount of absorbed 1973 nm light. Previous experiments described in Chapter 3 showed that up to 30% of the 1973 nm light is absorbed using 0.5 $mol\%$ doped fibre under low power conditions. This should have lead to a significant inversion when using highly doped fibre with higher powered versions of our 1973 nm pump source. The first unsuccessful attempts of lasing were undertaken using a heavily doped fibre with 4 $mol\%$ of Er^{3+} ions. We chose a fibre with a higher doping concentration for several reasons: Its commercial availability, the higher gain expected from a highly doped fibre overcoming internal losses in the fibre and the possibility of using shorter fibre resulting in lower overall internal losses. These were all important factors because of the low emission cross-section (see section 2.5) and hence the gain of the $^4F_{9/2} \rightarrow {}^4I_{9/2}$ transition. In addition, this doping was identified as the minimum needed to achieve efficient lasing on the $^4I_{11/2} \rightarrow {}^4I_{13/2}$ transition at 2.75 μm [114]. The absence of lasing obtained when using the 4 $mol\%$ Er^{3+} doped FiberLabs fibre raised questions as to the root cause of the problem and whether a new approach was needed.

This chapter details the additional investigations undertaken to identify the reasons why lasing did not occur. It provides a closer look at the spectroscopic properties of Er^{3+}:ZBLAN under dual-wavelength pumping (DWP). During the investigations detailed in this chapter, we identified a lifetime quenching effect of the upper laser level $^4F_{9/2}$ under DWP conditions. We then identified a previously unknown energy-transfer process that is the likely cause of the lifetime quenching. Using a set of experiments, we measured

the magnitude of this ET effect. Our improved understanding of the dynamics of the system led us to use a lower doped fibre in our later experiments. This allowed us to achieve the first lasing on the 3.5 μm transition using DWP as described in Chapter 6.

This chapter begins with a description of the system used throughout the experiments conducted from this point in this thesis and onwards (section 5.2). We continue by reporting on investigation of the dynamics of the Er^{3+}:ZBLAN system under DWP conditions. This involved measuring the lifetime of the upper laser state $^4F_{9/2}$ under DWP (section 5.3). This measurement found an unexpected lifetime quenching effect. We hypothesise this effect to be the result of a previously undocumented energy-transfer (ET) effect and not due to thermal effects (which are analysed in greater detail in Appendix E). In section 5.4, we provide additional evidence to the existence of this ET effect and we calculate the magnitude of the ET constant. This was done by first measuring the fluorescence from different Er^{3+} energy levels under DWP conditions. These fluorescence intensities were proportional to the population densities of the observed levels. Their absolute population densities were found by normalising the fluorescence reading at low pump power according to modelled population densities determined using a rate-equation simulation. The ET process was then included in the rate equations and its magnitude was determined by fitting it to the experimental results of the lifetime measurement.

5.2   General purpose experimental setup for spectroscopy

All of the experiments described in Chapters 5 and 6 use a single setup with slight variations. This section describes this common setup and provides an overview schematic in Figure 5.1 while variations and changes are described separately in each section. Full schematics of this this setup can be found in Appendix D.

5.2.1   DWP pump sources

The 3.5 μm DWP laser system required combining two pump sources. We changed the sources used in Chapter 3 to two new, optimised sources. The pump sources described in Chapter 4 were used exclusively from this point onwards.

The first pump was a commercially available, 330 mW fibre-coupled laser diode, operating at 974 nm wavelength. This diode was described in detail in section 4.2.1. The diode was capable of narrow-band operation at either 985 nm or 974 nm by tuning the temperature of the diode. This source will be referred to as the "980 nm diode" from this point

onward. If the wavelength is relevant to the context, the diode will be referred to as the 974 nm or 985 nm diode, explicitly.

The second pump laser was an in-house built 1973 nm fibre laser, which was described in detail in section 4.3.1. This Tm^{3+} fibre laser (TFL) was pumped by a 35 W, 790 nm fibre-coupled diode. A high-reflectivity FBG was used to stabilise the wavelength. Its output was a single transverse mode and unpolarised with a wavelength of 1973 nm (see section 4.3.1 for details).

5.2.2 DWP general purpose experimental setup

The beams from the two pump sources were combined using a 45° dichroic mirror and coupled into the ZBLAN fibre. Each source was individually mode-matched into the core of the ZBLAN fibre prior to their combination. The diameters and divergence of each of
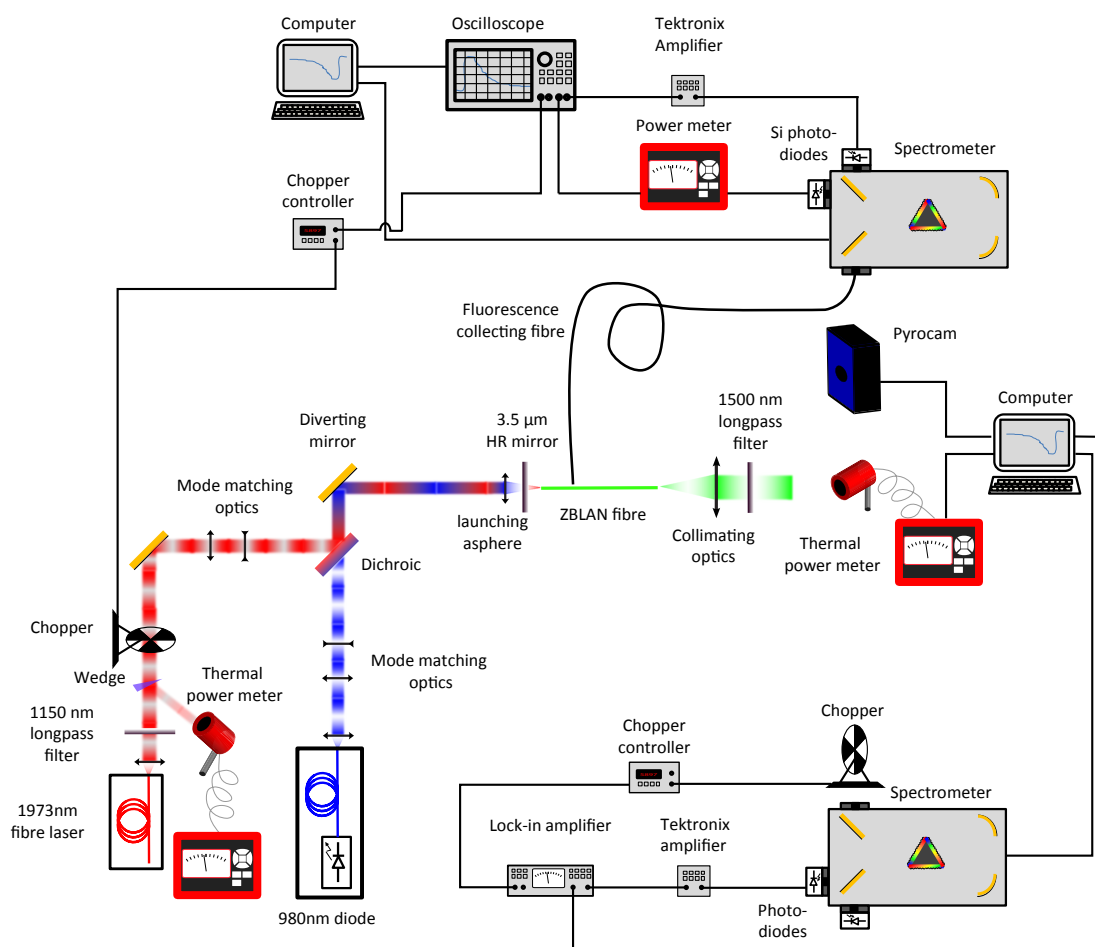
Figure 5.1: General purpose experimental setup for additional spectroscopy measurements. The beam emerging from the ZBLAN fibre could be directed towards either a thermal power meter, a thermal camera or a grating spectrometer.

the pump beams were adjusted using pairs of lenses to ensure waists of appropriate size for the core of the type of fibre used were located on the input face of the ZBLAN fibre (see Appendix D, Figure D.2 for detailed schematics).

Before combining with the 980 nm pump beam, the 1973 nm beam passed through a BK-7 wedge, which was used to sample the Tm^{3+} fibre laser power using a thermal power meter (Thorlabs S302C). The 1973 nm beam then passed through a mechanical chopper (Thorlabs MC1000) operating with a combination of two 10 slots blades in a $\sim 30\%$ duty-cycle configuration. This enabled operation in either CW mode or in chopped mode at frequencies up to 1 kHz and with a duty-cycle of $\sim 30\%$. The combined pump beams were reflected by a mirror into an aspheric lens (Thorlabs A220TM-C with $f = 11.0\ mm$). This lens launched the beams through an HR-coated dichroic laser mirror (Altechna 3 mm thick CaF_2) into the ZBLAN fibre (see Appendix D, Figure D.3 for detailed schematics). The HR mirror was either butt-coupled or displaced from the fibre tip, depending on the measurement performed.

The co-alignment procedure for the two pump beams is described in detail in Appendix G and a summary of the process is provided below. The beams were made to propagate over a long distance by removing the diverting mirror shown in Figure 5.1. The two combined beams were co-aligned to ensure they coincided closely and were parallel over the length of the optical table. This was necessary to ensure that both focused beams were co-axial after the aspheric lens.

The diverting mirror was then replaced, directing the pump beams through the centre of the launching asphere (Thorlabs A220TM-C or AL1815 depending on the ZBLAN fibre used). A knife-edge apparatus with two perpendicular blades was mounted on a translation stage. This apparatus was employed to locate the waists and verify co-location. A tedious process to correct small deviations of the waists of both beam was performed (see details of the apparatus and process in Appendix G, sections G.3 and G.2).

Firstly, the exact waist locations along the optical axis of both pump beams were found. Minor adjustments to the individual mode-matching were performed to ensure the waist location differed by less than 10 μm. This process ensured that the waists overlapped well within the Rayleigh range of the focused beams (typically 40 μm and 60 μm for the 980 nm and 1973 nm, respectively). At the same time, the lateral position overlap of the centres of the beams was verified by the micrometre resolution knife-edge apparatus to be within 2 μm perpendicular to the optical axis in both horizontal and vertical directions. This process ensured that both pump beams were well within the acceptance mode of the core numerical aperture (NA). This was especially important when using the double clad FiberLabs ZDF fibre, which had a relatively low NA = 0.12. In this fibre, light that

was not coupled into the core propagated easily in the first cladding with little overall absorption or attenuation.

After alignment, both beams were launched into the fibre, which rested in a groove in the fibre holder block. The transmitted pump beams and the fluorescence that emerged from the far end of the fibre were collimated using a CaF_2 lens (Thorlabs LA5315 $f = 20$ mm nominal). This lens was later replaced with an off-axis parabolic (OAP) mirror (Thorlabs MPD127127-90-M01 $f = 25.4$ mm), to mitigate issues with the alignment to the spectrometer cause by chromatic focal-distance shift of the CaF_2 lens. The transmitted pump and the fluorescence from the fibre were then incident on one of three possible detectors:

- Thermal imaging camera - Ophir Pyrocam III. This camera was used to validate that the 1973 nm beam was propagating in the core of the FiberLabs fibre. This was necessary since the normalised frequency (V-number denoted as $V_{\# core}$) of the core of this fibre at 1973 nm was very close to the single-mode limit of $V_{\# core} = 2.4$, requiring good mode-matching of the beam to the fundamental mode of the fibre. If the 1973 nm beam was coupled well into the core, then an image of the core would form rather than a random speckle pattern associated with propagation in the inner cladding and poor alignment.

- Power meter - Ophir 50 W L50A-SH connected to a Nova II console. This power meter measured the residual transmitted pump through the ZBLAN fibre. It enabled calculating the absorbed 1973 nm pump power by subtracting the transmitted 1973 nm pump power with and without the 980 nm pump. The transmitted 980 nm pump was rejected by using a 1500 nm longpass filter (Thorlabs FEL100).

- Triple grating spectrometer - Acton SP2557i with multiple possible detectors. This was used to determine the fluorescence spectrum and the lasing wavelength.

The initial alignment of the fibre to the pump beams was obtained by maximising the green and red fluorescence from the $^4S_{3/2}$ and $^4F_{9/2}$ levels, respectively, when under DWP. The output from the fibre was directed through a 2500 nm longpass filter (Spectrogon 713.709.290) and the beam was matched to the numerical aperture of the spectrometer using an OAP mirror (Thorlabs MPD127254-90-M01 $f = 50.8$ mm). When operating in CW a mechanical chopper wheel was used to chop the input fluorescence at 5986 Hz to enable detection with a lock-in amplifier (LIA). This frequency was used as it was the highest frequency available with our chopper, whilst maintaining good mechanical stability.

Spectral measurement used one of the three internal diffraction gratings of the spectrometer according to the wavelength band observed. The grating densities available were 600, 300 and 150 grooves per mm, which were blazed for maximum efficiency at 1 μm, 2 μm and 4 μm, respectively. The majority of the spectrum measurements conducted later in this thesis, concerning the 2.75 μm and 3.5 μm fluorescence and lasing, used the 4 μm blazed grating. Inside the spectrometer, the light was imaged at a one to one magnification by an OAP mirror from the input slit to the output slit while being diffracted by the grating on the way, which acted as a flat, wavelength-selective mirror. The light intensity was then measured using various detectors which are described in each specific experiment. In the measurements where light at wavelengths longer than 2.5 μm was observed, the signal was detected by a liquid nitrogen cooled InSb detector (Teledyne Judson J10D-M204-R04M-60) connected to a matched transimpedance amplifier (Judson PA-9). The output of the amplifier was connected to a LIA (Stanford SR830) synchronised to the 5986 Hz chopper. The output of the LIA was sent to a digitiser unit connected to a computer (Acton SpectraHub) that used the software for the spectrometer (Acton Spectra-sense).

5.3 $^4F_{9/2}$ lifetime measurement

Our initial attempts at lasing were conducted using the FiberLabs ZDF fibre with a doping of 4 $mol\%$ of Er^{3+} ions. We could not achieve lasing with this fibre despite repeated attempts. A study of absorbed power versus incident power at 1973 nm using a 6 cm long Er^{3+}:ZBLAN fibre (see Figure 5.2) suggested that we should be effectively populating the $^4F_{9/2}$ level. An estimate of the inversion obtained in our case and based on Többen's results in [117] suggested that the level of absorbed power should have been sufficient in our resonator design to obtain inversion and reach lasing threshold with absorbed 1973 nm power level between 75 mW and 100 mW. One possible explanation was that other processes were removing ions from the $^4F_{9/2}$ level, meaning the expected inversion from absorbed 1973 nm light was not achieved. We therefore decided to investigate the dynamics of the $^4F_{9/2}$ level.

5.3.1   Objective of measurement

We saw in section 2.4.3 that cross-relaxation (CR) processes, which involve energy sharing between ions in different energy levels, exhibit an exponentially decaying fluorescence from the excited level. Energy-transfer upconversion (ETU) processes involving two ions from the same level exhibit fluorescence decay rates which are non-exponential.
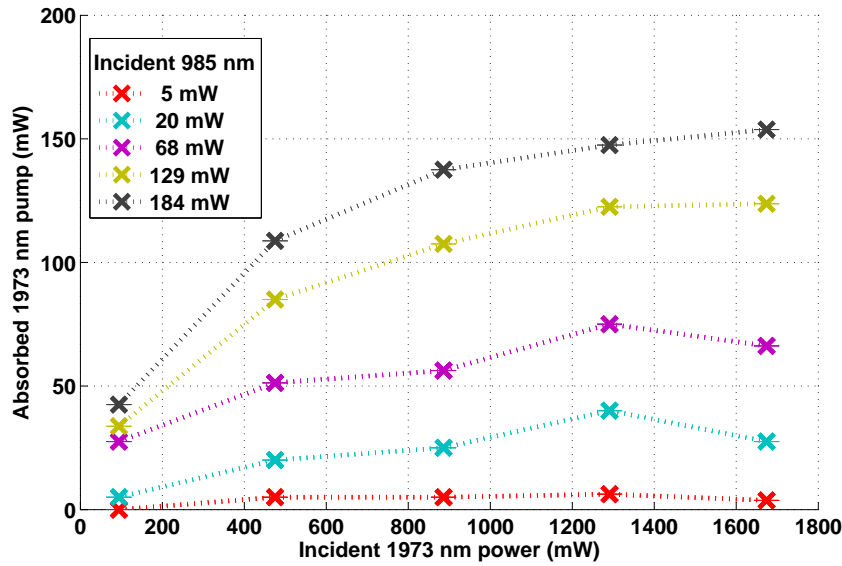
Figure 5.2: Absorbed 1973 nm pump as a function of both pump powers. Each curve represents a fixed incident 985 nm pump power while the 1973 nm incident power was changed. The fibre used was a 6 cm long, double-clad, FiberLabs ZDF fibre, which was doped with 4 $mol\%$ Er^{3+} ions. This fibre had a core of 14 μm diameter, an NA = 0.12 and a "D" shaped inner cladding with a diameter of ~ 300 μm.

Therefore, we can examine the changes in the decay rates, or inversely, the lifetime of the fluorescence from the upper laser level $^4F_{9/2}$. The shape of the fluorescence decay curve together with changes in the decay rate as a function of pump power were expected to be a good indicator of the existence of CR and ETU processes. We therefore set to measure the lifetime (the inverse of the decay rate) of the $^4F_{9/2}$ level under varying DWP conditions.

In the following experiment, we examined the population change in the $^4F_{9/2}$ level by observing the 657 nm fluorescence to the ground. Fluorescence from this level at this wavelength was proportional to the population density of the $^4F_{9/2}$ level. By recording how this changed with time, we were able to measure the lifetime of the upper lasing level and show that a significant lifetime quenching process was taking place as a function of 980 nm pump power, as we discuss in detail below. The decay curve closely followed an exponential decay, which could not be described by an ETU process. The decay was consistent with either multi-phonon decay, a CR process, or an ET process which involves different energy level. We saw in section 2.4.2 that multi-phonon decay rates were dependent on the fibre temperature. We calculated the change in fibre temperature with absorbed pump (see Appendix E), which showed that the lifetime quenching by multi-phonon decay was expected to increase the decay rate by approximately 10%. This could therefore only have a small contribution to the lifetime quenching effect. The bulk of the lifetime quenching of the upper laser level was likely to be caused by a

previously unknown ET process, or by an entirely different spectroscopic effect (clustering for example). We would use the results from this experiment to show first that a new ET effect can explain the lifetime quenching and later, in section 5.4, measure the magnitude of the ET parameter.

5.3.2   Experimental setup

The experimental setup for measuring the 657 nm fluorescence lifetime is described below. Since the fluorescence lifetime measurement was sensitive to re-absorption of fluorescence along the fibre, fluorescence was therefore collected from the side of the fibre. We used a large diameter, high numerical aperture fibre for collecting the fluorescence and delivering it to the spectrometer used in our experiment. This allowed the fluorescence to be effectively collected from only a small segment of the fibre. By collecting fluorescence from the side, we could ensure minimum re-absorption. This was similar to collecting fluorescence from the edge of a bulk samples while using a pinhole to restrict re-absorption [164].

The basic experimental arrangement was similar to the one shown in Figure 5.1 and described in section 5.2.2. Two pump beams of 985 nm and 1973 nm were combined and launched into the ZBLAN fibre under test. In this measurement, we used two types of fibre. The first was the double-clad ZDF fibre by FiberLabs with 4 $mol\%$ doping of Er^{3+} that was used previously. This fibre had a 14 μm core, with an NA = 0.12 and a $\sim$ 300 μm, "D" shaped inner cladding with an $\sim$ NA = 0.5. A second type of fibre was a single-clad fibre with 10 μm diameter core with an NA = 0.15 and 125 μm diameter cladding. This fibre, which was manufactured by IR-Photonics, had an Er^{3+} ion doping concentration of 1.7 $mol\%$. A more detailed discussion of the IR-Photonics fibre is presented in section 6.2.1. The difference in core sizes between the fibres necessitated using a different pair of lenses for the mode-matching on the 980 nm arm. This resulted is a slight reduction in the maximum incident power in the case of the ZDF fibre.

The lifetime measurement was a temporal measurement, therefore additional equipment and procedures were necessary to collect the fluorescence, store the data and analyse it. Moreover, as the experimental setup required a significant amount of synchronisation between different devices, a Matlab® instrumentation control code was written to automate the acquisition and control, synchronise the equipment and eventually perform automated data analysis. The equipment and procedure described below were automated, resulting in much faster and more consistent results compared with similar manually conducted measurements that we performed before automating the measurements.

To measure the fluorescence decay, it was necessary to chop the 1973 nm pump using a mechanical chopper while the 980 nm pump was operated in CW during the experiments. The 1973 nm beam passed through a mechanical chopper (Thorlabs MC1000A) which either blocked the beam or allowed it to incident on the ZBLAN fibre. The beam was chopped at up to 1000 Hz. For easier separation of the decay between successive pulses, two chopper wheels were assembled together on the optical chopper head to provide a duty-cycle of $\sim 30\%$. A transmission duration of 300 μs of the pump was obtained at the highest frequency of chopper operation. We will refer to this time period where the 1973 nm is incident on the ZBLAN fibre as the pump being "on." Such a pump duration is about twice as long as the lifetime of the $^4F_{9/2}$ level, thus allowing for sufficient population build-up. The transition time of the edge of the chopper blade across the beam was measured to be 35 μs.

The residual beams and the fluorescence emerging from the other side of the fibre were collimated using an $f = 40\ mm\ CaF_2$ lens (Thorlabs LA5370) for the case of the ZDF fibre. In the case of the IR-Photonics fibre, an $f = 25\ mm$ gold coated OAP mirror (Thorlabs MPD127127-90-M01) was used. The transmitted residual pump power and fluorescence were measured using a thermopile-based power meter (Ophir 50W L50A-SH connected to a Nova II console) which provided a time-averaged reading of the 1973 nm pump. These readings were used to ensure consistent power levels of the pumps and were monitored by the Matlab® application. Monitoring the power meter also enabled observation of the average power of both pumps transmitted through the fibre when operating individually. An additional 1500 nm longpass filter was added after the collimating lens in most measurements to block the residual 980 nm pump. This allowed measuring the average absorbed 1973 nm pump power by taking the difference between the observed 1973 nm pump with and without the 980 nm pump operating.

The fluorescence observed from the side of the ZBLAN fibre was collected by a large core (1000 μm diameter), polymer clad, multi-mode fibre (Thorlabs BFH48-1000). This fibre had a large numerical aperture of NA = 0.48, enabling effective collection of the fluorescence. The input end of the collecting fibre was located within 0.5 mm of the ZBLAN fibre. The fluorescence collecting fibre gathered fluorescence from approximately a 1 mm length segment of ZBLAN fibre according to the numerical aperture of the collecting fibre and the distance of the tip from the ZBLAN fibre. The collecting fibre could be moved along the length of the ZBLAN fibre to collect fluorescence from various locations along the ZBLAN fibre.

The fluorescence collected by the fibre was delivered to a second spectrometer (Acton SP2557i) that had two output ports. Due to the large diameter of the delivery fibre, it was necessary to have both of the spectrometer input and output slits open to a width

of 1.5 mm. This resulted in a resolution of $\sim 3\ nm$ and $\sim 6\ nm$ when operating with the 600 and 300 grooves per mm gratings, respectively. The former was used with the Si detector for measuring the 657 nm fluorescence decay curves, while the latter was only used for conducting relative measurements of the intensity of the fluorescence from the $^4I_{13/2}$ level at 1535 nm. An amplified Si photo-detector (Thorlabs PDA36A) and an InGaAs integrating sphere (Thorlabs S144C) were mounted on the two alternative ports of the spectrometer. The two detectors enabled measuring both temporal behaviour and fluorescence levels covering the visible range to 1700 nm (although not at the same time, as switching between the ports required a few seconds to flip a mirror mount internally). The voltage outputs of the detectors were connected to an oscilloscope (Tektronix TDS2024B) which was controlled by the computer that also logged the data. The output of the Si detector was also connected to a LIA (Stanford 830) and then to a digitiser unit connected directly to the computer (Acton SpectraHub). This additional channel was used to adjust the 980 nm pump power in order to obtain comparable fluorescence levels from the $^4I_{11/2}$ level when different pump wavelengths of 974 nm or 985 nm were used. The similar fluorescence level obtained indicated comparable population density and hence closely matching conditions.

The temporal response of the entire system when using the Si detector was tested by observing a tightly focused HeNe laser beam mechanically chopped at the focal point. It was shown that the rise and fall times were better than 10 μs, which was sufficient for this measurement.

5.3.3   Experimental procedure

Three datasets were collected with each step of the automated acquisition process: 128 fluorescence decay waveforms at 657 nm were collected and averaged for each 985 nm or 974 nm pump power level. The average transmitted 1973 nm power was measured with and without the 980 nm pump and the absorbed 1973 nm was deduced. Peak fluorescence intensities at 551 nm, 657 nm, 800 nm, 995 nm and 1535 nm were also collected for reference. The fluorescence intensities allowed us to deduce the relative changes in population densities of the different levels as a function of pump power. In addition, the changes in the intensity of the fluorescence at these wavelengths provided real time monitoring of the progress of the automated acquisition system.

The $^4F_{9/2}$ level lifetime was measured by observing the fluorescence decay waveform on the oscilloscope. This waveform was then read into the computer using our Matlab$^\circledR$ application, which analysed the waveform and fit an exponential decay with a decay lifetime τ_{int}. The fit was weighed towards the latter part of the decay curve. The reason

was that although the 1973 nm pump beam was chopped at its waist position along the 1973 nm arm, the mechanical chopper transition time over the beam was in the order of ~ 30 μs. The software would then compare the calculated decay constant of all the measurements conducted with different levels of 974 nm or 985 nm and 1973 nm pump levels and provide graphical output showing the behaviour of the lifetime, fluorescence levels and other parameters of interest.

We conducted a large number of measurements using different combinations of fibre, type of 980 nm pump used and pump wavelength while collecting the fluorescence at successive locations along the fibre. A separate set of measurements was conducted with each of the available fibres, the IR-Photonics fibre and the FiberLabs ZDF fibre. In all experiments, the 1973 nm pump beam was launched into the core of the fibre. In most cases, the 980 nm pump was also launched into the core, except in the case of the FiberLabs ZDF fibre. With this fibre we were also able to launch a 974 nm beam into the inner cladding of the fibre. This became possible by replacing the FBG stabilised high-brightness diode with a high-power, low brightness diode that could only operate at 974 nm (see section 4.2). In all cases where the 980 nm diode was core pumping, a different dataset was taken for either 974 nm or 985 nm wavelength of operation. Our fluorescence collecting fibre could also be moved along the ZBLAN fibre, thus enabling observation of the change in the fluorescence lifetime as a function of distance from the pump input side. The full experimental procedure is detailed in Appendix F.

5.3.4   Lifetime measurement results and analysis

Each of the fluorescence measurement datasets was analysed to extract the fluorescence lifetime. An exponential decay was fitted to the observed waveform. Figure 5.3 shows an example of this fit. In some measurements, especially when conducting the lifetime measurements with the ZDF fibre, it was noted that using a double exponential decay provided a slightly better fit. This double exponent, following Bogdanov [135], was of the form $Aexp(-t/\tau_1) + Bexp(-t/\tau_2)$, which can indicate the presence of an energy-transfer upconversion process of some sort. However, the differences between the single and double exponential decays were insignificant for our purpose. Therefore, the results provided in the following section are based on a fit with a single exponential decay time constant.

The typical behaviour of the $^4F_{9/2}$ level lifetime, inferred from the 657 nm fluorescence as a function of the power of both pumps, is shown in Figure 5.4. The $^4F_{9/2}$ level lifetime decreased with increasing 985 nm pump power and remained approximately constant with changing 1973 nm pump power.
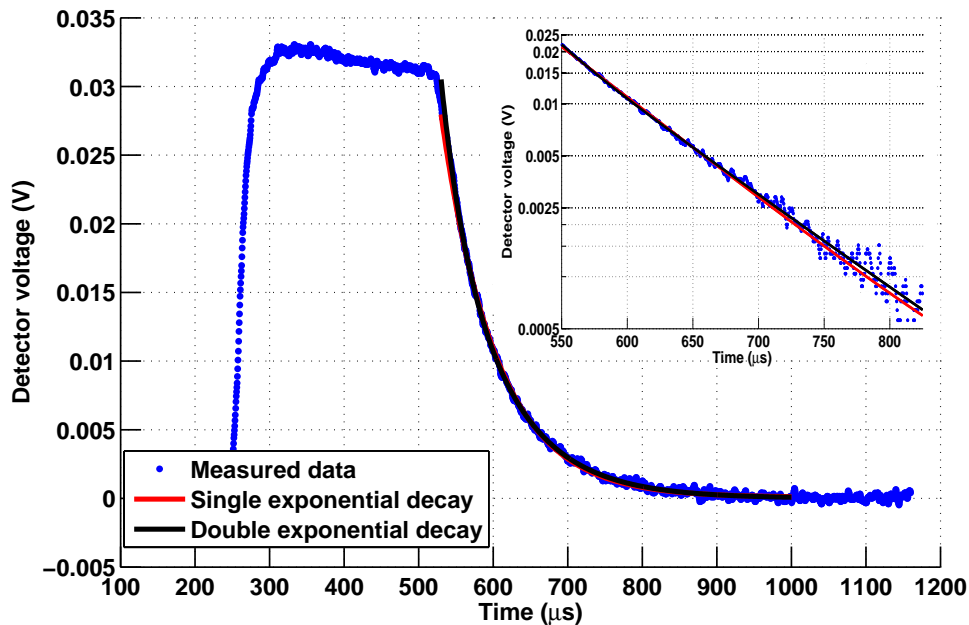
Figure 5.3: Example of 657 nm fluorescence decay waveform on the oscilloscope. Single and double exponential decays are fitted. The stronger fluorescence observed on the leading edge of the pulse is the result of a temporary increase in the 1973 nm pump caused by different feedback conditions when blocking by the chopper was suddenly removed. The inset shows the decay part of the waveform on a logarithmic scale together with both fit options. This waveform example was taken from a measurement with a FiberLabs ZDF fibre.
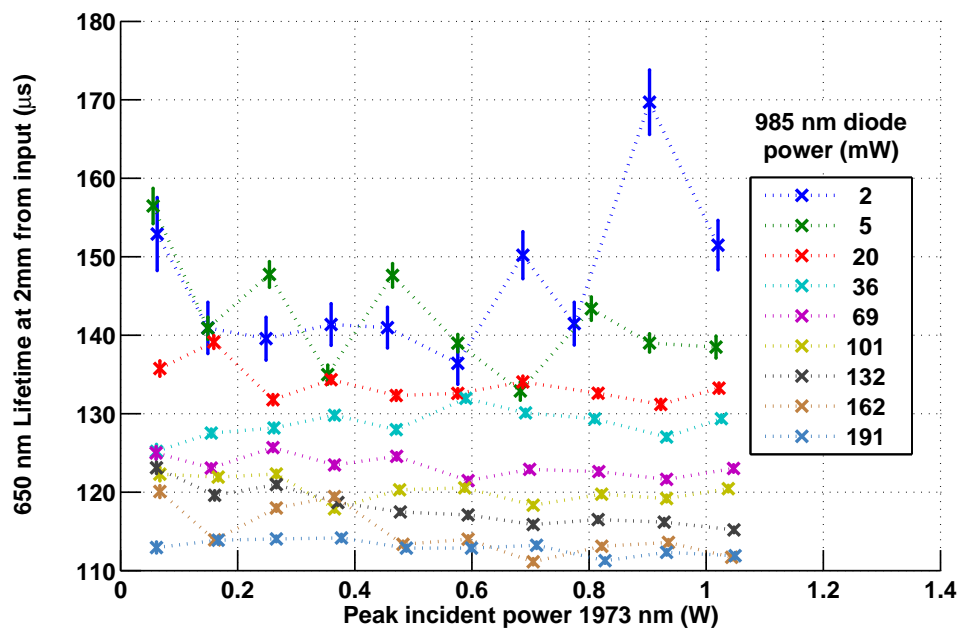
Figure 5.4: Example of $^4F_{9/2}$ lifetime changes with pump power in IR-Photonics fibre. Each coloured curve represents a fixed 985 nm pump power, while the 1973 nm pump power was increased. Fluorescence collected at 2 mm from the fibre input side.
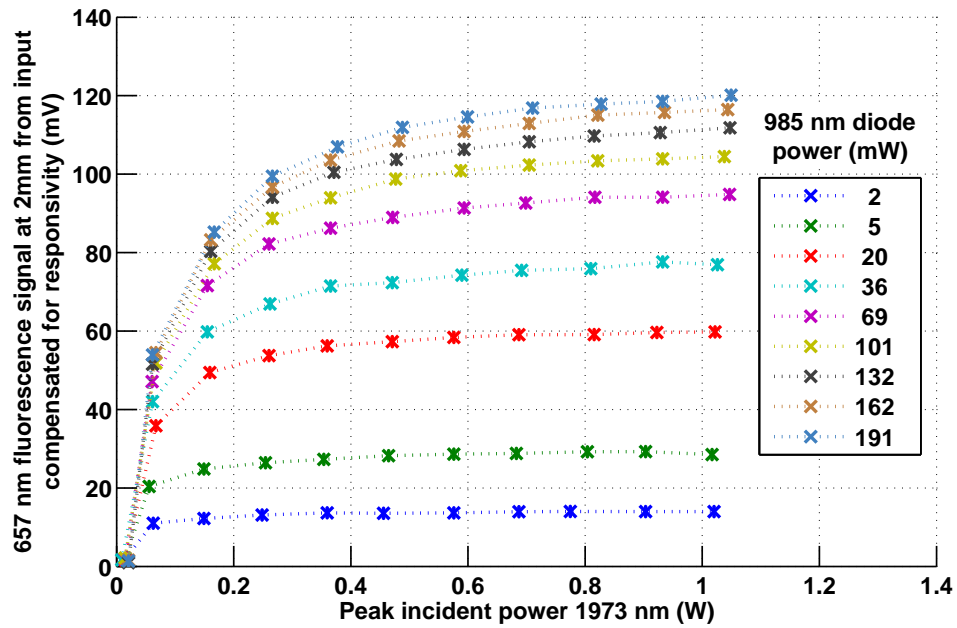
Figure 5.5: Rise of the 657 nm fluorescence with increasing 1973 nm pump power in the case of the IR-Photonics fibre. The fluorescence intensity is proportional to the $^4F_{9/2}$ level population density.
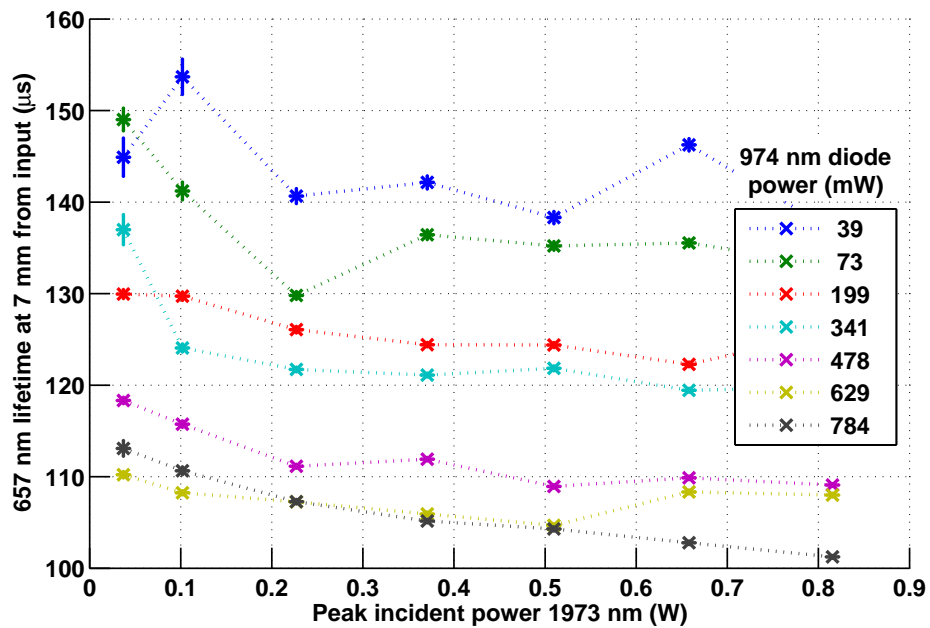
Figure 5.6: $^4F_{9/2}$ lifetime with varying pump power for a clad-pumped ZDF fibre measured 7 mm from the fibre tip. Each coloured curve represents a fixed 974 nm pump power while the 1973 nm pump power was increased.

The insensitivity to the incident 1973 nm was surprising, because increasing the incident 1973 nm pump resulted in elevated $^4F_{9/2}$ population density as evident by the higher 657 nm fluorescence observed (see Figure 5.5). The insensitivity to 1973 nm power was maintained for all cases examined under 985 nm pumping, including both core and clad pumped ZDF fibre (see for example Figure 5.6) and with the IR-Photonics fibre.

The 1973 nm pump had almost no effect on the fluorescence lifetime, therefore we can average over all the lifetime readings with the same 980 nm pump. We thus compare the average of all the lifetime measurements performed under core pumping using varying 980 nm power levels (see Figure 5.7). The figure shows the lifetime measured with core pumped ZDF and IR-Photonics fibres when the wavelength of the first pump is 974 nm or 985 nm and as a function of pump power. This comparison is based on 650 nm fluorescence lifetime collected at a distance of 2 mm from the input side, along the length of the fibre.
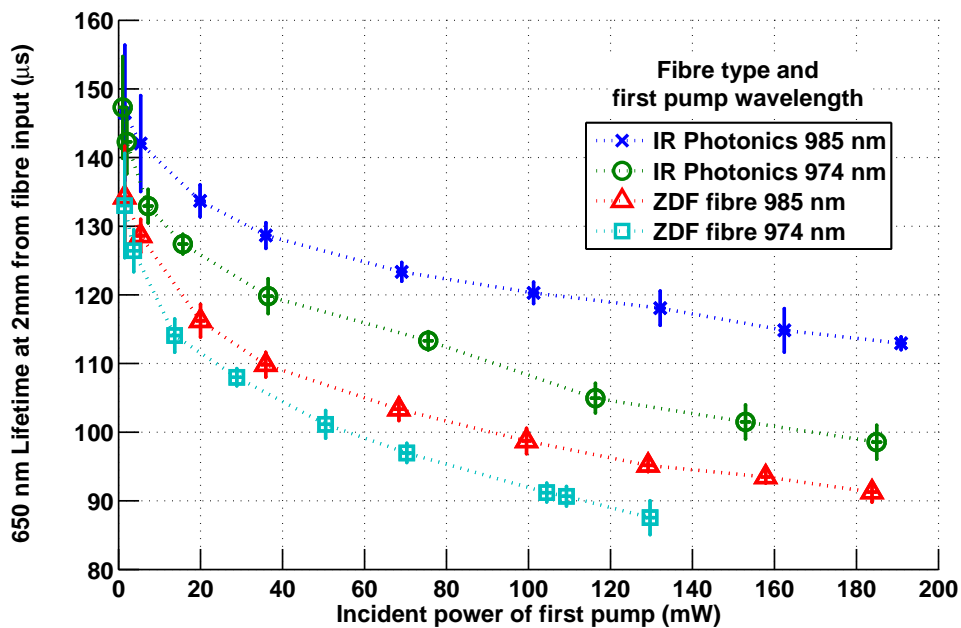
Figure 5.7: Comparison of average 657 nm fluorescence lifetime between ZDF and IR-Photonics fibres using varying 980 nm first pump and core pumping. All measurements taken 2 mm from the fibre tip.

For each fibre, the lifetime was measured with different levels of 985 nm incident pump power and fluorescence was collected perpendicular to the fibre at 995 nm. Each set of lifetime measurements was repeated a second time for each fibre with the first pump wavelength shifted to 974 nm. This time, however, instead of maintaining the same incident power as in the case of the 985 nm pump, the power was adjusted until similar

fluorescence levels were collected at 995 nm. This arrangement ensured similar population densities of the $^4I_{11/2}$ level (as indicated by the 995 nm fluorescence) and an objective comparison of lifetime dependency on the first pump wavelength. The wavelength of 995 nm was chosen to provide sufficient separation from the 974 nm and 985 nm pump wavelengths while still being able to observe significant fluorescence. The results are also shown in Figure 5.8 as a function of 995 nm fluorescence intensity
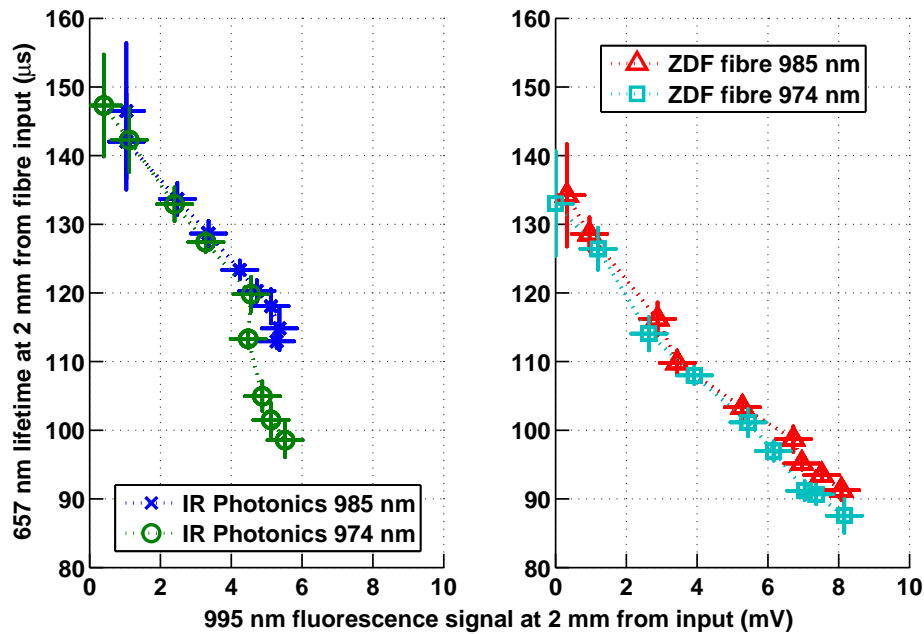
Figure 5.8: Comparison of average $^4F_{9/2}$ lifetime between 974 nm and 985 nm first pump wavelength as a function of 995 nm fluorescence, which is proportional to $^4I_{11/2}$ population density. All measurements were taken 2 mm from the fibre input side. The results of the two fibres cannot be compared directly because the experiments with the IR-Photonics and ZDF fibres were conducted at different times and under different mode-matching and collecting fibre conditions. This is likely to have resulted in different collecting efficiency of the 995 nm fluorescence.

Figures 5.7 and 5.8 show a few significant trends:

1. The lifetime was significantly lower in the ZDF fibre, which had a doping concentration two and a half times that of the IR-Photonics fibre.

2. For the lower doped IR-Photonics fibre, the 650 nm lifetime started at approximately 150 μs and consistently decreased as a function of 980 nm pump.

3. The lifetime quenching observed in Figure 5.7 trended towards saturation in all cases with the pump power available to us. The saturation value depended on the specific combination of the fibre and first pump wavelength. Full saturation was not reached and would seem to require additional power from a 980 nm pump.

4. Using the 974 nm pump resulted in a shorter lifetime compared with 985 nm pumping under the same incident power. In the IR-Photonics fibre, the reduction was more substantial, with a 10-15 μs reduction, while in the ZDF fibre it was on the order of 5 μs for a similar population of $^4I_{11/2}$.

5. When comparing the lifetime under 974 nm or 985 nm pumping as a function of $^4I_{11/2}$ population, the advantage of pumping at 985 nm over 974 nm is maintained, although reduced. In the IR-Photonics fibre, a significant difference exists only at population densities exceeding 80% or more, of its maximum value of population density. With the ZDF fibre, a consistent difference of 3-5 μs is maintained at all pump levels.

Further evidence supporting our hypothesis that the lifetime quenching results from a ET mechanism is displayed in Figure 5.9. In this figure, we present the measured decay rate ($^1/\tau_{int}$) as a function of observed 995 nm fluorescence. This fluorescence is proportional to the population density of the $^4I_{11/2}$ level under DWP conditions. Each set of similar coloured markers represent a fixed 1973 nm incident power level while the 985 nm pump power was increased, resulting in higher 995 nm fluorescence and hence $^4I_{11/2}$ population. When the population of the $^4I_{11/2}$ level is low, the decay rate of the
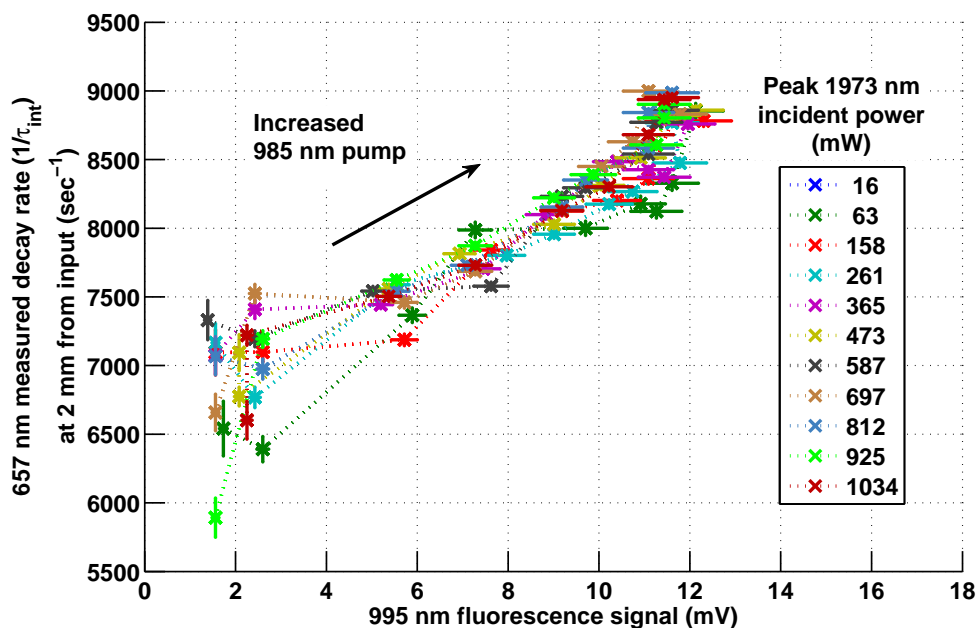
Figure 5.9: Change in the decay rate of the $^4F_{9/2}$ level as a function of $^4I_{11/2}$ population in IR-Photonics fibre. The 995 nm fluorescence intensity is proportional to the $^4I_{11/2}$ population. Markers of the same colour represent readings taken with a fixed 1973 nm pump while the 985 nm pump power was changed. Lines between markers are only used as a guide to the eye.

$^4F_{9/2}$ level is at its lowest, while it increases by about 30% at the highest 985 nm pump power, corresponding to the highest $^4I_{11/2}$ population. The increase in rate seems to follow a linear trend with $^4I_{11/2}$ population, which is consistent with a CR-type, or ET decay mechanism that preserves the exponential decay behaviour.

We also examined the changes in the $^4F_{9/2}$ level lifetime when the ZDF fibre was cladding-pumped with a high power, low brightness 974 nm diode. This diode delivered up to a few watts of 974 nm from a 200 μm multi-mode fibre that was imaged into the inner cladding of the ZDF fibre.

Pumping into the inner cladding significantly reduced the heat load per unit length compared with core pumping. In addition, the absorption profile along the fibre was much more uniform and over significantly longer absorption lengths. Hence, this data could indicate whether a thermal gradient along the fibre was the dominant cause of the lifetime-quenching effect, as will be explained shortly.

Figure 5.10 shows the average measured $^4F_{9/2}$ level lifetime at different locations along a 143 mm long ZDF fibre as a function of incident 974 nm pump diode while clad-pumping. For this measurement, we used the high-power, low brightness diode. As the lifetime
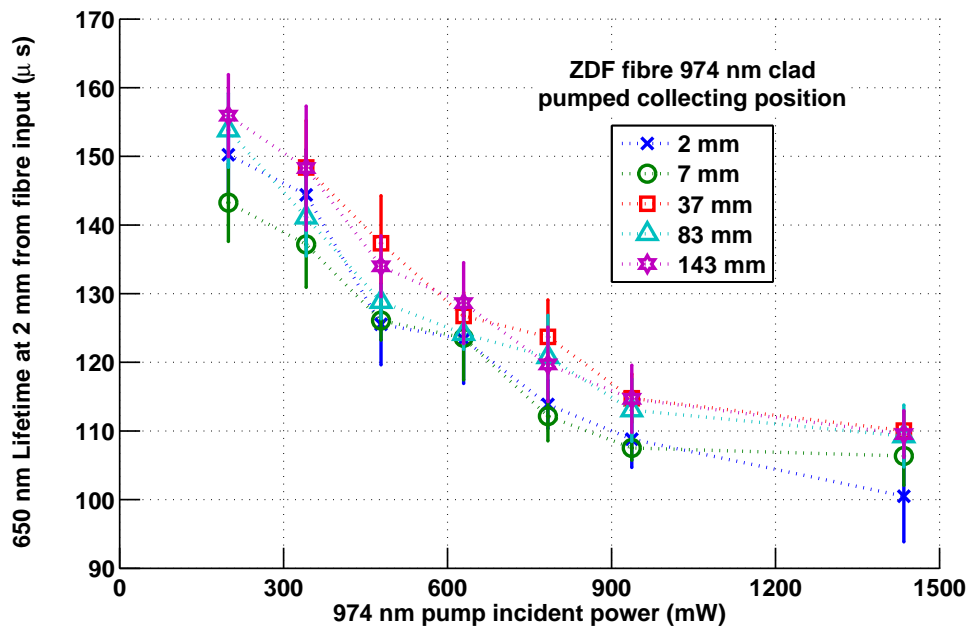
Figure 5.10: Measured $^4F_{9/2}$ level lifetime at different locations along a 143 mm long ZDF fibre when clad pumping. High power low brightness 974 nm diode was used.

was approximately independent of the 1973 nm pump, each point on each of the curves represents the average value over different 1973 nm pump power at a specific location

along the fibre. The different symbols correspond to the different fluorescence collection position along the fibre.

The observed average lifetime started at 150 μs and consistently dropped with increasing 974 nm pump power. This trend persisted at all locations tested along the fibre. These results were similar in nature to the ones obtained using core-pumped IR-Photonics fibre shown in Figure 5.7. We observed a small discrepancy at low 974 nm pump between core and clad pumped ZDF fibre when comparing Figures 5.7 and 5.10. Lifetime results observed along the fibre 2 mm from the fibre input side were $\sim$ 134 μs when core pumping compared with $\sim$ 148 μs when clad pumped. The reason for this discrepancy is not fully understood and warrants future investigation. It was not possible to tune the wavelength of this diode to 985 nm and thus corresponding values with a 985 nm pump are not available.

We now examine the possibility that the lifetime quenching is the result of heating of the fibre. Table 5.1 displays the calculated absorbed 980 nm pump power at the first 2 mm of the different fibres used in our lifetime measurements. The calculated upper limit on the absorbed pump in the case of clad pumping was an order of magnitude lower than in the core pumping cases assuming negligible bleaching of the pump. Such low pump power absorption would result in negligible heating of the fibre per unit length, therefore

Table 5.1: Calculated upper limit on absorbed 980 nm pump in the first 2 mm of fibre used for lifetime measurement. Values were obtained based on absorption cross-sections of $\sigma_a = 2.1 \times 10^{-21}$ cm^2 and $\sigma_a = 0.93 \times 10^{-21}$ cm^2 for 974 and 985 nm respectively. IR-Photonics fibre ion density was 2.72×10^{20} $ions/cm^3$ while the ZDF fibre ion density was 6.4×10^{20} $ions/cm^3$ and the core to clad ratio was 1/338. The following values do not take into account bleaching of the ground or pump absorption saturation.

Fibre and pump wavelength (%)	Calculated absorption coefficient α		Percentage of 980 nm pump absorbed in first 2 mm (%)	Upper limit on absorbed power in first 2 mm of fibre based on maximum incident pump power (mW)
	(dB/m)	(m^{-1})		
IR-Photonics, core pumped 974 nm	271	57.1	12%	< 23.3
IR-Photonics, core pumped 985 nm	109	25.3	5%	< 8.5
ZDF, core pumped 974 nm	639	134	25%	< 48.5
ZDF, core pumped 985 nm	258	59.5	11%	< 18.7
ZDF, clad pumped 974 nm	1.89	0.44	0.09%	< 0.86

causing only negligible change to multi-phonon decay rates. Moreover, as Figure 5.10 demonstrates, the reduction in lifetime is observed consistently under relatively low pump power conditions that could not have results in a significant increase of the multi-phonon decay rate. We can therefore hypothesise that the increased heat load associated with higher 980 nm pump power was not the primary cause of the change in lifetime. This assumption was investigated further and validated using a theoretical and numerical analysis in Appendix E.

Our hypothesis of an ET mechanism was also supported by observing the fluorescence behaviour from levels other than $^4F_{9/2}$ while DWP. Examples for the observed waveforms are shown in Figure 5.11.
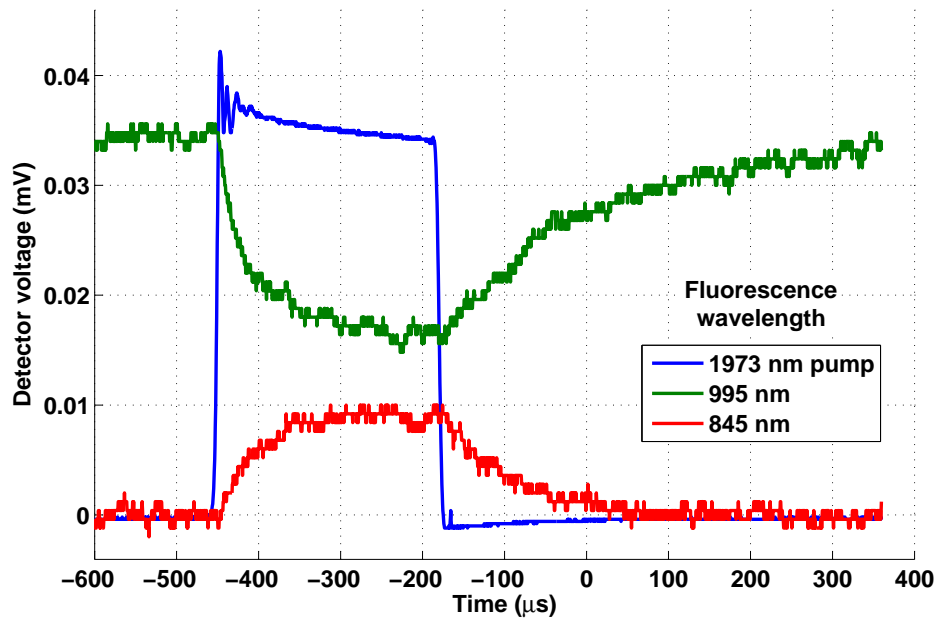
Figure 5.11: Fluorescence waveform at 995 nm and 845 nm when using DWP. The 1973 nm pulse used to generate 657 nm fluorescence (not shown in this figure) also altered the fluorescence from other levels. 995 nm fluorescence from $^4I_{11/2}$ to the ground was reduced while 845 nm fluorescence corresponding to the $^4S_{3/2} \rightarrow {}^4I_{13/2}$ transition increased. The 995 nm and 854 nm signals were recorded using DC coupling in the oscilloscope while the 1973 nm signal used AC coupling. This waveform was recorded at a measurement that used the FiberLabs ZDF fibre.

The reduction of 995 nm fluorescence when the 1973 nm pump was incident was not surprising as it depopulated the $^4I_{11/2}$ level. It was also observed that the 845 nm fluorescence increased, which corresponded to the $^4S_{3/2} \rightarrow {}^4I_{13/2}$ transition, as did the 1550 nm fluorescence (not shown in Figure 5.11 since it required a different detector), which corresponded to the $^4I_{13/2} \rightarrow {}^4I_{15/2}$ transition. This result and the previous results are explained further in the following section, which discusses the previously undocumented $^4F_{9/2} + {}^4I_{11/2} \rightarrow {}^4S_{3/2} + {}^4I_{13/2}$ ET processes.

5.4   A new energy-transfer process influencing the decay dynamic under DWP

In the previous section, we studied the temporal behaviour of the $^4F_{9/2}$ level in the ZDF and IR-Photonics fibres. A lifetime-quenching effect was observed and was suggested to be the result of a previously unreported ET process. In this section, we lay out the theoretical framework and derive the value of the newly found ET parameter. The value is found based on the the lifetime quenching measured previously and additional experiments measuring the changes in fluorescence from the first five excited energy levels of Er^{3+}:ZBLAN under varying DWP conditions. The analysis is applied to both the 1.7 $mol\%$ and 4 $mol\%$, Er^{3+} ions doped IR-Photonics and FiberLabs ZDF fibre with the ET parameters for both fibres presented.

Our approach was based on conducting a set of measurements that recorded the fluorescence collected from the side of a ZBLAN fibre under various DWP conditions in CW. We then used a simplified rate equation numerical model, based on the equations from section 1.5.4. This model allowed us to establish a one-to-one fit between the observed fluorescence intensity at low 980 nm pump power when the 1973 nm pump was off and the simulated population density of the first five excited states in Er^{3+}:ZBLAN. The rate equation for the $^4F_{9/2}$ level was solved based on the absolute population densities of the relevant levels and an estimated value for the ET parameter. The eventual value of this ET factor was determined by fine-tuning its value until a good fit between the calculates and observed fluorescence decay rates was reached. Introducing the new ET factor into the rate equation for $^4F_{9/2}$ allowed replicating the observed lifetime quenching effect observed in section 5.3. The importance of this ET process lies in its detrimental effect on lasing on the 3.5 μm transition. Gaining a better understanding of this process is therefore necessary for future numerical analysis aimed at optimising this laser system.

5.4.1   The relation between population dependency on pump, fluorescence decay rate and energy-transfer factors

The energy difference between the initial and final states in the $^4F_{9/2} +^4 I_{11/2} \rightarrow$ $^4S_{3/2} +^4 I_{13/2}$ ET process is 502 cm^{-1} of surplus energy assuming transition between line-centres. This difference is exothermic and smaller in magnitude than the energy of a single phonon in ZBLAN glass. This ET process is therefore likely to occur and have a high ET constant. Under ordinary pumping schemes used with 2.75 μm lasers, this process is not strong because the population of the $^4F_{9/2}$ level is small, which is the likely cause for it being unreported so far. However, the additional pumping at 1973 nm

pump under DWP conditions creates a large population density in both the $^4F_{9/2}$ and $^4I_{11/2}$ levels, therefore, intensifying the influence of this process. Strictly speaking, this process is an inverse CR process or an ETU, with the energetic states of the two ions further apart at the end of the process. However, from a mathematical perspective, the rate term of this process is similar to that of a CR. Therefore, to avoid confusion with the other ETUs described in this work, we designate this process only as an ET.

The ET process has an additional effect beyond the re-distribution of population among various levels. As is shown below, the ET process reduces the lifetime of the $^4F_{9/2}$ level with increasing $^4I_{11/2}$ population. Therefore, if the population densities in the fibre in CW were known, we could calculate the magnitude of the ET parameter.

In order to derive an expression for the value of the ET parameter, we shall refer back to the relevant rate equations from section 1.5.4 which incorporate this ET process. A few simplification assumptions are used to arrive at a single rate equation which ties the temporal behaviour of the $^4F_{9/2}$ level with that of the $^4I_{11/2}$ and $^4S_{3/2}/^2H_{11/2}$ level.

We begin by inspecting the rate equation associated with the $^4F_{9/2}$ level (Equations 1.2c). This rate equation includes the term for the $^4F_{9/2} +^4 I_{11/2} \rightarrow {}^4S_{3/2} +^4 I_{13/2}$ ET process, which we denote by W_{42}. For ease of reference, Figure 5.12 provides a simplified energy level diagram of Er^{3+}:ZBLAN, which includes the numbering of the energy levels and the fluorescence lines recorded in the following experiments. A complete energy level diagram can be found in the fold-out at the end of this thesis. Population densities N_i and decay lifetimes τ_i in the following derivation relate to the appropriate levels in Figure 5.12.

Following the notation of section 1.5.4, the ET constant W_{42} can be found from

$$dN_4(z)/dt = R_{P_2}(z) + \beta_{64}\tau_6^{-1}N_6(z) + \beta_{54}\tau_5^{-1}N_5(z) - \tau_4^{-1}N_4(z)$$
$$- W_{42}N_2(z)N_4(z) - R_{SE43}(z). \qquad \text{(1.2c revisited)}$$

Some terms in Equation 1.2c could be eliminated. During the lifetime measurements, the decay was observed after the 1973 nm pump beam was blocked by the mechanical chopper. The pump rate $R_{P_2}(z)$ can thus be assumed to be zero. There were no resonator mirrors in place, therefore, the stimulated emission term $R_{SE43}(z)$ could be omitted. In addition, the term $\beta_{64}\tau_6^{-1}N_6(z)$ was neglected since the $^4F_{7/2}$ level is thermally coupled to the $^4S_{3/2}/^2H_{11/2}$ levels, resulting in an almost instantaneous re-distribution of ions between all three levels. The fluorescence from these levels can therefore be regarded as coming from a single level, which we shall refer to as the $^4S_{3/2}/^2H_{11/2}$ level. The resulting equation involving the ET constant W_{42} is

$$dN_4(z)/dt = -N_4(z)\{\tau_4^{-1} + W_{42}N_2(z)\} + \beta_{54}\tau_5^{-1}N_5(z). \qquad \text{(5.1)}$$
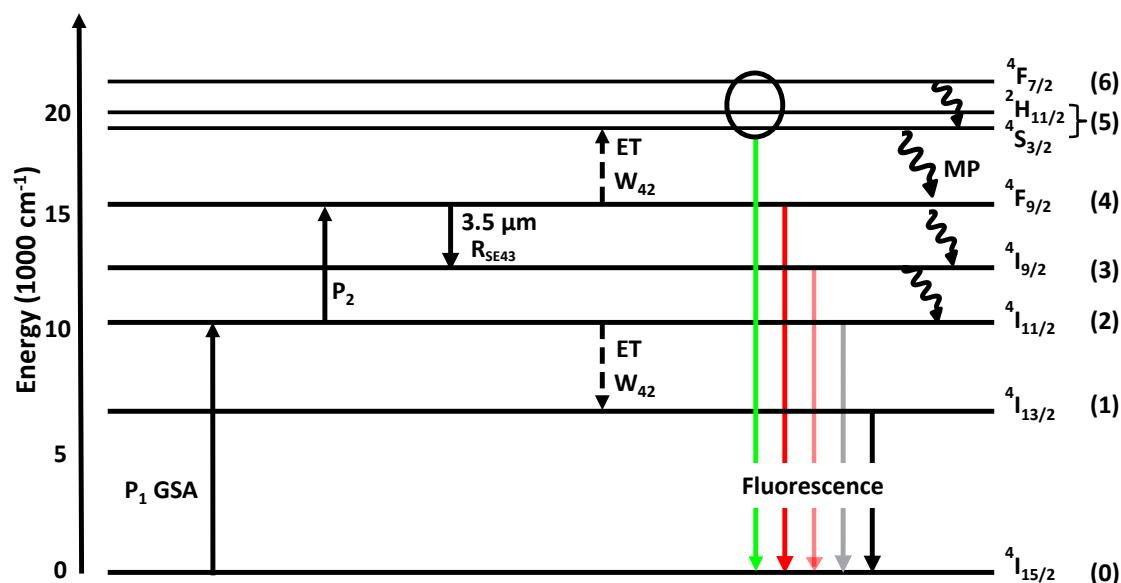
Figure 5.12: Simplified energy level diagram of Er^{3+}:ZBLAN. The diagram shows the pump transitions, the fluorescence transitions used in the following analysis and the ET process investigated. A complete diagram, which includes all the processes relevant to DWP in Er^{3+}:ZBLAN, is available in Figure FO.1 in the fold-out.

We can now find a solution to Equation 5.1 while considering the effect of the last term in Equation 5.1 on the behaviour of the system under DWP. This term has a relatively small effect under DWP for a few reasons. Firstly, the value of the transition $^4S_{3/2}/^2H_{11/2} \rightarrow {}^4F_{9/2}$ branching ratio, $\beta_{54} = 0.25$, reduces the effect of this term. The value for this branching ratio is based on literature data that can be found for this transition and others in Appendix E, Table E.2. In addition, the intrinsic lifetime of the $^4S_{3/2}/^2H_{11/2}$ levels, τ_5, is Er^{3+} concentration dependent and varies between 560 μs at very low doping concentrations to ~ 15 μs at very high ones (9 $mol\%$) [163]. For the case of the IR-Photonics fibre, interpolation of literature values for the case of 1.7 $mol\%$ concentration results in a lifetime of ~ 320 μs which is 2-3 times longer than the $^4F_{9/2}$ lifetimes obtained in section 5.3.4. In this case, the change in N_5 was small during the decay time of N_4 and hence could be treated effectively as constant, N_5^0. Under these conditions with the additional assumption, which will be discussed shortly, of a constant N_2, the solution to Equation 5.1 follows a simple exponential decay with a decay time constant of the form $\tau_4^{-1} + W_{42}N_2(z)$.

In the case of the FiberLabs fibre with its 4 $mol\%$ Er^{3+} concentration, the literature value for the lifetime of $^4S_{3/2}/^2H_{11/2}$ is ~ 100 μs [163]. This lifetime is comparable to our measured lifetime and could not be assumed to be constant. This results in a varying N_5 population. After pumping had stopped, we can assume the population of N_5 to follow approximately an exponential decay of the form $N_5^0 e^{-t/\tau_5}$ because the initial population N_5^0 is depleted by multi-phonon decay and fluorescence. With these

assumptions, we cannot use the simple exponential decay waveform suggested for low doping of Er^{3+}:ZBLAN. Using these conditions and with the additional assumption of a constant N_2 population, Equation 5.1 which is a non-homogeneous, linear differential equation, has the following closed-form solution (the longitudinal dependency was omitted for brevity)

$$N_4(t) = N_4^0 e^{-(\frac{1}{\tau_4} + W_{42}N_2)t} + \frac{\beta_{54}N_5^0}{\frac{\tau_5}{\tau_4} + W_{42}N_2\tau_5 + 1} e^{-\frac{\beta_{54}t}{\tau_5}}. \tag{5.2}$$

N_4^0 is the $^4F_{9/2}$ initial population density at the beginning of the decay.

This solution to Equation 5.1 requires a constant population density of N_2, $(^4I_{11/2})$ as a function of time. Without this assumption, a closed form solution for Equation 5.1 could not be found. The lifetime of $^4I_{11/2}$ is on the order of 7 ms, which is 40 times the measured lifetime of $^4F_{9/2}$. Therefore, under low power 1973 nm pumping conditions, the N_2 population can be assumed constant.

Although useful as a starting point for measurements with low or moderate 1973 nm pump power, the assumption of a fixed N_2 population did not hold for higher 1973 nm pump power, as can be seen for example in Figure 5.11. The changes in the $^4I_{11/2}$ population were due to the ESA from the $^4I_{11/2}$ level by the 1973 nm pump. As seen in Figure 5.11, the changes in $^4I_{11/2}$ population were occurring at the same time as the change in $^4F_{9/2}$ population. To account for that, we assumed that once the 1973 nm pump was blocked, N_2 population followed an exponential increase of the form

$$N_2 = N_{2\,no\,1973\,nm} + (N_{2\,with\,1973\,nm} - N_{2\,no\,1973\,nm})e^{-\frac{t}{\tau_4}}, \tag{5.3}$$

where $N_{2\,no\,1973\,nm}$ is the $^4I_{11/2}$ population when only the first pump is operating and $N_{2\,no\,1973\,nm}$ is the $^4I_{11/2}$ population when DWP. Taking into account the change in N_2 population resulted in approximately a 30% reduction in the ET factor calculated compared with calculations based on a fixed N_2 population.

At this stage, if the population densities of N_2, N_4 and N_5 were known in steady state, we could use these values as the initial population densities prior to blocking the 1973 nm beam in the lifetime measurements of section 5.3. We already measured the waveform of the decay from $N_4(t)$, therefore we could fit the right-hand side of Equation 5.2 to $N_4(t)$ by adjusting the value of the ET parameter W_{42}. If a good fit was to be obtained, the value for W_{42} used was the ET constant we were after.

In the next sections, we describe the experimental setup used for determining the population densities of the first excited state in our Er^{3+}:ZBLAN fibres while using DWP with varying power levels of both pumps. The population densities found in this experiment are later used together with the lifetime values measured previously to determine the magnitude of the ET parameter.

5.4.2   Experimental setup for measuring fluorescence dependency on pump power and finding the energy-transfer constant

To find the population densities of the different energy levels, we started by collecting fluorescence from the side of our Er^{3+}:ZBLAN fibre under DWP conditions. The same setup used for lifetime measurements (Figure 5.1) was used with minor modifications to measure the fluorescence dependency on pump power. First, both the 980 nm and 1973 nm pumps were used in CW. The second change was that the fluorescence collecting fibre was connected to a Yokogawa ANDO AQ6315E optical spectrum analyser (OSA) instead of the spectrometer.

Using the OSA over the individual spectrometer-mounted photo-diodes had two main advantages:

1. The OSA provided a fast scan over the entire 350-1700 nm band with one detector which took into account the instrument response due to wavelength changes.

2. The OSA had a high dynamic range of at least 90 dB, allowing the measurement of very weak signals as well as strong ones with very good linearity.

Using a large core collecting fibre allowed collecting a few orders of magnitude more fluorescence than when using a single mode fibre. One disadvantage of collecting fluorescence with a large core fibre was that the OSA achieved optimal wavelength accuracy with a single mode fibre connected at its input. Spectral broadening on the order of a few nm of the signals collected occurred due to the large core size of the collecting fibre. This broadening, however, was insignificant compared with the 30 nm-100 nm width of the different transitions. Moreover, our measurements were comparative by nature, thus the slight broadening did not pose a problem.

The following Matlab® semi-automated procedure was used for collecting the wideband fluorescence intensity method under varying DWP conditions:

1. We positioned the collecting fibre above the tip of the ZBLAN fibre while it was almost touching it.

2. A background scan of the OSA without any signal was obtained.

3. The 985 nm pump was changed to a pre-determined power level and an OSA scan was performed.

(a) The 1973 nm pump power was adjusted to the first power level and an OSA scan was conducted.

(b) The 1973 nm pump power was increased and a scan was performed. This process was repeated until maximum 1973 nm pump level was reached.

4. Stage 3 was repeated with an increased 985 nm power until maximum 985 nm power was reached.

5. Stage 3 was repeated with the diode wavelength tuned to 974 nm (see section 4.2.1). The diode power was adjusted until the 995 nm fluorescence level matched the one obtained under 985 nm pumping conditions.

6. Stages 3 and 4 were repeated with the diode operating at 974 nm until the maximum 1973 nm power was reached.

7. The fluorescence intensity at the 551 nm, 657 nm, 800 nm, 995 nm and 1535 nm bands that were extracted in each scan were analysed and plotted by a Matlab® script.

5.4.3 Fluorescence dependency on pump power - results and analysis

Our measurements were conducted with increasing levels of incident 980 nm and 1973 nm pumps to observe the changes in fluorescence and hence population densities of the $^4I_{13/2}$ to $^4S_{3/2}/^2H_{11/2}$ levels. Examples of the change in 551 nm and 995 nm fluorescence when pumping with the 985 nm pump and increasing 1973 nm pump power are shown in Figures 5.13 and 5.14.

The curves in Figures 5.13 and 5.14 exhibit saturation behaviour with increasing 985 nm pump power. This saturation effect is the result of collecting the fluorescence above the pumped end of the fibre. This side is expected to experience strong reduction in absorption of both pumps because of significant ground state bleaching caused by the 980 nm pump and bleaching of the $^4F_{9/2} \rightarrow {}^4I_{9/2}$ transition, resulting in saturation of the absorption of the 1973 nm pump as well.

Beyond the value of obtaining the fluorescence data for estimating the ET constant, additional information can be obtained from the results regarding the spectroscopy of the Er^{3+}:ZBLAN system under DWP conditions. In the following pages, the reader is advised to refer to Figure 5.12 or to the fold-out at the end of this thesis for ease of reference. First, observing fluorescence behaviour under DWP at a steady state revealed another advantage of using a 985 nm pump over 974 nm for the first pump source.
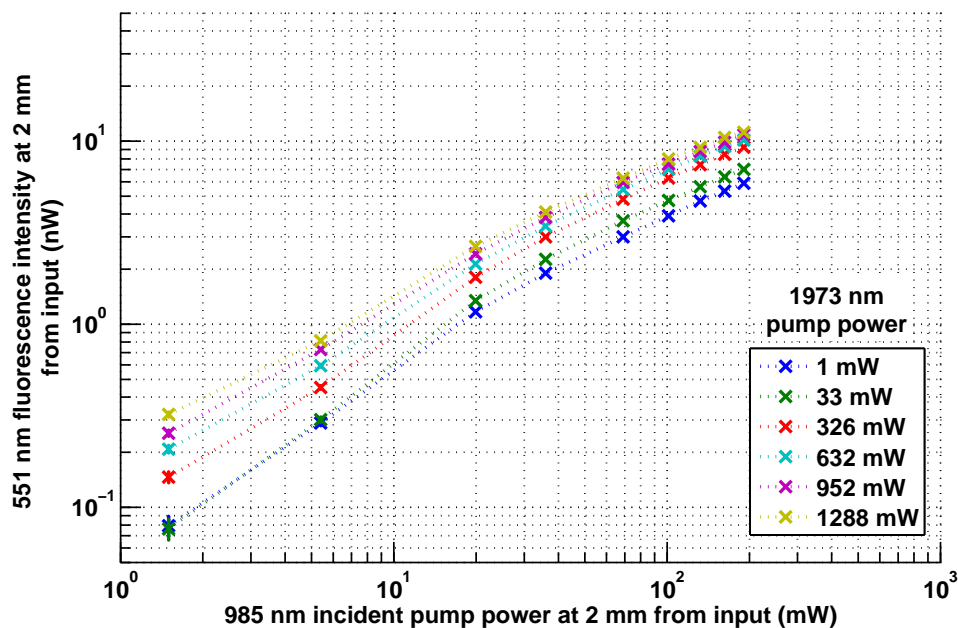
Figure 5.13: Example of change in the 551 *nm* fluorescence with increasing 1973 *nm* pump. The fibre used was 180 *mm* long IR-Photonics. Each coloured set of data represent a fixed 1973 *nm* pump power.
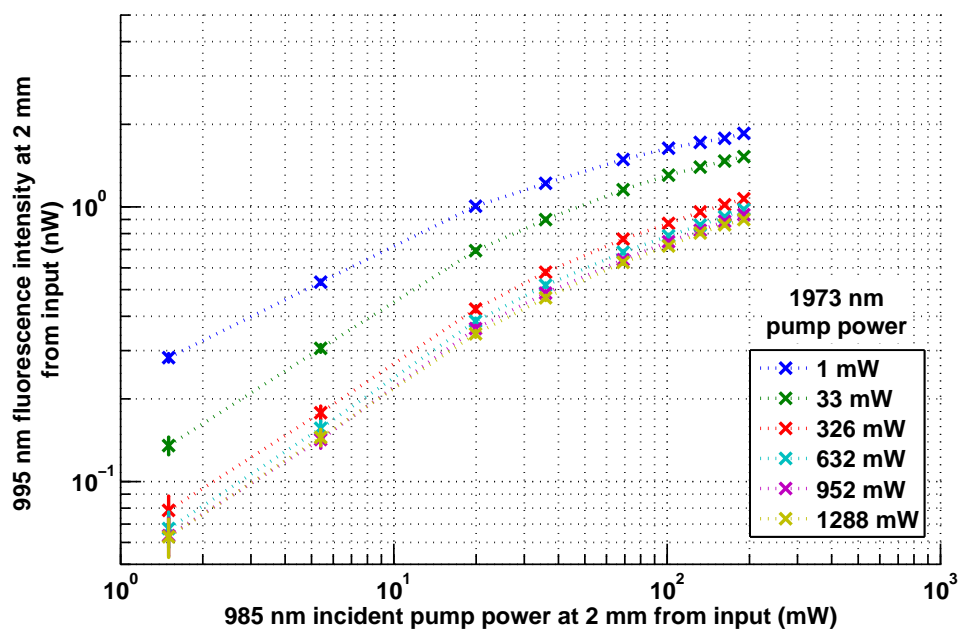
Figure 5.14: Example of change in the 995 *nm* fluorescence with increasing 1973 *nm* pump. The fibre used was 180 *mm* long IR-Photonics. Each coloured set of data represent a fixed 1973 *nm* pump power.
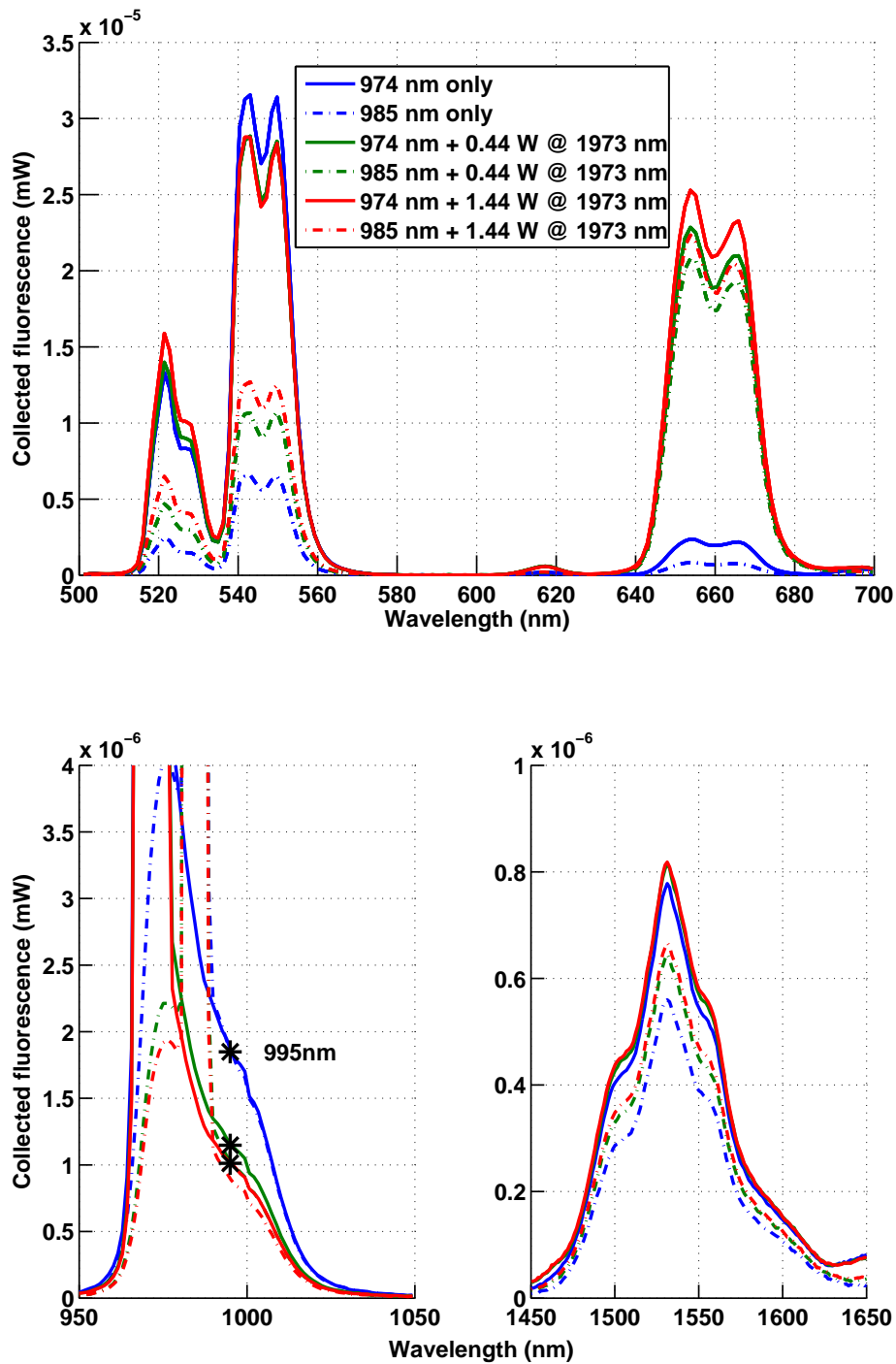
Figure 5.15: Wideband fluorescence comparison between 974 nm (full lines) and 985 nm (dashed lines) pumping when DWP using IR-Photonics fibre. Fluorescence at the 520-560 nm and 640-680 nm bands are from the $^4S_{3/2}/^2H_{11/2}$ and $^4F_{9/2}$ level, respectively. The fluorescence from the 960-1020 nm and 1470-1620 nm bands are from the $^4I_{11/2}$ and $^4I_{13/2}$ levels, respectively. The fibre used was 180 mm long with 1.7 $mol\%$ of erbium ions. In all cases, the 985 nm incident power was 191 mW, while 974 nm pump power was adjusted to achieve similar level of fluorescence at 995 nm (marked with a star). The curves of the 960-1020 nm band are truncated to only show the fluorescence part of the curve and not the scattered pump signal at 974 nm and 985 nm.

Figure 5.15 shows a fluorescence comparison between the two wavelengths in a CW measurement taken with the IR-Photonics fibre under 974 nm and 985 nm pumping with similar population levels at the $^4I_{11/2}$ state.

With the 1973 nm pump turned off (blue lines in Figure 5.15), the $^4I_{11/2}$ level had similar populations for both 974 nm and 985 nm pumps (marked with stars at 995 nm). The population of $^4F_{9/2}$ level (657 nm fluorescence) was smaller for 974 nm pumping compared with 985 nm. At the same time, significantly stronger fluorescence was observed from $^4S_{3/2}/^2H_{11/2}$ and $^4I_{13/2}$ levels (551 nm and 1550 nm fluorescence, respectively), when pumping with 974 nm compared with 985 nm.

Once the 1973 nm pump was turned on, we could observe a strong increase in the 657 nm fluorescence in both the 974 nm and 985 nm cases. This was expected because the DWP mechanism was populating the $^4F_{9/2}$ level at the 960-1020 nm band. In addition, a reduction in fluorescence from the $^4I_{11/2}$ level was observed. This reduction was expected as a result of depopulating of the level by the 1973 nm pump ESA.

Observing the $^4S_{3/2}/^2H_{11/2}$ fluorescence at the 520-560 nm band shows that pumping with 985 nm (dashed line) results with significantly reduces population compared to pumping at 974 nm. When the 1973 nm pump is off, there is effectively no ET contribution to the population of this level. Therefore, this level is populated by either ESA or the ETU from the $^4I_{11/2}$ level. This mean that pumping at 985 nm results in a lower number of ions excited to the $^4S_{3/2}/^2H_{11/2}$ levels. This is beneficial for a DWP system since it should increase the available population at the upper laser level $^4F_{9/2}$. Moreover, lower ESA reduces the heat-load in the fibre generated by cascades of multi-phonon decays from the $^4S_{3/2}/^2H_{11/2}$ levels back to the $^4I_{11/2}$ level (see Appendix E).

Figure 5.15 also shows the marks of the $^4F_{9/2} +^4 I_{11/2} \rightarrow ^4S_{3/2} +^4 I_{13/2}$ ET mechanism discussed previously. The increase in the population of the $^4S_{3/2}$ level with increased pumping was also accompanied by an increase of the 1535 nm fluorescence from $^4I_{13/2}$ when pumping with 985 nm. This change could not be explained by simple relaxation from the $^4I_{11/2}$ level since its population was decreasing with higher 1973 nm pump.

A complete analysis of the entire dataset relating the fluorescence at 995 nm to 1535 nm and 551 nm to 657 nm can be seen in Figures 5.16 and 5.17. Earlier we saw in Figures 5.11 and 5.15 that the $^4S_{3/2}/^2H_{11/2}$ level population increased under DWP conditions. Here we see that the $^4I_{13/2}$ population was increased as well. Each coloured curve represents operation with a different 985 nm pump power, while within each curve the 1973 nm power increased from right to the left. As the 1973 nm power increased, the 995 nm fluorescence, which was proportional to the $^4I_{11/2}$ population, decreased substantially
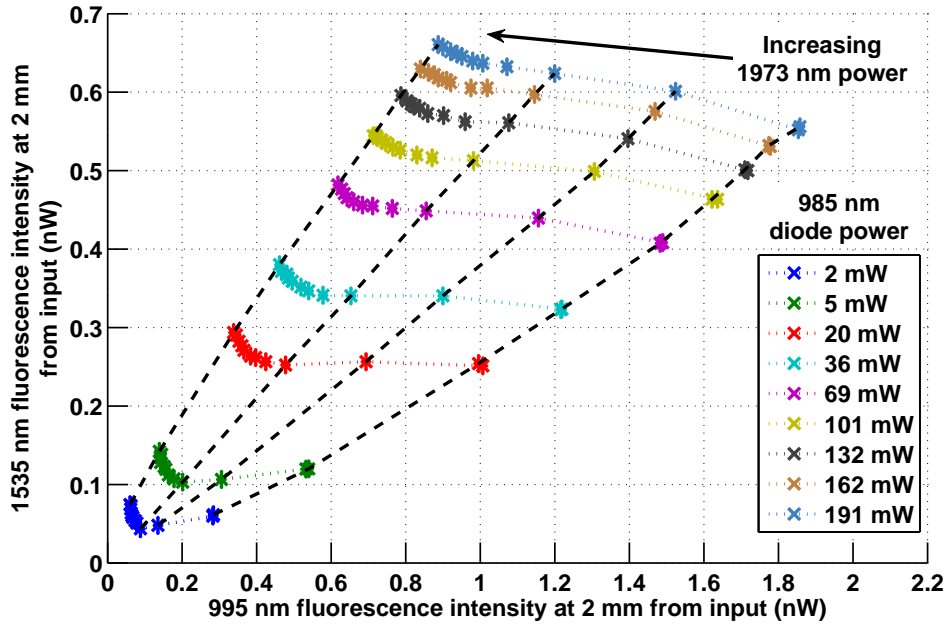
Figure 5.16: 1535 nm fluorescence as a function of 995 nm fluorescence in IR-Photonics fibre under DWP with 985 nm pumping. Fluorescence collected 2 mm from fibre tip with both pumps in CW. Note that 1973 nm power increases on each coloured set of data from right to left. The dashed lines are only added as a guide to the eye for data with similar 1973 nm pump power.

due to absorption of the 1973 nm pump exciting ions on the $^4I_{11/2} \rightarrow {}^4F_{9/2}$ transition. At the same time, the 1535 nm fluorescence, which was proportional to the $^4I_{13/2}$ level population increased. If we assumed that there were no ET, ETU and CR processes present, the population of the $^4I_{13/2}$ should be proportional to the population of the $^4I_{11/2}$ level. Their population ratio of 1:2 (see section 3.3.2.1) is determined according to the branching ratio of the decay $^4I_{11/2} \rightarrow {}^4I_{13/2}$ and the respective lifetimes. After its excitation with DWP, the $^4F_{9/2}$ level was expected to relax mostly via a cascade of multi-phonon decays $^4F_{9/2} \rightarrow {}^4I_{9/2} \rightarrow {}^4I_{11/2}$. Therefore, it could not have contributed to the increase in $^4I_{13/2}$ population under these assumptions.

A similar picture is portrayed with the data from Figure 5.17. At very low 1973 nm pump, there is a simple linear relation between the 551 nm fluorescence and 657 nm fluorescence. This relation is the result of the $^4F_{9/2}$ level population created exclusively by multi-phonon decay from the $^4S_{3/2}/^2H_{11/2}$ level. Once the 1973 nm pump is turned on, a large population is built at the $^4F_{9/2}$ level. The $^4S_{3/2}/^2H_{11/2}$ population is expected to shrink because its main population mechanism is by ESA from the $^4I_{11/2}$ level, which has its population reduced. The ETU and CR processes W_{11} and W_{50} previously documented in Er^{3+}:ZBLAN, (shown in Figure 1.17) cannot provide an explanation for this increase or to the increase in 1550 nm fluorescence as a function of increasing 995 nm fluorescence.
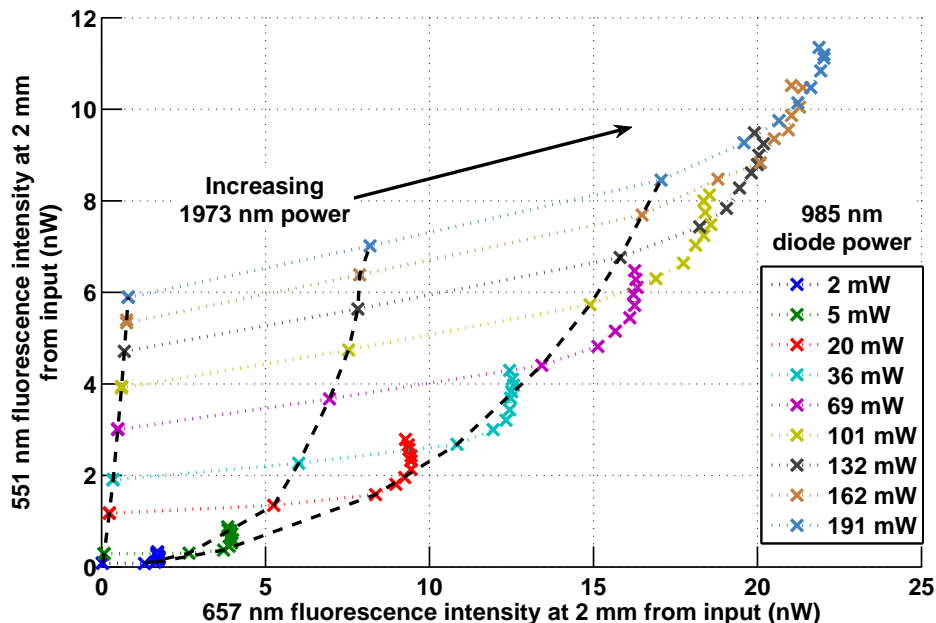
Figure 5.17: 551 nm fluorescence as a function of 657 nm fluorescence in IR-Photonics fibre under DWP with 985 nm pumping. Fluorescence collected 2 mm from fibre tip with both pumps in CW. The order of magnitude increase in the collected fluorescence compared with Figure 5.16 is the result of displaying fluorescence intensity at wavelengths close to the peak emission of these bands, unlike the case of the 995 nm. In addition, the fibre used had much higher attenuation, on the order of 1 dB/m at the 980 nm band and about 10 dB/m at the 1550 nm band, resulting in significantly less intensity reaching the OSA at these wavelengths. Note that 1973 nm power increases on each coloured set of data from left to right. The dashed lines are only added as a guide to the eye for data with similar 1973 nm pump power.

The W_{22} ETU process is also unlikely to explain this behaviour because it cannot explain the increase in 1550 nm fluorescence and is considered to have a low rate at lower doping concentrations, as in our case. We thus reach the conclusion that only our suggested ET mechanism can explain the combination of fluorescence changes.

To this point we have seen multiple evidence for the existence of the ET process $^4F_{9/2} + ^4 I_{11/2} \rightarrow {}^4S_{3/2} + ^4 I_{13/2}$. In the next section, we describe how we determined its magnitude based on the available data from our collected data so far.

5.4.4   Calculating the cross-relaxation constant - results and analysis

To quantify the ET parameter W_{42} using Equation 5.2, it was first necessary to find the absolute population densities in the fibre under DWP conditions. This was achieved by following a procedure that established a normalisation factor for each energy level based on the relative fluorescence readings and a numerical simulation. The relationship

between the observed fluorescence and ion population densities was found using the following method:

1. Fluorescence was collected in CW from the side of both the FiberLabs and IR Photonics fibres with 974 nm and 985 nm pumping and at different 1973 nm pump levels.

2. From the wideband fluorescence curves collected by the OSA, the area under the fluorescence curves was calculated at each of the following bands: 551 nm, 657 nm, 800 nm, 995 nm and 1535 nm. Since the OSA measures power and we were interested in the relative population of the levels, the results were normalised according to the different energies of photons at varying wavelength bands and thus accounted for actual excited ions population.

3. The observed results without the 1973 nm pump of each wavelength band were normalised to the population densities predicted by a simple rate-equation simulation. This simulation was based on the rate equation from section 1.5.4, which provided population densities of the appropriate energy levels, while assuming no additional CR and ETU effects beyond those currently found in the literature (see Table 2.6). The normalisation factor was determined based on the fluorescence obtained with the second lowest 980 nm pump power measured. This power level was advantageous because it exhibited low uncertainty and was not affected by CR and ETU processes because of the relatively low population densities created at this power level.

The normalisation created a one-to-one relation between observed fluorescence and ion population density at a certain energy level. An example of the agreement between the observed fluorescence and the shape of the curves can be seen in Figure 5.18. Significantly better agreement was achieved for the population of the $^4F_{9/2}$ level once the appropriate ET factor (found later in this section) was included in the simulation (see dashed lines in Figure 5.18).

We chose to use this population normalisation method for multiple reasons. First, a numerical analysis can predict the variations along the fibre, while simple calculations which assume average values cannot account for them. Secondly, directly fitting a power level measured with the OSA to a known population overcomes the compound effects of the detector response, fibre attenuation and OSA grating and detector calibration (assuming their linearity, which was verified) all with their respective (and sometimes unknown and difficult to measure) wavelength dependencies. In addition, operating in
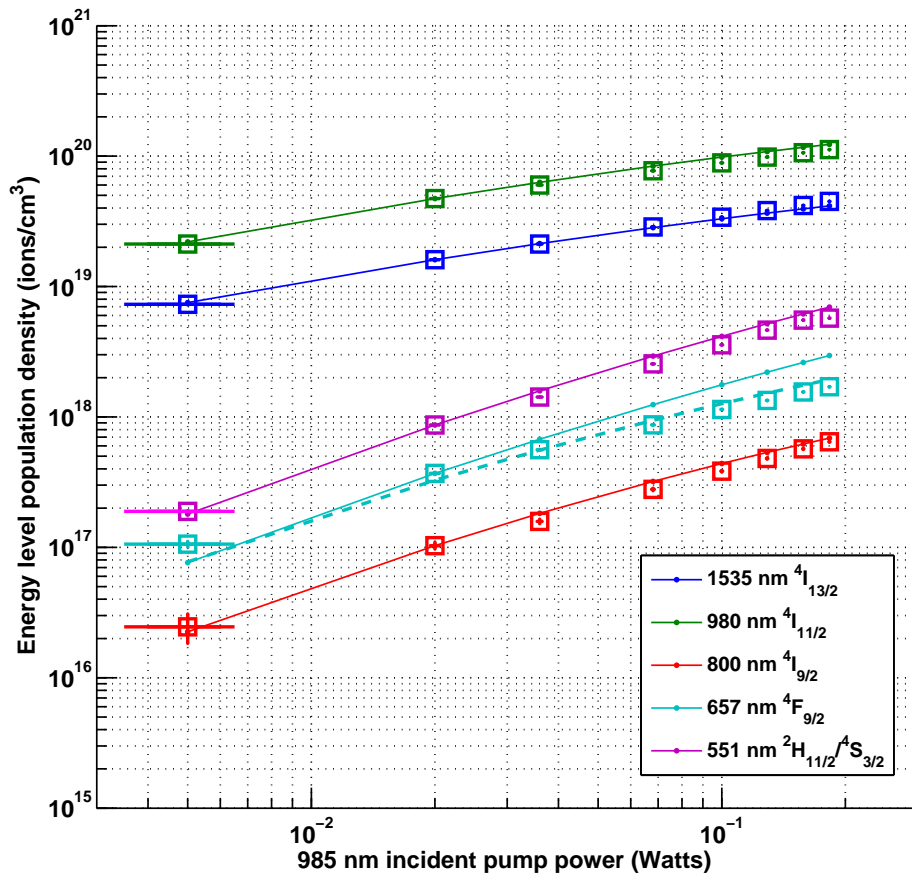
Figure 5.18: Normalisation of simulated results (lines) to observed fluorescence (boxes) trend is shown for the case of pumping a ZDF fibre with 985 nm. The fibre was 63 mm long and fluorescence was collected and simulated at 2 mm from the input side. The continuous curves represent the simulated results assuming no ET. The dashed line for the $^4F_{9/2}$ level represents the simulated values assuming ET as calculated later in this section, while the squares represent the observed fluorescence intensity normalised to the second data point of population density calculated for each wavelength. This point was selected because the behaviour at this power level was still close to linear while pump power uncertainties were low.

CW and normalising to a known population took into account the effect of the intrinsic fluorescence lifetimes differences between the energy levels.

Figure 5.18 is an example for calibration curves as explained above. The calibration used both simulated and measured results using the first pump only (to account for different first pump wavelength used, calibration curves for both 974 nm and 985 nm were produced). The measured intensities (squares in Figure 5.18) at the various energy levels were superimposed on the simulated values (curves) and a calibration factor between the two was established. The appropriate factors were maintained for each level under the same measured and simulated conditions.

To obtain the ET factor, the following procedure was followed:

1. We gathered the fluorescence data from all CW measurement and assigned population densities to each level according to the normalisation values found numerically. A separate set of calibration values was calculated for each possible combination of conditions (974 nm or 985 nm, ZDF/IR-Photonics fibres and "strong" or "weakly interacting" approach, explained below).

2. We could now substitute the population densities from all the experiments into Equation 5.2 for each of the combinations of 974 nm or 985 nm and 1973 nm pump powers. It is not possible to rearrange Equation 5.2 to present the ET factor W_{42} in an explicit form as a function of the population densities and the decay waveform. Thus, a certain value was assumed for W_{42}, which together with the population densities was substituted into Equation 5.2, resulting in a calculated $N_4(t)$ decay waveform for each combination of pump conditions in all fibres tested.

3. A decay lifetime was fitted to each simulated $N_4(t)$ based on an exponential decay model.

4. The calculated decay lifetimes for each of the measurement conditions were compared to the actual measured values from section 5.3.4.

5. The W_{42} constant was changed and stages 1-4 were repeated until the sum of least squares between the calculated and measured results was minimised and this W_{42} value was assumed to be the ET constant.

6. The uncertainty in the ET parameter was estimated by varying the assumed W_{42} value until it resulted in a lifetime changes of $\pm 10\%$ compared with the best fit to the measured lifetime data at the maximum pump power.

We should note that equation 5.2 described a decay behaviour which was dominated by the τ_4 time constant at the beginning of the decay and changed to be dominated by τ_5 at the later stage of the decay. In the lifetime measurements of section 5.3.4, the smaller population of $^4S_{3/2}/^2H_{11/2}$ compared with $^4F_{9/2}$ made the second term contribution to the decay fairly small in many instances. Even in cases where the second term could not be ignored, the later decay behaviour was mostly obscured in the oscilloscope noise floor due to the low dynamic range of the experimental setup. The decay lifetimes were hence determined by fitting the obtained decay waveforms to a single exponential term (see example in figure 5.3) that achieved good match to the decay waveforms.

Figure 5.19 shows an example of a comparison of the results obtained with the analysis based on Equation 5.2 to the measured lifetime results of the ZDF fibre. We obtained good
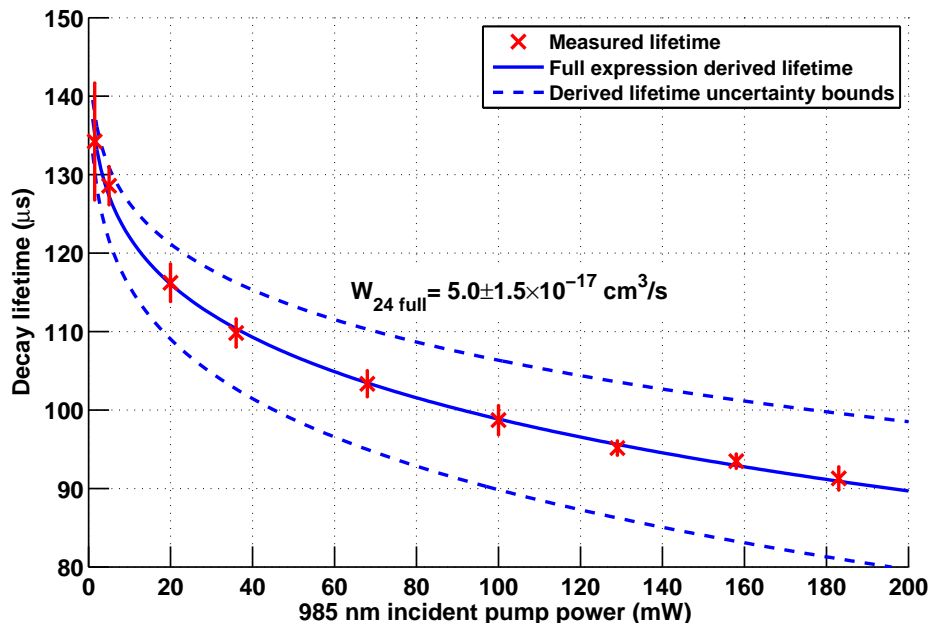
Figure 5.19: Fitting lifetime example for obtaining energy-transfer constant. Best fit of W_{42} values are compared to measured lifetime results in FiberLabs ZDF fibre using 985 nm pumping. This fit does take into account the change in $^4I_{11/2}$ during 1973 nm pumping. The uncertainty is estimated on variations of the calculated W_{42} ET value resulting in lifetime changes of $\pm 10\%$ compared with the measured lifetime at the maximum pump power. Both curves of best fit and uncertainties were interpolated from the simulated data calculated at the same power levels as the measured data.

agreement between the model and the measured lifetime results. This good agreement was the norm for almost all combinations of experimental and measured data analysed. The only free parameters in our fit were the ET constant W_{42} and the intrinsic lifetime of the $^4F_{9/2}$ level. Since the intrinsic lifetime was measured directly for low excitation of $^4F_{9/2}$ (and thus negligible effect of the ET process), we only needed to vary the ET constant in the calculated fit until good agreement with experimental data was reached.

We used in our rate equation simulations both the commonly used "strong interaction" parameters (SI) and the "weakly interacting" (WI) values, both described in detail in section 2.4.3. The SI approach uses relatively high CR and ETU rate parameters on the order of 10^{-17} cm^3/s, which were measured in bulk ZBLAN glass by Golding et al. [77]. The WI approach asserts that CR and ETU processes are considerably weaker in ZBLAN fibres than in bulk glass, with values on the order of 5×10^{-19} cm^3/s. The WI-based CR and ETU parameter values were found numerically by Gorjan et al. when fitting experimental data to a set of rate-equations. Because both SI and WI approaches are still in use, we obtained different fitted ET values based on population density normalisation using both approaches. The values of the literature CR and ETU parameters used in our normalisations can be found in Table 2.6 in section 2.4.3.
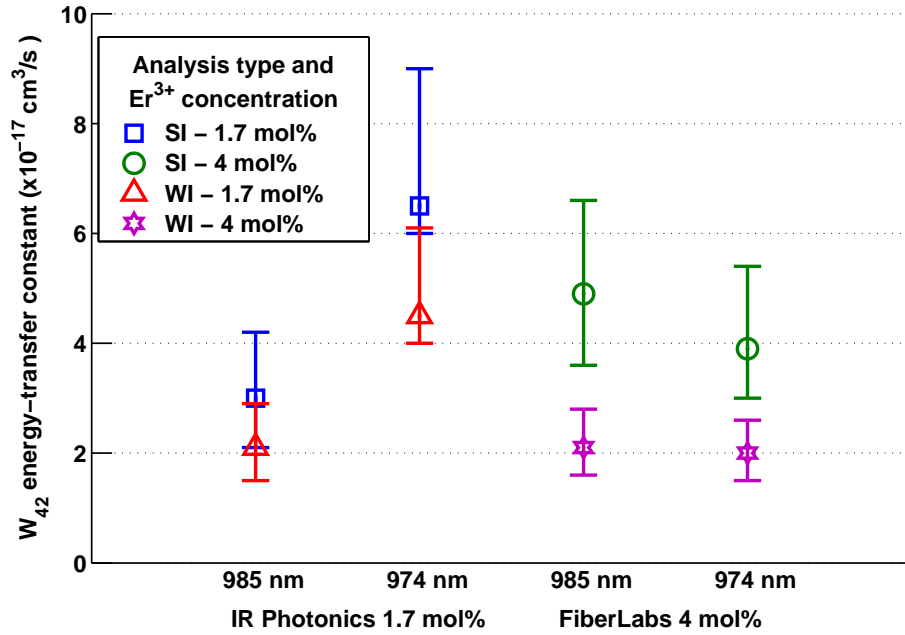
Figure 5.20: Energy-transfer coefficient $^4F_{9/2} +^4 I_{11/2} \rightarrow {}^4S_{3/2} +^4 I_{13/2}$. Comparison of all values obtained using IR-Photonics fibre containing 1.7 $mol\%$ of Er^{3+} ions and FiberLabs ZDF fibre containing 4 $mol\%$ of Er^{3+} ions. Results for both the SI and WI approaches are shown. The uncertainty of each value is estimated based on variations of the calculated W_{42} ET value resulting in lifetime changes of $\pm 10\%$ compared with the measured lifetime at the maximum pump power.

Figure 5.20 displays the ET constant results obtained with both IR-Photonics and FiberLabs fibres under 974 nm and 985 nm pumping conditions. Although other CR and ETU parameters are considerably different between the SI and WI regimes, both approaches provided our newly reported ET process constants with the same order of magnitude: $4.5 \pm 1.5 \times 10^{-17}$ cm^3/s for SI and $2.7 \pm 1.2 \times 10^{-17}$ cm^3/s for WI. The relatively large ET factor of the $^4F_{9/2} +^4 I_{11/2} \rightarrow {}^4S_{3/2} +^4 I_{13/2}$ process is not surprising because of the high absorption and emission cross-sections of both levels involved. With the current results, it did not seem that there was a clear dependency on the Er^{3+} concentration, although this could not be ruled out due to the uncertainties in the calculated values. The strength of this ET process was expected to cause significant changes in the laser dynamics, which will be investigated numerically in future work.

Using the values of ET and typical population densities found in this chapter we can revisit Equation 5.1 and evaluate the effect of different scenarios on the decay rate from the $^4F_{9/2}$ level of the ZDF fibre used as an example.

$$dN_4(z)/dt = -N_4(z)\{\tau_4^{-1} + W_{42}N_2(z)\} + \beta_{54}\tau_5^{-1}N_5(z) \qquad (5.1 \text{ revisited.})$$

When only the 985 nm pump is used, Figure 5.18 shows absolute population densities at the pumped tip of the fibre as a function of pump power varying between 5 mW and 184 mW. The $^4I_{11/2}$ population density would vary in the ZDF fibre between 10×10^{19} and 10×10^{20} $ions/cm^3$, the $^4S_{3/2}/^2H_{11/2}$ levels population changes between 2×10^{17} and 5×10^{18} $ions/cm^3$ and the $^4F_{9/2}$ population would be one half of the population of the $^4S_{3/2}/^2H_{11/2}$ at low power level, since it is populated by multi-phonon decay from these levels. We substitute into Equation 5.1 the ET value found for the WI case, $W_{42} = 2.7 \times 10^{-17}$ together with $\beta_{54} = 0.25$, the branching ratio from the $^4S_{3/2}/^2H_{11/2}$ level to the $^4F_{9/2}$ level. The lifetimes of the $^4F_{9/2}$ and $^4S_{3/2}/^2H_{11/2}$ levels required are $\tau_4 = 148$ μs and $\tau_5 = 100$ μs, respectively. The calculated values for the terms in Equation 5.1 under low and high, 985 nm pumping conditions are $W_{42}N_2 = 270 \rightarrow 2700$ s^{-1} with $N_4\{\tau_4^{-1} + W_{42}N_2\} = 7 \times 10^{20} \rightarrow 2.4 \times 10^{22}$ $ions/s$ and $\beta_{54}\tau_5^{-1}N_5 = 5 \times 10^{20} \rightarrow 1.3 \times 10^{22}$ $ions/s$.

This results in the the first right-hand side term of Equation 5.1 ($N_4\{\tau_4^{-1} + W_{42}N_2\}$, denoted as the first term) to be dominated by the intrinsic rate $\tau_4^{-1} = 6757$ s^{-1}, with the ET factor having only a minor effect on this term at low pump power. The second term ($\beta_{54}\tau_5^{-1}N_5$) has a similar magnitude to the first one, therefore both terms affect the decay from the $^4F_{9/2}$ level at low pump power. At higher pump powers, the $^4I_{11/2}$ level population density becomes significant. Therefore, the $W_{42}N_2$ term is more prominent, resulting in a noticeable reduction in lifetime that is followed by a reduction in the CW population of the $^4F_{9/2}$ level at high power, as seen in Figure 5.18.

Under DWP condition with the 985 nm pump at its maximum power, the $^4F_{9/2}$ population density is expected to follow the population density of the $^4I_{11/2}$ level and have a lower, but similar magnitude population density. $^4S_{3/2}/^2H_{11/2}$ population density is expected to be lower than the $^4F_{9/2}$ one (unless 974 nm pumping is used, which results in strong ESA to the $^4S_{3/2}/^2H_{11/2}$ levels). The first term of Equation 5.1 would become dominant over the second term, resulting in an exponential decay, with the new decay constant of $\tau_4^{-1} + W_{42}N_2(z)$. This decay constant is only dependant on the population of the $^4I_{11/2}$ level, which is populated by the 985 nm pump. Some reduction in the $^4I_{11/2}$ population is caused by the 1973 nm pumping. However, this observed 30% reduction in fluorescence when DWP in CW operation does not vary significantly for all power levels of 1973 nm. Its effect is therefore consistent, resulting with lifetime changes only as a function of the 985 nm pump power as shown in Figure 5.7.

5.5   Summary

In this chapter we investigated the reasons that prevented our Er^{3+}:ZBLAN fibre from achieving lasing during initial investigations.

We examined the reduction in the lifetime of the upper laser level $^4F_{9/2}$ as a function of both pump intensities. The lifetime was observed to reduce significantly from an initial value of 148 ± 10 μs to between 80 μs and 110 μs depending on the fibre used and the pumping conditions.

We derived the population densities of the energy levels during our lifetime measurements using a fit of the magnitude of observed fluorescence to a numerical model. This allowed us to estimate the magnitude of a previously undocumented ET mechanism $^4F_{9/2} + ^4I_{11/2} \rightarrow ^4S_{3/2} + ^4I_{13/2}$ with its value determined to be $4.5 \pm 1.5 \times 10^{-17}$ cm^3/s and $2.7 \pm 1.2 \times 10^{-17}$ cm^3/s under the assumptions of the SI and WI approaches, respectively.

This ET process can strongly affect Er^{3+}:ZBLAN fibres when using DWP by ejecting ions from both highest populated levels in the lasing cycle. The ET process was also likely to have contributed to the poor efficiency in the case of the 3.5 μm laser results presented by Többen [117] when pumping directly to the upper laser level, $^4F_{9/2}$. The reason is that without the cycling mechanism created under DWP, ions which were excited to the $^4F_{9/2}$ level eventually ended in the $^4I_{11/2}$ and $^4I_{13/2}$ levels because of the multi-phonon cascades from the $^4F_{9/2}$ level and the $^4I_{11/2} \rightarrow ^4I_{13/2}$ fluorescence. The ET process would have removed additional ions from the $^4F_{9/2}$ and $^4I_{11/2}$ levels into the $^4S_{3/2}/^2H_{11/2}$ and $^4I_{13/2}$ levels. 70% of the ions at the $^4S_{3/2}/^2H_{11/2}$ levels would eventually fluoresce directly to the ground and the $^4I_{13/2}$ level, intensifying the bottlenecking problem present. The long lifetime of both $^4I_{11/2}$ and $^4I_{13/2}$ levels would have resulted in a significant proportion of the ion population accumulating in these levels at the expense of the ground state, resulting in ground-state bleaching and low laser efficiency.

The findings described in this chapter were important to our investigations for two reasons: First, the previously unrecognised ET effect was proven to be detrimental to our laser experiments. We had believed that high doping concentration of Er^{3+} ions was necessary to obtain lasing; the results of this chapter proved that the opposite was correct. A low concentration of Er^{3+} ions was necessary to prevent this concentration quenching effect. This effect was created by the depopulation of the virtual ground state and lifetime quenching of the upper lasing level due to the ET process. Following these lines, as described in Chapter 6, we used a lower concentration fibre leading to our first successful demonstration of a 3.5 μm laser. Second, the new spectroscopic data found will be essential for the optimisation of the 3.5 μm laser behaviour based on our future planned numerical model.

The results presented in this chapter helped us gain a better understanding of the issues that prevented our system from achieving lasing on the $^4F_{9/2} \rightarrow ^4I_{9/2}$ transition. Our new laser system design used a lower doped fibre. Chapter 6 presents the improved system and the performance of the DWP 3.5 μm laser demonstrated for the first time.

Chapter 6

Dual-wavelength pumped laser

6.1 Overview

$\mathbf{I}$N this chapter, we present our results for an erbium doped ZBLAN glass fibre laser operating at 3.5 μm with an average output power of over 250 mW. This power level is more than 30 times higher than previously reported for this transition while obtaining an order of magnitude improvement in efficiency. This laser is the first rare earth doped fibre laser that produces power approaching half a watt at a wavelength significantly longer than 3 μm. Our laser also produces the longest wavelength emission from a rare-earth doped fibre laser operating at room-temperature.

We describe the layout of the laser and detailed measurements of the 3.5 μm laser behaviour. Section 6.2 details the laser setup and the diagnostic tools used to analyse its behaviour. The laser characterisation is discussed in sections 6.3-6.4, including output power and efficiency results for CW and long pulse operation. These results were taken with output couplers with reflectivities ranging from 80% to 99.3%. Internal loss, gain, emission cross-section and inversion parameters are obtained from the analysis of these results. In section 6.5 we examine additional laser characteristics, including output power stability, beam quality and spectral content. The later also includes an examination of spectral variations that result from using different output couplers. The results of the laser measurements are concluded in section 6.6.

6.2 Structure of the laser system

The laser setup used is similar to that of the energy level lifetime measurement described in section 5.3 and in Figure 5.1, but with a few variations. Additional analysis and diagnostic tools are incorporated into the setup as discussed in the following sections. We start by describing the fibre used as a gain medium, then describe the basic design of the laser system experimental setup. Variations on this basic design will be explained as needed for each section.
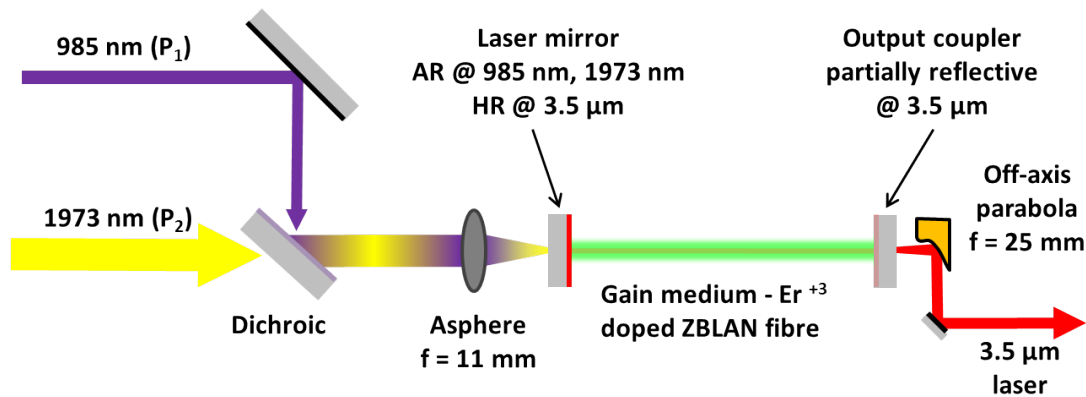
Figure 6.1: Schematic of DWP laser. The gain medium used is an 18 *cm* long ZBLAN fibre, doped with 1.7 *mol%* of Er^{3+} ions. Various output-couplers were used with reflectivities ranging from 80% to 99.3%.

6.2.1   IR-Photonics Er^{3+}:ZBLAN fibre

Our laser experiments used a custom made Er^{3+}:ZBLAN fibre from IR-Photonics. The following attributes were required of the custom fibre:

1. Single clad construction to simplify manufacturing and reduce costs.

2. A numerical aperture and core size that support single transverse mode operation at 3.5 *μm* for good beam quality. It was requested that the fibre support multiple transverse modes at both pump wavelengths to enable good pump absorption. These were the requirements because the combination of a single mode operation at the laser wavelength while preserving multi-mode behaviour at the pump wavelengths allows for a good overlap between the laser and pump modes, resulting in higher gain [195].

3. Light doping of erbium ions to minimise energy transfer and prevent or significantly reduce lasing of the 2.75 *μm* transition ($^4I_{11/2} \rightarrow {}^4I_{13/2}$).

The fibre that was delivered was doped with 1.7 *mol%* of erbium ions. Although higher than the 1 mol% originally requested, this relatively low concentration reduces the heat load per unit length due to the absorption of pump light and reduces the risk of thermal damage and misalignment of the fibre tip where the absorbed power is highest.

The fibre design specifications were a core diameter of 10 *μm* and a numerical aperture of 0.27. These parameters mean that the fibre was designed to exhibit single mode operation at 3.5 *μm*, as well as allow easy launching conditions for both pumps, an issue identified with previous fibres tested. The numerical aperture of the fibre supplied was measured

to be between 0.13 and 0.15, which was significantly lower than the requirement. This reduction in numerical aperture caused the fibre to be on the cusp of only supporting a single transverse mode of the 1973 nm pump. This imposed a much more stringent restriction on the pump light launching conditions and reduced the overlap between the fibre core and the pump mode. The lower numerical aperture also reduced the overlap between the expected laser mode at 3.5 μm and the fibre core, consequently reducing gain. In addition, the reduction in absorbed 1973 nm pump power increased the lasing threshold power and reduced slope efficiency.

6.2.2 Pump sources

Figure 6.1 shows an overview schematic of our 3.5 μm fibre laser, which consists of two separate pump sources. Detailed block-diagram schematics including all electronic, mechanical and optical components of the laser are displayed in Appendix D. The first pump is a commercially available, 330 mW fibre-coupled laser diode that we modified to operate at 985 nm. The second pump laser is an in-house built 1973 nm Tm^{3+}:silica fibre laser (TFL). Both pump sources are described in detail in Chapter 4.

The output beams from both the 985 nm and 1973 nm pump sources are collimated and mode matched to the core of the ZBLAN fibre. Details of the mode-matching optimisation and alignment procedure are given in Appendix G. The beams are combined and launched into the core of the ZBLAN fibre using an aspheric lens. The 3.5 μm laser can operate in CW or quasi-CW. When operated in quasi-CW, i.e. long pulse mode, the 1973 nm beam is chopped using a mechanical chopper (Thorlabs MC1000A) at a duty-cycle of 30%, resulting in the beam transmitted through the chopper for 300 μs. This time is equivalent to two to three fluorescence lifetimes of the upper lasing level $^4F_{9/2}$ (see section 5.3).

6.2.3 The laser resonator

The pump beams are launched through a dichroic mirror that is highly reflective (HR) at 3.5 μm and is transmissive at both 985 nm and 1973 nm. The ZBLAN fibre is butted against the HR surface of the dichroic mirror. An 18 cm long Er^{3+}:ZBLAN fibre made by IR-Photonics is used as the laser gain medium. With a core diameter of 10 μm and a numerical aperture of less than 0.15, the fibre supports a single transverse mode at 3.5 μm because the fibre's V-number is 1.36, resulting in a mode-field diameter of 21 μm. The fibre is also on the cusp of single mode operation for the 1973 nm pump with a V-number of 2.39, therefore slight variations in diameter and numerical aperture can

alter the mode behaviour between single and multi-mode operation. The behaviour at 985 nm pump is multi-mode with a V-number of 4.78. Despite having a significantly lower numerical aperture than specified, the fibre is still capable of lasing at 3.5 μm and provides a single transverse mode profile at the laser wavelength with good beam quality.
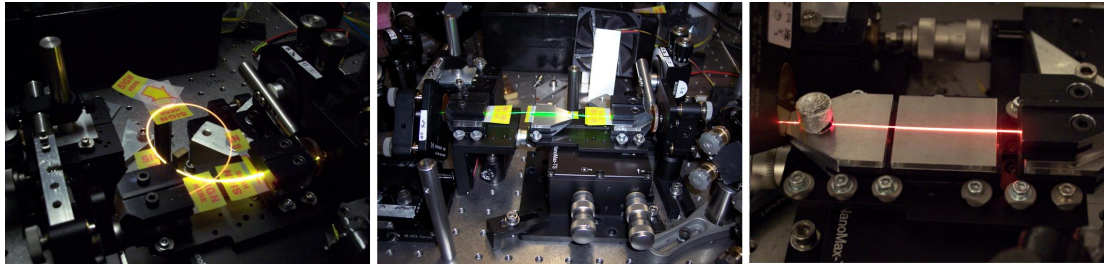
Figure 6.2: V-groove holders for different lengths of fibre tested

Different lengths of fibre, shown in Figure 6.2, are mounted in a straight line v-groove on a translation stage. The output couplers are partially reflective dichroic mirrors ranging in reflectivity from 80% to 99.3% (the same as the HR mirror) at 3.5 μm. These are butt-coupled to the output side of the fibre.

The beam emerging from the ZBLAN fibre is collimated with a gold-coated 25 mm focal length off-axis parabolic mirror (Thorlabs MPD127127-90-P01). The collimated beam is then separated into its constituents using a wavelength separation setup.

6.2.4   Wavelength separation system

Not all of the pump power is absorbed in the ZBLAN fibre. Therefore, the beam emerging from the laser resonator contains residual 985 nm and 1973 nm pumps of tens of mW and many hundreds of mW, respectively. In addition to the 3.5 μm laser present above its threshold, the resonator has sufficient round-trip gain to lase at 2.75 μm when the 3.5 μm is below threshold or when the 1973 nm pump beam is blocked. In order to measure power at each of these wavelengths at the same time, we constructed a wavelength separation system, which we denote the "wavelength separator" (shown in Figure 6.3). The wavelength separator also includes a branch where the beam is imaged onto a thermal camera (Ophir Pyrocam MKIII) or a 0.5 m grating spectrometer (Princeton Instruments, Acton SP2500i) depending on the measurement.

The wavelength separator consists of a 2500 nm longpass filter (Spectrogon LP-2500) which transmits wavelengths in excess of 2450 nm. The shorter wavelengths are reflected and separated by a dichroic mirror (Thorlabs DMSP1500). The dichroic mirror reflects the 1973 nm residual pump into a 50 W-thermal power meter head (Ophir L50A-SH)
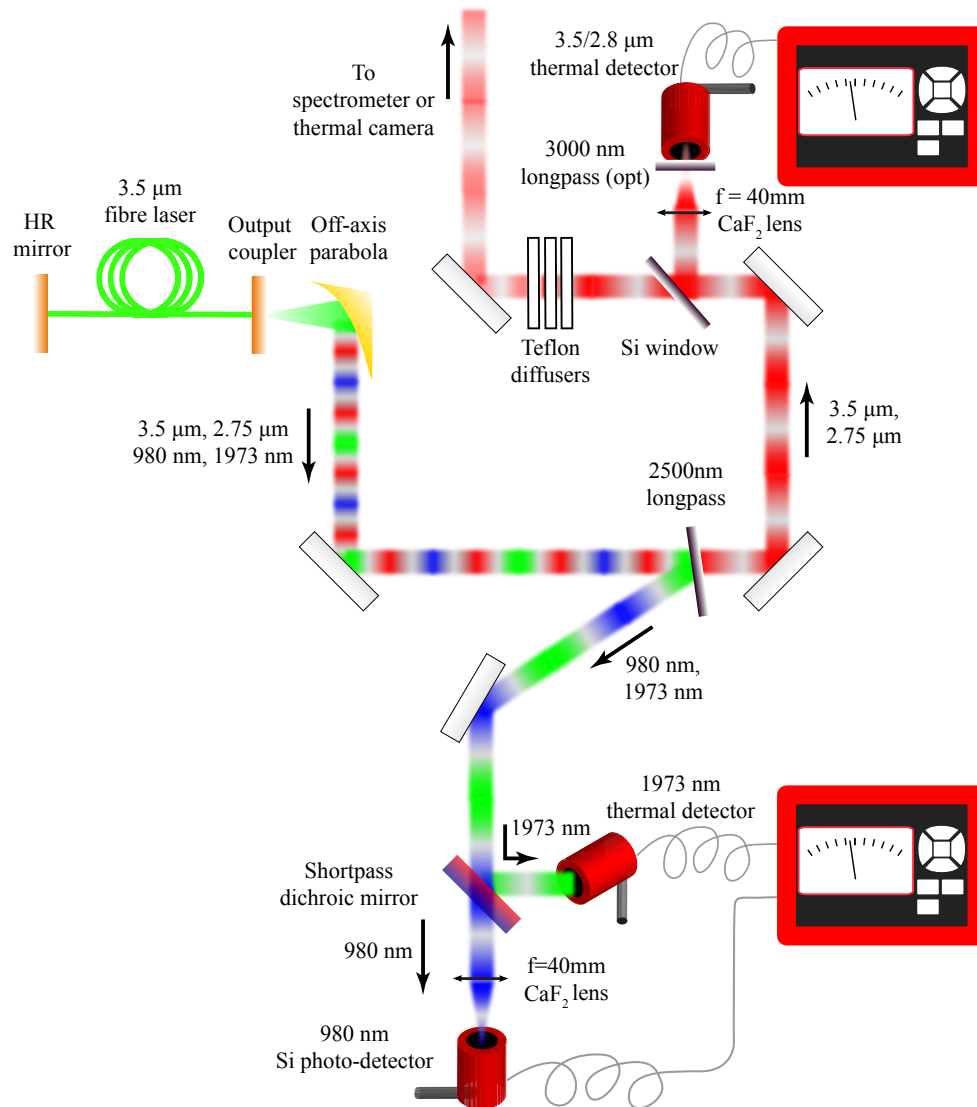
Figure 6.3: Wavelength separation system at the output of the 3.5 μm laser. The 3.5 μm laser and the 2.75 μm parasitic lasing are separated from the residual 985 nm and 1973 nm pumps transmitted through the fibre using a 2500 nm longpass filter. The pumps are separated further using a shortpass dichroic mirror. The power of the 3.5 μm or 2.75 μm lasers is measured with a thermopile detector which samples 40% of the laser beam power reflected by a Si filter. The remaining beam continues to a spectrometer (often attenuated by Teflon sheets) or a thermal camera.

and transmits the remaining 985 nm pump. The 985 nm beam is then focused onto a silicon photo-detector (Thorlabs S144C) using a 40 mm focal length lens. The long wavelengths passing through the LP-2500 filter are split using an uncoated Si window (Edmund Optics #68-523). Approximately half of the power is reflected through a 40 mm focal length CaF_2 lens onto a thermal power meter (Thorlabs S302C) and the rest is transmitted towards the spectrometer or the thermal camera.

The high gain of the $^4I_{11/2} \rightarrow^4 I_{13/2}$ transition sometimes overcomes the relatively low reflectivity of the resonator mirrors at 2.75 μm (about 40%) resulting in lasing at 2.75 μm.

This occurs when the 985 nm pump diode is operating at close to maximum power and the 1973 nm pump beam is blocked or operating at low power on the order of 25 mW or less, which is below the threshold power of the 3.5 μm wavelength. Increasing the 1973 nm pump power incident on the fibre extinguishes this unwanted 2.75 μm lasing in all cases.

Two approaches are taken to distinguish the 2.75 μm and 3.5 μm power detected by the thermal power meter: subtracting the 2.75 μm power from the reading or blocking the 2.75 μm beam using a 3000 nm longpass filter. Both are only used in quasi-CW, since the 2.8 μm wavelength is always off under DWP when the 3.5 μm wavelength is lasing in CW. The first approach is when the 2.8 μm power is of interest. In this method, the 2.75 μm power reading is taken when the 985 nm pump is continuously incident on the fibre while the 1973 nm pump is blocked (therefore the 3.5 μm is not lasing, but 2.75 μm is). Taking the complement of the quasi-CW duty-cycle into account, the reading is then subtracted from the total power observed when both pumps are incident on the fibre, which includes both the 3.5 μm and 2.75 μm lasers. This approach allows more power to reach the detector, therefore improving the low signal-to-noise, which is the result of the the low average power in quasi-CW. In addition, it permits monitoring the 2.75 μm lasing power.

The later approach is used when the wavelength of interest is only 3.5 μm. In this case, we verify first that 2.75 μm and 3.5 μm pulses do not coincide temporally. Then, instead of subtracting the 2.75 μm beam, an additional longpass filter which rejects wavelengths shorter than 2950 nm (Spectrogon LP-3000) is added. The simplified wavelength discrimination achieved with the 3000 nm longpass comes at the expense of reducing the power reaching the detector at 3.5 μm by 20%.

6.2.5   Laser analysis segment

6.2.5.1   Spectral analysis

The laser beam is focused into a 0.5 m triple-grating spectrometer (Princeton Instruments Acton SP-2500) using a 50.8 mm focal length off-axis parabolic mirror (Thorlabs MPD127254-90-M01). This focal length was used to best match the numerical aperture of the spectrometer and fill its diffraction grating. The beam is chopped using a mechanical chopper (Thorlabs MC1000A) before entering the spectrometer entrance slit for easier detection of low signal using a lock-in amplifier.

Mid-IR detection is achieved using a liquid nitrogen cooled InSb photo-detector (Teledyne-Judson J10D-M204-R01M-60) or a thermo-electrically cooled PbSe photo-diode (Horiba

DSS PbSe). The InSb detector is used exclusively when observing the weak fluorescence at 3.5 μm when the laser is below threshold. Above threshold, both detectors can be used. Using the 4 μm blazed, 150 grooves/mm grating enables measuring spectra with a resolution of 0.1 nm. However, most measurements are conducted with a resolution of 1 nm, unless otherwise specified. Sub-lasing operation scanning with the spectrometer is conducted with the spectrometer slits wide open (1 mm) to increase the signal to noise ratio. This introduces a problem when approaching threshold, where the laser power could damage to the sensitive InSb and PbSe detectors when lasing beyond a few mW. In addition, it is common to reach saturation of the detectors when observing the strong 2.75 μm fluorescence when operating below the 3.5 μm laser threshold. To resolve this issue, we use Teflon sheets to scatter the beam. The laser beam is effectively attenuated in a wavelength insensitive fashion by passing through multiple Teflon® sheets with 2-3 mm thickness. Sheets are added or removed to achieve the desired detector signal level. Teflon® sheets are used when low spectral resolution can be tolerated (for example when aligning the laser resonator). They are removed for measurements which require accurate bandwidth and wavelength determination using very narrow slit sizes of 10-20 μm.

6.2.5.2   Beam profiling

For beam quality measurements, a wedge is added to split off a sample of the beam and direct it towards a thermal camera (Ophir Pyrocam). Beam quality measurements are conducted by first reducing the beam size 2.5x times with a beam reducer constructed from two CaF_2 lenses. Further beam focusing is done with a 250 mm focal length CaF_2 lens. The initial reduction of the beam is done to achieve a longer and wider beam waist, therefore obtaining a higher accuracy for beam size measured by the thermal camera which has a relatively large pixel size of 100 μm.

The image in Figure 6.4 shows the layout of the entire laser system. The pump sources are on the right and the mode-matching optics, which lead to the laser section, are at the centre. The wavelength separator and diagnostics segment are on the left.
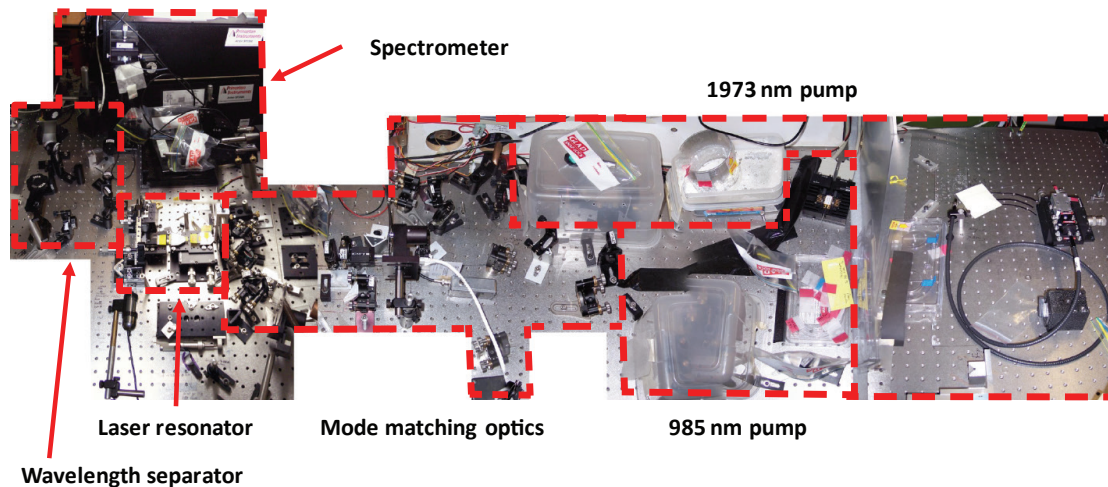
Figure 6.4: Compound image of the full laser setup. The dashed lines encircle the different parts of the laser setup.

6.3   CW operation

The simplest mode of operation is CW mode, where both pump sources and the laser operate without any pulsing. A detailed account of the process to align the system and obtain lasing is presented in Appendix G. The following section details the experimental setup and the laser results obtained in CW mode. Output power, slope efficiency and threshold values are obtained. From these results, we calculate the internal resonator losses, small signal gain and the emission cross-section.

6.3.1   Analysis of CW results

All of the laser results presented in this chapter are based on the IR-Photonics fibre. The 90% absorption length at 985 nm for the 1.7 $mol\%$ Er^{3+} doped IR-Photonics fibre is calculated to be 10 cm based on the GSA cross-section of Er^{3+}:ZBLAN (see section 2.3.3). This characteristic length holds only for very low power levels of 985 nm pump because at higher power levels the ground state starts becoming bleached. Our laser usually operates at the maximum 985 nm pump power available, which is a few times over the pump saturation power $P_{sat} = 24$ mW, where the saturation power is calculated according to [196]

$$P_{sat} = A_{core} \cdot h \cdot c / (\lambda_{P1} \cdot \sigma_{P1\,GSA} \cdot \tau_{4_{I_{11/2}}}). \tag{6.1}$$

Here, A_{core} is the core area of the fibre, h Plank constant, c speed of light, λ_{P1} the pump wavelength, $\sigma_{P1\,GSA}$ the pump absorption cross-section and $\tau_{4_{I_{11/2}}}$ the lifetime of the $^4I_{11/2}$ level. Measurements of the transmission of the 985 nm pump through different

lengths of fibre show that the absorption length is increased to approximately 21 cm when the maximum available incident power of 194 mW is used. Unfortunately, the IR-Photonics fibre contains a large number of internal break points in the core, which are randomly located along the fibre. It is observed that when light travels through these points, it is strongly attenuated and is scattered in all direction. The abundance of these points along the fibre core make it almost impossible to achieve an uninterrupted length of fibre in excess of 18 cm. Therefore we use an 18 cm length of fibre as the benchmark for laser power measurements, unless otherwise mentioned. Significantly shorter fibres than 18 cm are expected to lase less efficiently and hence were not tested. It would be of interest in the future to conduct a comparison of laser power and efficiency using different lengths of a more robust fibre.

Table 6.1 summarises output and efficiency results of the 18 cm long fibre laser. Maximum power obtained, initial slope efficiency and 1973 nm pump threshold power are shown for a range of output coupler reflectivities when both pumps are operating in CW mode.

Table 6.1: Summary of laser parameters with varying output couplers for 18 cm long IR-Photonics fibre. Slope efficiency is relative to the 1973 nm pump with a fixed 985 nm maximum incident pump power of 194 mW.

Output coupler reflectivity (%)	Maximum output power (mW)	Maximum initial slope efficiency relative to 1973 nm pump power (%)		Laser threshold relative to 1973 nm pump power (mW)	
		Incident power	Absorbed power	Incident power	Absorbed power
80	175	27.5 ± 1	46 ± 7	196	160
90	260	26.6 ± 0.7	57 ± 4	111	59
95	120*	15.5 ± 1	47 ± 3	106	61
99.3	72**	4.9 ± 0.2	9.7 ± 0.7	89	50

* Unfortunately, the measurement with the 95% output coupler was not completed, therefore power saturation was not reached. We assume that the maximum power that could have been reached in this case is 30% higher than the power obtained in the experiment. ** The maximum output power in the case of HR mirror used as an output coupler assumes equal output power through both resonator mirrors. Value displayed is therefore double the measured power on one side.

With the exception of section 6.4.3, all of the results presented in this chapter include the 985 nm pump operating with a fixed incident power of 194 mW, of which we estimate 90% is launched into the fibre and 140 mW is absorbed when the fibre laser is below threshold and about 170 mW is absorbed when lasing. These estimates are based on our below-threshold measurements of transmission of the 985 nm pump through different lengths of fibre and on the change in the transmission of the 985 nm pump through

the fibre once lasing starts (see section 6.3.4). We define the launch efficiency to be the fraction of the light that enters the fibre and is guided by its core relative to the power incident on the fibre endface. The launch efficiency takes into account Fresnel losses at the interface, misalignment between the incident beam and the core and modal mismatch.

We used a second HR mirror as an output coupler for comparison with the lower reflectivity output couplers. The HR dichroic mirror has a measured transmission of 0.7% in the range of 3100 nm-3600 nm. Since both resonator mirrors used in this case have the same reflectivity, the laser emits beams through both resonator mirrors. Gain clamping in CW operation ensures that the round trip gain is very low because of low transmission of the end mirrors. This means that the circulating power at either end of the fibre is near identical and hence the power emitted from either ends of the fibre laser will be near identical. Therefore, as an approximation useful for comparison purposes, we assume both forward and backwards laser beams to have the same power, hence, the output power values presented in Table 6.1 and Figures 6.5 and 6.6 are twice the amount measured on the laser output side. We use this approximation since the backward propagating power cannot be measured in our setup as it is absorbed in the pump launching asphere. The double power figure and its associated efficiency will be used from this point onwards when using an HR mirror as an output coupler.

Figures 6.5 and 6.6 show the full datasets of the results summarised in Table 6.1. The curves show the output power of the 3.5 μm lasers with different output couplers ranging from 80% to 99.3% when both pumps are operating in CW mode. When operating with the 90% output coupler, the laser exhibits the highest CW output power reached by our system. A maximum of 260 mW is obtained when pumping with over 2 W of incident 1973 nm pump. The initial slope efficiency relative to incident 1973 nm pump power in this case is 25.4%.

The slope efficiency relative to the incident 1973 nm pump power (not counting a fixed 985 nm power) is highest at 27.5% using the 80% output coupler. The slope efficiency diminishes with increasing output coupler reflectivity, reaching 4.9% (see second comment in Table 6.1) when using an HR mirror as an output coupler. This efficiency is significantly better than the maximum theoretical slope efficiency achievable by directly pumping from the ground to the upper laser level (18.3%).

We are also interested in the relation between the laser power and the absorbed power of the second pump. We can define an "internal slope efficiency" ($\eta_{internal}$) as the laser slope efficiency relative to the derived absorbed 1973 nm pump power:
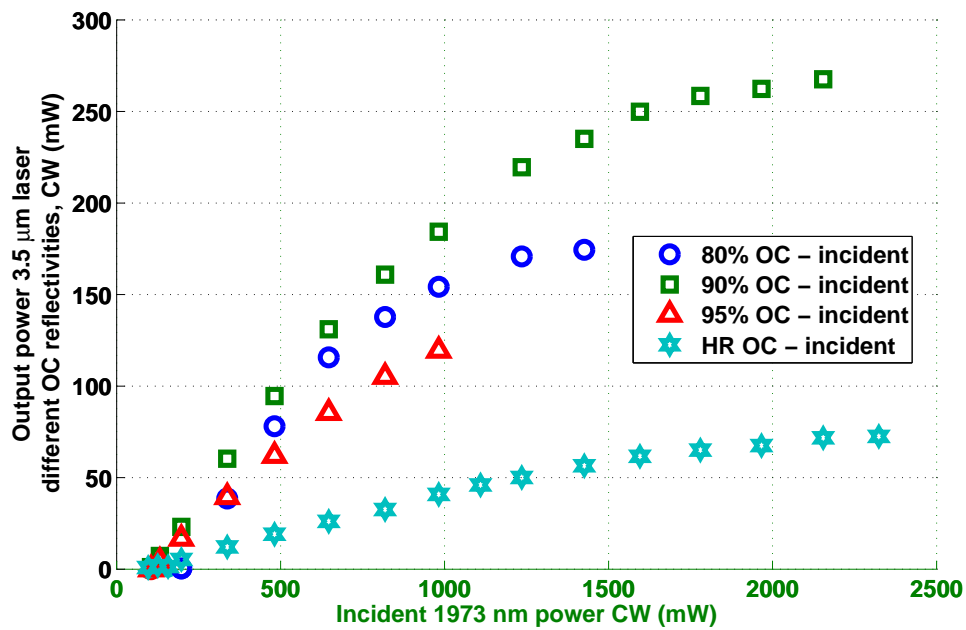
Figure 6.5: Output power results of 18 *cm* long, 3.5 *µm* fibre lasers with different output couplers in CW operation relative to incident 1973 *nm* pump.
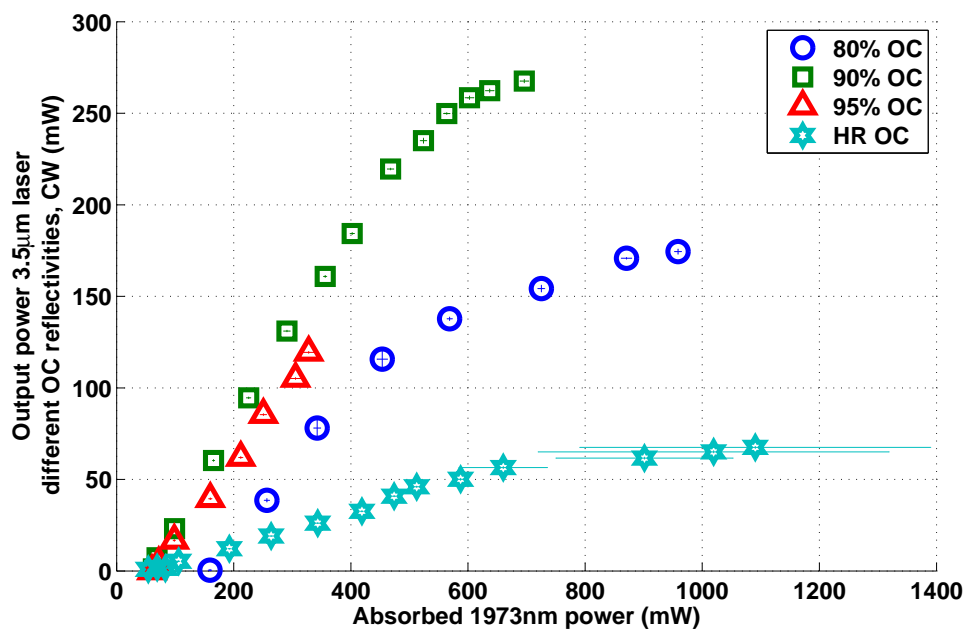
Figure 6.6: Output power results of 18 *cm* long, 3.5 *µm* fibre lasers with different output couplers in CW operation relative to calculated absorbed 1973 *nm* pump

$$\eta_{internal} = \frac{P_{laser} - P_{laser\ @\ threshold}}{P_{1973nm} - P_{1973nm\ @\ laser\ threshold}} \tag{6.2}$$

The explanation of how we derive the absorbed 1973 nm power is given later in section 6.3.3. The initial internal slope efficiency obtained for the 90% OC case is $57 \pm 4\%$. These results are an order of magnitude improvement over the efficiency previously demonstrated by Többen (2.8%, see [117]). The results also demonstrate that employing a DWP scheme can improve the laser efficiency beyond the theoretical Stokes efficiency of a single wavelength pumped laser.

The 3.5 μm laser threshold relative to the 1973 nm pump is low, as expected from a four level laser. The 1973 nm power necessary to reach threshold reduces with decreasing output coupling fraction, from 196 mW using an 80% output coupler to 89 mW with the HR mirror as an output coupler.

The maximum achievable power is dominated by the slope efficiency because of the relatively low threshold using all output couplers. The achievable power starts to saturate with all output couplers when the incident 1973 nm pump power is increased beyond 800-1000 mW for a fixed 985 nm pump. The laser output power completely saturates with approximately 30% of additional output power when the incident pump reaches about 2-3 times its value in the linear regime.

6.3.2 Internal resonator losses, small signal gain, emission cross-section and other parameters

The results described previously enable us to calculate the internal losses in the laser resonator, its efficiency factor, emission cross-section, small signal gain, optimal output coupling fraction and inversion density. The internal losses of the resonator were calculated using the formulation described by Koechner [197], which follows the work of Findlay and Clay [198]. These losses include the reflections off the fibre facets as well as scattering and absorption within the glass fibre. The threshold condition for lasing is

$$R_1 R_2 exp(2\mathrm{g}_0 l) = 1, \tag{6.3}$$

where R_1 and R_2 are the reflectivity of the resonator mirrors, g_0 is the small signal gain coefficient (at threshold in this case) and l is the fibre length. We can now add a double pass loss term δ, which includes all the internal loss mechanisms

$$R_1 R_2 exp(2\mathrm{g}_0 l - \delta) = 1. \tag{6.4}$$

In similar analyses, it is common to merge the reflectivity R_1 into the cavity losses coefficient δ. In this case, we keep the reflectivity value for the HR coated mirror R_1 on the pump input side for the sake of including only true internal cavity losses. Reflectivity values for all resonator mirrors used are provided in Table 6.1 on page 151. The Fresnel reflections and the Fabry-Perot (FP) behaviour created by the fibre tip and the resonator mirrors need to be taken into account. This is somewhat similar to the case of non-AR coated laser crystal addressed by Findlay and Clay in their original analysis [198]. In our experiments, the fibre was butted hard against the mirrors while optimising output power, so it is reasonable to assume maximum feedback conditions from the mirror. However, a small gap between the core of the fibre and the mirrors, in the order of a few microns, cannot be completely ruled out due to the fibre endfaces not being completely parallel to the surface of the mirrors. In this case, we can follow Findlay and Clay's argument: The fibre endface is well within the Rayleigh range, therefore the beam is not diverging yet. The fibre resonator contains a very large number of longitudinal modes. The modes are separated by the free-spectral range of $\Delta \nu = c/2Ln = 566 \ MHz$, for the 18 cm long fibre resonator with refractive index of $n = 1.47$. The 4% reflectivity of the fibre endface together with the mirror reflectivity result in a very low finesse value of $F = 1.7$ for even the HR mirror case. Therefore, even though the small gap between the fibre endface and the mirror results in free-spectral range on the order of many THz, the low finesse ensures that there will always be a resonator axial mode that satisfies the FP condition for maximum reflection when considering the FP caused by the gap between the mirror and the fibre. To take this effect into account, we replace the resonator mirrors reflectivity R_1 and R_2 with an equivalent reflectivity representing the maximum reflectivity available from a Fabry-Perot resonator with unequal mirrors

$$R_1' = \frac{(\sqrt{R_F} + \sqrt{R_1})^2}{(1 + \sqrt{R_F R_1})^2} \tag{6.5}$$

$$R_2' = \frac{(\sqrt{R_F} + \sqrt{R_2})^2}{(1 + \sqrt{R_F R_2})^2}, \tag{6.6}$$

where R_F is the reflectivity of the straight-cleaved fibre tip due to Fresnel reflection (4%). If we now substitute Equation 6.5 into Equation 6.4 and rearrange, we end with

$$- \ln R_1' R_2' = 2\mathrm{g}_0 l - \delta. \tag{6.7}$$

We can now substitute into Equation 6.7 the relation between small signal gain g_0 and absorbed pump power P_{abs}

$$\mathrm{g}_0 = \sigma_e \tau_f \eta P_{abs} / h\nu_{Laser} V_{v \ core}, \tag{6.8}$$

where σ_e is the emission cross-section, τ_f is the upper laser level lifetime, h is Planck's constant, ν_{Laser} is the laser optical frequency and $V_{v\,core}$ the doped volume. η is an efficiency coefficient associated with the absorbed pump power P_{abs}, which is the product of

$$\eta = \eta_Q \eta_{St} \eta_B. \tag{6.9}$$

In Equation 6.9, η_Q is the quantum efficiency, or the ratio between the number of laser photons produced to pump photons absorbed. η_{St} is the Stokes efficiency, or the ratio between the energy of a laser photon to a pump photon, η_B is the overlap coefficient between the laser and pump beams.

We can now substitute the saturation power density [197]

$$I_s = \frac{h\nu_{Laser}}{\sigma_e \tau_f}, \tag{6.10}$$

together with g_0 and the combined result is

$$2\mathrm{g}_0 l = 2\eta P_{abs}/I_s A_{core}. \tag{6.11}$$

This can now be substituted into Equation 6.7, resulting in a form which relates the resonator equivalent reflectivities to the efficiency, saturation intensity, doped area A_{core}, absorbed power and resonator losses δ

$$-\ln R_1' R_2' = (2\eta/I_s A_{core})P_{abs} - \delta. \tag{6.12}$$

Since the same HR mirror is maintained at the input side for all measurements, Equation 6.12 establishes a linear relation between the absorbed 1973 nm pump power (at threshold) and the output coupler reflectivity. We can now plot the laser threshold power with varying output couplers. When extrapolating to 0 mW absorbed pump, the intersection point with the $-\ln R$ axis represents the double pass internal resonator losses. As Findlay and Clay show in [198], this method is very general and is independent of pump geometry or pump pulse shape and duration since those changes cancel out. The method does assume, however, that all of the pump power launched into the medium is absorbed. We therefore used the absorbed threshold power readings to satisfy the requirements of this method. This is because only negligible amount of 1973 nm power was transmitted through the fibre at threshold when operating with the maximum available 985 nm power of 194 mW. In addition, as shown in Chapter 3, the population of the upper laser level ${}^4F_{9/2}$ is negligible when only the 985 nm pump is operating and the 1973 nm pump is turned off, regardless of the 985 nm pump power. We therefore do not need to take into account the 985 nm pump power in this analysis.
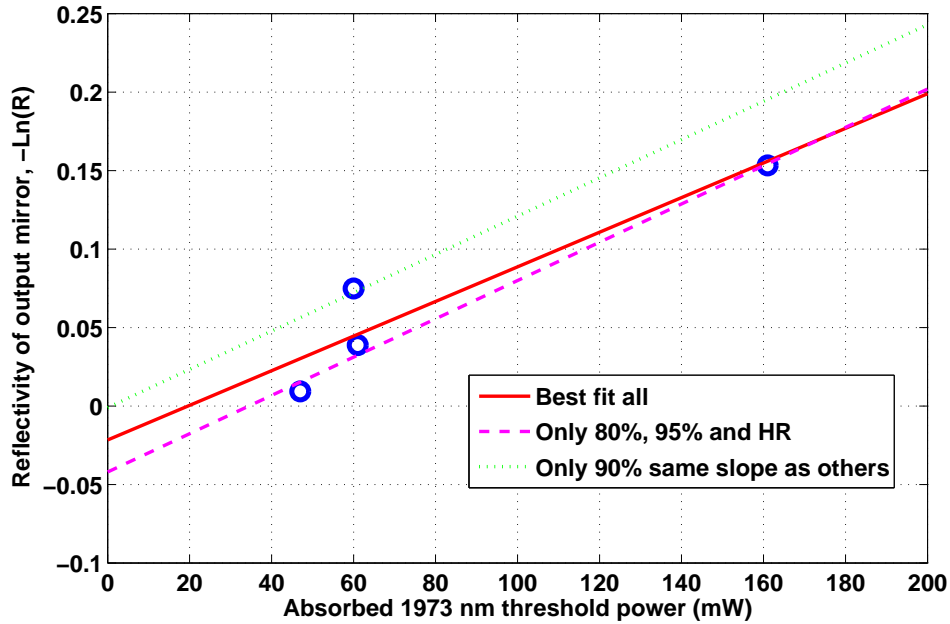
Figure 6.7: Findlay-Clay analysis to extract internal losses. The threshold power is in mW of absorbed 1973 nm for the 80%, 90%, 95% and HR output coupler.

Figure 6.7 shows the result of the Findlay-Clay analysis. The intercept point for the best fit for all data points is $\delta = 2.2\% \pm 3.5\%$, corresponding to a single-pass loss coefficient of 0.0006 ± 0.0002 cm^{-1}. The data point of the 90% mirror is a low-loss outlier which significantly increases the error margin. The measurements with various output couplers are conducted with different pieces of fibre from the same spool which were cleaved to the same length. Fibre replacement is a necessity due to fibre tip breakage and its continuous degradation. The fibre tip deterioration is the results of repeated butting and separating of the fibre and mirrors, required during optimisation of the laser power due to the FP effects. Visual observations reveal that some fibres have distinct scattering points which are made clear by observing the strong green upconversion, or when looking at the fibre through an IR-viewer. Those scattering points can be the cause of slight differences in the internal losses of different pieces of fibre and contribute to the large error bounds of the extrapolation. It is therefore possibly more instructive to look at different cases of linear fits (shown in Figure 6.7).

If we exclude the 90% data point and take the fit for the combined data of 80%, 95% and the HR mirrors, we obtain $\delta = 4.2\% \pm 1.9\%$. If we use the same slope and apply it to the 90% outlier, we end with a negligible loss of $\delta = 0.001\%$, or 3×10^{-7} cm^{-1}. This shows that we cannot assume that all fibre segments from the same spool are created equal and that significant variations in internal fibre losses are possible.

We can compare our measured result to other published values. The fibre manufacturer, IR-Photonics (which was acquired by Thorlabs) publishes a loss of approximately 0.1 dB/m ($\delta = 0.8\%$, or 0.0002 cm^{-1} for an 18 cm fibre) at 3.5 μm for an undoped ZBLAN fibre. This is about a third of the loss we calculated for our laser resonator. Iwanus et al. reported recently [199] a background loss of 0.6 dB/m (equivalent to a double pass loss of $\delta = 4.8\%$ or 0.0014 cm^{-1}) in a Ho^{3+}:ZBLAN fibre made by FiberLabs. Their measured value is also significantly higher compared to the published values from FiberLabs website [200] of 0.1 dB/m ($\delta = 0.8\%$, or 0.0002 cm^{-1} for an 18 cm fibre) at 3.5 μm for an undoped ZBLAN fibre. Our measured results are therefore reasonably similar to other published results.

By using the threshold power P_{th}, launched pump power P_{in} and laser output power P_{out}, we find the slope efficiency η_s from Equation 6.13

$$P_{out} = \eta_s(P_{in} - P_{th}).\tag{6.13}$$

We can now calculate the combined efficiency factor of the laser η, (see Equation 6.9) using the loss term δ and the laser slope efficiency η_s.

$$\eta_s = \frac{(1 - R_1'R_2')\eta}{\left[1 + \sqrt{\frac{R_1'R_2'}{1-\delta}}\right]\left[1 - \sqrt{R_1'R_2'(1-\delta)}\right]}.\tag{6.14}$$

In Equation 6.14, we use the complete form for the equation which applies for all values of reflectivity. As before, the etalon effects are accounted for by using the modified reflectivities and under the assumption of obtaining the maximum reflectivity possible with each output coupler and the HR mirror. Calculating the efficiency factor η using the absorbed power slope efficiency values obtained in section 6.3.1 for all output couplers provides us with $\eta = 60 \pm 19\%$. As seen in Equation 6.9, η is the product of three separate efficiency factors. The quantum efficiency factor is taken to be $\eta_Q = 1$ in this case since ions are excited to the upper lasing level directly, while the Stokes efficiency is $\eta_{St} = 0.57$ for the case of generating 3.5 μm laser photons by pumping with 1.97 μm photons. The laser mode diameter is larger than the pump mode, which results in an overlap coefficient of $\eta_B = 1$, according to the formulation in the Findlay-Clay analysis. The product of all the efficiency factors is therefore 0.57, which is within the error range of the value obtained from the measurement.

Using the efficiency factor derived from the measurements and the slope of the best-fit curve in Figure 6.7, we can calculate the power saturation density I_s according to

$$K_s = \frac{2\eta}{I_s A_{core}}.\tag{6.15}$$

In Equation 6.15, K_s is the slope of the curve in Figure 6.7 and A_{core} is the fibre core area ($8 \pm 1.5 \times 10^{-7}\ cm^2$ for core diameter of $10 \pm 1 \mu m$). The saturation power density obtained is $I_s = 1400 \pm 400\ kW/cm^2$.

As derived by Koechner [197], in a four level laser system, the relation between the saturation intensity and the emission cross-section is

$$I_s = \left(W_p + \frac{1}{\tau_f} \right) \frac{h \nu_L}{\gamma \sigma_e}, \tag{6.16}$$

where W_p is the 1973 nm pump rate, h is Planck's constant, ν_L is the laser frequency ($8.63 \times 10^{13}\ Hz$ for emission at $\lambda = 3470\ nm$) and τ_f is the upper laser level lifetime. γ is a factor which corresponds to the inversion reduction after one photon has been emitted and is equal to one in the case of four level lasers. It is common to assume that $W_p \ll \frac{1}{\tau_f}$, but that is not the case here since the pump rate is quite high, due to the small cross-section of the fibre core. We therefore maintain the full expression and use the lifetime value found in section 5.3 of $\tau_f = 148 \pm 10\ \mu sec$. Once we rearrange to solve for σ_e, we arrive at a value of $\sigma_e = 9 \pm 4 \times 10^{-22}\ cm^2$. This value is used to normalise the 3.5 μm fluorescence curve, measured using the IR-Photonics fibre, to obtain the emission cross-section (see Figure 6.8). The large uncertainty in the cross-section value is mainly the result of the uncertainties in the absorbed power slope efficiency and the absorbed 1973 nm pump when using the 80% output coupler.

The above value can be compared with the emission cross-section calculated using the fluorescence spectral shape in conjunction with the Fuchtbauer-Ladenburg method, which is based on the Einstein coefficients (see section 2.5). The spontaneous emission lifetime τ_f, fluorescence lineshape and the emission cross-section are related by

$$\frac{1}{\tau_f} = \frac{8\pi n^2}{c} \int \nu^2 \sigma_e(\nu) d\nu. \tag{2.30 revisited}$$

We cannot use our measured value of the lifetime of the $^4F_{9/2}$ (see section 5.3) because the decay from this level is dominated by non-radiative decay, while Equation 2.30 requires the radiative lifetime. We therefore use literature values obtained using Judd-Oflet analysis. Literature values of τ_f for the $^4F_{9/2} \to {}^4I_{9/2}$ transition (which is a product of the $^4F_{9/2}$ level lifetime with the $^4F_{9/2} \to {}^4I_{9/2}$ branching ratio β) vary significantly between different literature sources. This is because β is rather small and prone to large uncertainty, with values varying between $\beta = 0.001$ [151] and $\beta = 0.0034$ [146], compared with the branching ratios of transition to the ground that are smaller than but on the order of one. Using the average literature values for β, we reach an average maximum cross-section value of $7.5 \times 10^{-22}\ cm^2$. The full range of possible cross-sections, based on the variations of the β values, has about 50% uncertainty with values ranging between
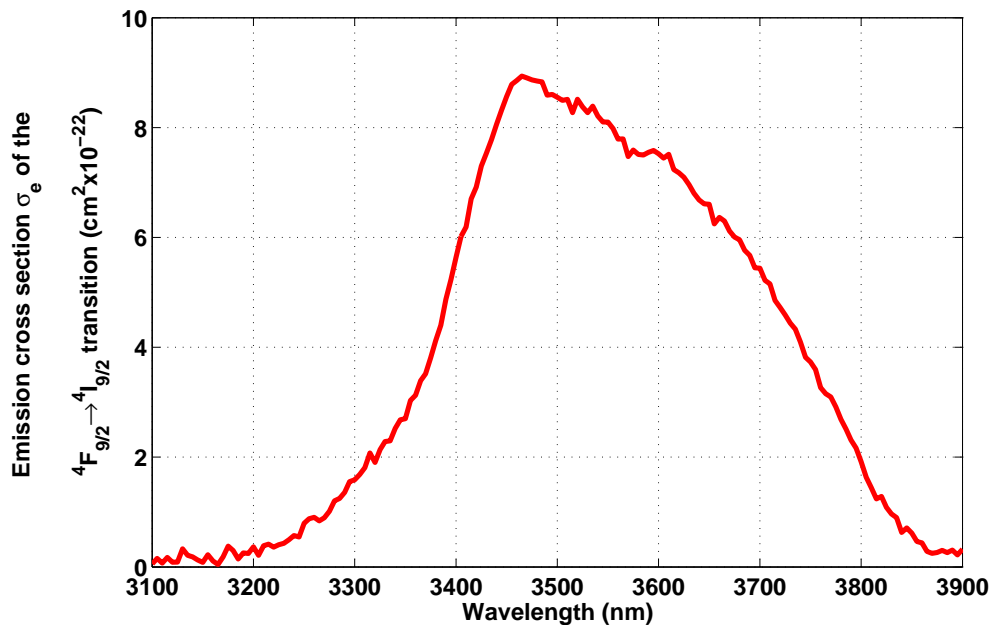
Figure 6.8: Emission cross-section of the $^4F_{9/2} \rightarrow {}^4I_{9/2}$ transition. The peak value is derived using the Findlay-Clay analysis normalising the fluorescence collected with the IR-Photonics fibre. Note that the curve is based on direct reading of fluorescence measured without compensating for the absorption of air.

$4.1 - 11.9 \times 10^{-22}$ cm^2. The emission cross-section values calculated using the saturation intensity method and the Fuchtbauer-Ladenburg method are in reasonable agreement within their respective uncertainties.

This transition is an order of magnitude weaker than the values of $3 - 5 \times 10^{-21}$ cm^2 for emission cross-sections of other rare-earth ions in long wavelength transitions using ZBLAN glass fibres [1]. This low cross-section is not surprising, however, because the wideband emission spectrum of this transition affects the cross-section. The oscillator strength of this transition is proportional to the integral of the cross-section curve. This curve is spread over a wide spectral band, resulting in a low peak cross-section value compared with other transitions that have similar oscillator strengths, but narrower spectral widths.

We can find the small signal gain coefficient g_0 as a function of absorbed pump power using I_s, η and the fibre length $l = 18$ cm. This small signal gain value is only valid when the laser is operated near threshold and does not include effects of bleaching of the pump.

$$g_0 = \frac{\eta}{l} \frac{P_{abs}}{I_s A}. \tag{6.17}$$

For threshold operation at 60 mw of absorbed power, which is applicable to the laser operating with 90% and 95% output couplers (see Table 6.1 on page 151), the small signal gain coefficient calculated is $g_0 = 0.0019 \, cm^{-1}$.

From the small signal gain and the cross-section, we can deduce the inversion average density n_{inv} by using

$$g_0 = n_{inv}\sigma_e. \tag{6.18}$$

At threshold (occurring at 60 mW of absorbed 1973 nm pump, which is equivalent to approximately 110 mW of incident pump power), the inversion density calculated is $n = 3.2 \times 10^{17}$ ions/cm^3 which corresponds to 1% of the total ion density of $n_{total} = 2.72 \times 10^{20}$ for 1.7 $mol\%$ of Er^{3+} ions in the IR-Photonics ZBLAN fibre. A summary of the parameters obtained so far is presented in Table 6.2.

Table 6.2: Summary of additional laser parameters based on Findlay Clay analysis.

Definition	Parameter symbol	Value
Internal resonator losses	δ	$2.2 \pm 3.5\%$
		$0.0006 \pm 0.0002 \, cm^{-1}$
		$180 \pm 60 \, dB/km$
Efficiency factor	η	$60 \pm 19\%$
Fibre core area	A_{core}	$8 \pm 1.5 \times 10^{-7} \, cm^2$
Laser frequency (for $\lambda = 3470 \, nm$)	ν_L	$8.64 \times 10^{13} \, Hz$
Upper laser level $^4F_{9/2}$, lifetime	τ_f	$148 \pm 10 \, \mu sec$
Saturation power density at 3470 nm with 10 μm fibre core	I_s	$14 \pm 4 \times 10^5 \, W/cm^2$
Emission cross-section of $^4F_{9/2} \to ^4I_{9/2}$ transition	σ_e	$9 \pm 4 \times 10^{-22} \, cm^2$
Small signal gain at threshold	g_0	$0.0019 \, cm^{-1}$
Ion density 1.7 $mol\%$ Er^{3+}:ZBLAN	N_{Er}	$2.72 \times 10^{20} \, ions/cm^3$
Inversion density - 110 mW threshold	$n_{inv \, th}$	$3.2 \times 10^{18} \, ions/cm^3$

We can now use the values summarised in Table 6.2 to obtain an estimate of the optimum output coupling fraction in the laser system. Figure 6.9 shows the results of section 6.3.1 using the laser output power as a function of output coupling fraction with the available optics. The power level used in these measurements is 194 mW of 985 nm power and 818 mW of incident 1973 nm power, which is at the end of the laser's linear behaviour regime and before laser power saturation dominates. The figure also shows a theoretical Rigrod analysis [201], which uses the values from Table 6.2, together with the fibre length l, according to

$$P_{out} = \frac{AI_s[(g_0 - \delta)l + ln\sqrt{R_1R_2}]}{1 - \frac{\delta l}{\ln\sqrt{R_1R_2}}}, \tag{6.19}$$
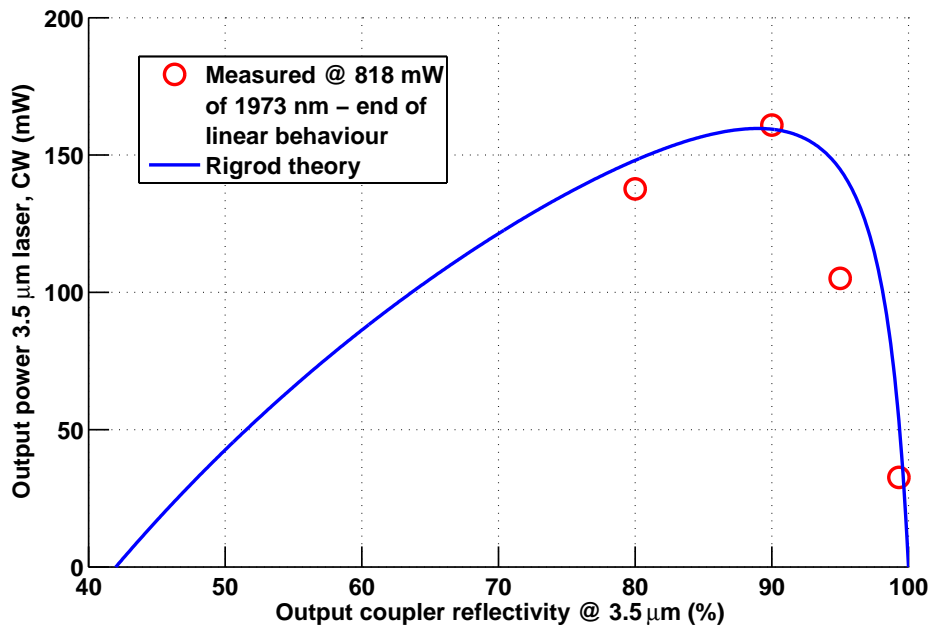
Figure 6.9: Output power as a function of output coupler reflectivity compared with Rigrod theory. The circles represent the power obtained at the end of the laser's close-to-linear behaviour, when it is pumped with 818 mW of 1973 nm pump. The continuous line follows Equation 6.19 from Rigrod [201] using the parameters found in Table 6.2 with a modified small signal gain $g_0 = 0.0247$ $cm6{-}1$ because of the higher pump level. HR mirror output power presented here assumes double the measured amount.

to find the laser output power when the output coupling fraction is varied. To obtain a reasonable fit, we needed to assume a much higher small signal gain of $g_0 = 0.0247$ cm^{-1} than the one calculated at threshold. All other parameters from Table 6.2 were maintained.

The Rigrod analysis assumes that the measurements are taken with the laser far from saturation condition. In our case, the laser does not follow the incident pump in an accurate linear fashion, we therefore cannot assume it is not experiencing some saturation effects. Therefore, the Rigrod analysis presented here is only an approximation. The theoretical curve suggests that the optimal output coupler reflectivity for obtaining maximum laser power is between 85% and 90%. The location of the peak along the reflectivity axis is quite insensitive to the small signal gain value used in fitting. Variations of g_0 $^{+100\%}_{-70\%}$ result in changes of $\mp 5\%$ in the optimum reflectivity required. The measured results compared with the theoretical curve suggest that both the 80% and 95% cases did not reach the maximum power expected under optimal experimental conditions.

6.3.3 Laser efficiency and 985 nm power

Slope efficiency to this point has been measured relative to the change in 1973 nm power only. Since slope efficiency is a convenient comparison parameter between different

resonator configurations, it raises the question of how does the power of the 985 nm pump influence efficiency. This question is addressed in the following pages.

The conventional definition of slope efficiency is

$$\frac{Power_{Laser \,@\, pump\, power}}{Power_{Pump\, power} - Power_{pump\, power\,@\,threshold}}. \tag{6.20}$$

From Equation 6.20, we see that if the 985 nm pump power is fixed, it will not change the slope efficiency, which is determined by the second pump alone. This was the case in the experimental data presented to this point. However, the 985 nm pump does supply energy to the system and therefore its contribution to the optical-to-optical efficiency of the laser must be considered.

We define here the total optical-to-optical efficiency η_{op2op} of a dual-wavelength pumped (DWP) laser as the ratio between the laser output power P_{out} and the total incident optical power of both pumps $P_{inc_1}(985nm)$ and $P_{inc_2}(1973nm)$

$$\eta_{op2op} = \frac{P_{out}}{P_{inc_1}(985nm) + P_{inc_2}(1973nm)}. \tag{6.21}$$

This efficiency is maximised at the onset of laser power saturation after which the efficiency starts to drop, as seen in Figure 6.10, which shows different ways to calculate the laser efficiency:

1. The slope efficiency based solely on the incident 1973 nm pump.

2. "Internal" slope efficiency, or slope efficiency based solely on the absorbed 1973 nm pump.

3. Optical-to-optical efficiency of the absorbed power of the 985 nm and 1973 nm pumps.

4. Total optical-to-optical efficiencies based on total incident power.

The figure shows that even the measured total optical-to-optical achieves unprecedented efficiency for this transition. In our measured results, the total optical-to-optical efficiency relative to incident power peaks at 15.9% compared with 2.8% that was obtained by Tobben with pumping directly from the ground state. Our measured value also compares well with the theoretical Stokes efficiency of 18.3% of a singly pumped 3.5 μm laser. The efficiency of our laser could be improved by increasing the absorption of the 1973 nm pump. This will be addressed in future implementation of the laser in one of the following
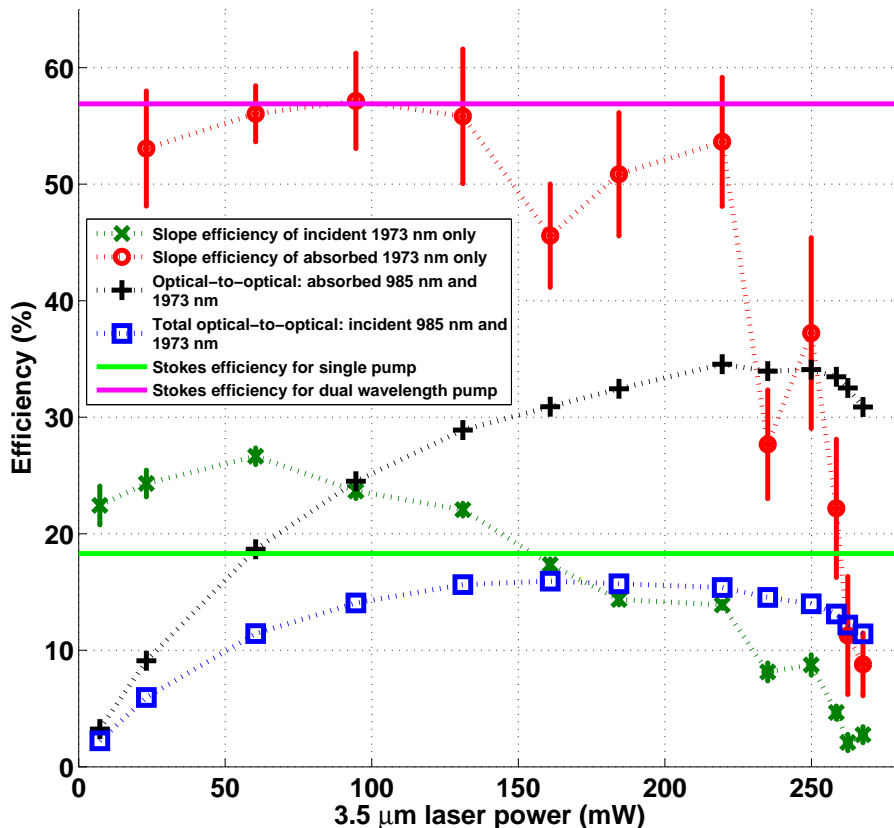
Figure 6.10: Efficiency calculation methods comparison for the 90% output coupler case. Laser operates in CW mode.

ways: by increasing the 985 nm pump power, by pumping from both ends of the fibre or by using a double clad fibre geometry.

The internal slope efficiency, i.e. the slope efficiency relative to absorbed 1973 nm pump power, is quite high. The internal slope efficiency approaches, within the experimental uncertainty, the theoretical Stokes efficiency of 56.9% for 3.5 μm lasing using 1973 nm pumping with a fixed 985 nm pump power. We are unsure about the nature of the processes which allow such a high slope efficiency in this relatively lossy fibre (see Table 6.2). Higher-than-Stokes efficiency behaviour has been theorised and demonstrated for some laser transitions in Er^{3+}:ZBLAN fibres due to energy-transfer processes that recycle ions' energy. An example of such a lasing transition is the 2.75 μm transition in highly doped Er^{+3}:ZBLAN [92] in which higher than Stokes efficiency has been recently obtained [136]. Further investigation is required to learn whether such a mechanism exists in our case, however, this is beyond the scope of this thesis.

The calculation of the internal slope efficiency in this case is not obvious and a detailed discussion of the errors is appropriate. The absorbed 1973 nm pump power is measured by using the wavelength separator shown in Figure 6.3. First, when the 3.5 μm laser is operating, the laser power and the residual 1973 nm pump light that is transmitted through the fibre are recorded. The 985 nm pump is then blocked (causing the 3.5 μm laser to cease operation) and the amount of 1973 nm pump transmitted is recorded again. The change in the transmitted 1973 nm pump between both cases is recorded. By accounting for the losses of the wavelength separator, we arrive at an initial figure for the absorbed 1973 nm power. This method can be used when the system is lasing, when it is operated below threshold and also when the resonator mirrors are removed.

There are a couple of effects that have to be considered when calculating the absorbed 1973 nm power:

1. The actual 1973 nm power incident on the fibre changes when the 985 nm pump is switched on and off due to changing feedback conditions caused by the reflection from the ZBLAN fibre tip. This is probably the result of slight changes in the butting conditions with the HR mirror in place and slight drooping of the fibre tip from thermal expansion when the mirror is removed.

2. A strong etalon effect can be observed with slight variations in the fibre and laser mirrors' butting conditions. These are caused by variations in the physical distance between the fibre core and mirror surface. Etalon effects can be observed with both the combination of the input side of the fibre and the HR mirror as well as the etalon effect caused by the output side of the fibre and the output coupler mirror.

The power of the 1973 nm laser is monitored using a small pick-off located prior to the pump combining dichroic mirror (see description in section 5.2.2, Figure 5.1). This configuration allows the monitoring of the incident 1973 nm power, which enables us to ensure consistent 1973 nm incident power levels when the 985 nm pump is also incident on the fibre or when it is blocked.

The etalon effect is observed when the fibre and mirror are in close proximity. The beam emerging out of the fibre is well within the Rayleigh range and therefore has approximately planar wavefront causing interference between the beam and its reflection off the mirror. The etalon effect influences both the laser output power and the 1973 nm transmitted pump. This is caused by modulation of the effective reflectivity of the fibre tip and resonator mirror combination with slight changes in their separation. Such modulation alters the amount of 1973 nm pump entering (on the HR mirror side) and

emerging (on the output coupler side) out of the resonator. As a rule of thumb, the laser output power is maximum when the transmitted 1973 nm pump is minimal.

The 1973 nm pump is partially reflected back into the fibre by the output coupler. The 80% output coupler has the highest measured reflectivity at 1973 nm (55%) and thus is affected the most by etalon effect. Reflecting the 1973 nm pump has three consequences:

1. A fraction of the 1973 nm that was not absorbed and would have otherwise been transmitted through the fibre is reflected back into it by the output coupler. Assuming optimal butting of the mirror, the reflected fraction would vary between 10% when using the HR mirror to 55% with the 80% output coupler. In absolute terms, this corresponds for example to 220 mW of reflected when 1420 mW is incident on the fibre for the case of the 80% output coupler. This reflected power figure is based on the measured amount of transmitted power at this incident power level. The reflected power is therefore not negligible and is thus expected to increase the lasing power, which depopulates the $^4F_{9/2}$ level more rapidly and increases the number of ions in the $^4I_{11/2}$ level. This should lead to higher 1973 nm pump absorption. The process is expected to continues until an equilibrium is reached.

2. Less 1973 nm pump is transmitted through the fibre due to the etalon effect. Variations of up to 50% in the transmitted 1973 nm power can be observed, although the large changes are associated with the laser starting and ceasing operation under high 1973 nm pump power. More typical fluctuations observed when the output coupler is moved with the laser operating are on the order of 25-30%. This effect must be taken into account. Otherwise, the difference between the transmitted pump with and without 985 nm pump would be greatly underestimated, resulting in an increased internal slope efficiency.

3. The counter propagating 1973 nm light is effectively coupled back into the 1973 nm laser which can cause instability due to feedback effects and thus further modify the incident power. This is evident especially when the 985 nm pump is turned off and the 1973 nm laser is operating close to its threshold. In this case, moving any of the possible output couplers can result in the laser fluctuating between going below threshold and operating with up to 100 mW. The effect becomes much less pronounced with the 985 nm pump operating at maximum power of 194 mW of incident power. The fluctuations become especially pronounced when the 80% output coupler is used due to its high reflectivity of 55% at 1973 nm. With this output coupler, we have observed strong instabilities of up to 150 mW in the 1973 nm power when using approximately 2 W of incident power. This also resulted in very unstable operation of the 3.5 μm laser. Spectral effects of

the instability are discussed further in section 6.5.2. The changes in the 1973 nm incident power are monitored continuously using a power meter that measures a sample of the 1973 nm beam reflected off a BK-7 wedge (see Figure 5.1).

The second consequence above is accounted for, in part, by measuring the reflectivity of the output couplers using a Perkin-Elmer Spectrum 400 FTIR spectrometer. Contribution of the measured reflectivity at 1973 nm is included in the absorbed pump power calculation. In this case, we assume that the maximum laser power is obtained when we get maximum reflection back into the laser resonator. This is while using the same assumption as before that there is always a longitudinal mode that corresponds to maximum reflection conditions. We now have to add an addition assumption that all power reflected is absorbed in the resonator. Without this assumption, unrealistically high internal slope efficiencies of 80%-100% are calculated based on our data. The estimate of the internal slope efficiency in the previous graphs is based on this assumption.

The assumption that the reflected power is absorbed does not hold for very high incident 1973 nm power and therefore sets an upper limit on the amount of absorbed 1973 nm power. Figure 6.11 illustrates this scenario using two hypothetical cases of propagation of the 1973 nm power through a DWP fibre. In these scenarios we assume that both 985 nm and 1973 nm pump beams are incident on a fibre resonator from the left side of Figure 6.11 and are both propagating towards the right of Figure 6.11 (Forward propagation). The 985 nm beam is absorbed and excites ions to the $^4I_{11/2}$ levels. The 1973 nm pump beam is absorbed along the fibre according to Beer-Lambert law as well, however, the local $^4I_{11/2}$ population is not constant hence the transmission profile is not exponential. Residual 1973 nm pump that reaches the other end of the resonator undergoes a 50% reflection by the output coupler. In the case of the lowest 1973 nm power, there is a sufficient population in the $^4I_{11/2}$ level to absorb all reflected 1973 nm power. When significantly higher 1973 nm power is launched into the fibre, it bleaches the $^4I_{11/2}$ population at the far side of the fibre. Thus, reflected 1973 nm pump from the output coupler cannot be absorbed over a significant portion of the fibre and much of it is transmitted back through the fibre input side.

The above suggested explanation is supported by the instability observed with the 80% output coupler while it was absent when using other output couplers with lower reflectivity at 1973 nm. An additional experimental evidence is shown in Figure 6.12. In this figure, we plot both the transmitted and the calculated absorbed 1973 nm pump as a function of the incident 1973 nm power. The data used is from the lasing experimented with the 18 cm long, IR-Photonics fibre while it was lasing with the 90% output coupler, as shown in Figures 6.5 and 6.6. The transmitted pump follows an initial slope which changes
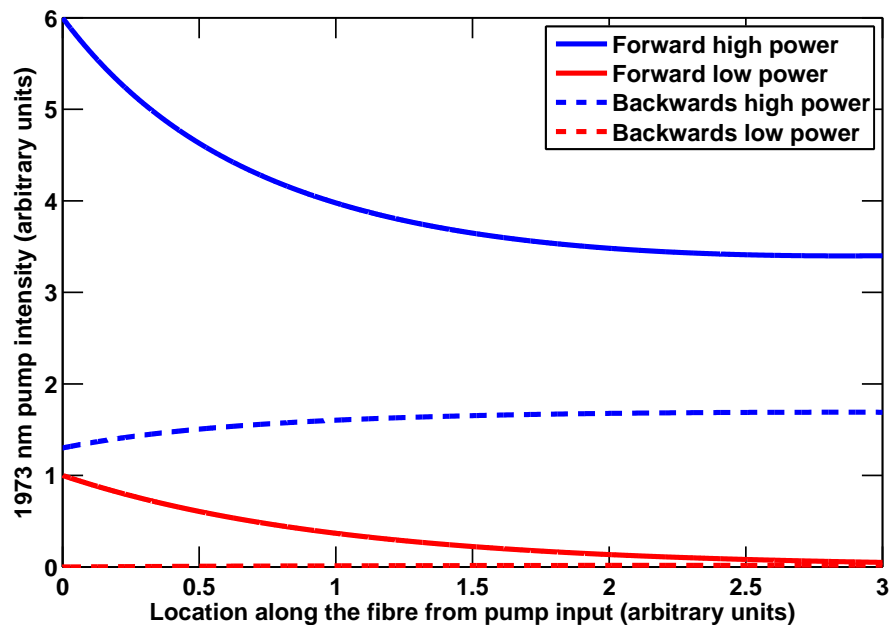
Figure 6.11: Illustration of 1973 nm pump propagation inside a DWP fibre and its reflection by the output coupler. Two hypothetical cases are shown based on low power and high power of 1973 nm pump. In both cases we assume that both the 985 nm and 1973 nm beams are incident on a fibre resonator from the left side of the figure. The 1973 nm beam transmitted through the fibre is also partially reflected by the output coupler on the right side of the figure. The 985 nm pump propagating from the left excites ions to the $^4I_{11/2}$ level and the excitation profile is assumed exponentially decaying along the fibre following Beer-Lambert law. Residual 1973 nm pump is 50% reflected by the output coupler on the right end of the resonator. The 1973 nm transmission shown is calculated based on absorption following Beer-Lambert law with changing population density along the fibre. These curves are for illustration purpose only and are not based on a detailed rate equation analysis of the IR-Photonics fibre.

to a different, more steep slope, around 818 mW of incident power. An increase in the slope of the transmitted pump power from a fibre is an indication of pump absorption saturation where the ion density at the lower and upper levels of the pump transition start to become comparable. This results in the reduction of the amount of pump that can be absorbed. At the same time of the slope change in the transmitted curve, the curve of the calculated absorbed power changes from a linear behaviour to one that appears to be saturating. This is another indication of the pump absorption saturation. The incident power where this saturation behaviour starts appears to be fairly consistent around the 818 mW mark for all output couplers used. The derived absorbed power at this point is also consistent at about 350 mW in CW. Below this absorbed power level, additional pump photons are absorbed readily. We can now suggest this absorbed power level in CW as the upper limit where our assumption of reflected power being absorbed is likely to be valid. Beyond this point, we can only assume that some of the reflected power is absorbed.
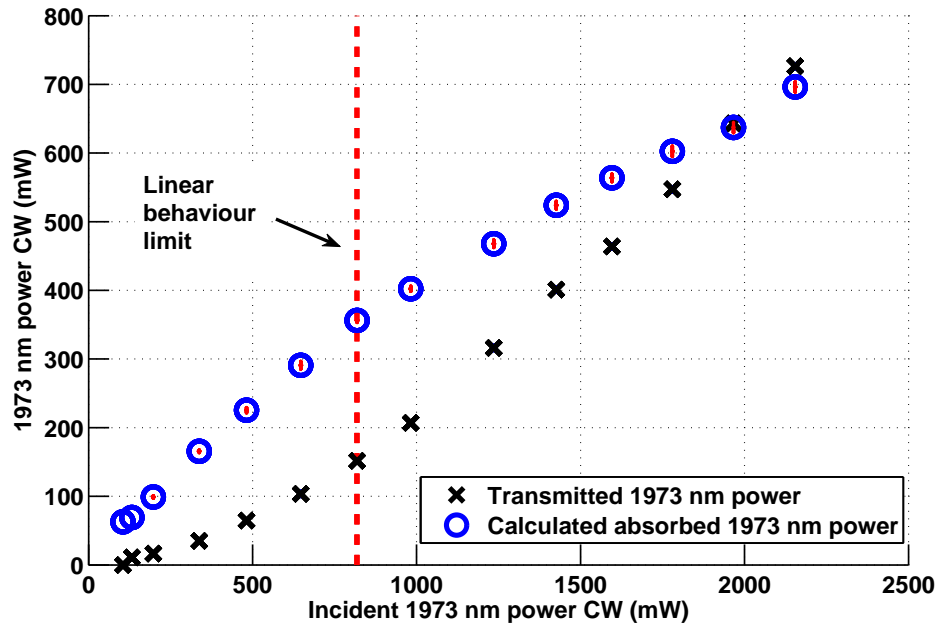
Figure 6.12: Transmitted and calculated absorbed 1973 nm power and the linear behaviour limit. Results shown are from an 18 cm long IR-Photonics while lasing with 90% output coupler. The end of the linear behaviour regime appears to approximately coincide with the 818 mW data point.

Lastly, the absorption of the 985 nm pump causes some heating of the fibre, which is estimated to result in an increase in temperature of about 10°C (see Appendix E). The 1 to 2 mm of exposed ZBLAN glass at the input tip expands because it is not cooled effectively by conduction to the fibre holder as the rest of the fibre. We estimate this expansion to be approximately 0.5 μm according to the thermal expansion coefficient of ZBLAN ($17.2 \times 10^{-6}/K°$ [57]). Thus, slight misalignment and small alterations of the mode matching conditions occur when the 985 nm pump is turned off, which is necessary for reference measurement of the 1973 nm beam through the fibre without absorption. It is possible to observe shifting of interference fringes using the iris by monitoring the back-propagating 985 nm pump (see Appendix G, Figure G.3). Care was taken to minimise this effect by performing the final alignment and butting of the fibre with the 985 nm pump operating at maximum power, yet this effect could not be completely avoided. This is because the calculation of the absorbed 1973 nm pump necessitates blocking the 985 nm beam at every power level that is used with the 1973 nm pump. Variations in the fibre tip temperature with 985 nm pump incident or blocked are inevitable, especially when operating at higher 1973 nm pump power that changes the amount of 985 nm pump and introduces additional heating of the fibre tip as well.

6.3.4   Changes in the absorption of the 985 *nm* pump when lasing

When the laser is operating and the 1973 *nm* pump power is increased, there is a noticeable decline in the transmitted 985 *nm* (see Figure 6.13). The reduction is especially significant as the 1973 *nm* just reaches threshold for lasing at 3.5 *μm*. The reduction in transmitted 985 *nm* power continues after threshold at a lesser rate and appears to saturate in-step with the saturation of the laser power. An additional 10% of 985 *nm* pump power is absorbed beyond the value obtained at threshold when the laser is operating at its highest output power.
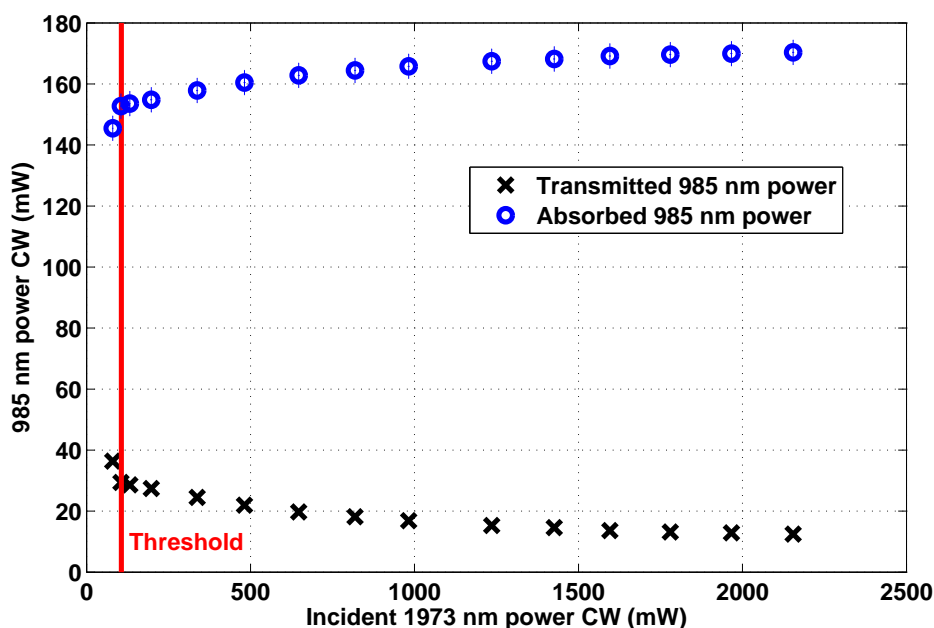
Figure 6.13: Changes in absorbed and transmitted 985 *nm* pump power when lasing as a function of incident 1973 *nm* pump. Laser with 90% output coupler operating in CW.

This reduction can be explained as the result of changed dynamics of the system once lasing commences. The 1973 *nm* pump elevates a significant fraction of the population from the $^4I_{11/2}$ level to the upper laser level. We saw in section 5.4 that the $^4F_{9/2} + {}^4I_{11/2} \rightarrow {}^4S_{3/2} + {}^4I_{13/2}$ energy-transfer process is strong and can depopulate both $^4F_{9/2}$ and $^4I_{11/2}$ levels. Once lasing starts, the increased rate at which ions are removed from both levels effectively reduces the number of ions participating in the lasing and pump cycle by ejecting them to the $^4I_{13/2}$ and $^4S_{3/2}$ levels. The long lifetime of the $^4I_{13/2}$ in particular is very effective in storing these ions. This allows for additional ions to be excited from the ground state to the $^4I_{11/2}$ level. The reduction in transmitted 985 *nm* pump varies slightly between the different versions of the laser which is probably due to slightly different launching conditions.

6.4 Quasi-CW operation

In this section we look at quasi-CW operation of the DWP laser obtained by chopping the 1973 nm pump. Output power, slope efficiency and the dependency of the laser power on the 985 nm pumping conditions are investigated.

An interesting observation in Többen's initial 3.5 μm laser demonstration was the improvement in the laser peak output power when the 655 nm pump beam was mechanically chopped [117]. Többen did not report additional experiments to clarify this observation. A similar improvement in our 3.5 μm laser peak output power and threshold reduction is observed when the 1973 nm pump is mechanically chopped compared with CW operation. Two possible causes for the improvement are:

1. Reduction in thermal load decreasing the temperature of the core, therefore reducing the rate of multi-phonon decay of ions from the upper lasing level (see section 2.4.2). As shown in Appendix E, the core temperature increase is only on the order of 10°C. Therefore, the expected increase in multi-phonon decay rate is on the order of 3%. Such a small change would have negligible effect on the overall decay rate and cannot explain the observed lifetime quenching. Thermal effects are subsequently unlikely to be the cause of the four-fold improvement in laser power observed by Tobben when chopping the pump beam [117].

2. A second possibility is that the large populations maintained in CW operation at both $^4F_{9/2}$ and $^4I_{11/2}$ levels can exchange energy via the $^4F_{9/2} +^4 I_{11/2} \rightarrow$ $^4S_{3/2} +^4 I_{13/2}$ energy-transfer process discussed in section 5.3 and remove energy from the lasing cycle more efficiently in CW than under a quasi-CW regime.

We suggest an explanation for two separate quasi-CW regimes: Long pulses on the order of 10 ms under single pumping as in Többen's case and shorter, 300 μs pulses using DWP, with experimental results given in section 6.4.2. In Többen's case, operating in CW using a single pump exciting directly to the $^4F_{9/2}$ level, the population at the $^4F_{9/2}$ level is clamped at the threshold level. Any additional ions would relax after lasing via the multi-phonon quenched $^4I_{9/2}$ level to the long-lived $^4I_{11/2}$ level. As a consequence, sufficient population densities are present in both the $^4F_{9/2}$ and $^4I_{11/2}$ levels to allow for the $^4F_{9/2} +^4 I_{11/2} \rightarrow ^4S_{3/2} +^4 I_{13/2}$ energy-transfer process discussed in Chapter 5 to depopulate the upper laser level. Moreover, the decay from the $^4I_{11/2}$ level is predominantly by fluorescence, with about a third of the ions relaxing to the $^4I_{13/2}$. This means that effectively almost all of the excited population under CW lasing conditions is bottlenecked at the long lived $^4I_{11/2}$ and $^4I_{13/2}$ levels. This effect would
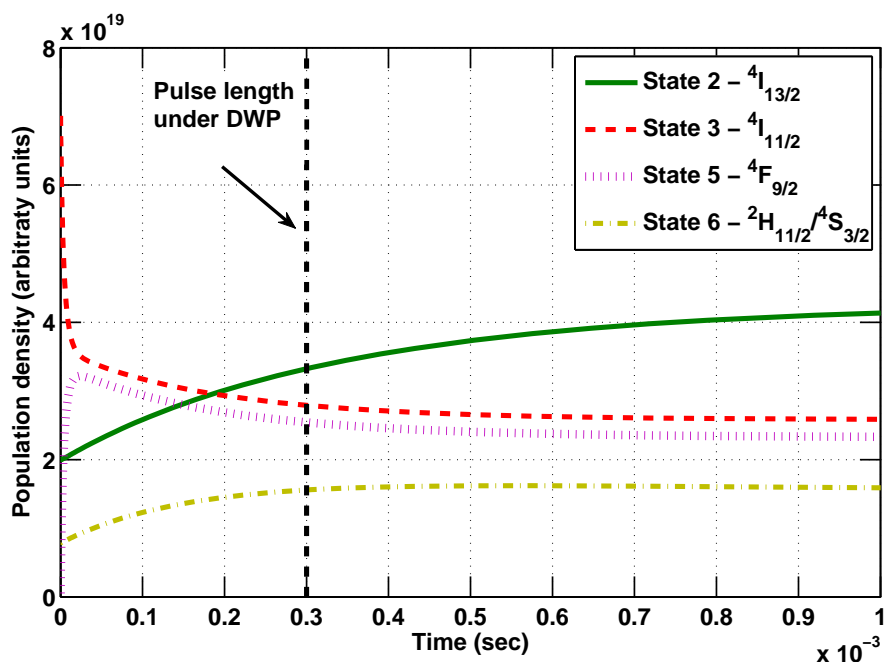
Figure 6.14: Modelled temporal behaviour of ion density with CW 985 nm pump and long 1973 nm pulses below laser threshold. The initial stable population achieved under the CW 985 nm pump changes abruptly when the 1973 nm is incident. The energy of the laser pulse is proportional to the area under the $^4F_{9/2}$ state curve. The energy in the first 300 μs is $\sim 30\%$ larger than after the transient has subsided due to the energy-transfer process subsiding. This model is based on a rate equation model using the equations of section 1.5.4 but without taking lasing into account.

become even more pronounced under high pump power densities causing bleaching of the ground. In that case, most of the ions in the system would end in the $^4I_{11/2}$ and $^4I_{13/2}$ levels and not in the ground state. The large population of these levels would result in a poor slope efficiency because of reduced availability of ions to be pumped from the ground state.

When Többen was chopping the pump with about 8.5 μs long pulses, the dynamics changed. This pulse length is an order of magnitude longer than the lifetime of the $^4F_{9/2}$ level, which would therefore reach steady-state conditions even without lasing. Assuming a 50% duty-cycle (value is not provided in [117]), the time between pulses is about 15% longer than the lifetime of the $^4I_{11/2}$ level and is comparable to the lifetime of the $^4I_{13/2}$ level. This results in the $^4F_{9/2}$ level reaching a similar excitation level as in CW. The population density bottlenecking at the $^4I_{11/2}$ and $^4I_{13/2}$ level was only at about a third of its value at the beginning of the next pump pulse compared to CW conditions, resulting in a much higher population available at the ground state. In addition, the reduced population at the $^4I_{11/2}$ level at the beginning of the next pulse results in a

lower energy-transfer rate. Pumping from the ground was thus more efficient, resulting in increased slope efficiency and higher overall output power at 3.5 μm.

When using DWP in CW, similar population density conditions are reached as the ones described above for the singly pumped case. Laser efficiency is improved because of ions cycling from the $^4I_{11/2}$ level directly to the upper lasing level. Under quasi-CW conditions, with pulses on the order of 300 μs, transients are still dominant. Accumulation of ions which do not participate in the lasing cycle at the $^4I_{13/2}$ level still occurs, although to a lesser extent than in CW. Both $^4F_{9/2}$ and $^4I_{11/2}$ level are sufficiently populated to allow for the energy-transfer process to be effective. The data in section 5.3 suggests a decay constant associated with this energy-transfer process of 300-400 μs for the case of the IR-Photonics fibre. This case is presented in Figure 6.14 showing simulated population densities of the relevant levels based on the simple rate equation model, which was used previously. The initial conditions here are of a CW operating, 985 nm pump at 194 mW of incident power. In the figure, we see that immediately after the 1973 nm pump beam is unblocked, the $^4F_{9/2}$ level population builds-up at the expense of the $^4I_{11/2}$ level population. The maximum level obtained is about 20% higher than the level in steady-state (at about a millisecond). With the initial increase in $^4I_{11/2}$ and $^4F_{9/2}$ levels populations, energy-transfer effects depopulate both levels further until a steady state is reached within the first 300 μs. The model in Figure 6.14 does not take lasing into account, however when operating above threshold the laser pulse energy is proportional to the area under the $^4F_{9/2}$ level curve. The area under the first 300 μs of the $^4F_{9/2}$ level population curve in Figure 6.14 contains about 30% more energy than a later 300 μs time span after transients have subsided. In this case, when using a slow, thermopile-based detector (as is used in our case) would result in a higher peak power reading compared with both pumps operating in CW.

6.4.1   Quasi-CW experimental setup

The experimental setup for quasi-CW operation is very similar to the setup used for the CW mode of operation, as discussed in section 5.3.2. The 985 nm pump is operated continuously, while the 1973 nm TFL beam is chopped using a mechanical chopper at a duty-cycle of 30% with the beam transmitted through the chopper for 300 μsec. This transmission time is equivalent to between two and three lifetimes of the upper lasing level $^4F_{9/2}$ below lasing threshold. The laser power and the residual power through the fibre of both pumps is measured using the wavelength separator, as shown in Figure 6.3. In between the 3.5 μm laser pulse, the resonator lases at 2.75 μm when the 1973 nm beam is blocked. This contributes to the average power reading obtained from the slow thermal detector. Our results take this effect into account by subtracting the 2.75 μm laser power from the reading following the method described in section 6.2.4.

6.4.2   Quasi-CW results summary

A summary of the laser behaviour in quasi-CW with different output couplers is presented in Table 6.3. Figures 6.15 and 6.16 depict the laser's behaviour as a function of incident and absorbed 1973 nm pump power when it is mechanically chopped at a 30% duty-cycle.

Table 6.3: Summary of laser parameters with varying output couplers for 18 cm quasi-CW IR-Photonics fibre. Slope efficiency is relative to the 1973 nm pump peak power with a fixed 985 nm maximum pump power in CW. The peak power value is based on average power measured with a thermal power meter then divided by the chopper duty-cycle and compensated for 2.75 μm lasing.

Output coupler reflectivity (%)	Maximum peak output power (mW)	Maximum initial slope efficiency (%)		Laser threshold relative to 1973 nm pump peak power (mW)
		Incident power	Absorbed power	
80	347	23 ± 2	49 ± 7	161
90	333	23.5 ± 2	57 ± 5	67
95	248	16 ± 2	$24 \pm 4^*$	34

* The 95% in quasi-CW was performed on a different fibre segment than in CW.

We observe an increase in the peak power emitted by the laser compared with the CW case shown in Figures 6.5 and 6.6. The increase varies from 25% in the cases of the 90% and 95% output couplers, to almost 100% increase in the case of the 80% output coupler. There is also a reduction in the 1973 nm threshold peak power compared to the CW case. The slope efficiency remains similar, however, although its linearity is extended to higher peak powers. The abscissa of Figure 6.16 is terminated at 1000 mW because beyond 650 mW of absorbed power, reflected 1973 nm pump from the output coupler is not likely to be completely absorbed in the fibre. The value of 650 mW was found from the data of the quasi-CW laser experiment to be the absorbed power where the change in the slope of the transmitted 1973 nm pump occur. Values close to 650 mW were found consistently for all output couplers used. This power level was determined in a similar manner to the 350 mW level found for the CW case, which is shown in Figure 6.12.

The improvement in performance in quasi-CW compared with CW operation is unlikely to be the result of a reduced thermal load because the expected core temperature rise for CW pumping is less than 10°C (see Appendix E). Such a small temperature rise results in a negligible increase in the multi-phonon rate. A thermal induced effect that cannot
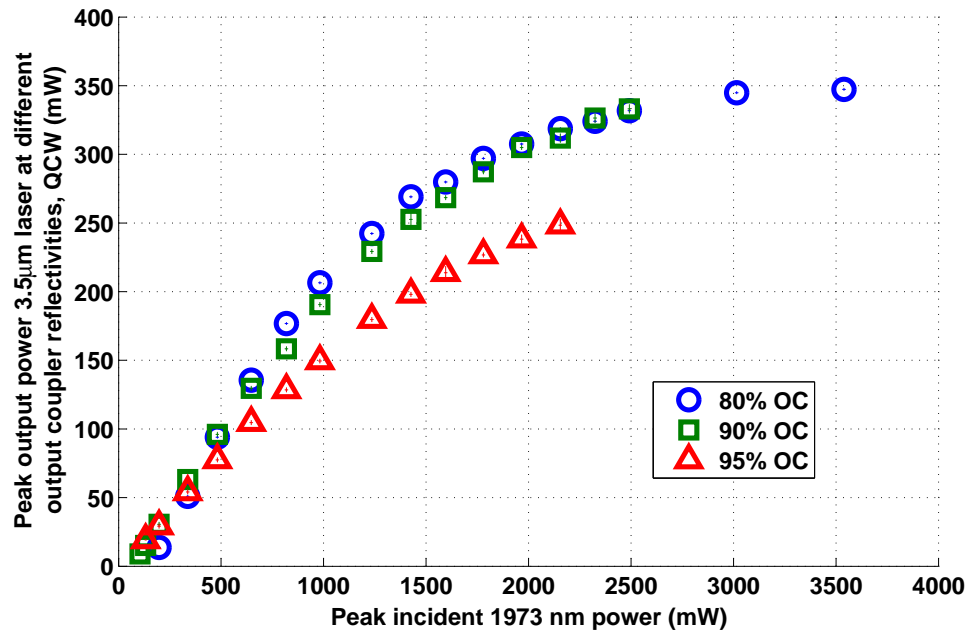
Figure 6.15: Comparison of results for 18 *cm* long, 3.5 *µm* fibre laser with different output couplers in quasi-CW operation as a function of incident 1973 *nm* pump.
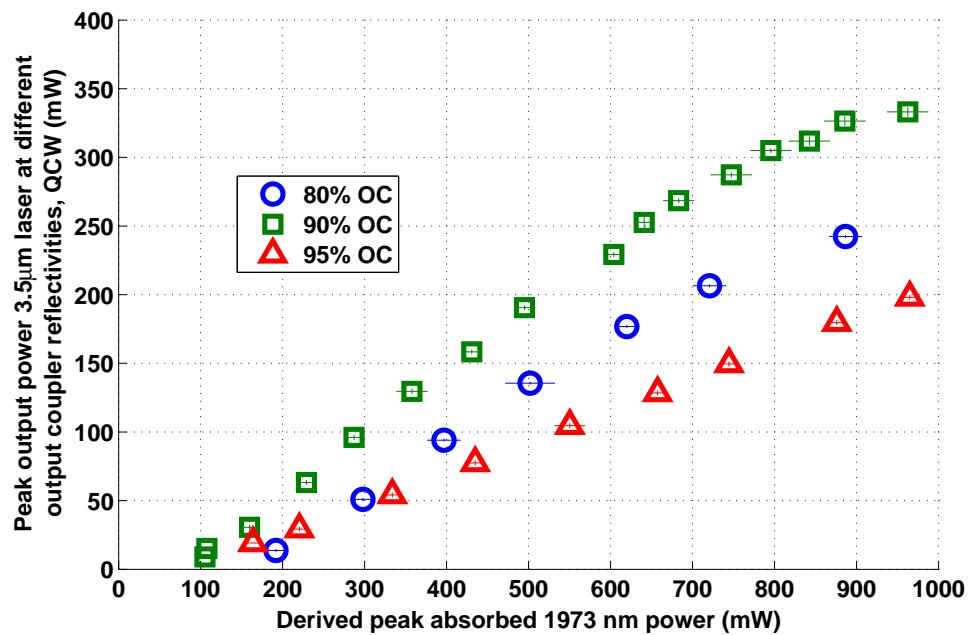
Figure 6.16: Comparison of results of 18 *cm* long, 3.5 *µm* fibre laser with different output couplers in quasi-CW operation as a function of derived absorbed 1973 *nm* pump. The horizontal scale is terminated at 1000 *mW* of absorbed power. This is because our assumption that all the 1973 *nm* power, which is reflected by the output coupler is eventually absorbed in the fibre is unlikely to be true beyond 650 *mW* of absorbed power.

be excluded, however, is the possibility that reduced thermal load on the input fibre tip reduces stresses caused by contact of the fibre endface with the resonator mirror. This is a consequence of the experimentally observed strong sensitivity of the laser power to butt-coupling conditions (as discussed in section 6.3.3).

In all of the results presented so far, the 985 nm pump diode was operating at its maximum CW power in order to obtain the highest laser power at 3.5 μm. This means that the lifetime quenching effect observed in section 5.3 is already fully manifested. Since the lifetime saturation onset with 985 nm pump is relatively early on, it was not expected that turning the 985 nm pump operation from CW to long pulses of 20 ms or longer, which are needed for sufficient $^4I_{11/2}$ population build-up, would make a significant difference in the laser behaviour. This was verified on multiple accounts when operating the 1973 nm in CW while using long pulses with the 985 nm pump. The peak 3.5 μm laser power observed was identical to the CW power with the same 985 nm pump power.

The second possible explanation is that the chopped pump with its 300μs long pulses reduces the energy-transfer process $^4F_{9/2} +^4 I_{11/2} \to {}^4S_{3/2} +^4 I_{13/2}$ by decreasing the temporal overlap between the populations of the $^4F_{9/2}$ and $^4I_{11/2}$ levels. The theoretical discussion at the beginning of section 6.4 and spectroscopic measurements of changes in fluorescence of $^4S_{3/2} +^4 I_{13/2}$ levels have shown that this is a likely explanation when there is no lasing action (see section 5.4). However, additional measurements are required to provide supporting evidence for this hypothesis when lasing. As such, this question remains open.

6.4.3   Laser power saturation and dependency on the 985 nm pump

For essential characterisation of the laser behaviour, we conducted a set of experiments to determine the laser power with varying 985 nm pump. These measurements were conducted in quasi-CW using the 95% output coupler. Similar behaviour to the one portrayed below was observed in CW operation.

In the following experiments, the laser output power was measured with different combinations of 985 nm and 1973 nm pump powers. At every measurement, the 1973 nm pump levels were fixed while the 985 nm pump was varied. For example, the 1973 nm pump would be fixed at an incident level of 0.55 W peak power, while the 985 nm pump varied between 0 mW to 194 mW incident power.

The results of varying the level of the 985 nm pump are presented in Figure 6.17 and show a consistent saturation effect. These results show that the output power is not

a linear function of the incident 985 nm pump power and that increasing the 985 nm pump above a certain level does not significantly increase the output power at a constant 1973 nm.

Despite the apparent differences between the curves of Figure 6.17, there are some similarities between them. Figure 6.18 demonstrates that if we normalise each curve to its maximum power level, we end with all of the curves having a similar shape. This behaviour is consistent with improved absorption of the 1973 nm pump when more ions are present at the $^4I_{11/2}$ level. We suggest that the saturation behaviour represents a similar saturation mechanism for the different power levels.

This assumption of improved 1973 nm pump absorption with increased $^4I_{11/2}$ population receives further support from Figure 6.19. In this figure, we plot the absorption of the 1973 nm pump as a function of absorbed 985 nm using the data from Figure 6.17. Figure 6.19 follows a similar pattern to the one in Figure 6.17 with the exception of its pre-threshold behaviour. The figure shows that prior to reaching threshold at $\sim 120~mW$ of absorbed 1973 nm, there are only small differences in the amount of 1973 nm pump absorbed for different incident power levels. This can be expected because prior to reaching threshold, the population of the $^4I_{11/2}$ level is completely dependent on the relative lifetimes of the Er^{+3} ions levels. Once the threshold is crossed, the increasing rate of stimulated emission depopulates the $^4F_{9/2}$ level, therefore allowing more ions in the $^4I_{11/2}$ level to absorb 1973 nm pump photons.
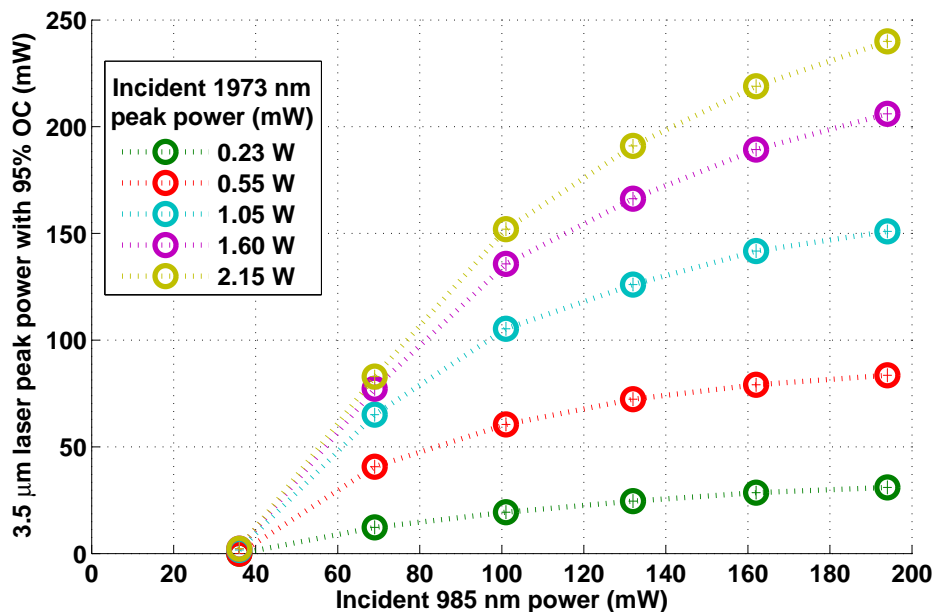
Figure 6.17: Dependency of laser power on 985 nm pump. 18 cm long IR-Photonics fibre with 95% output coupler. 1973 nm pump is operating in quasi-CW.
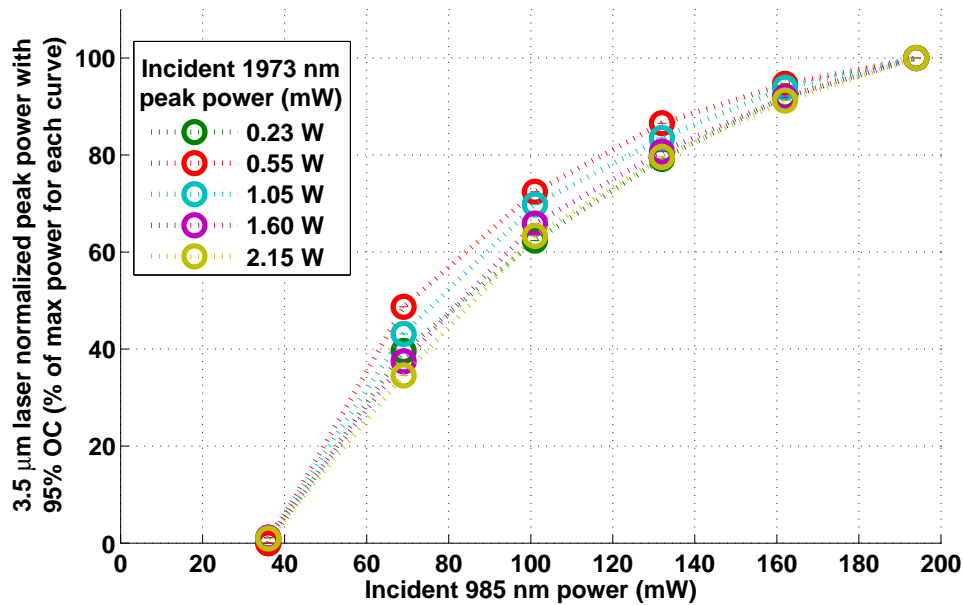
Figure 6.18: Dependency of laser power on 985 nm pump with each curve normalised to its maximum. 18 cm long IR-Photonics fibre with 95% output coupler. 1973 nm pump operating in quasi-CW.
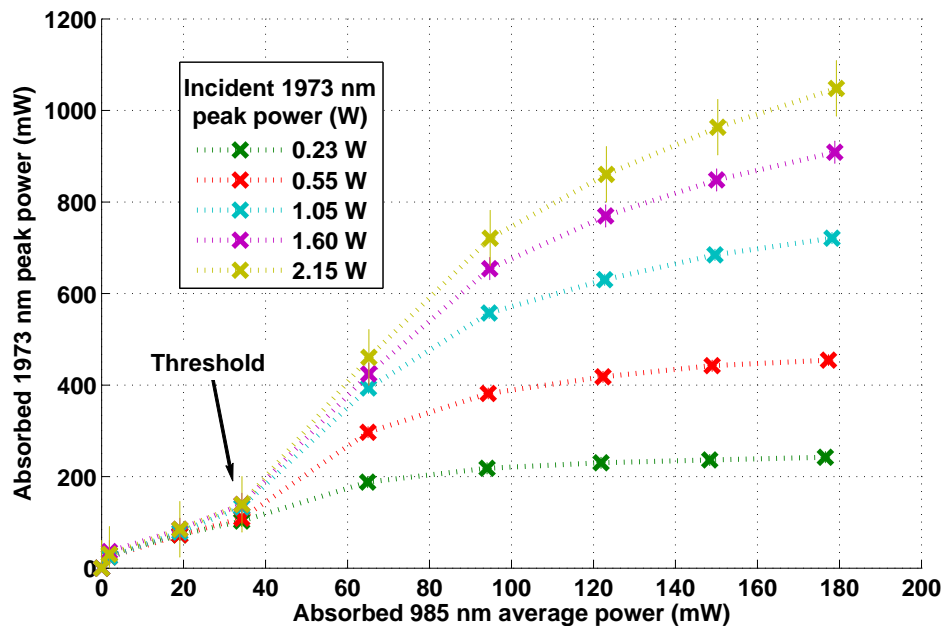
Figure 6.19: Dependency of absorbed 1973 nm pump on absorbed 985 nm pump. 18 cm long IR-Photonics fibre with 95% output coupler. 1973 nm pump operating in quasi-CW. Laser threshold is reached at about 35 mW of absorbed 985 nm pump.

Figure 6.19 also demonstrates that at the lower levels of incident 1973 nm pump, the absorbed 1973 nm power and hence the laser power are limited by the 1973 nm pump. Once higher incident 1973 nm pump is used, more of it is absorbed with a corresponding increase in the maximum laser power obtained. However, this increase comes at the expense of a reduction in the fraction of the 1973 nm pump absorbed. This reduction is the result of reduced absorption due to bleaching of the 1973 nm pump. The bleaching occurs since the $^4I_{11/2}$ population is depleted and the $^4I_{11/2} \rightarrow {^4F_{9/2}}$ transition begins to reach transparency. Observing the incident and absorbed 1973 nm power taken from Figures 6.15 and 6.16, this becomes evident, for example, in the case of the 90% OC results. When the laser operates with 100 mW of peak output power, the absorbed 1973 nm pump corresponds to 60% of the incident power. As the laser power increases, this fraction decreases to 50% and 40% at 200 mW and 300 mW of laser power, respectively.

The consistent improvement in laser power demonstrated with increasing both 985 nm and 1973 nm pump powers suggests that more 985 nm pump power would increase the laser power. This would be the result of an increase in the population of the $^4I_{11/2}$ level and in cases where the 1973 nm is the limiting factor, higher laser power is likely to be achieved. Future work on a complete numerical model of the DWP system using higher pump power could provide additional data on the expected behaviour. The system efficiency is currently limited by the brightness of available 985 nm sources. New single-mode sources that are brighter have recently become available and should enable an increase in the laser power. In addition, polarisation combining and pumping from both sides of the cavity should allow for a significant increase in the population of the $^4I_{11/2}$ level along the fibre.

Figures 6.18 and 6.19 hint that the threshold power for the 985 nm pump power varies very little between the different 1973 nm power levels. A closer look at the laser threshold behaviour as a function of the absorbed 1973 nm pump in the forward direction, provided in Figure 6.20, confirms that the threshold does not vary. In this figure, we plot all the data from Figures 6.17-6.19 as a function of absorbed 1973 nm pump that is travelling in the forward direction, prior to its reflection by the output coupler. Each colour represents measurements taken with a fixed 1973 nm pump level, while each symbol is indicative of a different 985 nm incident pump level. With the laser system operating in quasi-CW while using 95% reflectivity output coupler, lasing starts once 120 mW of 1973 nm pump is absorbed. The threshold power does not seem to change under the different combinations of incident 985 nm and 1973 nm pump powers. This is because a certain population is required in the upper lasing level $^4F_{9/2}$ to achieve an inversion level that overcomes the internal material losses and the output coupling fraction. This inversion can be achieved with low 985 nm pump and high 1973 nm pump or vice versa, as long as
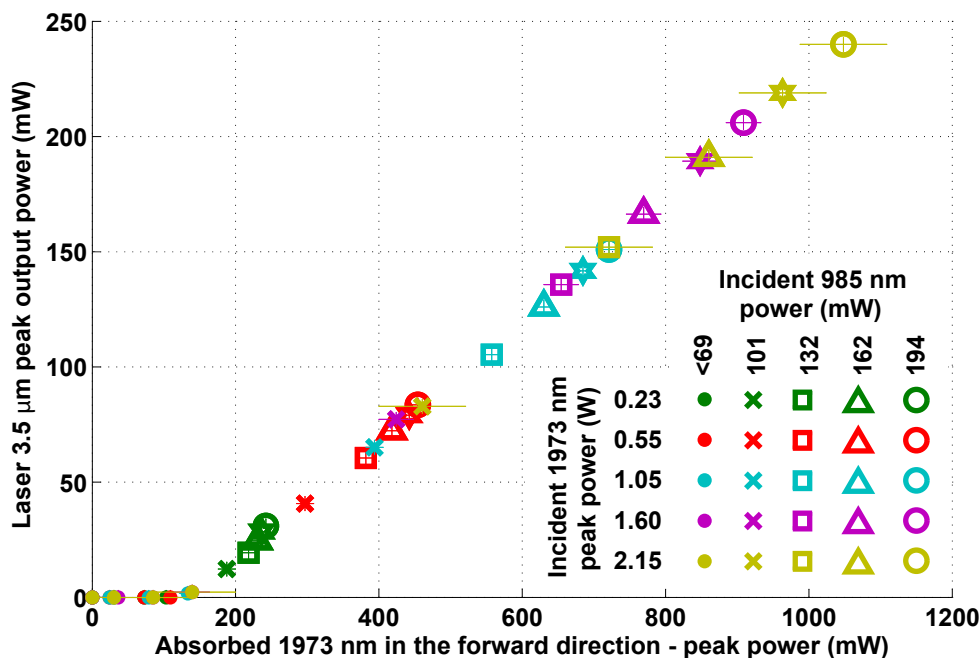
Figure 6.20: Dependency of laser power on absorbed 1973 nm pump in the forward direction with respect to incident 985 nm pump. Data points of the same colour represent data taken with the same fixed 1973 nm incident power while varying the incident 985 nm pump power. The shape of the data point corresponds to the incident 985 nm power at that point. The absorbed 1973 nm power calculated in this figure is in the forward direction only and does not include absorption of the reflected pump due to output coupler reflectivity, unlike the data in Figures 6.6 and 6.16. This is because we could not measure the absorption of the backwards propagating pump and the large differences in 1973 nm absorption when varying 985 nm pump levels would not allow assuming that all of the backwards propagating pump is absorbed. Data taken with 18 cm long IR-Photonics fibre with 95% output coupler. 985 nm pump operating in CW while 1973 nm pump operating in quasi-CW.

120 mW of 1973 nm are absorbed, regardless of which pump is dominant. This result is consistent with our understanding that the purpose of 985 nm is to populate the virtual ground state and compensate for loss of ions from this state.

Figure 6.20 shows that the 3.5 μm power is linear with respect to the absorbed 1973 nm pump in the forward direction. This is evidence of the laser power saturation being the result of bleaching of the 1973 nm pump because of insufficient population at the $^4I_{11/2}$ level. The shape of the curve is true for all power levels, unlike in Figures 6.6 and 6.16. This is because the derivation of the absorbed 1973 nm pump power in the forward direction is independent of the assumption that all reflected power is absorbed, which is only valid up to 650 mW of total (forward and backward propagating) 1973 nm pump, as discussed previously.

To conclude, it appears that the mechanism creating the saturation behaviour is the interplay of populating the virtual ground state $^4I_{11/2}$ by ground-state absorption together

with excited-state absorption and stimulated emission on the $^4I_{11/2} \rightarrow {}^4F_{9/2}$ transition. When a large population of ions is created at the $^4F_{9/2}$ level, additional 1973 nm pump power cannot be absorbed effectively while it stimulates back transfer to $^4I_{11/2}$ from $^4F_{9/2}$. The results shown in Figures 6.18-6.20 indicate that the 1973 nm absorption is the limiting factor to the laser output power. Increasing the absorption of the 1973 nm pump requires increasing the 985 nm pump power as well, which would necessitate brighter 985 nm diodes for the current IR-Photonics fibre used. Although we obtained some understanding of the dependency of the 3.5 μm laser system on pump condition, there is much more to explore. The full answer to the saturation question would likely require a full numerical analysis, which is planned for future work.

6.5   Additional laser attributes

In addition to the power and efficiency examined in the previous sections, other attributes of the laser behaviour were investigated. These included power stability, beam quality and spectral content, all of which are presented below.

6.5.1   Power stability

The stability of the laser output power is evaluated for the 18 cm long fibre laser using the 90% output coupler (see Figure 6.21). The laser power is measured using the wavelength separator by recording the output of the Thorlabs S302C thermopile power meter head at a rate of 10 Hz. In a measurement lasting 15 minutes, the laser maintained a constant output power of slightly above 100 mW (about 40% of the laser's saturation power) with 0.37% standard deviation. Degradation is observed in other, shorter measurements when operating close to the laser's maximum power with power stability of ±3% often encountered. A slow drift is often present on the order of 5 mW per minute, which is probably related to a slight misalignment due to thermal drift of the fibre tip at the input end. The laser power can change abruptly when the optical table is bumped, often resulting in a drastic loss of power and even the destruction of the fibre input side.

The power stability observed with the 90%, 95% and 99.3% output couplers under normal operating conditions is not maintained when operating with the 80% output coupler. Power fluctuations of 1% − 2% are common while ±10% − 15% are observed occasionally with instability of the absorbed 1973 nm reading. Those fluctuations are accompanied by significant spectral broadening of the output, which is possibly the result of constant mode hopping (see section 6.5.2 and Figure 6.25).
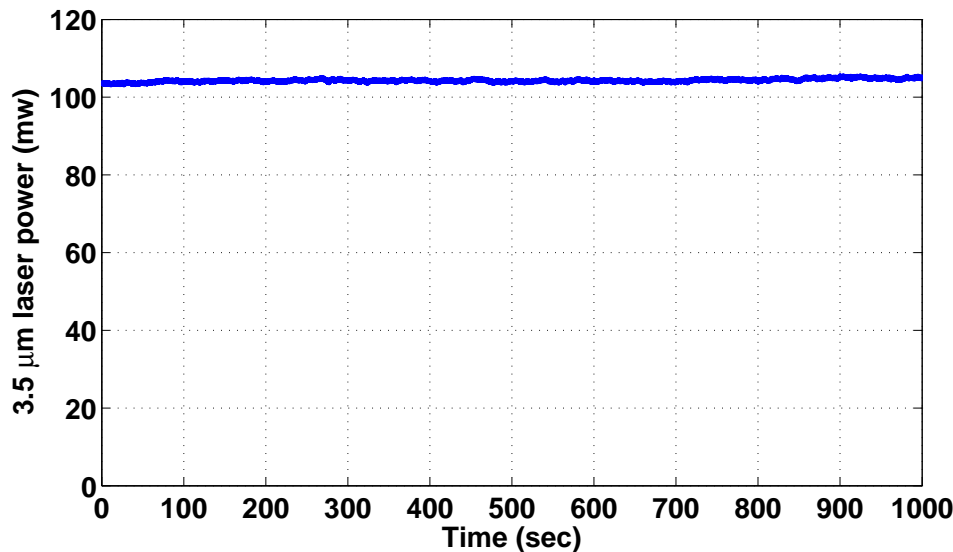
Figure 6.21: Laser power stability with 90% output coupler. Mean output power 104.3 mW with ± 0.37 mW standard deviation.

These power fluctuations can be attributed to power fluctuations in the 1973 nm pump. The pump fluctuations are caused by strong feedback due to the high reflectivity at 1973 nm (55%) of the 80% output coupler (see discussion in section 6.3.3, page 167). Such high reflectivity at 1973 nm strongly increases back propagating 1973 nm pump into the TFL (even when the 3.5 μm laser is below threshold or with the 985 nm pump turned off), resulting in instability and mode-hopping.

The instability could be mitigated by adding an isolator after the 1973 nm pump. Other output couplers which exhibit lower reflectivity at the 1973 nm pump demonstrate similar power fluctuations only at much higher 1973 nm incident pump power. In those cases, the 3.5 μm laser power is already saturated.

6.5.2 Laser spectral content

Figure 6.22 shows a typical spectrum of the laser output together with a measured fluorescence spectrum of the $^4F_{9/2} \rightarrow ^4I_{9/2}$ band transition. The broadband emission is collected from the IR-Photonics fibre while being double-pumped, but without resonator mirrors.

Once resonator mirrors are in place, up to three laser lines at 3.472 μm, 3.538 μm and 3.604 μm are observed. To the best of our knowledge, the 3.604 μm line is the longest rare-earth doped fibre laser emission at room temperature demonstrated to date. At
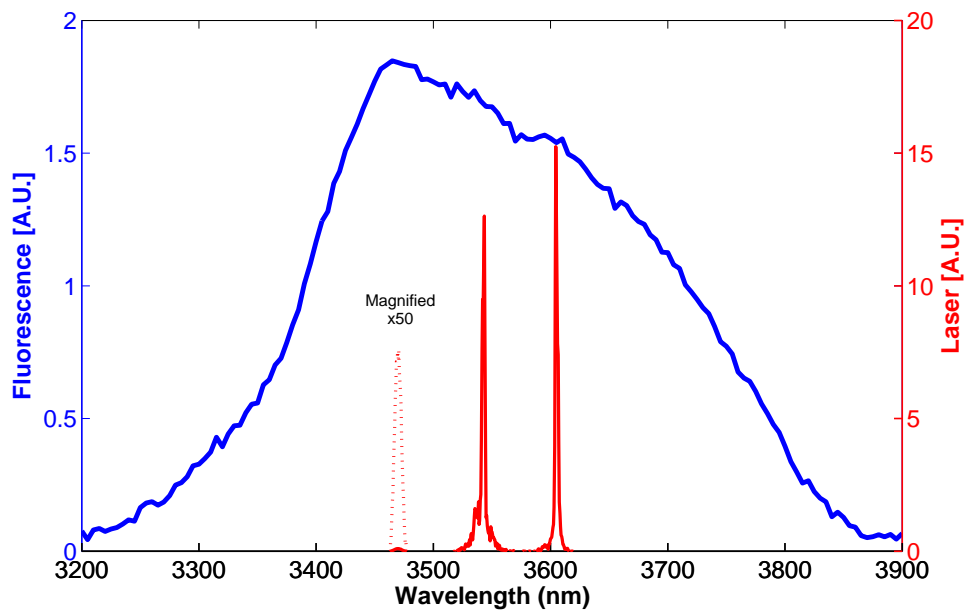
Figure 6.22: Typical spectra of fluorescence and laser emissions with 90% output coupler. The shortest laser line at 3.472 μm is magnified 50 times. Laser is operating in quasi-CW with 180 mW peak power.

the lowest 1973 nm pump power, the laser operates on the shortest line and progresses to the longest one when the 1973 nm pump power is highest. When the pump is in the mid-range, all three lines can appear at the same time with their relative intensities depending on the pump power. A typical behaviour of the relative power distribution between the laser lines as a function of 1973 nm power is shown in Figure 6.23. This figure shows a typical case, although significant differences can exist between different incarnations of the fibre laser. Those differences are often the result of different output coupler butting conditions.

The exact wavelength of each laser line can vary slightly, up to $\pm 5nm$ with different pumping levels. Slight variations are observed when using sections of fibre from different locations along the fibre spool. Modifying the HR and output coupler mirrors butting conditions can also have an effect. It is worth noting that the 3.604 μm line is not always present. This is especially common at low output power, though the existence of the 3.604 μm line seems to depend significantly on the output coupler mirror's butting condition. Even at low output power, it is possible to manually adjust the output coupler butting condition until the 3.604 μm line appears.

The red shifting of the wavelength of the laser lines is likely due to the increased population of the lower lasing level. The shift can be explained by considering the population of the lower Stark sub-levels of the lower lasing level $^4I_{9/2}$. Near threshold, all the Stark
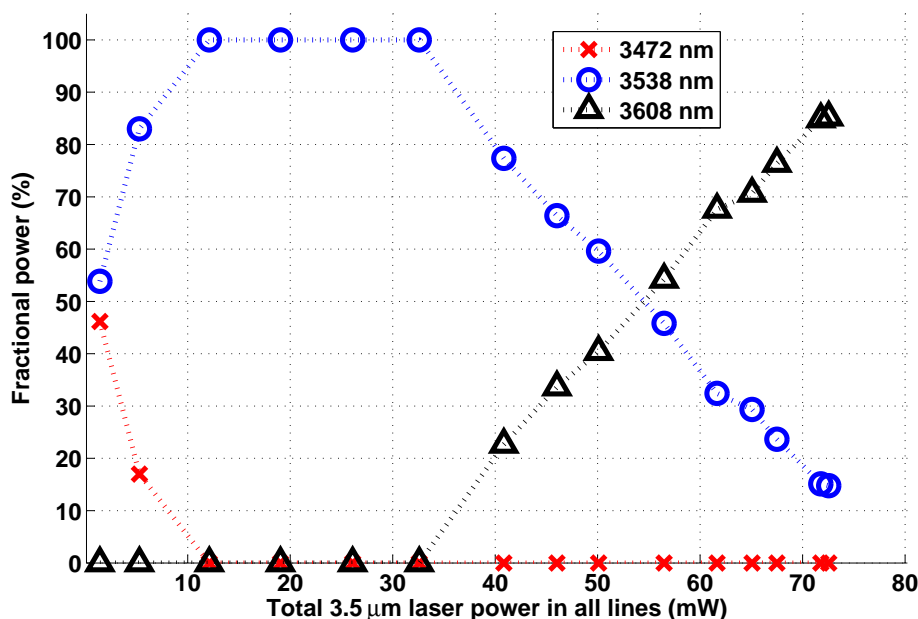
Figure 6.23: Lasing lines' relative intensity as a function of laser power - HR mirror. Each curve shows the fraction of power at a certain laser line with respect to the total laser power. The example shown is for 18 cm long fibre with an HR mirror as an output coupler.

sub-levels of the lower lasing level $^4I_{9/2}$ are almost empty. Therefore, lasing occurs at "line centre," between the bottom Stark sub-levels of both manifolds, which is on the shortest line with the highest emission cross-section. As soon as a population starts to build in the lower lasing level, the lowest sub-levels start to fill up. This reduces the inversion of the laser transition, particularly at shorter wavelengths. Hence, the laser will shift to a longer wavelength, associated with a transition to a higher Stark sub-level of the lower laser level manifold, which has a lower cross-section but higher gain at that stage. This behaviour is similar in nature to the behaviour observed on the 2.75 μm transition in Er:ZBLAN fibre lasers [107].

Additional stable features around the laser lines can be resolved when we operate the spectrometer at its resolution limit of 0.1 nm using 10 μm wide slits (see Figure 6.24). In order to get a clear signal under these conditions, it is important to ensure the focusing off-axis parabola is properly matched to the acceptance cone of the spectrometer and is well aligned. Similar features to the ones seen in Figure 6.24 have been observed at the other laser lines and while using other output couplers (except the 80% output coupler, see below). Further investigations in which we eliminated elements one-by-one along the optical path suggested that the features originate from the laser itself and are not the result of etalon effects along the path to the InSb detector. The 1.5 nm spaced features (equivalent to 36 GHz at 3.535 μm) are too far apart to be longitudinal laser

modes, which are expected to have a free-spectral range of 566 MHz for the 18 cm long
resonator. A similar etalon effect at this wavelength range generated by two parallel
surfaces would have required a separation of about 2 mm. This therefore excludes the
air gaps between the fibre tips and resonator mirrors (estimated to be on the order
of a few microns) from being the source of the fringes. The depth of the modulation
and the detector specification preclude the possibility of etalon effects from the InSb
wedged detector window as well. Thus the nature of these spectroscopic features remains
unresolved.
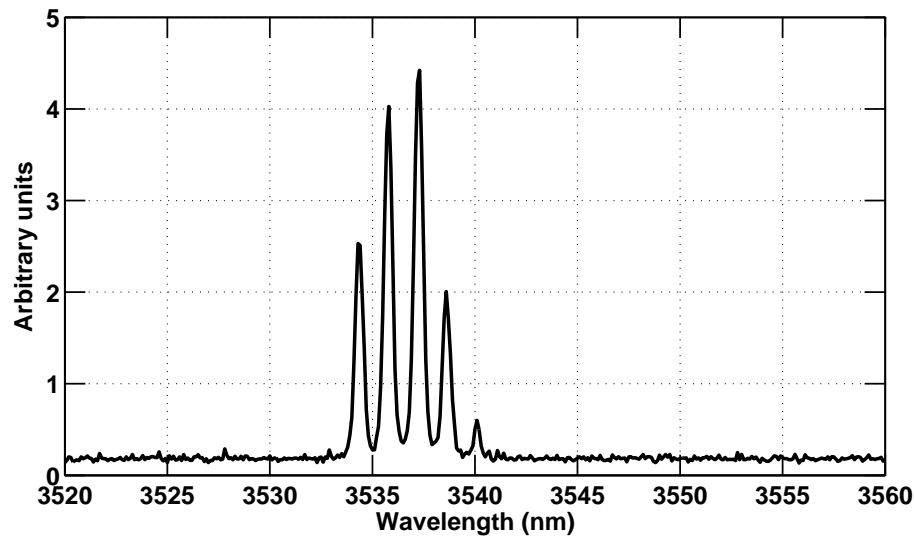
Figure 6.24: High-resolution spectrum of lasing line using 90% output coupler. Features
with 1.5 nm spacing are observed, the origin of which is unclear. Laser operating at
170 mW, spectrometer resolution is 0.1 nm.

Operating with the 80% output coupler features very significant line broadening as shown
in Figure 6.25. This broadening was not present using any other output coupler with a
lower reflectivity at 1973 nm. We therefore suggest that the broadening is the result of
significant instability in the output power of the 1973 nm pump which results in strong
mode-hopping behaviour of the 3.5 μm laser. The instability of the 1973 nm pump is
due to substantial feedback effect at 1973 nm from the 80% output coupler mirror, as
discussed in section 6.3.3. In the future, this feedback could be avoided by adding an
optical isolator along the 1973 nm pump path.

The multi-line operation is to be expected of a glass host where the dopant ions do not
occupy exact lattice locations, resulting in inhomogeneous broadening behaviour and
wider emission lines. However, the relatively high efficiency demonstrated by this laser
and the existence of multiple lines covering 130 nm suggest a degree of homogeneity.
Többen also observed different 3.5 μm lines operating at the same time [117, 118] and
attributed their appearance to the splitting of the Stark levels combined with local
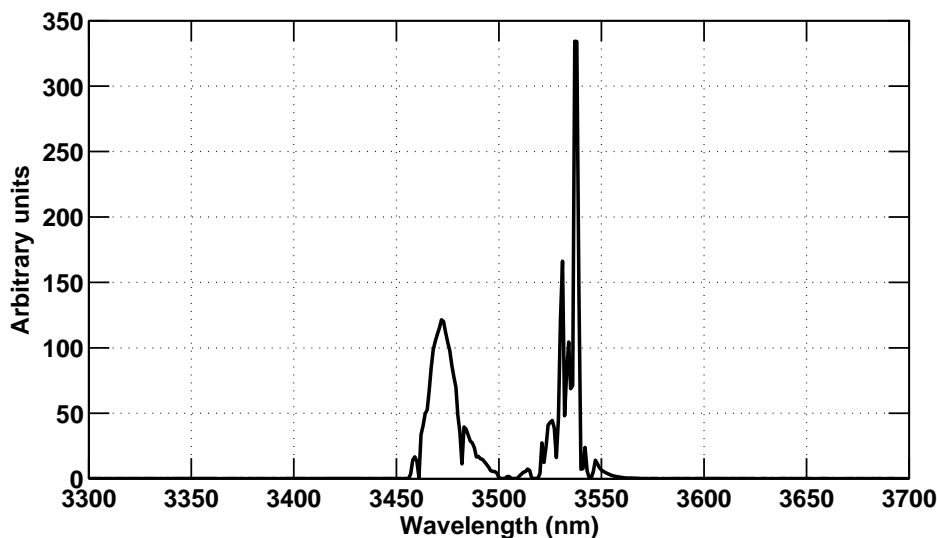
Figure 6.25: Typical spectrum of the laser when operating with 80% output coupler. Note the wide lasing lines, which are probably caused by strong instability created by the significant fluctuations of the 1973 nm pump affected by feedback. Laser operating at 140 mW, spectrometer resolution is 1 nm.

variation in the electric field at different ion sites. A great deal of work has been put into investigating similar inhomogeneous broadening behaviour in ZBLAN and silica based fibre lasers. For example, Bigot et al. [202] and Jarabo et al. [203] showed that dopant ions can have different coordination numbers (essentially the number of the closest neighbours) in the glass matrix which cause different energy-transfer interactions and thus enable lasing at different wavelengths. Guy et al. [204] and Srinivasan et al. [88] examined the effects of ion clustering that can result in separate populations competing (and cooperating), resulting in multi-line operation and change in the peak of fluorescence emission on the order of 100 cm^{-1}, which is similar to the separation observed in our case. Changes in lasing wavelength in a 2.75 μm, Er^{3+}:ZBLAN fibre laser were found experimentally and later reproduced numerically by Gorjan et al. [205] under the assumption of competing populations with slightly different energy levels. In their work, they showed that multiple laser lines spanning about 30 nm on the 2.75 μm transition are present at the same time and constantly compete. Gorjan et al. were able to obtain similar dynamics to their measured result using a rate equation model. Their model considered two sets of Er^{3+} ion families with slightly different energy levels that compete for pump absorption and interact via energy-transfer processes.

Table 6.4 presents the Boltzmann factors associated with the Stark splitting of the $^4I_{9/2}$ and $^4F_{9/2}$ levels. The calculated values are based on Stark level energies determined by Huang et al. in Er^{3+}:ZBLAN glass under cryogenic conditions. The width of all levels is significant and is the result of the variation in the crystal field between different ion sites

Table 6.4: Stark splitting and Boltzmann factors of the $^4I_{9/2}$ and $^4F_{9/2}$ levels. Data presented is based on low-temperature measurement in ZBLAN glass by Huang et al. [188]. All Stark levels in the $^4I_{9/2}$ and $^4F_{9/2}$ have the same degeneracy. The assignment order of the stark levels is taken from [206]. The Boltzmann factors are necessary for calculating the gain and stimulated emission rates in a future numerical analysis.

Stark level	Energy (cm^{-1})	Width of level (cm^{-1})	Boltzmann factor
Stark splitting of $^4I_{9/2}$			
9/2	12413	4	0.328
3/2	12472	35	0.247
7/2	12538	40	0.179
5/2	12604	73	0.131
1/2	12630	99	0.115
Stark splitting of $^4F_{9/2}$			
9/2	15271	26	0.287
3/2	15301	44	0.249
1/2	15361	47	0.186
7/2	15398	8	0.156
5/2	15449	62	0.122

[188]. We can estimate the Stark levels between which the laser transition occurs using the information in Table 6.4. By comparing the energy of the laser transitions with all possible permutations of the energy gap between initial and final Stark levels, the relevant transitions between the appropriate Stark levels are found. The combined Boltzmann factors of the relevant level for each laser transition are presented in Table 6.5 on page 188. The spreading of the Stark levels in glass can allow for a few Stark levels to interact with the laser field. It is therefore somewhat difficult to determine the exact Stark levels involved in each laser transition and the results in Table 6.5 should, therefore, be taken as a guide only. The width of the individual Stark levels and their interactions can explain the wideband fluorescence curve shown in Figure 6.22. Decay from the topmost Stark level of the upper laser $^4F_{9/2}$ to the lowest Stark level in the lower laser level $^4I_{9/2}$ would result in emission at 3298 nm. Transition from the lowest Stark level of the upper manifold to the highest Stark level at the bottom manifold results in fluorescence at 3786 nm. The width of the Stark levels and their overlap provides an avenue for fluorescing at any wavelength in between these two (and slightly beyond because of the width of the topmost and lowest levels). Figure 6.26 depicts the presumed transitions between the Stark split manifolds in ZBLAN glass associated with the wavelengths observed in our 3.5 μm laser.

Earlier in this section, we discussed the shifting emission of the 3.5 μm laser to longer wavelength lines. This shift is possibly the result of an increased population at the lower

Table 6.5: Boltzmann factors of the 3.5 μm laser transitions. Calculations are based on data from Huang et al. [188]. In this table we consider levels to be involved in a laser transition if the energy gap between them is within $\pm 15\ cm^{-1}$ of the energy of the observed laser transition.

Laser transition wavelength (nm)	Transition energy (cm^{-1})	Initial Stark levels in $^4F_{9/2}$	Final Stark levels in $^4I_{9/2}$	Boltzmann factors	
				lower b_l	upper b_u
3472	2886	3/2, 1/2	9/2, 3/2	0.58	0.43
3538	2832	3/2, 1/2	3/2, 7/2	0.42	0.43
3604	2780	5/2	5/2, 1/2	0.25	0.16

lasing level which causes the laser transition to be terminated at a higher Stark level, thus shifting the laser emission to a longer wavelength. Small shifts of $\pm 5nm$ were also observed by all laser lines with higher pump power. The mechanism causing these shifts is not clear. We suggest that it is related to the slight heating of the fibre with increased pumping. Such heating causes small changes in the Boltzmann distribution between the different Stark levels, each having a width of a few tens of cm^{-1} [188]. These small changes might eventually result in small shifts of the observed emission wavelength.

Although we do not yet completely understand the behaviour of the laser lines, the broad
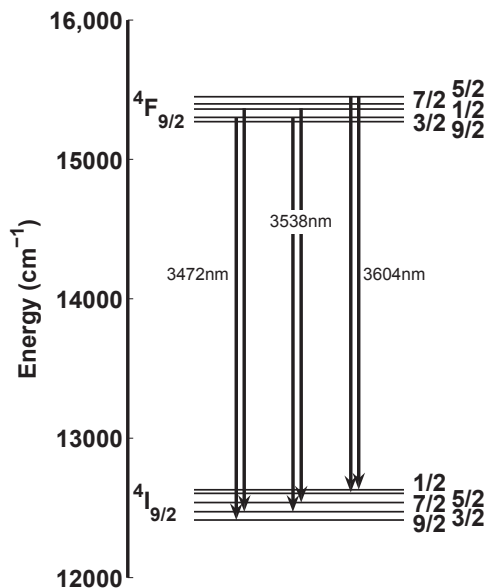
Figure 6.26: Stark splitting in ZBLAN and relevant laser transitions. The arrows connect the two Stark levels which correspond to the appropriate energy difference associated with the lasing line wavelengths. Data based on the work of Huang [188].

fluorescence band suggests that the output wavelength can be tuned over a very wide wavelength range, covering an important part of the mid-infrared spectrum where many organic molecules have absorption lines [207]. The work of Többen in [118] demonstrated the feasibility of tuning the emission wavelength of a 3.5 μm fibre laser. In that work, Többen showed continuous tuning of a laser line over 30 nm using changes in temperature from 5°C to 41°C. An additional line which was also continuously tuned was present in part of the tuning range and was the only one present when the temperature was tuned up to 61°C. No wavelength selecting elements were used to limit the emission to a single line. This suggests that wavelength tuning is possible and that wavelength selection elements are probably required for single line operation.

6.5.3   Beam quality

The laser output beam seen in Figure 6.27 is of near Gaussian nature, as can be expected from a single mode fibre. The laser also exhibits a reasonably good beam quality with an upper limit on the M^2 factor of better than 1.34 (see Figure 6.28). The M^2 factor, which is a measure of the deviation in the beam quality from a perfect TEM$_{00}$ Gaussian beam, was fitted using the curve fitting tool in Matlab®. Initially the beam waist size ω_0 and the beam divergence half angle θ, measured along the optical axis relative to an arbitrary initial location z_0, were fitted to a parabola according to [208]

$$\omega^2(z) = \omega_0^2 + \theta^2(z - z_0)^2. \tag{6.22}$$

Once both are known, the M^2 factor is calculated from

$$M^2 = \frac{\omega_0 \theta \pi}{\lambda}, \tag{6.23}$$

with λ being the wavelength of the laser. A perfect TEM$_{00}$ beam would have an M^2 of one because it divergence is $\theta = \lambda/\pi\omega_0$. The exact number could not be resolved sufficiently well with the Pyrocam used for beam quality measurements because its pixels are 100 μm wide and thus too large to resolve the beam waist created by the longest focal length optics available to us.

A mid-IR zoom lens or telescope were not available, thus to improve the quality of the measurement, we constructed a beam-reducer to allow an increased waist size after focusing. This ensures the focused spot size is sufficiently large to be registered properly with the Pyrocam. Although this somewhat improves the ability of the Pyrocam to resolve the beam, it does not completely solve the low resolution issue and thus the above mentioned number of $M^2 = 1.3$ might improve using better diagnostic methods
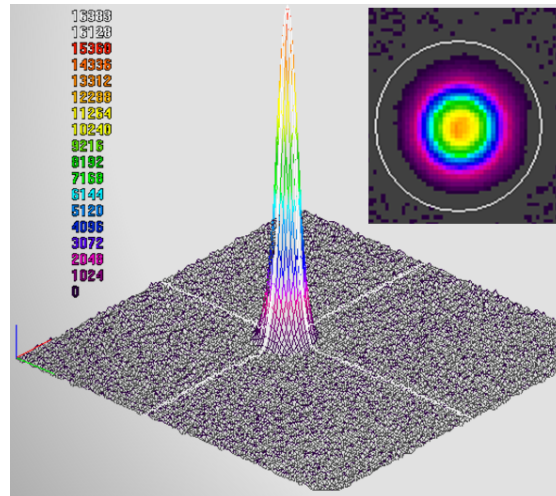
Figure 6.27: 3.5 μm laser beam shape.

using a higher resolution beam profiler or a method based on a knife edge measurement. The improved resolution uncovers that the observed focused spot size does not follow a perfect parabolic pattern near the expected beam waist, as seen in Figure 6.28.
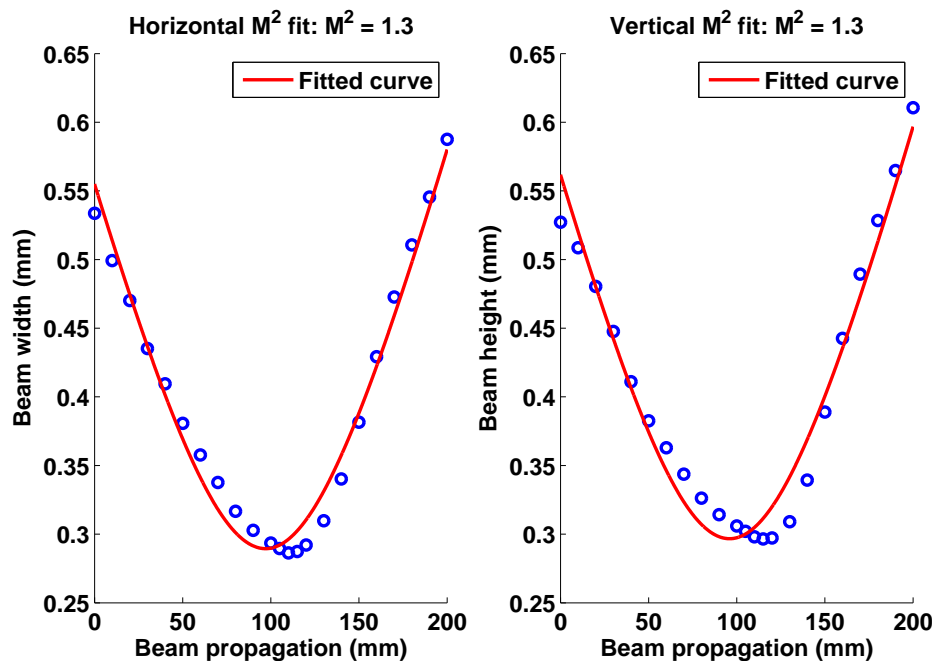
Figure 6.28: 3.5 μm laser beam M^2 measurement. Laser output power during measurement is 50 mW.

We suspect that the biased, non-parabolic behaviour near the waist of the focused beam is the result of comma-like aberrations. These aberrations could be created by the off-axis parabolic mirror used to collimate the laser output beam. The current mechanical nature of the laser setup did not permit changing the mirror with an aspheric lens, thus our hypothesis could not be confirmed experimentally.

6.6 DWP laser summary

In this chapter, we demonstrated the ability of the DWP technique to increase significantly the output power generated at 3.5 μm by an erbium doped fibre laser. This Er^{3+}:ZBLAN fibre laser achieved in CW 260 mW with 26% slope efficiency relative to the second pump, and 16% optical-to-optical efficiency including both pumps. These results are an order of magnitude improvement in power and efficiency compared with the previous state of the art. To the best of our knowledge, at 3604 nm, this laser operates at the longest wavelength observed from a room-temperature rare-earth-doped fibre laser.

Laser performance in CW has been characterised using an 18 cm long butt-coupled resonators with output couplers ranging from 80% to 99.3%. From these results and using a Findlay-Clay analysis, we were able to find the internal losses in the fibre, small signal gain and emission cross-section at 3.5 μm. The results of the latter agree well within the uncertainty to the cross-section value derived using the Fuchtbauer-Ladenburg method, which is found in section 2.5.

We explored the behaviour of the laser under long-pulse regime, with the second pump mechanically chopped. With the same configurations as in CW, we observed up to 347 mW of peak power. This was a significant improvement in the peak output power compared with the CW case. Similar improvements were found with all output couplers tested.

We investigated the dependency of the laser power on the 985 nm pump power and found evidence that the available 985 nm power is currently the limiting factor in obtaining a higher laser power. In future work we would like to test this hypothesis by using a 985 nm source which is brighter than the ones currently available to us.

Additional laser attributes were investigated, including beam quality, power stability and spectral behaviour. The combination of the very short lower lasing level lifetime and the extremely broad nature of this transition leads to the promise of a wavelength tuning range within the 3.2-3.9 μm.

The possible tuning range of a 3.5 μm Er^{3+}:ZBLAN fibre laser is of interest because as seen in Figure 1.1, important carbohydrate gasses have strong absorption lines close to the short-wavelength edge of the fluorescence curve presented in Figure 6.22. In Figure 6.29 we present fluorescence at 3.5 μm band obtained from the literature and throughout this work. The figure shows that there is significant variability in the short and long edges of the fluorescence when using different fibre varieties. The origin of this variability is not clear, although Figure 6.29 suggests that the short edge is dependent
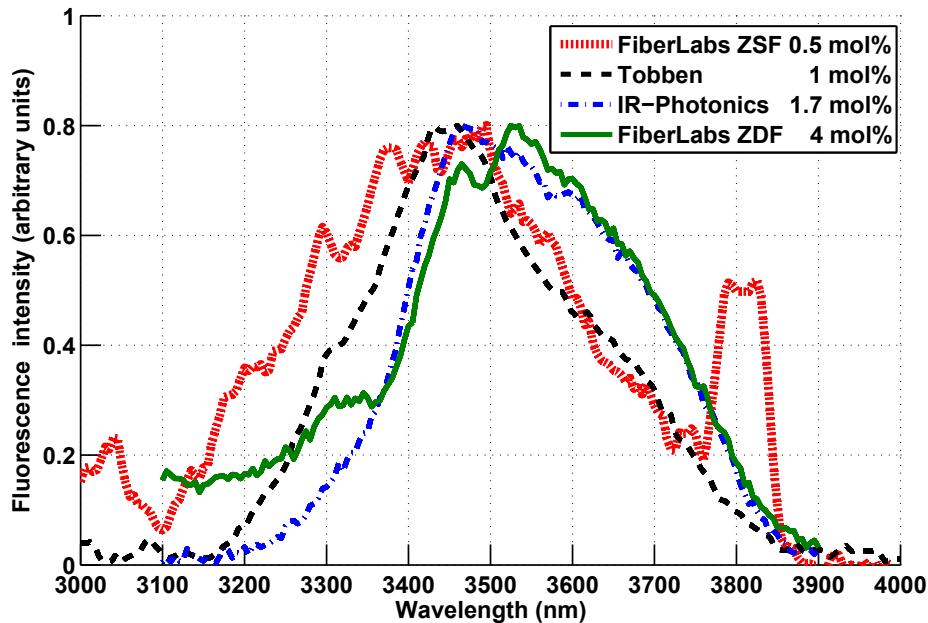
Figure 6.29: Comparison of 3.5 μm fluorescence emitted by different fibre varieties. All fluorescence curves were normalised to the same maximum intensity. The distinctive feature at 3820 nm in the FiberLabs ZSF curve is the result of stray light from the 1909 nm pump source. Er^{3+} doping density of the different fibres: FiberLabs ZSF - 0.5 $mol\%$, Többen - 1 $mol\%$, IR-Photonics - 1.7 $mol\%$, FiberLabs ZDF - 4 $mol\%$. The FiberLabs ZDF fibre was double-clad, while all other fibres were single clad. Although the different curves were collected from fibres with different lengths, this should not have affected the fluorescence width because the re-absorption by the sparsely populated $^4I_{9/2}$ level was negligible.

on the doping concentration. Future understanding of the cause of this difference and its control are essential for spectroscopy applications, which require operating closer to the C-H bond fundamental absorption line at 3.34 μm.

The relatively long lifetime of the $^4F_{9/2}$ level suggests that this laser can achieve high peak power. The demonstration of wavelength tunability and short-pulse operation are the subject of planned future work, which is described together with a summary of this thesis in the next chapter.

Chapter 7

Conclusions

7.1 Highlights

$\mathbf{I}$N this thesis, we report the demonstration of a mid-infrared (MIR) fibre laser operating around 3.5 μm. This laser achieved all the requirements originally set in this project:

- Laser operation around 3.5 μm from an Er^{3+}:ZBLAN fibre

- Highly effective dual-wavelength pumping (DWP) method for obtaining significant power and efficient MIR operation in fibre lasers.

- Significantly more power than 10 mW and good efficiency. Over 260 mW at 3.6 μm were obtained with an overall optical-to-optical efficiency of 15.9% and a maximum slope efficiency of 27.5% relative to incident 1973 nm pump.

This work is only the beginning of research efforts to improve our understanding of the DWP system and its capabilities, namely achieving higher output powers, obtaining better efficiencies and demonstrating wavelength tunability.

7.2 Summary of results

We started in Chapter 1 with a review of MIR lasers and fibre lasers in particular. The state-of-the-art in MIR fibre lasers prior to this work was discussed, with emphasis on rare-earth-doped fibre lasers operating well beyond 3 μm. Proven methods of improving the output power and efficiency of infrared fibre lasers were discussed. These were based on Er^{3+} and Ho^{3+} doped ZBLAN fibre lasers operating around 2.75 μm which were used

as examples. We then presented the premise of this project, i.e. using DWP to improve power and efficiency of a 3.5 μm Er^{3+}:ZBLAN fibre laser.

In Chapter 2, we delved into the spectroscopy reported in the literature relating to Er^{3+}:ZBLAN glass, which is relevant to the implementation of a 3.5 μm fibre laser. By reviewing the various available sources, we obtained a consistent set of spectroscopic parameters. This set was used later in this thesis for estimating the behaviour of the 3.5 μm fibre laser and will be used in the future in a comprehensive numerical analysis of the DWP system.

The set of parameters included absorption cross-sections of various Er^{3+}:ZBLAN transitions which was compared to our own measurements. Oscillator strength values from literature together with radiative probabilities and branching ratios relevant to this work were presented. We estimated a value for the non-radiative multi-phonon decay rate in ZBLAN glass by combining multiple literature sources. We showed that by using $W_{mp} = Cexp^{-\alpha\Delta E}$ (Equation 2.20) with the parameters $\alpha = 0.0063\ cm^{-1}$ and $C = 1.8 \times 10^{11}\ s^{-1}$, a good agreement between reported energy levels lifetimes from various sources is reached. We calculated the peak of the emission cross-section for the 3.5 μm transition and found it to be $7.5^{+4.5}_{-3.5} \times 10^{-22}\ cm^2$ by using the Fuchtbauer-Ladenburg method based on the fluorescence data provided by Többen [117].

In Chapter 3, we concentrated on determining the appropriate pump sources for a DWP system. It was shown from the literature that the first pump wavelength should be between 982-985 nm to minimise excited-state absorption (ESA) while maintaining reasonable pump absorption. A pump-probe measurement was presented, which resulted in the determination that the peak absorption wavelength of the ESA transition $^4I_{11/2} \rightarrow\ ^4F_{9/2}$ is at 1973 nm. Further investigation obtained the lineshape of ESA and showed that the peak absorption cross-section is $\sigma_{1973nm} = 2.3 \pm 0.8 \times 10^{-20}\ cm^2$. Our investigation was, to the best of our knowledge, the first experimental measurement of this ESA transition. These preliminary investigations concluded with the first demonstration of 3.5 μm fluorescence obtained using a sub-optimal DWP system.

Various pump sources were constructed for the DWP laser system. Chapter 4 describes the different sources and their performance. The final configuration used for the first pump was a commercial 974 nm high brightness single-mode diode that was modified to operate at 985 nm. The second pump source was a 790 nm pumped Tm^{3+} doped silica fibre laser. This fibre laser achieved up to 5 W of output power at 1973 nm.

Although 3.5 μm fluorescence was demonstrated, lasing was initially elusive. Possible limiting factors that prevented lasing were considered in Chapter 5. Our investigations

showed that there is a strong lifetime quenching of the upper lasing level. We measured the intrinsic lifetime of the $^4F_{9/2}$ level in the 1.7 $mol\%$, Er^{3+}-doped, IR-Photonics fibre to be ~ 148 μs under low power excitation by the first pump. The lifetime was shown to reduce when incident power of the first pump was increased and was mostly independent of the power of the second pump. Increased quenching was observed when the first pump was operating at a wavelength of 974 nm compared with 985 nm.

A higher doping concentration (4 $mol\%$ compared with 1.7 $mol\%$) exhibited stronger quenching. Together with theoretical thermal analysis (in Appendix E), these results suggested the influence of an energy-transfer process that depopulated the upper lasing level. We identified this energy transfer process using measurements of the fluorescence at various energy levels as a function of pump power. The previously undocumented energy-transfer process of $^4F_{9/2} + ^4I_{11/2} \rightarrow ^4S_{3/2} + ^4I_{13/2}$ was shown to be detrimental to lasing and its average rate value was experimentally determined to be $4.5 \pm 1.5 \times 10^{-17}$ cm^3/s or $2.7 \pm 1.2 \times 10^{-17}$ cm^3/s under the "strongly interacting" and "weakly interacting" assumptions, respectively.

We achieved lasing after optimising the DWP setup and by using the IR-Photonics fibre with its lower doping of 1.7 $mol\%$ Er^{3+} ions. The 3.5 μm laser performance is summarised in Chapter 6. Lasing on up to three lines was observed at 3472 nm, 3535 nm and 3605 nm. The later wavelength is, to the best of our knowledge, the longest line to be demonstrated in a rare-earth-doped fibre laser operating at room temperature.

The dependency of the laser power and efficiency were investigated as a function of output coupler reflectivity. A maximum output power of 260 mW (total of all lasing lines) was demonstrated with an 18 cm long fibre using a 90% reflectivity output coupler. A maximum slope efficiency of 27.5% relative to the second, 1973 nm incident pump was achieved. Overall optical-to-optical efficiency (including both pumps' incident power) peaked at 15.9% using a 90% reflectivity output coupler. The laser power saturation was shown to be related to the 985 nm pump power.

By using a Findlay-Clay analysis of the dependency of laser power on output coupler reflectivity, it was possible to estimate a few of the laser's parameters. Among these parameters were the internal losses in the fibre $\delta = 180 \pm 60$ dB/km, the inversion density at threshold $n_{th} = 3.2 \times 10^{18}$ $ions/cm^3$ and the emission cross-section $\sigma_e = 9 \pm 4 \times 10^{-22}$ $ions/cm^2$, which agreed well with the cross-section calculated using a fluorescence curve available from Többen's work [117]. Additional laser attributes were investigated. The spectral content of the laser as a function of pump power showed a tendency to operate at longer wavelengths with increased pump power. The power stability of the laser was shown to be better than 0.5% over a 15 minute period. Reasonably good beam quality of $M^2 = 1.34$ was measured, albeit this figure is likely to be an upper limit due to factors outside of the resonator.

7.3   Significance of results

The original motivation for this project was purely scientific. The interesting electronic structure of Er^{3+} ions in ZBLAN glass raised the possibility of using DWP to improve MIR laser efficiency.

In the course of this project, however, the significance of these results became apparent due to the applications that could be realised using such a laser. Operating in the MIR allows the identification of molecular fingerprints using light absorption and laser-radar based devices. Applications of such devices include monitoring greenhouse gasses such as water vapour, CO_2, methane, ethane and other volatiles. A tunable source can open opportunities such as early disease detection using breath analysis, stand-off detection of explosives and improved point-to-point communication. However, the lack of cost effective and affordable sources in the MIR has prevented these applications from being pursued beyond the laboratory setting.

In our work, we developed a fibre laser that operates in the MIR around 3.5 μm with over thirty times more power and ten times better efficiency compared to previously demonstrated fibre lasers [117]. Our work is the first to demonstrate a fibre laser operating well beyond 3 μm with power levels that are approaching those applicable to real-life applications. This laser also operates at the longest wavelength ever demonstrated by a room temperature rare-earth-doped fibre laser. The DWP method described in this thesis improves substantially the efficiency of the laser. In addition, the commercial availability of components suitable for DWP pumping reduces the cost of our laser compared with traditional MIR sources exhibiting similar power levels at this wavelength band.

The DWP method is not limited to the 3.5 μm transition nor to fibre lasers. It can also be applied to other suitable laser transitions and gain media. A patent application has been lodged based on the DWP method and laser results described in this thesis. The University of Adelaide is interested in pursuing further development of the technology for future commercialisation.

7.4   Future research directions

The development of this 3.5 μm fibre laser opens new possibilities. However, as this is the first investigation of a DWP laser on the relatively uncharted 3.5 μm transition, there is significant room to explore.

Three major avenues are important to promote the possible applications of this laser and its commercialisation. These are obtaining wavelength tunability, increasing the power of the laser to the watt level and obtaining short pulse operation. All are beyond the scope of this thesis, although some initial work has begun on all three fronts.

7.4.1 Wavelength tunability

There are currently three possible avenues considered for future wavelength tuning: an open cavity approach, a three-mirror resonator option and a seeded master-oscillator with a power amplifier approach.

In the open cavity configuration, the butted output coupler is removed. The light coming out of the fibre is collimated, sent through a dispersive element and then incident on the output coupler (see an example in Appendix D, Figure D.7). This method suffers from increased losses, however, due to losses at the multiple additional interfaces and Fresnel reflections from the fibre tip. Obtaining lasing requires minimising the higher losses to a manageable level.

A second approach for wavelength tuning is using coupled, or three-mirror resonators. In this way, a first resonator is formed by a fibre which is butt-coupled on both sides. A second concurrent resonator is formed using a dispersive element and a second output coupler.

The third approach is using a seeded resonator following a master oscillator and power amplifier approach. A beam from a low-power, tunable MIR source (for example a quantum-cascade laser diode) is mode-matched into the main resonator which is DWP. If the seed power is sufficiently strong, it will cause the DWP resonator to lock to the seed laser wavelength and amplify it. This would result in a tunable MIR laser system.

The increased complexity of the second and third methods compared with the open cavity scheme make them less attractive. However, all approaches will be investigated in the future for wideband wavelength tuning.

7.4.2 Higher power

Our investigations have shown that the laser power in CW is currently not limited by the 1973 nm pump but by the 985 nm pump. To achieve higher power at 3.5 μm, longer fibres and brighter 985 nm pumps are necessary. Additional pump and fibre configurations should be investigated as well. These include pumping both in the forward and backwards directions and using high-power, low brightness 985 nm diode with double-clad fibres.

7.4.3   Short pulse operation

Utilising the 3.5 μm laser for remote sensing applications requires short pulses of high peak power in some instances. Short pulse generation by gain-switching and mode-locking is the natural extension of our work in the CW and quasi-CW regimes. To achieve gain switching, fast modulation of the 1973 nm pump is necessary. This fast modulation can be achieved using the in-band pumped 1973 nm Tm^{3+}-doped fibre laser described in Appendix C, section C.2 and is planned as an extension to this work.

Q-switching of this laser requires adding a fast modulation of the losses in the resonator. Active Q-switching might be obtained using electro-optic modulators in an open cavity configuration. A different approach is using passive q-switching using saturable absorbers. Future use of graphene is planned to achieve fast switching. With proper resonator design, such saturable absorbers can lead to mode-locking of the laser behaviour. The $^4F_{9/2} \rightarrow {}^4I_{9/2}$ transition is broadband and hence mode-locked pulses shorter than a pico-second are expected. Such direct generation of MIR frequency combs will find many applications in MIR spectroscopy.

7.4.4   Additional investigations

A full rate-equation-based numerical analysis of this complex spectroscopic system is needed. Such a theoretical framework will enable optimisation of the laser and allow investigating parameters which are difficult or too expensive to determine experimentally. Such a simulation will enable optimising the active fibre parameters, including optimising length, doping, core diameter, numerical aperture and possibly co-doping. A numerical analysis will also help to determine whether it is possible to achieve 3.5 μm lasing in a double-clad fibre, despite our lack of success in doing so.

Future implementation of this laser might benefit from a fibre with higher numerical aperture (NA) and lower doping. Operating closer to the originally defined numerical aperture of NA = 0.27 should improve the mode overlap between the laser mode and the fibre core. This should improve the efficiency whilst also increasing the launching tolerances of both pumps. Using fibres which are more lightly doped can reduce ESA, energy-transfer, cross-relaxation and energy-transfer upconversion processes, which have been shown to be detrimental to the DWP operation.

To conclude, obtaining laser operation at 3.5 μm was a significant challenge. We have achieved our goals, although there is still much more to investigate. At this point we can look back and appreciate the significant road we have travelled and at the same time look to new and exciting future research.

Appendix A

Patent, publication and presentations resulting from this work

A.1 Publications resulting from this work

O. Henderson-Sapir, J. Munch and D. J. Ottaway.
"Mid-infrared fiber lasers at and beyond 3.5 μm using dual-wavelength pumping."
Optics Letters, 39(3):493-496, 2014.

Henderson-Sapir,O., Munch, J. and Ottaway, D.J. (2014). Mid-infrared fiber lasers at and beyond 3.5 μm using dual-wavelength pumping.
Optics Letters, 39(3), 493-496.

A.2   Patent resulting from this work

O. Henderson-Sapir, J. Munch and D. J. Ottaway.

"Dual wavelength pumped laser system and method."

Adelaide Research and Innovation Pty Ltd. Australian patent applications 2013901569 / 2013904852, May 2013.

A.3   Presentations resulting from this work

O. Henderson-Sapir, J. Munch and D. J. Ottaway.

"High power 3.5 um fibre laser" [Invited].

Advanced Solid State Lasers, OSA Technical Digest (online), ATu1A.3. Optical Society of America, 2014.

O. Henderson-Sapir, J. Munch and D. J. Ottaway.

"Mid-infrared 3.5 μm band Er^{3+}:ZBLAN fiber laser."

Australian Institute of Physics Congress, Australian Institute of Physics, 2014.

O. Henderson-Sapir, J. Munch and D. J. Ottaway.

"Development of efficient mid-infrared 3.5 μm fiber laser."

Frontiers in Optics, OSA Technical Digest (online), page fw4B.1. Optical Society of America, 2013.

Appendix B

Cleaving and polishing ZBLAN fibre

ZBLAN fibres are very fragile, soft and require extra care when handling, cleaving and polishing. In this appendix, we describe the methods developed in this work to cleave the IR-Photonics fibre and to polish the IR-Photonics and FiberLabs ZDF and ZSF fibres. We were not able to find a cleaving method that produced consistent results with the "D"-shaped ZDF fibre from FiberLabs.

B.1   Cleaving ZBLAN fibre

In this section, we describe the method used for cleaving the IR-Photonics fibre. The tools used in the cleaving process are shown in Figure B.1; the manual cleaver is shown in Figure B.4.

The cleaving method was as follows:

1. Mount the fibre on the flat aluminium block. Place a "Post-it" sticky flag about 2 cm from the tip to be cleaved. The sticky flags have sufficient adhesion to hold the fibre well and they can be removed from the fibre much more easily than ordinary sticky tape.

2. Use a scalpel to scrape slightly or make multiple slight incisions in the coating of the fibre. This will allow the solvent to penetrate better (see Figure B.2).

Figure B.1: Tools used for cleaving the IR-Photonics fibre. Clockwise from top-left: methanol, lint-free tissues, protective gloves, "Post-it" sticky flags, fibre stripper, scalpel, paint stripper, aluminium block and cotton swabs.

Figure B.2: Mounting the IR-Photonics fibre and creating incisions prior to cleaving.
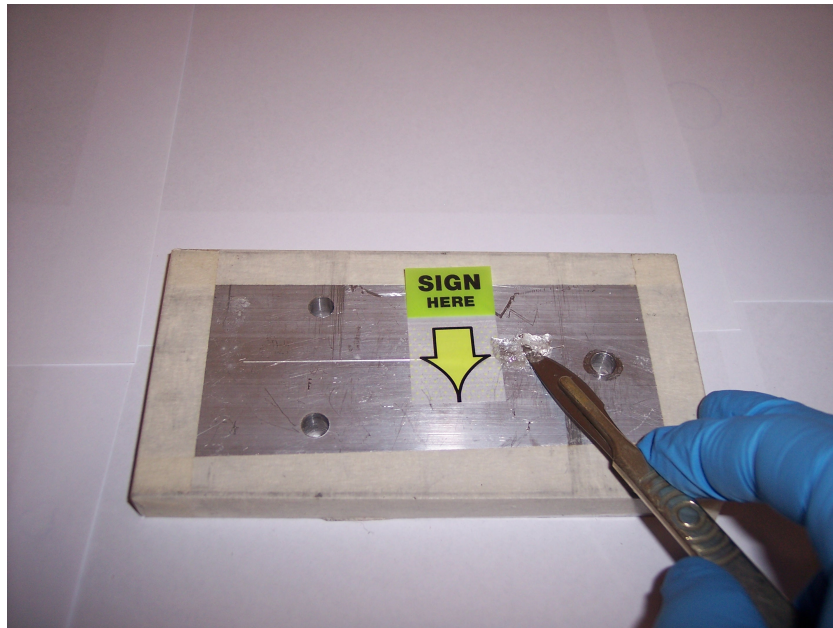
Figure B.3: Lifting the IR-Photonics fibre into the paint stripper prior to cleaving.

3. Cover the fibre beyond the sticky flag with di-chloro-methane (DCM) based paint stripper using a cotton swab. Insert the scalpel, or a thin screwdriver, between the fibre section that is covered with the paint stripper and the aluminium block. Very gently lift the tip of the fibre a few millimetres into the paint stripper blob above it (see Figure B.3). If the paint stripper is fresh, it will flow under the fibre; otherwise, move the fibre tip slightly with the scalpel and release it over the paint stripper. This ensures the paint stripper covers all sides of the fibre.

4. Wait 5-10 minutes for the paint stripper to take effect.

5. Very carefully lift the sticky flag with the fibre attached to it. If the fibre remains attached to the aluminium block, remove the flag and lift the fibre by hand.

6. Wipe off the paint stripper using a lint-free tissue soaked in methanol. Methanol is preferable since it has lower acidity than acetone and isopropyl-alcohol and is therefore more gentle on ZBLAN glass. Wipe along the length of the fibre towards the tip to remove all of the paint stripper. Try to apply enough friction to pull the coating of the fibre off the part that was exposed to the paint stripper. Achieving the right level of friction necessary requires practice. If that does not work, use the fibre stripper carefully on a position that was exposed to the paint stripper and carefully remove the coating.

7. About 2 cm of uncoated fibre is now ready to be cleaved. Do not clean or touch the exposed fibre.

8. Adjust the York cleaver to a tension of 100 grams. This level of tension is suitable for the 125 μm IR-Photonics fibre. Other ZBLAN fibres with different diameters are likely to require a different level of tension.

9. Mount the fibre in the cleaver with its curvature down. Cover the exposed side of the fibre with a small piece of lint-free tissue folded to create four layers (see Figure B.4). Lower the clamps **_without locking them_**. The purpose of the four-layered tissue is to reduce the clamping force of the clamp on the exposed glass. Without it the fibre will shatter.

Figure B.4: Fibre in York cleaver with tissue on it. Clamps are in the open position.

10. The following procedure for cleaving (see figure B.5) requires some practice to master:

   (a) With your left hand, apply downward pressure to both clamps using your fingers - do not reach the locking stage. This pressure needs to be light enough to not crush the fibre on the exposed glass side or deform the coating coating on the coated side. At the same time, it needs to be firm enough to prevent the fibre from slipping once the tension lever is released.

   (b) Using your right hand, release the tension lever. You must ensure that your left fingers only apply downward pressure. Otherwise, the tension on the fibre can be too high, causing a bad cleave, or too low, resulting in no cleave.

   (c) With the third finger of your left hand, release the "cleave" lever. The ultrasonic cleaver arm will reach the fibre. If the fibre is mounted properly and clamped with enough force, the fibre will be cleaved.

(d) Immediately after cleaving, lift the "cleave" lever back to retract the cleaver arm.

(e) If the fibre did not cleave, try the cleaving process (10a-10d) again. If this still fails, tension of the fibre might need to be readjusted or the fibre might need to be re-cleaned.

Figure B.5: Cleaving with the York cleaver when manually clamping the fibre. Leftmost lever is the "cleave" lever, two middle levers are the clamping levers and the rightmost lever is the "tension release" level.

11. Inspect the cleave using a microscope to ensure a straight cleave. If possible, inspect the endface as well. A fibre splicer is sometimes useful for the purpose of inspecting the fibre (see Figure B.6).

Figure B.6: Inspecting the fibre tip using a fibre splicer. The fibre on the left has an almost straight cleave, while the one on the right has an angled cleave.

B.2 Polishing of ZBLAN fibres

ZBLAN fibres are significantly softer than silica fibres and require a different polishing process. The following procedure was found to be effective when polishing ZBLAN fibres. We did not try to put connectors on fibres. For this purpose, the polishing process would have to be amended.

The tools used in the polishing process are shown in Figure B.7.
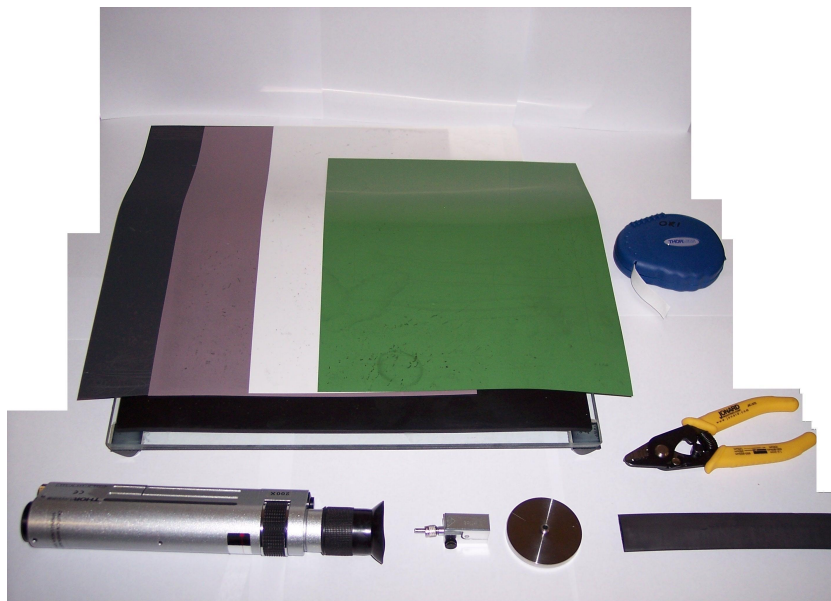
Figure B.7: Equipment used for polishing ZBLAN fibre. Clockwise from top left: Glass plate with rubber mat, lapping papers (5 μm - black, 3 μm - brown, 0.3 μm aluminium oxide - white, chromium oxide 10000 grit - green), fibre cleaner, fibre stripper, heat-shrink tubing, stainless steel puck, bare-fibre adaptor and fibre-viewing scope.

The polishing process of the IR-Photonics, 125 μm-diameter fibre is described below.

1. Clean the fibre using methanol.

2. Ensure that the coating of the fibre is in good condition all the way to the end of the fibre. A lumpy or uneven coating will prevent the fibre from entering the bare-fibre adaptor.

3. Mount the fibre in a bare-fibre adaptor fitted with a 260 μm SMA connector. Ensure that the fibre barely protrudes from the connector. If it extends too much beyond the endface of the connector, it will break during the polishing process.

4. Mount the fibre and adaptor onto the SMA polishing puck, ensuring both the puck and adaptor are oriented in a certain direction (see Figure B.8). Maintain the same direction for all polishing procedures. It is helpful to scribe a line on the puck for alignment purposes. If the direction is not maintained throughout the process, the polishing can result in multiple facets because of tolerances between the connector ferrule diameter and the polishing puck hole.

5. Place heat-shrink tubing on the back of the bare-fibre adaptor (see Figure B.8). This prevents the fibre from swaying too much during the polishing process, which can cause it to break. Heat-shrink was chosen as it has a similar diameter to the base of the bare-fibre adaptor and it has a slight stretch.
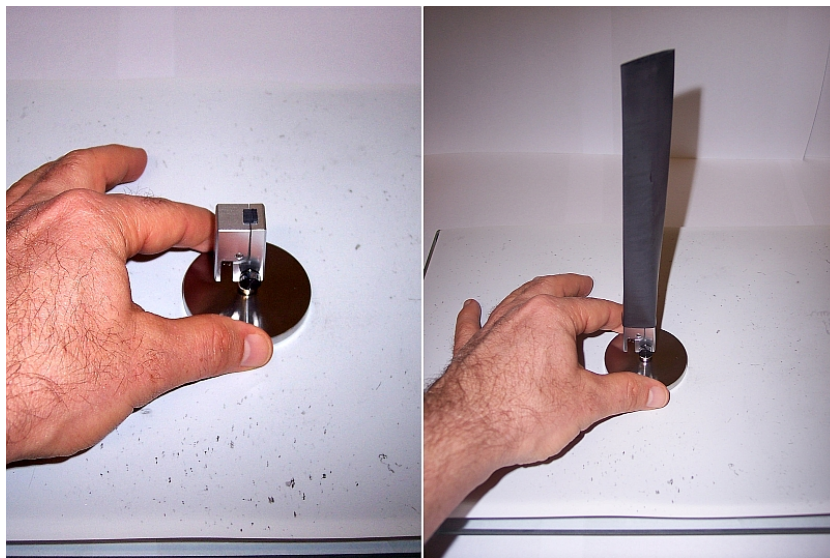
Figure B.8: Holding the polishing puck. Left - fibre mounted in polishing puck and connector oriented in a specific way. Right - heat shrink mounted on bare-fibre adaptor to prevent fibre from swaying during polishing process. It is important not to apply downward pressure to the polishing puck.

6. If the fibre tip is very jagged, start with a black lapping paper (5 μm). Place the lapping paper on top of a rubber mat placed on the glass surface. Start polishing in figure 8 motions. This is a very rough polish and can cause the fibre endface to be very jagged, so only minimal polishing (if any) using this lapping paper is recommended.

7. Remove the adaptor from the puck, tap the fibre tip multiple times with a sticky flag to remove large debris and inspect the fibre tip using the fibre-viewing scope. Both fibre and coating should be visible and the fibre facet should be scratched evenly but roughly (see Figure B.9 on the left).

8. Change to the brown lapping paper (3 μm) on top of the rubber mat on the glass surface and polish in figure 8 motions. It should be possible to get an almost scratch-free surface at the end of this stage.

9. Remove the adaptor from the puck and tap the fibre tip multiple times with a sticky flag. Then clean the fibre tip using the fibre cleaning tape with a drop of methanol and inspect the fibre tip using the fibre-viewing scope. Both fibre and coating should be visible and the fibre facet should be scratched very lightly (see Figure B.9 on the right).
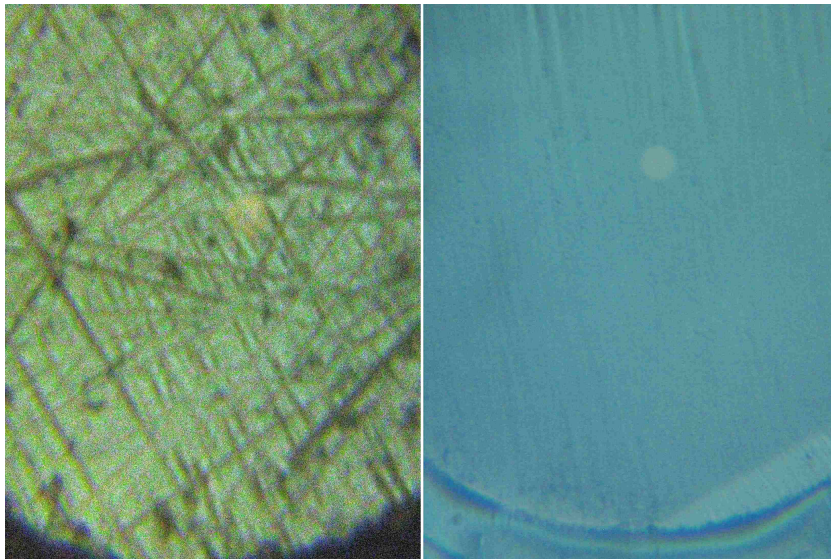
Figure B.9: Fibre endface quality after black and brown lapping papers. Left - after using the black lapping paper (5 μm); right - after using the brown lapping paper (3 μm).

10. Remove the rubber mat and change to chromium oxide lapping paper. Mount the adaptor with fibre in the puck and let the puck rest on the lapping paper. Drag the puck in straight lines a few centimetres each while rotating the puck. Do not apply any downward force. Repeat stage 9.

11. If fibre endface is not smooth, repeat stage 10.

12. If after few trials the endface is not sufficiently smooth after using the chromium oxide lapping paper, it is sometimes necessary to change to the white lapping paper (0.3 μm). Mount the fibre and adaptor. While applying slight downward force, polish in figure 8 motions.

13. If there are still very fine scratches, repeat stage 10.

14. When satisfied with the end face quality (i.e. no scratches or significant chipping of the fibre rim), disconnect bare-fibre adaptor from puck and remove the heat shrink.

15. Remove the fibre from bare-fibre adaptor by first pushing the fibre through the connector so it protrudes. This will dislodge debris from the tip of the fibre. Then pull the fibre backwards through the connector until it is free.

16. Using the fibre stripper, remove 1 mm of coating from around the fibre tip. This is necessary to ensure that the fibre endface can be butted against the mirror properly.

17. Inspect the fibre tip using a microscope or splicer for cleanliness and to estimate the angle of the endface.

18. If there is debris on the fibre tip from the removal process, try tapping the tip very gently with a sticky flag. If debris is still present, clean using fibre cleaning tape.

When polishing the FiberLabs fibre, a similar process is followed. The only difference is that a 510 μm connector is used instead of the 260 μm connector because both ZDF and ZSF fibres both have larger coating.

The polishing process of ZBLAN seems to work best as a dry process unlike the usual wet process in silica. It is especially important to keep the chromium oxide paper dry, otherwise the particles become dislodged and completely clog the connector.

Appendix C

In-band thulium-based fibre lasers

In Chapter 4 we describe the final version of the second pump source used to obtain 3.5 μm lasing using DWP. This version was based on a 790 nm pumped, Tm^{3+}-doped, silica fibre laser. Two earlier versions of the second pump source, also based on a thulium fibre laser (TFL), were constructed during this work. These two fibre lasers were based on a 1550 nm in-band pumped gain switched design. The first variant was used in our validation of the DWP concept, as described in section 3.3.3. The second variant was designed as a higher power version of the first fibre laser and was used during our initial, unsuccessful trials for achieving 3.5 μm lasing. The details of the construction and performance of these in-band pumped TFL sources are reported in this appendix.

C.1 Preliminary TFL based on gain-switched design

In experiments conducted at the University of Adelaide, Wu et al. [191] employed an in-band pumped TFL as a pump source for a gain-switched Ho^{3+} fibre laser. We obtained Wu's original laser and simplified it to operate it in CW mode. This was done to simplify laser construction and to clarify spectroscopic measurements performed. This TFL was used in the work described in section 3.3.3.

A schematic diagram of the initial TFL is shown in Figure C.1. This laser was a seeded in-band pumped, gain switched laser. A fibre-coupled 1551.4 nm laser diode (QPhotonics QDFBLD-1550-50) with an output power of 40 mW was used as a seed source. The diode was operated in CW and pulsed modes. The output from the diode was spliced into a fibre-coupled optical isolator (AFW ISOS-15-0-1-0). The seed signal was then passed through a 99%:1% coupler, with the 1% branch connected to an InGaAs diode (Thorlabs Det01CFC) for monitoring purposes.

The rest of the seed light continued into an erbium doped fibre amplifier (EDFA) stage. The EDFA stage consisted of a multi-mode fibre pump and signal combiner (3+1) and
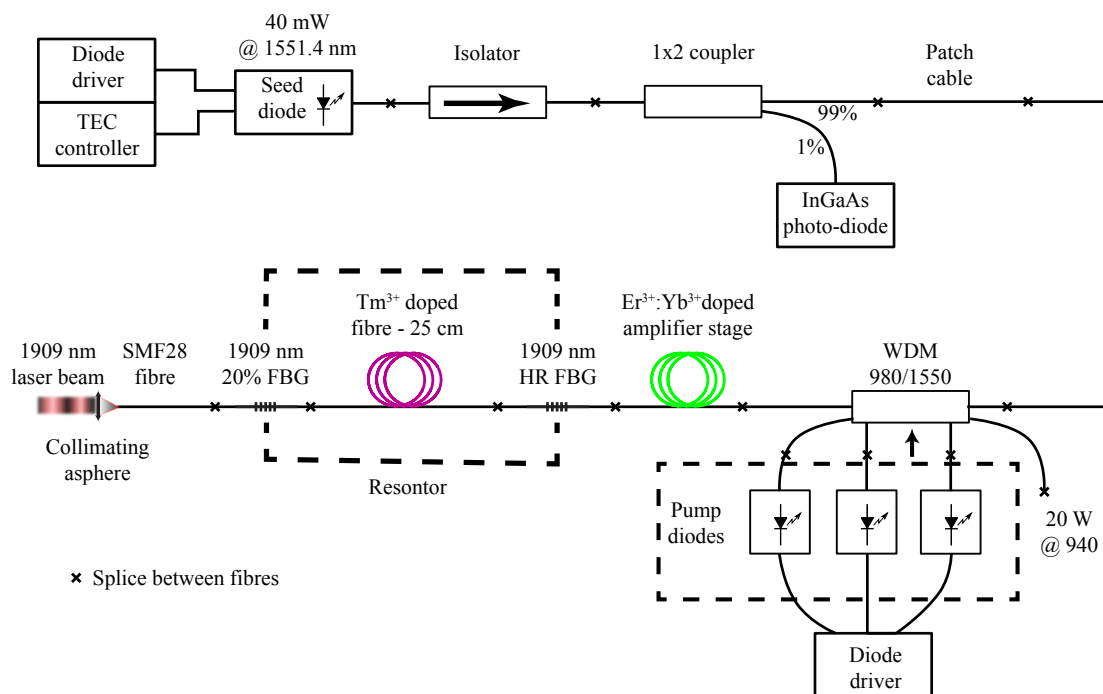
Figure C.1: Second pump source - initial configuration. Tm^{3+} fibre laser design is based on an in-band pumped, gain-switched Tm^{3+} fibre laser demonstrated by Wu et al. [191]. In our setup, the laser was operated in CW.

a doped fibre. A total of 20 W of 940 nm pump light from three multi-mode diodes (2xBookham MU8-940-01/04 and one JDSU 6396-L3 series) were combined and injected into the inner cladding of the pump and signal combiner. The 1551.4 nm signal was injected into the core of the "signal" fibre, which was part of the pump and signal combiner. The output fibre of the pump and signal combiner was spliced to the active fibre. This splice injected the pump light into the inner cladding of the double-clad active fibre with the seed light being amplified in the core of the active fibre (Nufern SM-EYDF-6/125-HE). The fibre had a 6 μm diameter core that was doped by a combination of Er^{3+} and Yb^{3+} ions. The core was surrounded by an inner cladding with a 125 μm diameter.

The amplified 1551.4 nm light from the EDFA entered the Tm^{3+} fibre resonator stage and was absorbed in it due to the ground state absorption of Tm^{3+} at this wavelength. The Tm^{3+} laser resonator stage consisted of a highly reflective fibre Bragg grating (FBG), an active Tm^{3+} fibre and a low reflectivity FBG acting as an output coupler. This stage was used as in the original configuration used by Wu et al. and was therefore optimised for short pulse operation for pumping a Ho^{3+} doped fibre laser. The highly reflective FBG was centred at 1909 nm (sourced from DSTO). The FBG was spliced to a 25 cm, Tm^{3+} doped fibre (Nufern SM-TDF-10P/130-HE). This fibre had a 10 μm core with a numerical aperture of NA = 0.15 and 130 μm of inner cladding. Ion concentration of the fibre core was 3.5% wt% Tm^{3+} ions. The fibre exhibited single transverse mode

behaviour in the 1900 nm band. The laser resonator was completed with an FBG with 20% reflectivity at 1909 nm. We maintained the 25 cm length of the active fibre from the original work of Wu et al. [191]. This length corresponded to Wu's maximum average power and coincided with the $\sim 90\%$ absorption length of the 1550 nm pump light [209]. An undoped extension of SMF28 fibre was spliced to the output of the 20% FBG fibre to allow easy delivery of the signal to the experiments.

The laser was operated in CW to simplify the spectroscopic measurements for which it was used. Figure C.2 shows the CW output power at 1909 nm of the laser as a function of the current of its pump diodes.
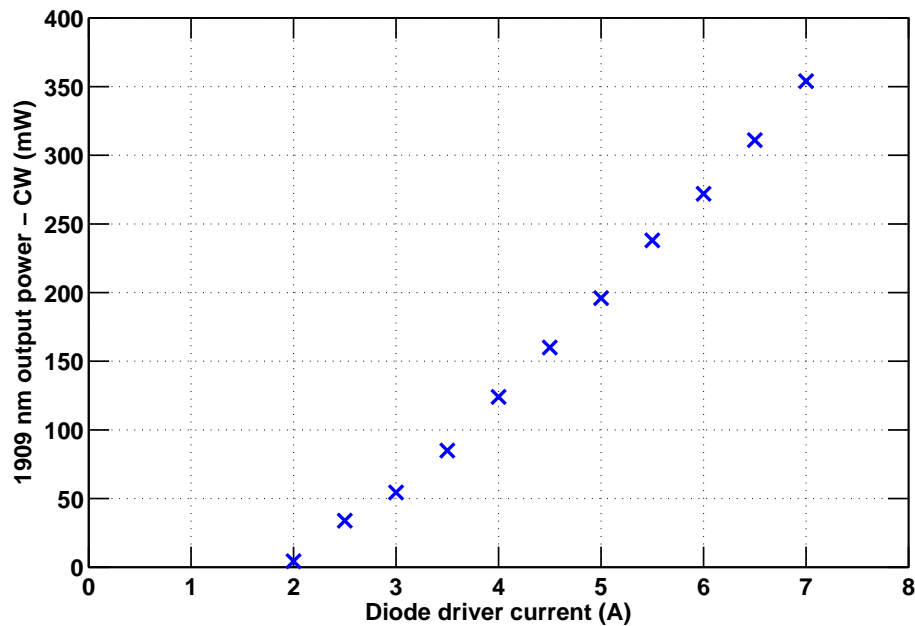
Figure C.2: First in-band pumped TFL variant - 1909 nm output power as a function of diode current in CW.

The Tm^{3+} doped stage produced a maximum of 350 mW at 1909 nm while operating at a driver current of 7 A. Driver currents higher than 7 A caused strong output power instability and were therefore avoided. The output power was strongly affected by the temperature of the Tm^{3+} stage. We passively cooled the Tm^{3+} fibre by submerging it in a shallow water tub. This resulted in the fibre laser producing its maximum output power of 350 mW. Due to the passive nature of cooling (no water circulating), the temperature of the fibre in the water increased over time, resulting in lower output power. The variability of the output power only enabled us to perform qualitative measurements (such as observation of increased 650 nm and 3.5 μm fluorescence in section 3.3.3). In addition, using the wavelength of 1909 nm was far from optimal since

its ESA cross-section was six times lower than the maximum possible at 1973 nm (see Figure 3.13). Due to all of these reasons, a higher power, more stable source operating at 1973 nm was needed for additional investigations.

C.2 TFL based on a higher power version of the gain-switched design

To achieve enhanced pumping of the $^4I_{11/2} \rightarrow {}^4F_{9/2}$ transition, a higher power, more stable source, operating closer to the peak absorption wavelength of 1973 nm was required.

Our second variant of a TFL was based on the design of Wu et al. in [191] for an in-band gain-switched TFL with modifications to enable higher power: a double-pass, pre-amplifier stage was added to increase the total gain of the system. This together with increased isolation between the different stages enabled stable operation at higher power levels than the ones obtained with the TFL described in section C.1. Figures C.3 and C.4 depict the schematics of this TFL.

The laser was constructed from four main building blocks: 1550 nm seed, 1550 nm pre-amplifier, 1550 nm power amplifier and a Tm^{3+} laser stage which are described below.

C.2.1 1550 nm seed segment

The 1551.4 nm seed stage was similar to the one described in section C.1 and its schematics are shown in Figure C.3. A fibre-coupled 1551.4 nm laser diode (QPhotonics QDFBLD-1550-50) with an output power of 40 mW was used as a seed source. This laser diode could be used in both CW and pulsed modes using a dedicated printed circuit board connected to a pulse generator. The pigtail fibre from the diode was spliced into a 99%:1% fibre coupler, with the 1% branch connected to an InGaAs diode (Thorlabs Det01CFC) for monitoring purposes. The main signal from the coupler passed through a fibre-coupled optical isolator (AFW ISOS-15-0-1-0), which protected the seed laser diode from feedback from the pre-amplifier.

Figure C.3: Second in-band pumped TFL variant - seed and pre-amplifier stages.
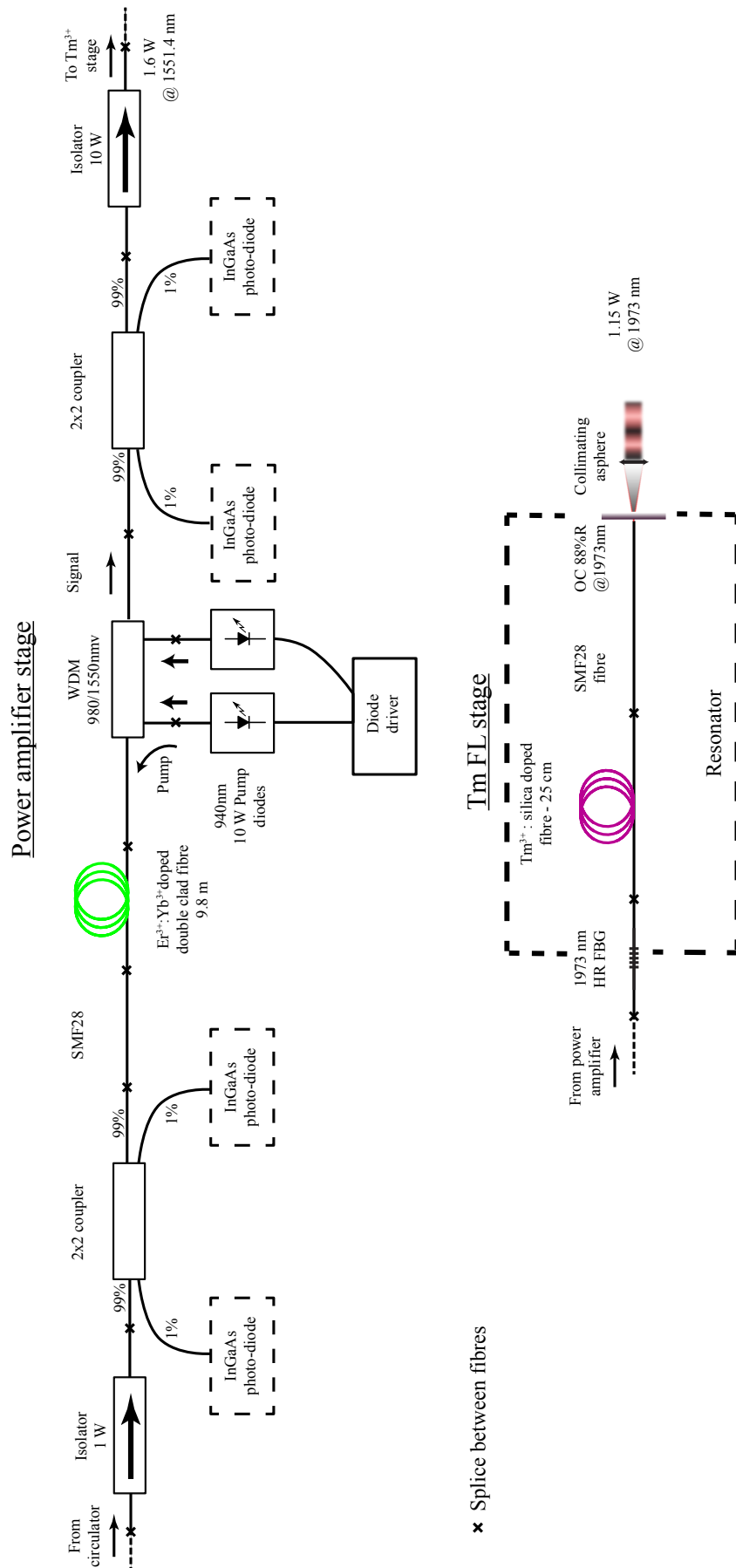
Figure C.4: Second in-band pumped TFL variant - second amplifier stage and Tm³⁺ stage.
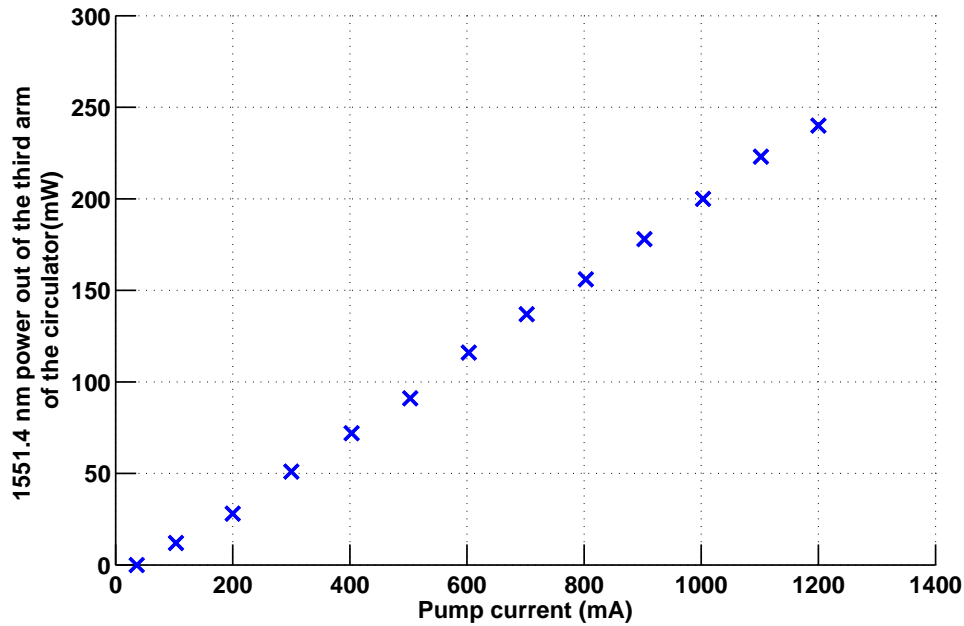
Figure C.5: Second TFL variant - output power of the pre-amplifier as a function of its pump current. Power was measured at the output of the third arm of the circulator leading to the power amplifier stage prior to splicing the amplifier stage. The incident 1551.4 nm seed power was kept constant at 28 mW.

C.2.2   Pre-amplifier segment

The pre-amplifier was a double-pass amplifier, see schematics in Figure C.3. Its role was to amplify the 1551.4 nm signal so that the final power amplifier was saturated. The output power of the pre-amplifier is shown in Figure C.5.

The signal from the seed-stage entered the first arm of a fibre-coupled circulator (AFW cir-3-15-L-1-0). The signal exited the circulator via the second arm of the circulator and entered a wavelength division multiplexer (WDM). This WDM (AFW WDM-SM-1-98/5-L-1-L-0) combined both the 1551.4 nm signal and light from a single mode, 700 mW high brightness 974 nm pump (Bookham LC96UF74-20R) into the core of its output fibre.

The 974 nm pump and the 1551.4 nm signal were injected into the active fibre where the 1551.4 nm signal was amplified. This fibre was a 1.5 m long single clad, single mode Er^{3+} doped fibre (Nufern SM-ESF-7/125). A high-reflector FBG centred at 1551.4 nm with a bandwidth of 0.6 nm was spliced on the other side of the active fibre. The FBG reflected the signal back into the Er^{3+} doped fibre for a second pass resulting in additional amplification.

The amplified signal continued travelling through the WDM and back into the circulator second arm. After double-passing the pre-amplifier, the incoming signal was amplified from 28 mW to 275 mW. Travelling in the opposite direction to its first time in the second arm of the circulator, the signal was reflected towards the third arm of the circulator. This arm was spliced to the power amplifier stage.

The spectrum of the signal travelling through the circulator towards the power amplifier is presented in Figure C.6. Reflecting the signal into the pre-amplifier with an FBG
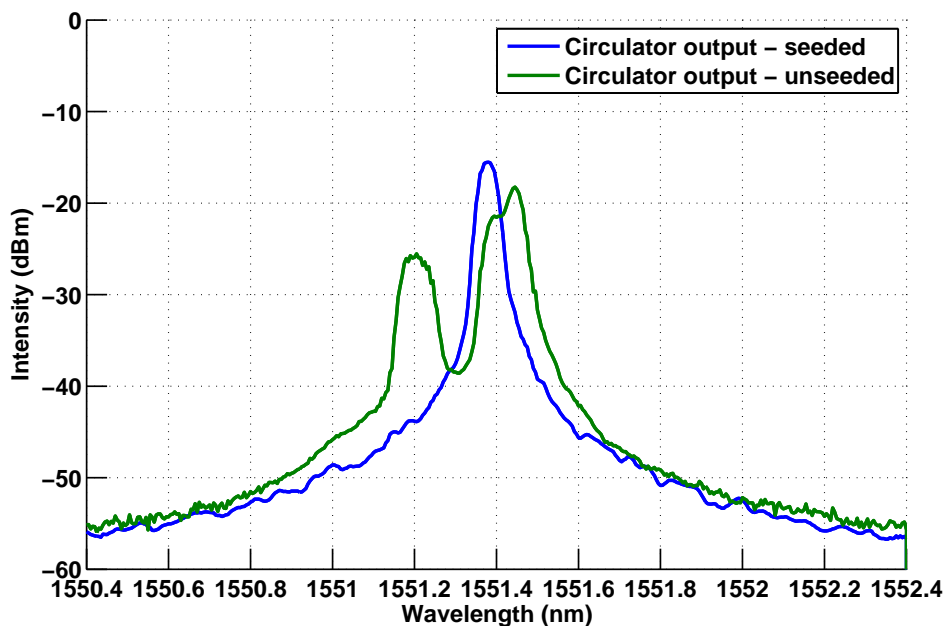
Figure C.6: Spectrum of the amplified 1551.4 nm signal after double-passing the pre-amplifier. When unseeded, most of the power is generated in the forward direction escaping the amplifier stage through the FBG due to wavelength mismatch.

helped the laser behaviour in two ways. It increased the gain of the pre-amplifier stage by double-passing. The double passing of the signal also improved the ratio between the signal and ASE noise. This was because the ASE was only amplified when travelling in the backwards direction, while the broadband forward travelling ASE was allowed to exit the amplifier through the narrowband FBG. Figure C.6 shows the spectrum of the signal on the exit arm of the circulator (arm three) after double-passing the pre-amplifier. Both seeded and unseeded cases are shown, demonstrating the significant narrowing obtained under seeded operation.

C.2.3   Power amplifier segment

The role of the power amplifier stage was to boost the 1551.4 nm signal power after the pre-amplifier by an order of magnitude to about two watts. This was achieved using a single-pass amplifier stage which consisted of an Er^{3+}:Yb^{3+} doped active fibre, pumped within the broad absorption band of the Yb^{3+} ions at 930 nm. Schematics of the second amplifier stage can be seen in Figure C.4.

The power amplifier stage consisted of a 1 W, polarisation-independent, fibre-coupled isolator (AdValue Photonics AP-ISO-1550P1-2-1,3). Its purpose was to protect the circulator and seed stage from back propagating power. After the isolator, a 2×2, 99%:1% single mode beam splitter/coupler (Thorlabs 10202A-99) was used to monitor the forward and backward propagating signal on the 1% branches.

A length of SMF28e, single mode fibre was spliced to the output port of the 2×2 coupler. The purpose of the SMF fibre was to remove any residual 930 nm pump light from propagating backwards in the fibre cladding. This was necessary since this amplifier stage was counter pumped. The active fibre consisted of 9.8 m of double-clad fibre doped with both Er^{3+} and Yb^{3+} ions in its core (Nufern SM-EYDF-6/125-HE). This fibre had a 6 μm core with a numerical aperture of NA = 0.18 and 125 μm diameter octagonal-shaped inner cladding with a numerical aperture of NA=0.45. The combination of core size and numerical aperture resulted in the core of this fibre support only a single transverse mode in the 1550 nm band.

The output side of the active fibre was spliced to a multi-mode, (2+1)x1 coupler (ITF labs MMC02112A61A). This coupler combined input from two 100 μm diameter multi-mode fibres coming from the high-power, low-brightness pump diodes, together with a pass-through, double-clad passive fibre that matched the active fibre geometry. Two fibre-coupled diodes using 100 μm diameter delivery fibres were used to pump the amplifier (JDSU L4-9894010-100E). The maximum power available from each diode was 10 W while operating at 930 nm. Each diode was cooled by passive conduction to a heat-sink with an attached fan.

Past the pump and signal combiner, an additional 99%:1% beam splitter/coupler (Thorlabs 10202A-99) was spliced for the purpose of monitoring the output signal from the amplifier. A high power, 10 W isolator was added (AdValue Photonics AP-ISO-1550PI-2-10,3) to isolate the amplifier stage from the next stage consisting of the Tm^{3+} active fibre. The output power of the power amplifier stage after the isolator and before it was spliced to the the Tm^{3+} stage is shown in Figure C.7.
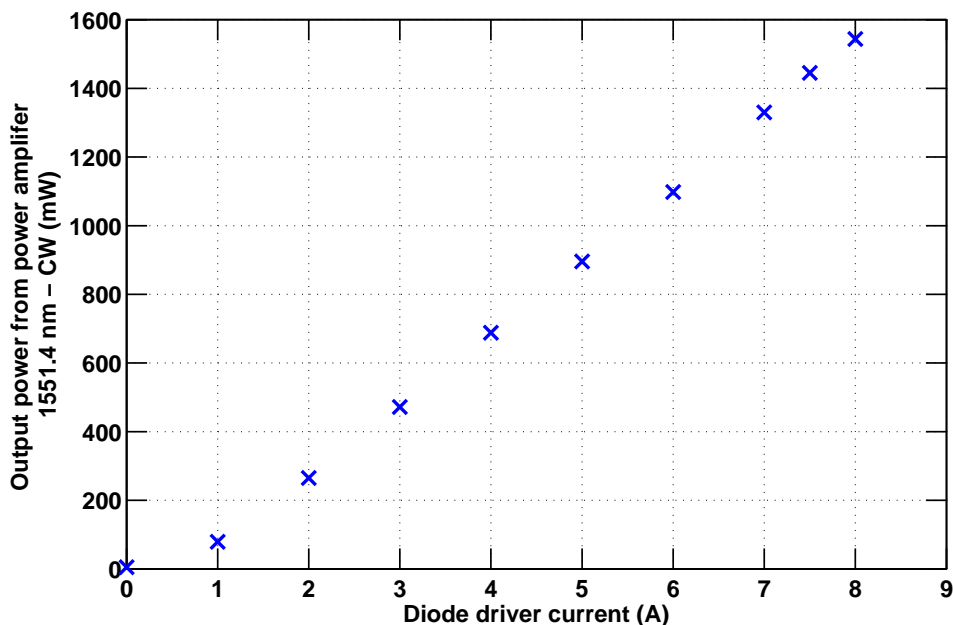
Figure C.7: Output power of the power amplifier stage in the second in-band pumped TFL variant operating in CW. Power is based on a seeded operation with incident signal after the pre-amplifier stage at a maximum of 230 mW.

The relatively low power demonstrated by the power amplifier stage is the result of strong spiking behaviour observed when operating at higher pump powers. The spiking was somewhat improved by angle cleaving the stage output (without the isolator), however, it could not be resolved completely. It was hypothesised that the spiking resulted from strong mode competition due to insufficient gain saturation by the pre-amplifier power when operating at higher pump power. Reflections at the fibre splices between the active fibre and other elements might have contributed as well. Despite the spiking observed, it was decided to add the Tm^{3+} laser stage, since the 1973 nm power predicted was deemed sufficient.

C.2.4 Tm^{3+} laser stage

The Tm^{3+} laser stage was added after the high power isolator as seen in Figure C.4. At first, an FBG acting as a highly-reflective resonator mirror was spliced in place (Teraxion PWS-HPR-1970-1.6-99.5-PM10/130-0-1). The FBG was then spliced to a 10.8 cm long Tm^{3+} doped, polarisation-maintaining, double-clad active fibre (Nufern PM-TDF-10P/130-HE). A short length of fibre was all that was needed to achieve good pump absorption since the 1551.4 nm pump was launched into the highly doped core of the fibre. This laser was only operated in CW mode, therefore extending the resonator

length with a passive fibre did not affect its behaviour. We therefore spliced an additional SMF28e fibre to the Tm^{3+} stage to allow for easier handling and beam delivery to the DWP experimental setup.

The output of SMF fibre was straight cleaved and then butt-coupled onto an output coupler mirror with 88% reflectivity at 1973 nm (Altechna PR-1940-88). This mirror was required to ensure stable operation at 1973 nm. Without the mirror, or when using lower reflectivities, the laser exhibited very erratic behaviour and would tend to lase at different wavelengths. The outgoing beam was collimated using an aspheric lens (Thorlabs C560-TME-C). The output power of the Tm^{3+} stage as a function of incident 1551.4 nm pump is shown in Figure C.8. The output beam was verified to have an excellent beam quality with a measured $M^2 = 1.01 \pm 0.21$ value to the beam divergence measured in one axis (see Figure C.9).
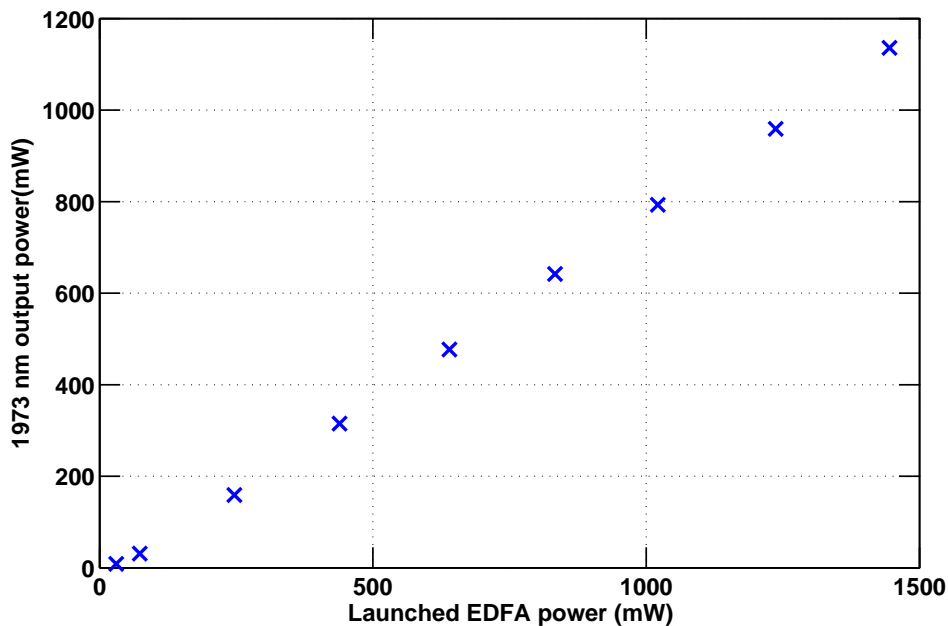
Figure C.8: Second in-band pumped TFL variant output power of the Tm^{3+} stage in CW. Output wavelength was 1973 nm. 10.8 cm long Tm^{3+} doped fibre was used. Output coupler reflectivity was 88%. Launched EDFA power is based on measured power from the power amplifier stage prior to splicing while accounting for splice loss.

Although operated and tested only in CW, this in-band TFL was designed while considering possible gain-switching, pulsed operation with only minimal modifications required. Pulsed operation could be achieved by replacing the seed laser driving electronics, which currently can only operate in CW, with a short-pulsed version. Additionally, the length of the Tm^{3+} stage must be minimised by removing the SMF fibre to ensure short pulses.
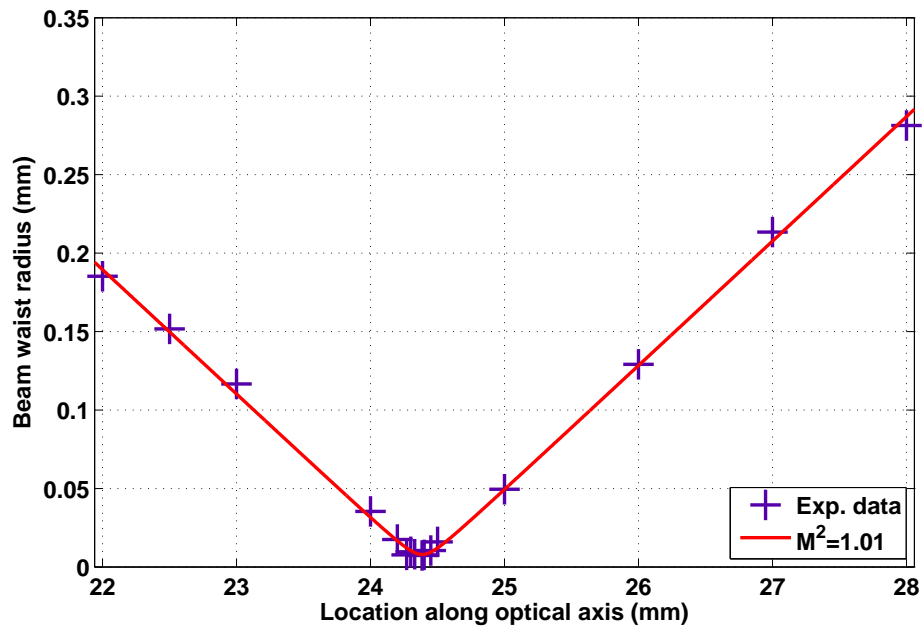
Figure C.9: Beam quality measurement of the second in-band pumped TFL variant. M^2 measured along the horizontal axis.

Gain switching of the 1973 nm source should enable gain switching of the 3.5 μm laser that could result in high peak power operation.

Appendix D

Detailed schematics of laser and future improvements

The following appendix contains block-diagram schematics of the current laser system detailing all the optical and mechanical components used (as mentioned in section D.1). Future free-space configurations using a smaller component count and configurations in "open cavity" format are suggested in section D.2. Section D.3 presents a possible all-fibre pump configuration.

D.1   Current configuration

This section contains the current layout of the 3.5 μm DWP laser system. Figure D.1 is devoted to the pump sources. The first pump is based on an off-the-shelf, 974 nm, fibre-coupled laser diode, which was modified to operate at 985 nm. The second pump source is an in-house built 1973 nm fibre laser, which is pumped by a fibre-coupled high power 790 nm laser diode.

Figure D.2 concentrates on the mode matching and beam combining optics. We expect to be able to significantly minimise the component count of this section in a commercial setting. This is especially true for an (almost) all fibre configuration. Figure D.3 displays the laser resonator itself with the ZBLAN fibre acting as the gain medium. In this configuration, both the high reflector mirror (HR) and output coupler mirrors are "butt-coupled" against the fibre endfaces.
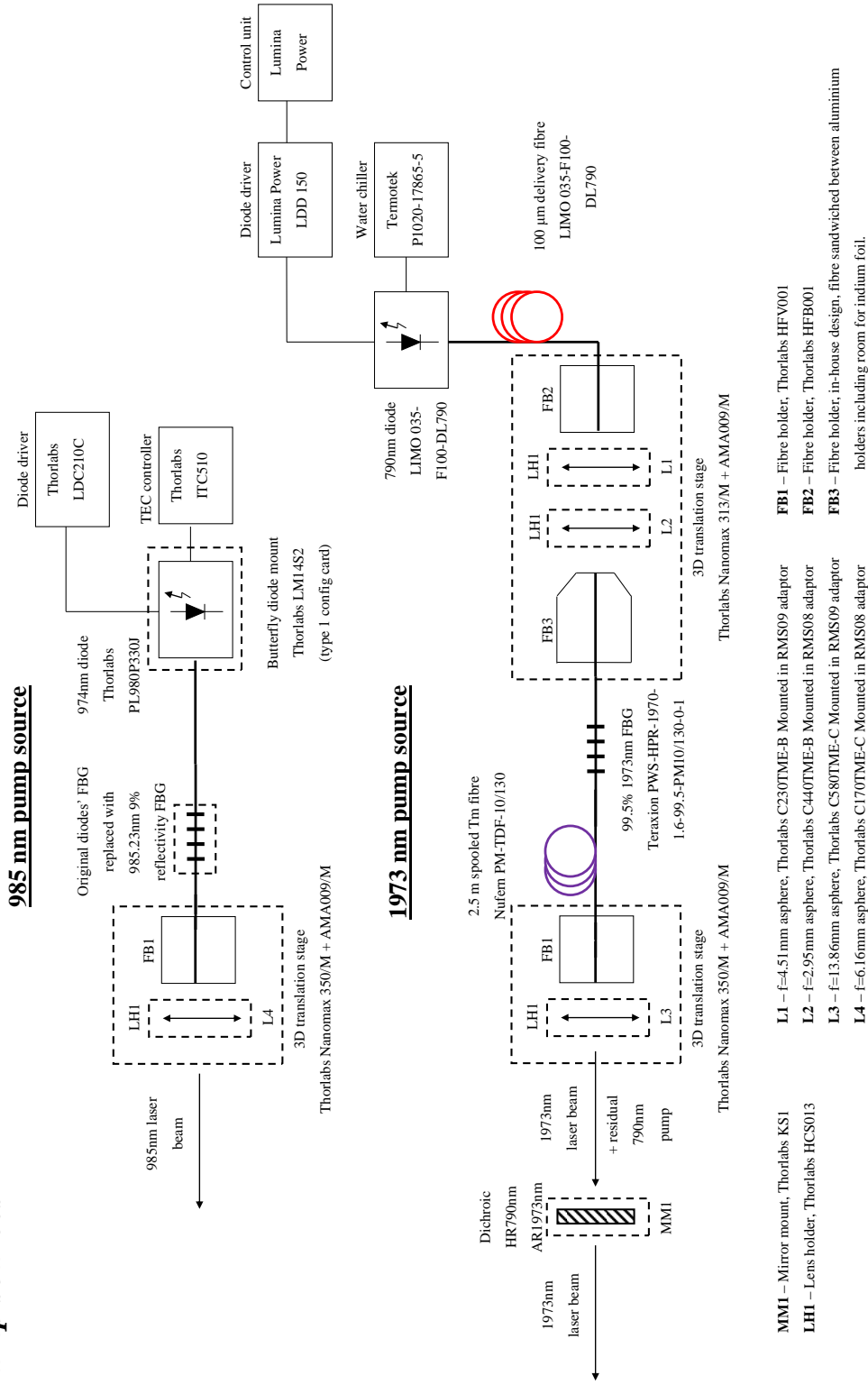
Figure D.1: Detailed block diagram schematics of current pump sources.
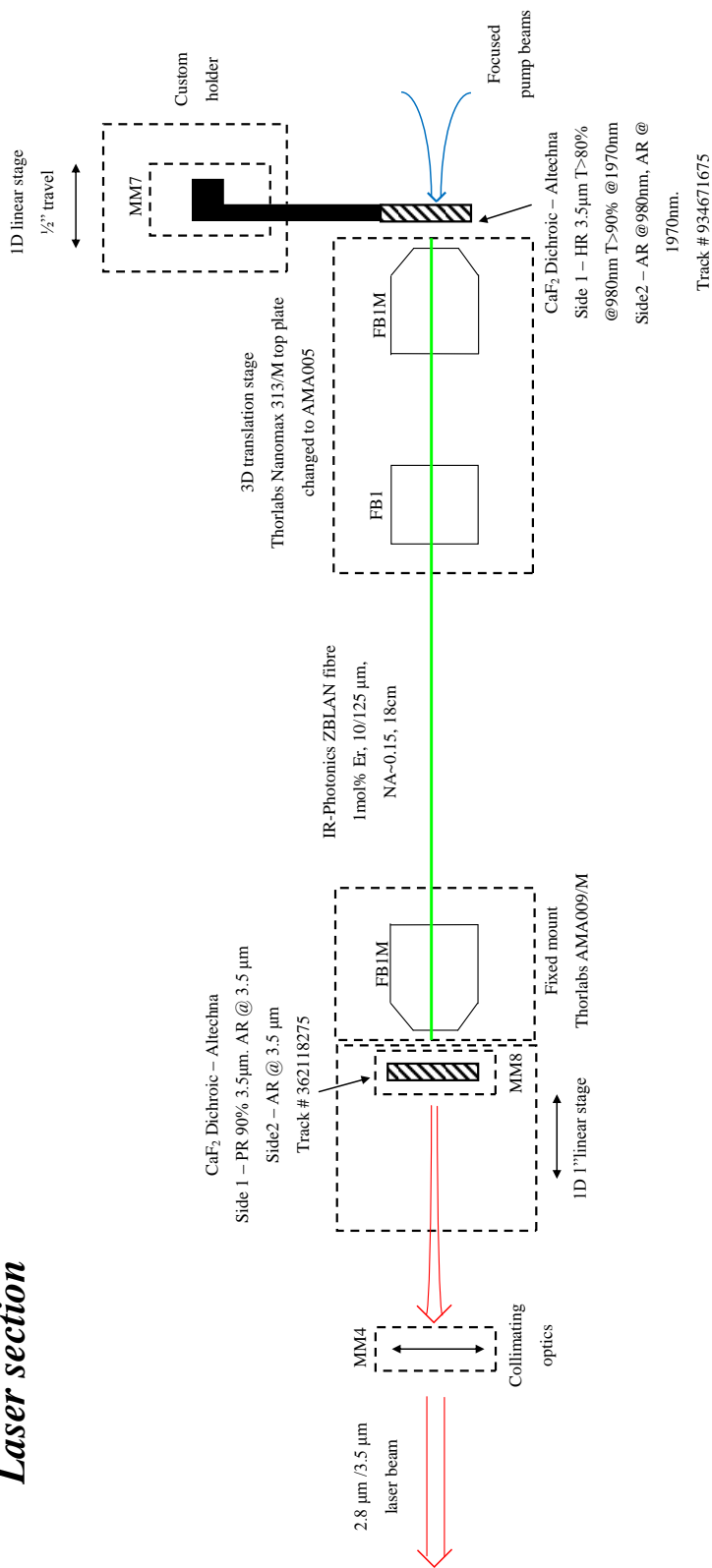
Figure D.2: Detailed block diagram schematics of current mode-matching section.

Laser section

Figure D.3: Detailed block diagram schematics of current laser section.

D.2   Suggested improvements for future configurations

The current configuration was designed with no space limitation in mind and hence is not efficient in space or component count. Significant improvements can be obtained with the following components:

1. All laser diode drivers and TEC (Peltier) controller can use OEM or in-house built electronics.

2. Once aligned properly, all optics can be fixed to their position.

3. All mirrors can be replaced with $1/2$" mirrors.

4. All spherical lenses can be replaced with $1/2$" lenses.

5. In the pump sources section:

   (a) Using a different fibre-coupled 790 nm diode should make it possible to directly splice the supply fibre to the 1973 nm highly-reflective fibre Bragg grating (FBG) using a 790/2000 nm WDM combiner. This will remove the first 3D translation stage and the associated optics.

   (b) Both 3D translation stages in the pump sources section can be replaced with a 1D stage (with movement along the optical axis) with micrometer resolution. Worse resolution might also be possible under certain conditions.

   (c) It is strongly recommended to add an isolator to the 1973nm pump arm. This might be possible using a fibre isolator (compared with expensive free space isolators), though further investigation is required.

6. In the mode matching section:

   (a) Both 1 μm and 2 μm AR coated windows can be removed.

   (b) Both lense pairs 5+6 and 8+9 can be replaced by an appropriate single lens with a less standard focal length. It might be possible to have only a single lens on the 985 nm arm, but this requires further investigation.

   (c) Lenses 5, 6, 8 and 9 can be completely omitted if lens 7 is replaced with an off-axis parabolic mirror. This will come at the expense of more difficult alignment. Another possibility is to use a custom made 985/1973 nm achromat lens combination as the launching optics.

   (d) It is possible to remove one steering mirror from both the 985 nm and 1973 nm arms and the second mirror from the 1973 nm arm. It might be possible as well to remove the second mirror from the 985 nm arm but at the cost of more difficult alignment.

   (e) Gold mirrors can be replaced with silver mirrors that have almost identical reflectivity at the pump wavelengths used, or with higher reflectivity dielectric mirrors.

   (f) If an isolator is added to the 1973 nm arm, it will be possible to completely remove the InGaAs detector. Otherwise it is possible to locate it on the second reflection from the BK7 wedge. Also, if properly attenuated and calibrated, an InGaAs detector can replace the thermopile detector (used for monitoring the 1973 nmnm output).

   (g) Lens mount MM4 (X-Y adjustable) can be replaced with a standard lens holder.

   (h) All kinematic mirror mounts can be standardised with a stainless steel, thermally stable 1" mounts (or $^1/2$" mounts if the optics is changed to $^1/2$").

7. In the laser segment:

   (a) A simpler mount for the HR mirror is needed.

   (b) HR and output coupler mirrors can be changed to $^1/2$" or smaller.

   (c) It is recommended to mount the fibre in a fibre holder that will span the entire length of the fibre and will clamp the fibre from both sides. This will improve thermal behaviour.

   (d) A better output coupler mirror holder is needed.

8. For future tuning:

   (a) Collimating optics are required and will be swapped with the current location of the output coupler mirror. It is preferable to use an appropriate mid-IR asphere for collimating over an off-axis parabolic mirror due to the difficulty associated with its alignment. However, the former is much more expensive.

   (b) A dispersive element will have to be introduced into the resonator, either a prism or a grating in Littrow configuration.

In Figures D.4-D.7, we display a minimal free space system based on the above comments. For simplicity, the current model and vendor have been maintained where there are no changes. Figure D.7 illustrates how a wavelength tuning design using a prism would operate.

Suggested pump sources

985 nm pump source

Diode driver
Thorlabs
LDC210C

974nm diode
Thorlabs
PL980P330J

TEC controller
Thorlabs
ITC510

Butterfly diode mount
Thorlabs LM14S2
(type 1 config card)

Original diodes' FBG
replaced with
985.23nm 9%
reflectivity FBG

LH1
FB1
L4

1D translation stage
Micrometer Z resolution

985nm laser
beam

Control unit
Lumina
Power

Diode driver
Lumina Power
LDD 150

Water chiller
Termotek
P1020-17865-5

790nm diode
LIMO 035-
F100-DL790

125 µm delivery fibre

99.5% 1973nm FBG
Teraxion PWS-HPR-1970-
1.6-99.5-PM10/130-0-1

1973 nm pump source

2.5 m spooled Tm fibre
Nufern PM-TDF-10/130

WDM combiner
790/1973nm

LH1
FB1
L3

1D translation stage
Micrometer Z resolution

1973nm
laser beam
+ residual
790nm
pump

Dichroic
HR790nm
AR1973nm

MM1

1973nm
laser beam

MM1 – Mirror mount, Thorlabs KS1
LH1 – Lens holder, Thorlabs HCS013

L3 – f=13.86mm asphere, Thorlabs C580TME-C Mounted in RMS09 adaptor
L4 – f=6.16mm asphere, Thorlabs C170TME-C Mounted in RMS08 adaptor

FB1 – Fibre holder, Thorlabs HFV001

Figure D.4: Detailed block diagram schematics of suggested minimal free space pump sources section.

Suggested mode matching section

1" silver mirror Thorlabs PF-10-03

MM2

Iris

MM5
L7

Dichroic 45degrees
HR@1973nm, AR@980nm
CVI SWP-45-RU1960-
TU980-PW-1025C

MM2

1" silver mirror
Thorlabs PF-10-03

MM2

MM5
L10

MM5
L6

1" silver mirror
Thorlabs
PF-10-03

MM2

985 nm
laser beam

Beam dump

MM1

BK7-wedge

Thermopile power
meter or properly
attenuated extended
InGaAs detector

1973 nm
laser beam

L5 – f=-75mm CVI, KPC037AR.18
L6 – f=100mm Thorlabs, C-coated
L7 – f=11.0 mm asphere, Thorlabs A220TM-C,
mounted in RMS09 adaptor
L10 – f= ~-150mm, Thorlabs

MM2 – Mirror mount, Newport Ultima U100A
MM5 – Lens mount, Thorlabs LMR1/M

Figure D.5: Detailed block diagram schematics of suggested minimal mode-matching section.

Figure D.6: Detailed block diagram schematics of suggested laser section.

Suggested laser section

output side with tuning

CaF$_2$ Dichroic – Altechna

Side 1 – PR 95% 3.5µm. AR @ 3.5 µm

Side2 – AR @ 3.5 µm

IR-Photonics ZBLAN fibre

1.7mol% Er, 10/125 µm, NA~0.15, 18cm

Collimating optics

CaF$_2$ prism

1D rotational stage
(micrometric or motorised)

MM7

2.8 µm /3.5 µm
laser beam
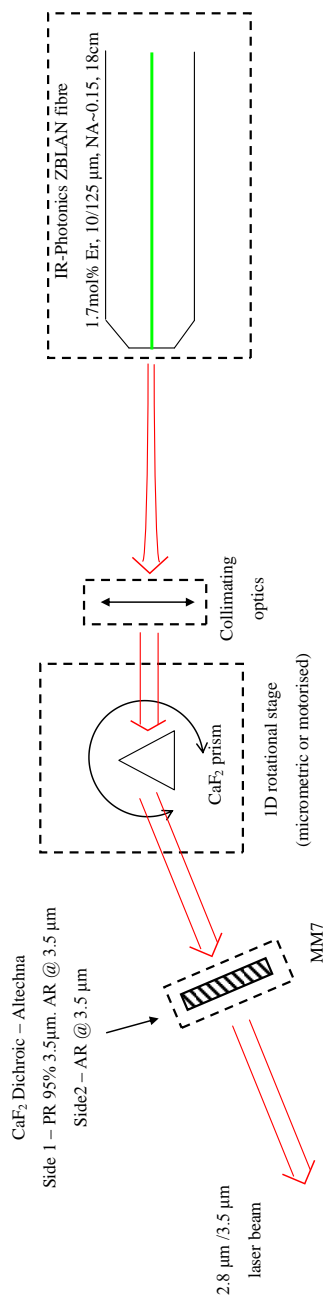
MM7 – Gimbal mirror mount, Thorlabs GM100/M

FB4 – Fibre holder, in-house design, spanning entire fibre length. Fibre sandwiched between aluminium holders including room for indium foil.

Figure D.7: Detailed block diagram schematics of suggested laser section with wavelength tuning.

D.3   All-fibre pump configuration

Fibre components for the 2 μm wavelength range are becoming more common off-the-shelf. This was not the case when this project was initiated. It is therefore possible to build an all fibre pump sources section, which would combine both pump beams in a single fibre.

Although splicing of silica-based fibres to ZBLAN fibres have been demonstrated in the past, it is usually a rather lossy and weak splice. If the all-fibre avenue is pursued, it is recommended to splice first the pump carrying silica fibre to an undoped ZBLAN fibre. This fibre would then be spliced to the doped ZBLAN fibre, with lower expected losses. Thermal and mechanical management of both ZBLAN splices would thus be significantly easier. There is currently little experience in splicing ZBLAN fibres at the University of Adelaide, therefore significant investments in time and resources would be needed to develop the appropriate processes.

Selecting a narrow bandwidth of operation in ZBLAN glass using an FBG has also been demonstrated, but the University of Adelaide does not have the appropriate equipment to do so in-house. To the best of our knowledge, there are currently no commercial avenues for creating FBGs in ZBLAN glass fibre. This might change in the coming years, though.

Figure D.8 portrays the configuration of an all fibre pump sources and their suggested launching optics. The laser segment would remain unchanged in its free-space form until future technical developments enable using an all-fibre configuration as well.
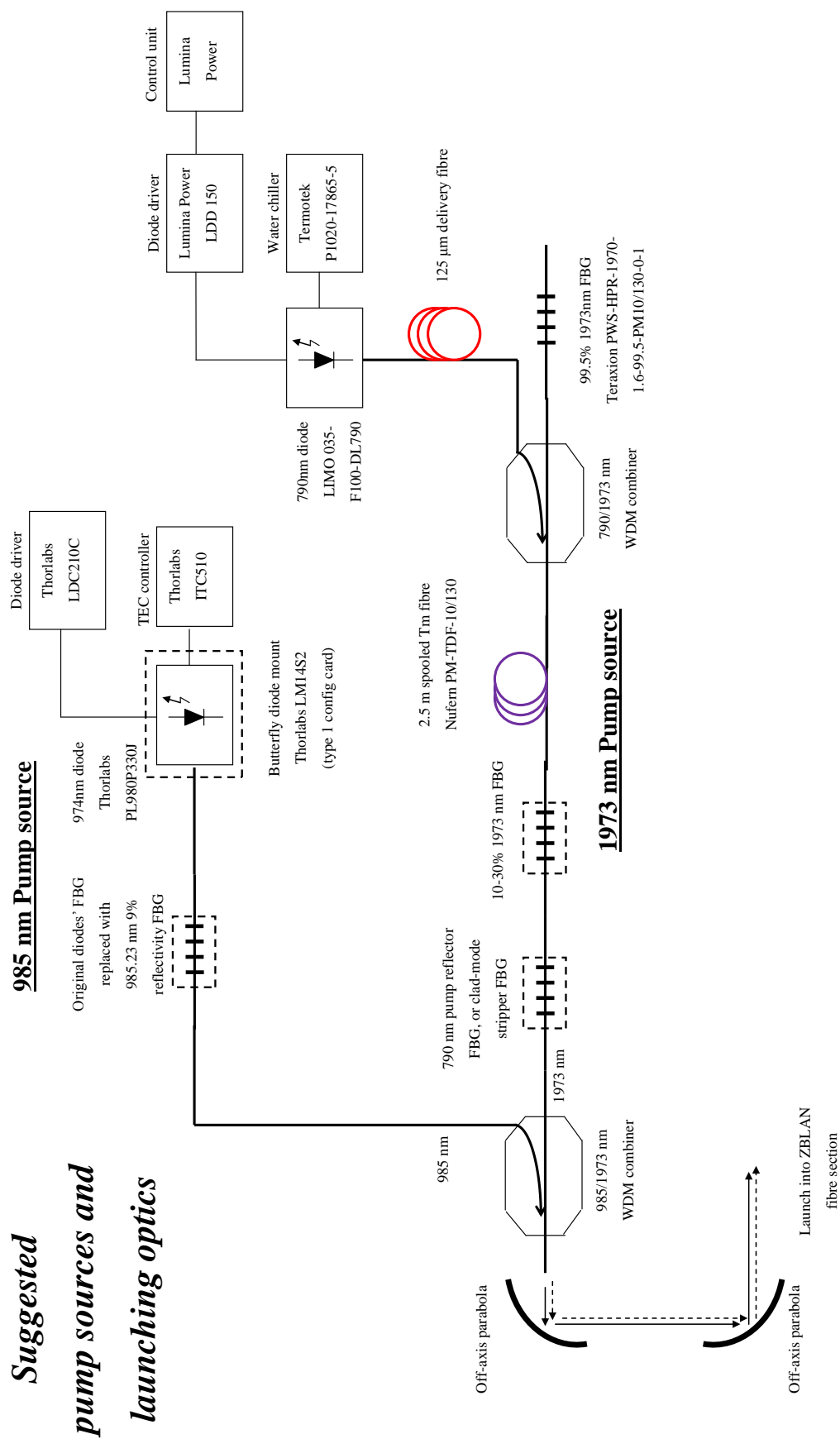
Figure D.8: Detailed block diagram schematics of suggested all-fibre pump section.

Appendix E

Thermal load in the fibre

Section 5.3 demonstrated a significant reduction in the $^4F_{9/2}$ level lifetime as a function of the 980 nm pump power. It was stated that the reduction is not likely to be the result of increased multi-phonon rate due to heating of the fibre. This claim is explained below.

E.1   Theoretical considerations

A significant amount of work has been done on the thermal analysis of fibre lasers [156, 174, 210–212] and it is generally accepted that the tip of the fibre on the pumped side requires special consideration. Heat is generated by the absorption of the pump and any phonon processes that result from the de-excitation of excited ions. Optical fibres are an extreme case of a system where the ratio of the length of the heat dissipating material is orders of magnitude larger than its cross-section. In all cases, the absorption length of the pump is significantly greater than the diameter of the fibre, meaning the heat transfer along the fibre is negligible. This results in a heat load density proportional to the pump absorption along the fibre [156, 213], with the highest absorption and hence temperature in the tip of the fibre. Due to this phenomenon, the fibre thermal equilibrium is completely based on lateral cooling by the materials surrounding the fibre core. This behaviour simplifies the thermal analysis to a radial heat transfer differential equations with no azimuthal dependency (assuming fibres with low or no eccentricity).

The equations governing the temperature distribution in the fibre at steady state are [211]

$$\frac{1}{r}\frac{\partial}{\partial r}\left(r\frac{\partial T_I(r)}{\partial r}\right) = -\frac{Q_0}{k(r)},\tag{E.1}$$

for the doped core region I ($0 \leq r \leq a$), and

$$\frac{1}{r}\frac{\partial}{\partial r}\left(r\frac{\partial T_{II}(r)}{\partial r}\right) = 0,\tag{E.2}$$

239

for the undoped cladding zone region II ($a \leq r < b$ and $b \leq r \leq c$). Here r is the radial coordinate from the centre of the fibre with a being the doped core radius, b the cladding radius and c the acrylate coating radius if present. T_0 is the temperature at the centre of the fibre while $T(r)$ is the temperature at radius r, Q_0 is the heat density and $k(r)$ the thermal conductivity of the appropriate fibre layer.

Applying the appropriate boundary conditions between the regions and Newton's law of cooling on the surface of the cladding, the equations could be solved analytically [211, 213]:

$$T_I(r) = T_0 - \frac{Q_0 r^2}{4k_1}, \quad (0 \leq r \leq a), \tag{E.3}$$

$$T_{II}(r) = T_0 - \frac{Q_0 a^2}{4k_1} - \frac{Q_0 a^2}{2k_1} \ln(\frac{r}{a}), \quad (a \leq r < b), \tag{E.4}$$

$$T_{II}(r) = T_0 - \frac{Q_0 a^2}{4k_1} - \frac{Q_0 a^2}{2k_1} \ln(\frac{b}{a}) - \frac{Q_0 a^2}{2k_2} \ln(\frac{r}{b}), \quad (b \leq r \leq c). \tag{E.5}$$

We assumed in Equation E.5 that the thermal conductivity of the core and cladding was the same k_1 and that the acrylate coating had a different thermal conductivity k_2. The temperature of the core relative to the coolant temperature T_c (air, heat sink, etc.) could be determined using

$$T_0 = T_c + \frac{Q_0 a^2}{4k_1} + \frac{Q_0 a^2}{2k_1} \ln(\frac{b}{a}) - \frac{Q_0 a^2}{2k_2} \ln(\frac{c}{b}) + \frac{Q_0 a^2}{2h_c c}, \tag{E.6}$$

where h_c is the convective heat transfer coefficient. The terms in Equation E.6 represent, from left to right after T_c, the drop in the temperature of the core region, the change in the cladding region, the drop throughout the coating and the temperature drop associated with convection at the acrylate coating-air boundary region.

We consider in this analysis that the fibre was free standing and the cooling mechanism was by air convection only. Under these conditions we could find the value of h_c using [174]

$$h_c = 50 \left(\frac{250}{r_{b,c}}\right)^{2/3} + 10, \tag{E.7}$$

where $r_{b,c}$ are the radii of the fibre's cladding or acrylate coating, if it exists, in μm.

Fibres cooled by the ambient air represent the worst case scenario and are usually taken as the case study for comparison between different fibre geometries, cooling methods and pump regimes. In our case, assuming cooling by conduction to air is indeed overly stringent. This is because parts of the fibre were either mounted between or on top of fibre holder blocks with indium foils that provided much better heat conductivity. In addition, using fans to increase the air flow around the fibre could significantly increase

the value of h. However, examining the theoretical behaviour of our fibres in air is useful as a comparison tool.

Lastly, the heat load density Q_0 could be evaluated using the launched pump power P_l, absorption coefficient of the fibre core α_c, the core radius a, the absorption length Δl and the pump and signal wavelengths λ_p and λ_s. The later were used under the assumption of heat generated due to the Stokes efficiency of the system.

$$Q_0 = \left(1 - 10^{-\alpha_{c\,dBm^{-1}}\Delta l/10}\right) P_l \frac{1 - \frac{\lambda_p}{\lambda_s}}{\pi a^2 \Delta l} \tag{E.8}$$

for $\alpha_{c\,dB/m}$ in dBm^{-1}, for α_c in cm^{-1} and δl in cm

$$Q_0 = \left(1 - exp^{-\alpha_c \Delta l}\right) P_l \frac{1 - \frac{\lambda_p}{\lambda_s}}{\pi a^2 \Delta l} \tag{E.9}$$

If pumping into the inner cladding, the reduction in absorption as a result of the ratio of the core to inner cladding area must be taken into account. In such circumstances, core and cladding areas are used to convert from the cladding absorption coefficient to the core absorption coefficient using

$$\alpha_d = \alpha_c \frac{a^2}{b^2}. \tag{E.10}$$

Equation E.6 is suitable for a general heat source case which does not assume lasing. Gorjan et. al. provided an equivalent equation which is derived from Equation E.6 and was applicable for ordinary, singly pumped lasers using common fibre laser parameters [156].

$$T_0 = P_{inc} \frac{(1 - \eta_s)\lambda_L \alpha_c V_{\#\,core} a}{8\pi^2 k b^2} \left[1 + 2\ln(\frac{b}{a}) + \frac{2k}{bh_c}\right]. \tag{E.11}$$

Here, η_s was the slope efficiency of the lasers which replaced the Stokes efficiency parameter, λ_L the wavelength of the laser, α_c the core absorption coefficient (in cm^{-1}) and $V_{\#\,core}$ the V number (normalised frequency) of the core. Equation E.11 assumes no coating, hence a single thermal conductivity coefficient k is used.

E.2   Thermal analysis of fibre used

We can now apply the theoretical considerations discussed in the previous section to the fibres used in our system. Figure E.1 shows the radial temperature variation relative to the ambient air temperature for a fibre with and without an acrylate coating. This example is based on lasing at 2.75 μm using an IR-Photonics fibre parameters (see Table E.1). This example is used to allow comparison with results from the literature,

where 2.75 μm fibre lasers are usually analysed. We assume a fixed heat load density based on the quantum defect of pumping at 985 nm and lasing at 2.75 μm. The temperature difference ΔT is calculated according to Equations E.3 and E.4 under natural convection conditions with no forced air cooling.
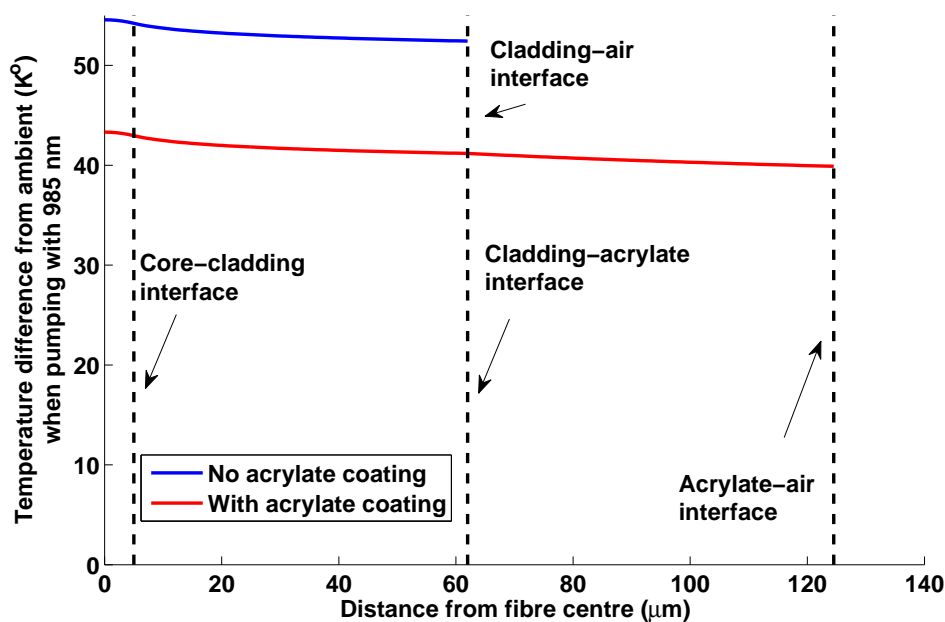

Figure E.1: Calculated lateral temperature difference from ambient at the input facet of a pumped doped fibre assuming quantum defect based heat load. The parameters used in this calculation are were based on the IR-Photonics fibre with an Er^{3+} ion doping concentration of 1.7 $mol\%$. Launched 985 nm pump power is 170 mW. In this plot we assumed a Stokes efficiency of 65% equivalent to lasing at 2.75 μm while only using a 985 nm pump.

The temperature distribution varied quadratically in the doped core while falling logarithmically in the cladding region. Although there was a clear temperature difference between the centre of the core and the cladding, this difference was essentially negligible compared to the difference between the ambient and the fibre core temperatures. This thermal distribution behaviour is typical of fibres in general [57, 213, 214].

Two effects common in fibre lasers can be observed in Figure E.1. The first is the small temperature variation across the fibre. This is the result of the relatively small distance between the heat generation region (the core) to the area being cooled by the surrounding air. The calculated temperature difference between the core and the fibre envelope was rarely more than 10% of the temperature difference between the core and ambient temperatures. This behaviour is true even for kW class fibre lasers [211]. The second effect was the reduction of the overall temperature rise with the

Table E.1: Thermal analysis parameters.

Definition	Parameter symbol	Value
Ambient air temperature	T_c	$291°K$
Maximum launched pump power	P_l	
@ 974 nm		$194\ mW$
@ 985 nm		$170\ mW$
Maximum heat load density	Q_0	
@ 974 nm		$3.6 \times 10^{10}\ W/m^3$
@ 985 nm		$6.9 \times 10^9\ W/m^3$
Core radius	a	$5\ \mu m$
Cladding radius	b	$62.5\ \mu m$
Acrylate coating radius	c	$125\ \mu m$
Thermal conductivity - core and cladding [57]	k_1	$0.632\ W/m\,°K$
Thermal conductivity - acrylate [212]	k_2	$0.24\ W/m\,°K$
Convective heat transfer coefficient	h_c	
No coating		$136\ W/m^2\,°K$
With coating		$89\ W/m^2\,°K$

introduction of the acrylate coating. The coating itself had a significantly lower thermal conductivity compared with the glass. However, the increased surface area associated with usual diameters of acrylate coatings more than compensated for the reduced thermal conductivity.

We have so far assumed that the heat generated was the result of the Stokes efficiency of the system and that energy not turned into lasing generated heat. Specifically in the case portrayed in Figure E.1, we assumed pumping at 985 nm while lasing at 2.75 μm. However, this assumption was the worst case scenario, since spontaneous emission is always significant and does not contribute to the heat load. This was also true in our lifetime measurements where there was no lasing present and strong fluorescence was observed at many wavelengths. Therefore, to get a more accurate estimate of the thermal load, we needed to take into account the actual decay rates, radiative and non-radiative from each level. Table E.2 details the lifetimes, branching ratios, radiative efficiency and energy lost for the transitions relevant for Er^{3+}:ZBLAN. The method for calculating the non-radiative rate and the branching ratios was taken from Pollnau [215], where the non-radiative rate from one state to the one below it was determined by

$$A_{i,NR} = \frac{1}{\tau_i} - \sum_{j=0}^{i-1} A_{i,j}. \tag{E.12}$$

Table E.2: Spectroscopic parameters, non-radiative decay percentage and energy lost by heating analysis. The lifetimes τ_i are the intrinsic lifetimes (i.e. including radiative and non-radiative decay) and are the average of literature values of measured lifetimes detailed in Table 2.5. Branching ratios β_{ij} take into account both radiative and non-radiative decay and are calculated using Equations E.13-E.15. Radiative lifetimes and radiative branching ratios are taken from Caspary [146].

Starting level and transition	Intrinsic lifetime τ_i (ms)	Branching ratios β_{ij} (%)	Non-radiative fraction of transition to next lower level $\eta_{i,i-1}$ (%)	Energy gap to next lower level (cm^{-1})
$^4F_{7/2} : \beta_{65}$		100	100	1330
$^2H_{11/2}/^4S_{3/2}$: $\beta_{5,4\rightarrow0}$	0.55	25, 3, 2, 20, 50	99.8	3149
$^4F_{9/2} : \beta_{4,3\rightarrow0}$	0.15	82.6, 0.8, 0.8, 15.8	99.9	2823
$^2I_{9/2} : \beta_{3,2\rightarrow0}$	0.009	100, 0, 0	100	2246
$^2I_{11/2} : \beta_{2,1\rightarrow0}$	7.32	29, 71	49	3651
$^2I_{13/2} : \beta_{1,0}$	9.1	100	0	6535
Average energy lost to heat for a single GSA transition $\sim 510\ cm^{-1}$				
Average energy lost to heat for a single ESA transition $\sim 3650\ cm^{-1}$				

Here, τ_i is the intrinsic, or measured, lifetime. For our purpose, we use the average of literature values summarised in Table 2.5. The $A_{i,j}$s are the calculated radiative transition rates from each level to the levels below it from Caspary [146]. The branching ratios include the non-radiative decay to the energy level below as well, according to:

$$\beta_{i,j} = (A_{i,j} + A_{i,NR})\tau_i \qquad \text{with } i - j = 1, \qquad (E.13)$$

$$\beta_{i,j} = A_{i,j}\tau_i \qquad \text{with } i - j > 1, \qquad (E.14)$$

$$\eta_{i,i-1} = A_{i,NR}/(A_{i,i-1} + A_{i,NR}). \qquad (E.15)$$

In Equation E.15, $\eta_{i,i-1}$ is the fraction of the transition from one level to the one below that is non-radiative and is therefore dissipated as heat. The total energy dissipated as heat for a GSA or ESA absorption is calculated using an iterative process following decay "chains" (see Figure E.2). In this process we count all possible decay avenues from the excited level to the underlying levels. Each of the decay "chains" is weighed according to decay probabilities, which are defined by the branching ratio. The heat deposited in this stage is the product of the branching ratio to the next lower level and the energy gap between the levels. We repeat this process with the next level, however, the fraction of ions that progress to the next lower level, relative to the total number of ions, is a product of two branching ratios. We continue in this fashion until all possibilities of decay to the ground level have been mapped, decay probabilities following a certain decay
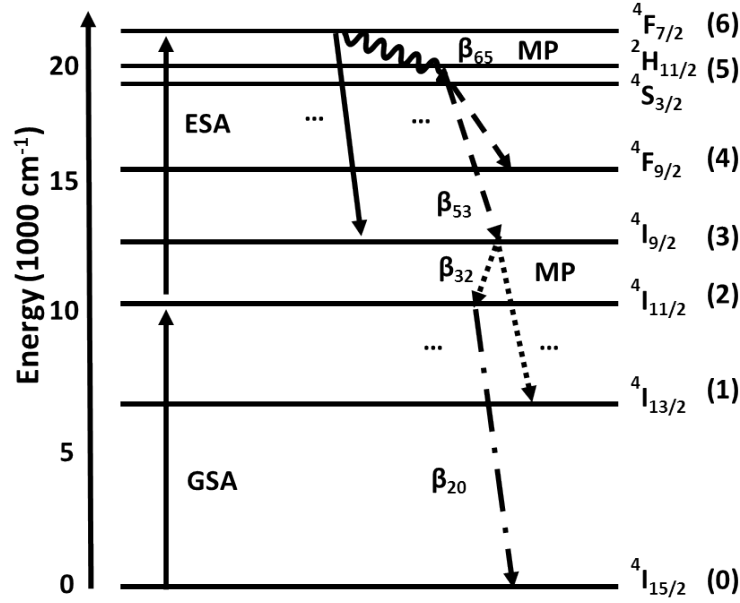
Figure E.2: Example of a decay chain for an excited ion following ESA. Ellipses represent additional decay possibilities which are not drawn. MP stands for multi-phonon decay and energy dissipated following this chain. The branching ratios shown (β_{ij}) are the ones followed in this particular chain.

"chain" have been found and the energy loss in every possible "chain" has been found. The total energy dissipated can thus be calculated by summing all decay chains with their respective energy loss. By using the non-radiative decay parameters in Table E.2, we calculated that the strongest contribution per single excitation was the result of ESA and not the decay from the $^4I_{11/2}$ level. This trend has been noted before in Er^{3+} doped LiYF$_4$ [114, 216]. Consequently, to reduce the heat load it was necessary to lower ESA and energy-transfer processes. This can be achieved by adjusting doping concentration, as well as changing the pump wavelength to one with a lower ESA cross-section.

From a quantitative perspective, the fraction of the absorbed pump power that was deposited as heat $\eta_{Q_{pump}}$ in the fibre was

$$\eta_{Q_{pump}} = \eta_{R\,GSA}(\lambda) \cdot \eta_{NR,GSA} + \eta_{R\,ESA}(\lambda) \cdot \eta_{NR,ESA}. \tag{E.16}$$

Here $\eta_{R\,GSA/ESA}(\lambda)$ are the fractions of ions that had undergone GSA or ESA transition out of all ions that absorbed a pump photon. This is equivalent to the ratio between the GSA or ESA pump rates to the total pump rate. This fraction is a function of the pump wavelength and its respective absorption cross-section. $\eta_{NR,GSA/ESA}$ are the fractions of energy lost to heat with every GSA/ESA transition. We can now substitute $\eta_{Q_{pump}}$ into Equations E.8 or E.9 instead of the $1 - \frac{\lambda_p}{\lambda_s}$ factor to obtain the fraction of absorbed power lost to heat. If the absorbed pump power is known, we can substitute it into

Equation E.9 and obtain

$$Q_0 = P_{abs} \frac{\eta_{Q_{pump}}}{\pi a^2 \Delta l}. \tag{E.17}$$

To estimate the fraction of GSA and ESA transitions $\eta_{R\,GSA/ESA}$, we used a simple rate equation simulation, which was based on the rate-equations in section 1.5.4, that calculated the GSA and ESA pump rates and the ionic population. The values obtained from the simulation of the highest pump power available are given in Table E.3.

Table E.3: Pump converted to heat parameters. For both pump wavelengths, the fractions of energy lost to heat due to non-radiative decay per photon are $\eta_{NR\,GSA}(\lambda) = 5\%$ and $\eta_{NR\,ESA}(\lambda) = 36\%$

Pump wavelength λ_p (nm)	Fraction of ions undergoing GSA transition $\eta_{R,GSA}$ (%)	Fraction of ions undergoing ESA transition $\eta_{R,ESA}$ (%)	Total percentage of absorbed pump converted to heat $\eta_{Q_{pump}}$ (%)
985	71	29	13.7
974	42	58	22.4

Pumping at 985 nm results in significantly lower heat load than 974 nm pumping. Only 13.7% of the absorbed pump was converted into heat when pumping at 985 nm compared to 22.4% when pumping at 974 nm. In both cases, however, the calculated percentage of energy lost to heat is significantly lower than the 65% predicted by the model using the Stokes efficiency approach (assuming all non lasing energy is turned into heat).

The simulation provided additional insight (see Figures E.3(a)-E.3(d)). We can conclude that the GSA and ESA rates were very different for pumping with 985 nm and 974 nm. Specifically, we calculated that the ESA rate exceeds the GSA rate for most pump powers when pumping with 974 nm. In addition, the distribution along the fibre was very different, with the absorption being much more evenly distributed when pumping with 985 nm compared with the shorter absorption length using the 974 nm for pumping.

The linear dependence of Equation E.6 in the heat load Q_0 results in a linear change in the temperature of the core of the fibre with an increase in the heat load density. This resulted in only a modest calculated temperature increase ΔT of $8 - 11°K$ in the core when pumping with 985 nm, while an increase on the order of $\Delta T = 40°K$ was calculated for a coated fibre under 974 nm pumping (see Figure E.4). These results can be compared with the temperature difference of $43 - 54°K$ from ambient shown in Figure E.1 using the Stokes efficiency approach.

These calculated results are still too severe because Equation E.9 assumes an exponential absorption of the pump, which is not applicable close to the fibre tip due to pump
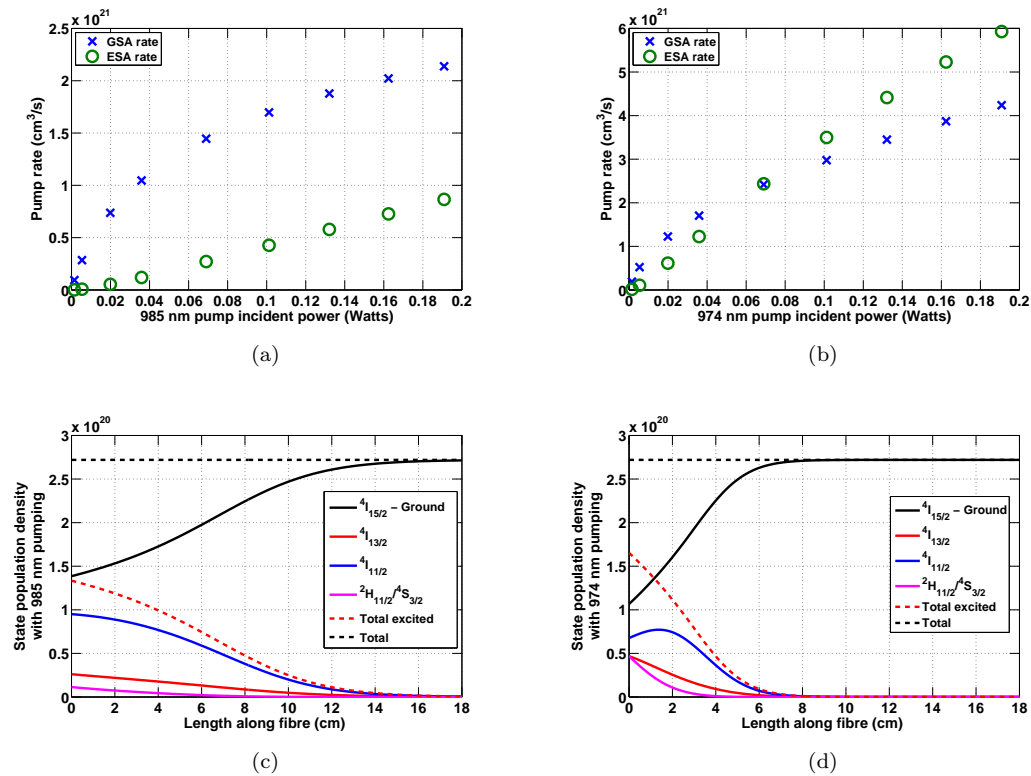
Figure E.3: Simulation of the ion density distribution along 18 cm IR-Photonics fibre. Maximum simulated pump power corresponds to 194 mW of incident power (about 170 mW launched power). (a) and (b) - GSA and ESA rates simulated at the first 1 mm segment of the fibre with first pump operating at 985 nm and 974 nm, respectively. (c) and (d) - Ion population density at different energy levels along the fibre at the highest pump power with 985 nm and 974 nm, respectively.
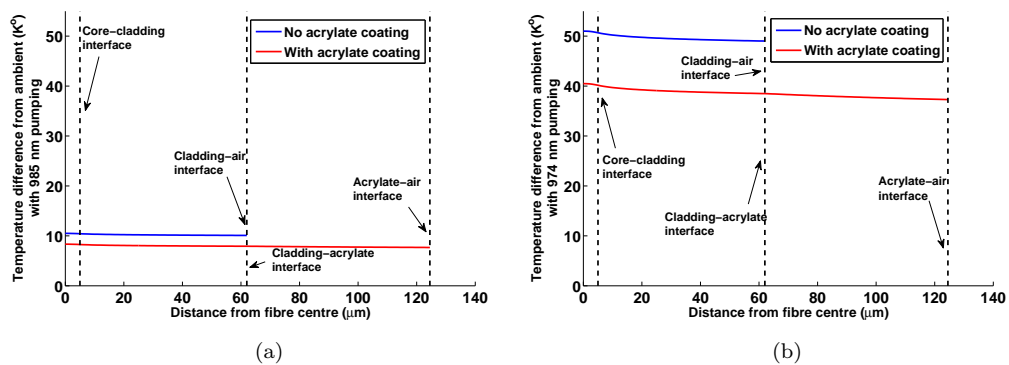

Figure E.4: Calculated heating of the core at the input facet of an IR-Photonics fibre with 985 nm and 974 nm pumping without considering bleaching of the pump. (a) Pumping with 985 nm, (b) pumping with 974 nm.

absorption saturation. The simulations allow us to estimate the actual amount of pump absorbed in the first 2 mm of the fibre and calculate the heat load density accordingly. The simulated absorbed pump power is only about one half of the calculated absorbed power with a pure exponential decay, resulting in approximately 50% reduction in the calculated fibre temperature. Final calculated temperature profiles are displayed in Figure E.5.
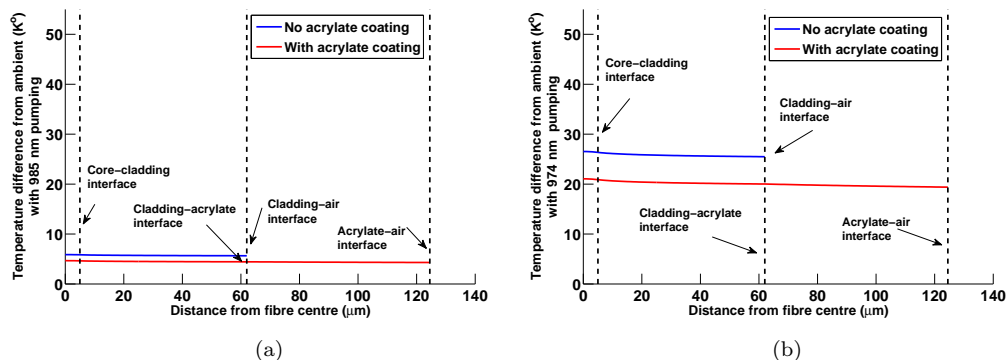

Figure E.5: Calculated heating of the core at the input facet of an IR-Photonics fibre with 985 nm and 974 nm pumping taking into account bleaching of the pump. (a) Pumping with 985 nm, (b) pumping with 974 nm.

In this appendix, we only consider the effect of absorption of the first pump because the 1973 nm pump absorption is strongly dependant on the population of the $^4I_{11/2}$ level, which is decaying along the fibre. Therefore, the propagating 1973 nm power does not follow an exponential pattern and is strongly affected by the launched power as well. We saw in section 5.3 that there was no significant change in the $^4F_{9/2}$ level lifetime when varying the 1973 nm pump level. Additional heating due to 1973 nm absorption would have had negligible contribution to the lifetime quenching effect. We therefore finish our theoretical thermal investigation at this point and the effects of heating due to the absorption of both pumps is left for future work.

E.3 Cooling of fibre

The aforementioned results demonstrated that there was no incentive to use a cooling method to improve the lifetime of the upper laser level ($^4F_{9/2}$) under 985 nm pumping, since the pump only caused a minor increase in the fibre temperature.

During some of our experiments, we tested whether there was any effect of using forced air cooling on the fibre. A small CPU fan was placed in proximity to the fibre to blow air on the fibre tip. This was done while operating in dual-wavelength pumping in some

fluorescence lifetime experiments as well as some lasing experiments (see Chapter 6). The changes observed in the results of lifetime experiments as well as lasing performance were mostly negligible, and actually disruptive at times due to increased movement of the fibre tip. The heat load in these situations was considerably different because of the addition of heating from the 1973 nm pump absorption and the change in ion density distribution along the fibre. Full analysis of these cases requires a comprehensive numerical model, which includes the effect of lasing and is thus left for future work.

The analysis in this appendix suggests that if in future experiments we would choose to operate with the 974 nm pump, it may be beneficial to apply cooling methods such as forced air cooling. Possible example for such a situation would be core pumping of a fibre such as the FiberLabs ZDF fibre. Due to its higher doping concentrations, the ZDF fibre would suffer from approximately two and a half times more heating per unit length compared to the IR-Photonics fibre, increasing the incentive to use active cooling methods. However, a double-clad fibre such as the FiberLabs one is expected to be pumped into its inner cladding, drastically reducing the heat load of the fibre tip unless very high incident power is used.

E.4   Thermal analysis - conclusions

This appendix shows that the lifetime quenching observed with increased power of the first pump cannot be attributed to heating of the fibre when pumping at 985 nm. This follows from the calculations of multi-phonon decay rates given in 2.4.2, which predicted only a modest increase in temperature of 10°K-20°K. This increase would result in a 3%-6% increase in the multi-phonon rate and therefore would create only a negligible reduction in the lifetime observed for the $^4F_{9/2}$ level. Even when operated at 974 nm with a temperature increase of 50°K, the expected reduction in $^4F_{9/2}$ lifetime due to thermal effect should have been less than 10 μs. The available evidence supporting operation at 985 nm as compared to 974 nm makes the fibre cooling issue not relevant until very high incident power levels are used. In that case, a double-clad fibre is more likely to be used, thus alleviating heating problems until pump powers of hundreds of watts are used.

Appendix F

Detailed experimental procedure for in-fibre lifetime measurement

The following procedure was used to observe and measure the lifetime of the $^4F_{9/2}$ level, using the rate of the 657 nm fluorescence as an indicator of its population under dual-wavelength pumping conditions. Figure 5.1 is repeated here and is used as the reference for the experimental setup.

1. Initially the alignment of both pump beams was verified, the detectors were turned on, the mechanical chopper was started and all instruments were tested to ensure communication with the controlling computer.

2. A reference scan was run with both pumps turned off to zero all instruments.

3. The 985 nm pump was run at different power levels. For each 985 nm pump power level:

   (a) A spectrometer scan was run between 960 and 1000 nm with the 1973 nm pump off. The detector voltage from the fluorescence at 995 nm was recorded. This value was later used as a reference so a similar fluorescence level (and therefore $^4I_{11/2}$ excited population levels) was obtained when the first pump wavelength was changed to 974 nm in step 5. 995 nm was used as it was sufficiently removed from both 974 nm and 985 nm that scattered pump light did not interfere with the natural $^4I_{11/2}$ fluorescence.

   (b) For each of the 1973 nm power levels, we followed the Matlab® prompts:

      i. The 985 nm pump beam was blocked.

      ii. The incident 1973 nm power from the pick-off was recorded and the transmitted 1973 nm pump power through the fibre was measured using the thermal power meter.
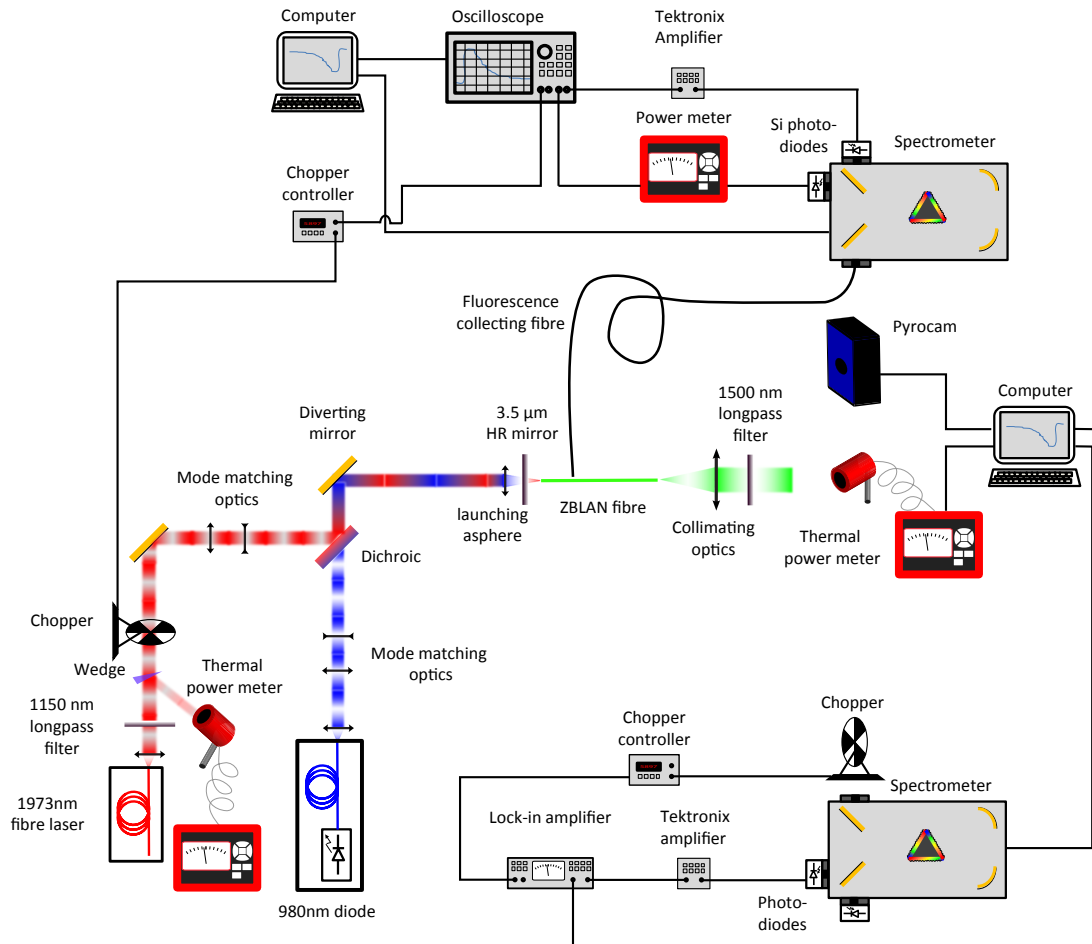
Figure F.1: General purpose experimental setup for additional spectroscopy measurements. The beam emerging from the ZBLAN fibre could be directed towards either a thermal power meter, a thermal camera or a grating spectrometer.

iii. The 985 nm beam was unblocked. After the power readings stabilised (3 seconds), readings were recorded of incident 1973 nm from the pick-off and the total transmitted power from the thermal power meter after the fibre. The 1500 nm longpass filter ensured the transmitted power reading only included the 1973 nm power.

iv. The spectrometer's wavelength was changed to 551 nm and peak fluorescence levels of the $^4S_{3/2} \to \, ^4I_{15/2}$ transition were recorded. This reading provided a pump-power-related relative measurement of the population changes at the $^4S_{3/2}$ level.

v. The spectrometer wavelength was changed to 655 nm. 655 nm fluorescence decay trace was recorded. This measurement was used for the lifetime analysis as well as for the relative measurement of population of the $^4F_{9/2}$ level. The recorded decay trace averaged over 128 individual traces.

vi. The wavelength of the spectrometer was changed to 800 nm and maximum fluorescence levels of the $^4I_{9/2} \to \, ^4I_{15/2}$ transition were recorded.

vii. The wavelength of the spectrometer was changed to 847 nm and maximum fluorescence levels of the $^{4}S_{3/2} \rightarrow {}^{4}I_{13/2}$ transition were recorded.

viii. The wavelength of the spectrometer was changed to 995 nm and maximum fluorescence levels of the $^{4}I_{11/2} \rightarrow {}^{4}I_{15/2}$ transition were recorded.

ix. The output port of the spectrometer was switched to enable readings using the InGaAs detector.

x. The wavelength of the spectrometer was changed to 1550 nm and maximum fluorescence levels of the $^{4}I_{13/2} \rightarrow {}^{4}I_{15/2}$ transition were recorded.

4. After reading fluorescence at all wavelengths, the first pump wavelength was changed to 974 nm by adjusting its Peltier cooling setting.

5. Stage 3 was repeated whilst at each step the 974 nm pump power was adjusted to achieve the same detector voltage reading measured in stage 3a when measuring fluorescence at 995 nm. This process ensured similar levels of population density at the $^{4}I_{11/2}$ level and a better comparison between pumping with 974 nm or 985 nm.

6. Waveform fitting on all results was conducted to extract the decay lifetime constant at each combination of pump powers. The data were saved to a file and plots were automatically generated.

Appendix G

Laser alignment methods

In this appendix, we describe the methods used for aligning the 3.5 μm laser based on the IR-Photonics fibre. These alignment methods are provided as a guide for future users of the current DWP system and for additional systems to come. Similar methods to the ones provided here were used through the work with other fibres as well, although no lasing at 3.5 μm was obtained using other fibres. Throughout this appendix, we refer to the first pump as the 980 nm pump, since the same procedure applied when using either 974 nm or 985 nm. The co-alignment of both pump beams is detailed in section G.1. This is followed by the procedure of mode-matching of the pump beams to the ZBLAN fibre, which also included finding the location of the highly-reflective (HR) resonator mirror (section G.2). We then describe the procedure to ensure both beams arrive parallel to the optical table past the launching aspheric lens (section G.3). The alignment of the ZBLAN fibre to the incoming pump beams is explained in section G.5. In section G.6 we describe the alignment of the off-axis parabola (OAP) necessary for observing the fluorescence coming from the ZBLAN fibre. Finally, we describe how the highly-reflective (HR) mirror and the output coupler (OC) resonator mirrors were positioned relative to the fibre to achieve initial lasing at 3.5 μm and then maximise its power.

G.1   Pump beams co-alignment

The initial co-alignment of both pump beams ensured that both the 980 nm and 1973 nm beams were coarsely incident at the same location on the dichroic mirror and pointing in the same direction. Very-fine tuning of the co-alignment was later achieved during the alignment of the pump beams' pointing direction in section G.3. Figure G.1 displays the components used throughout the beams co-alignment process. The beams are co-aligned by:
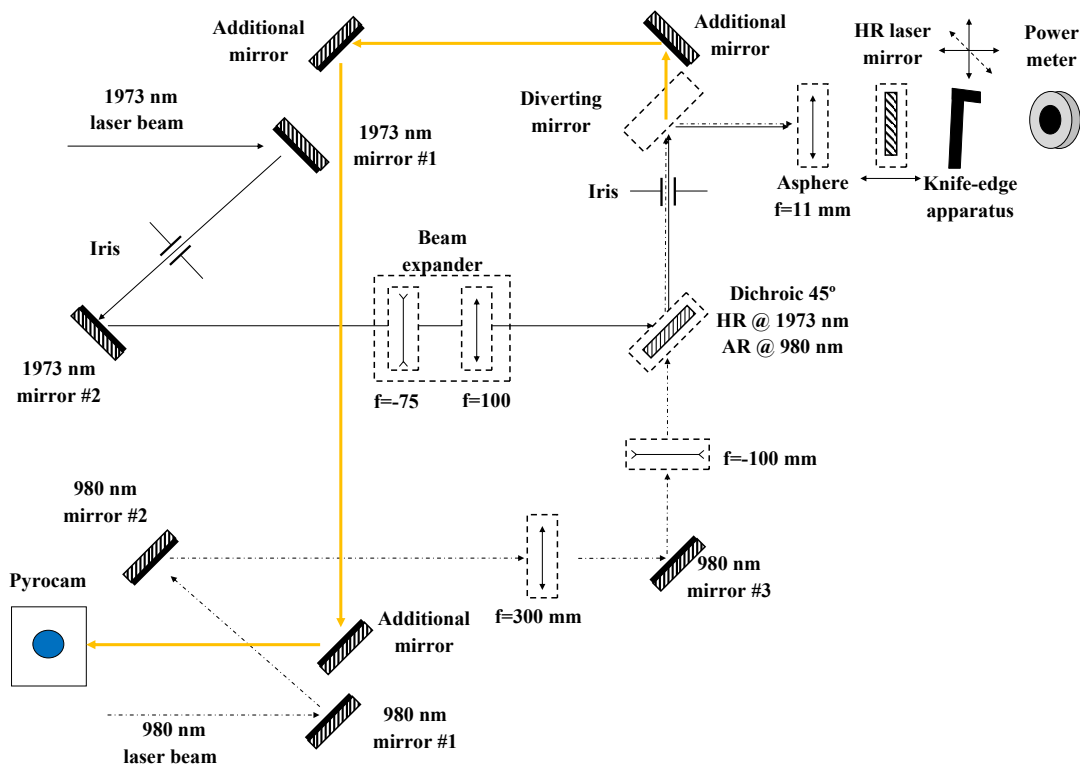
Figure G.1: Diagram of components used for mode-matching, co-alignment and beam pointing of pump beams.

1. Align the 980 *nm* beam to roughly hit the centre of the dichroic mirror by adjusting the first two steering mirror on the 980 *nm* arm.

2. Align the 1973 *nm* beam to roughly hit the centre of the dichroic mirror by adjusting the first two steering mirrors on the 1973 *nm* arm.

3. Remove the mirror diverting the beam towards the asphere. Mount three additional mirrors (for space reasons) that point the beams after the dichroic towards the end of the optical table.

4. Use the 980 *nm* beam as a guide (since it can be viewed easily with an IR-viewing card) and adjust the mirrors to ensure the beam is at a constant height of 75 *mm* above the optical table to the end of the table.

5. Place the Pyrocam at the end of the table with its centre at the 980 *nm* beam centroid. The Pyrocam is used instead of a second iris, because it makes locating the 1973 *nm* beam much easier.

6. Locate an iris centred on the 980 *nm* beam immediately after the dichroic mirror.

7. Repeat the following iterative process until both beams are perfectly co-aligned, starting with a fully open iris:

(a) Adjust the two steering mirrors on the 1973 nm arm to position the 1973 nm beam at the centre of the iris.

(b) Adjust the dichroic mirror to bring the 1973 nm beam to the centre of the Pyrocam.

(c) Reduce the iris opening.

8. If the dichroic is adjusted significantly in the horizontal direction, it will cause the 980 nm beam to shift from the centre of the iris. In this case, reposition the iris slightly to be centred on the 980 nm beam and repeat stages 7a-7c.

9. The beams should be co-aligned now. The diverting mirror prior to the asphere should be replaced.

G.2   Pump beams mode-matching

Both pump beams have to be mode matched into the ZBLAN fibre core. Mode-matching was adjusted prior to fine co-alignment of the pump beams because it was retained in the long term with occasional fine co-alignment due to thermal drift or changing the position of the fibre. Figure G.1 displays the components used throughout the beam mode-matching and co-alignment process.

The chromatic dispersion of the asphere that launches the pump into the fibre plays a significant role in determining the location of the waist of each pump beam because each pump operates at a very different wavelength. To compensate for chromatic dispersion and ensure the correct mode size at each pump wavelength, additional optical elements were inserted along the optical path of each pump beam.

We used a dual-axis, two blade, knife edge apparatus to measure the beam waist locations and divergences after the launching asphere (see Figure G.2). These knife edges were made from razor blades mounted at ninety degrees to each other with the flat sides facing towards the incoming pump beams. The knife edges were mounted on a 2D translation stage, allowing movement perpendicular to the incoming beams, with approximately 2 μm of resolution. The two-dimensional stage was mounted on an additional translation stage with 50 mm travel with positioning accuracy of about 5 μm resolution.

In order for the two pump waist locations to coincide, it was necessary to find the size and location of each waist and then modify the locations of the mode-matching optics for the relevant pump. To roughly find the location of the waist at 980 nm, it was possible to mount an IR-detection disk (Thorlabs VRC4D1) with a 1.5 mm hole in it
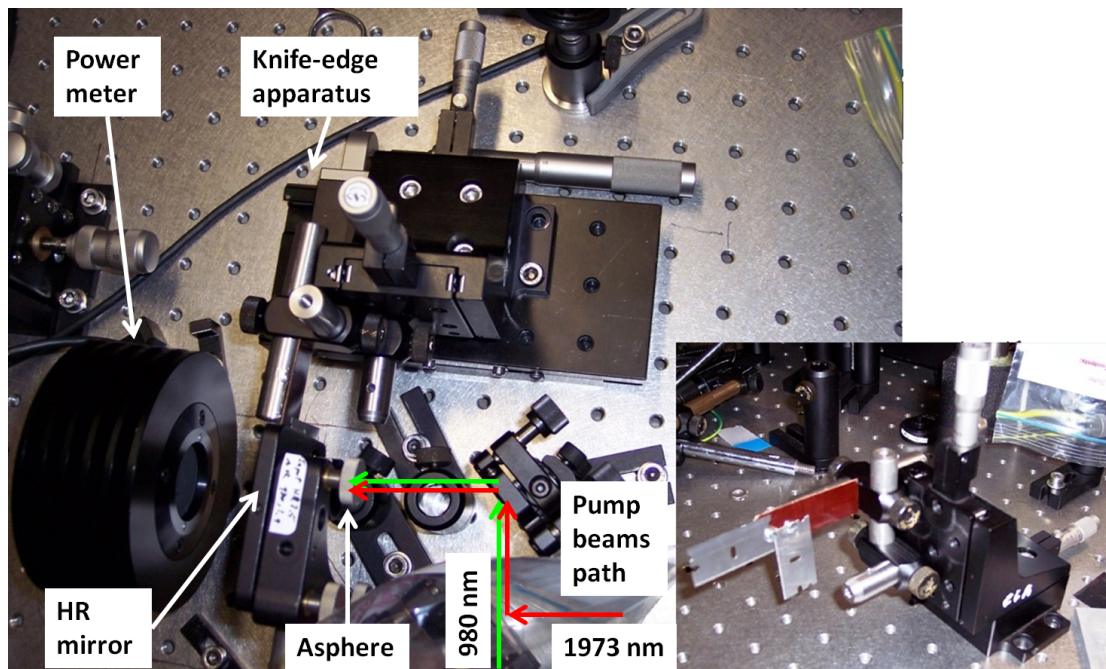
Figure G.2: The knife edge apparatus used for finding and measuring in three-dimensions the location and size of the waists of the pump beams and the divergence of the beams. The inset shows the two knife-edged apparatus. The same setup in conjunction with the beam steering mirrors was also used for adjusting the pump beam pointing, which is described in section G.3

after the second 980 *nm* pump diverting mirror. The disk was facing away from the propagating beam. The hole allowed the pump beam to pass through undisturbed while the reflected pump beam was registered by the disk. When the knife edge was moved to block the 980 *nm* beam, a fraction of the pump would scatter backwards towards the incoming pump. The backwards propagating light travelled the same path as the inbound propagating beam. Therefore, when the knife edge was close to the waist, it created an image of the reflected pump (see Figure G.3). The image is thus smallest (i.e. passing completely through the hole) when the knife edge is exactly at the waist and becomes larger and clearly visible when the knife edge is moved away from the waist until it fades away when the knife edge is sufficiently far from the waist. The above method enabled only a rough location of the waist since the knife edge, made from razor blades, had slight angles and curved tips on the microscopic scale. Therefore, the exact waist location deviated by a couple of tens of microns, which was still within the Rayleigh range.

A more accurate measurement of the size and location of the waist followed using a beam quality measurement. The knife edge apparatus was set at a certain location along the optical axis and the beam size was measured by translating the razor blade perpendicular to the beam. The apparatus was shifted along the optical axis and another beam diameter measurement was taken. After repeating this process at multiple locations sufficiently far
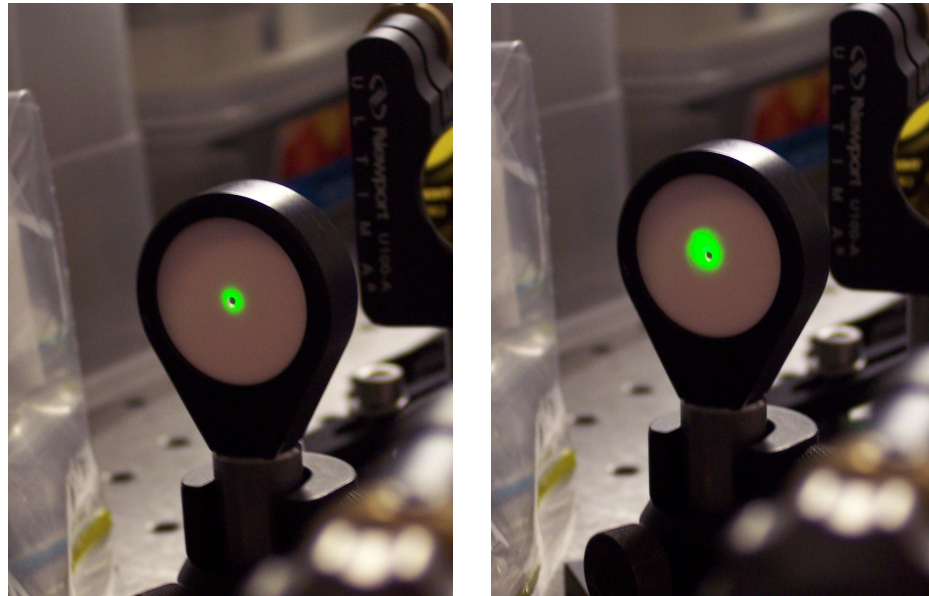
Figure G.3: Back-reflected image of the 980 nm pump. Left - near perfect position of the knife-edge; Right - knife-edge further from the waist.

from the waist, the waist location was calculated using the beam divergence. The exact location of the waist was verified by moving the apparatus by fine increments of 10 μm at a time. Through this process, the exact location of the waist, Rayleigh range and beam divergence were found. The 1973 nm pump beam could not be resolved optically in the same manner as the 980 nm beam, so its waist location had to be found using the more accurate method described above.

Once the location and size of the waists were determined, it was necessary to adjust the waists to match the mode-field-diameter of the fibre used at the relevant wavelength. In addition, it was necessary to adjust the divergence of the pump beams so they would compensate for the chromatic dispersion of the asphere, resulting in both waists being co-located after the launching asphere. The original 1973 nm beam size was designed for use with the FiberLabs fibre and thus produced a waist of approximately 14μm. The IR-Photonics fibre with its 10μm core needed a reduction of $\sim 30\%$ in diameter. For a constant focusing power, the waist size was inversely proportional to the beam size, hence a beam expander of $\sim 30\%$ was constructed on the 1973 nm arm, using confocal $f = -75$ mm and $f = 100$ mm lenses.

Control over the waist location was achieved using slight modifications of the collimating condition of the 1973 nm fibre laser. By shifting the collimating aspheric lens from the perfect collimating location, the beam divergence was changed. This shifted the waist location accordingly, i.e., if the aspheric lens was moved further from the 1973 nm fibre laser tip, the beam would slowly converge, thus the waist would occur earlier along the

beam's propagation path and vice verse. To achieve good launch efficiency of both beams, it was necessary for the waist locations to be within 10-20 μm of each other.

It was possible to calculate the changes required in the aspheric lens location to bring the 1973 nm waist closer to the 985 nm pump waist using ABCD law calculations [217]. A similar method was used on the 985 nm beam path. The 985 nm arm also needed compensation for the different waist size required for the IR-Photonics fibre. In addition, the changes achieved by shifting the 1973 nm waist by itself were not sufficient to make the two waists overlap. Therefore, it was necessary to shift the 985 nm waist towards the 1973 nm waist as well.

After the mode-matching was finalised, we used the IR-detection disk to find the proper location of the HR resonator mirror, which was placed on a different translation stage than the knife-edge apparatus. We moved the knife-edge apparatus further along the optical axis to a position where it did not interfere with the movement of the translation stage holding the HR mirror. The HR mirror was translated along the optical axis until an image would form on the IR-detection disk. This image was created by the Fresnel reflection from the glass-air interface of the HR mirror. By minimising the spot on the disk, we could infer that the front surface of the mirror was within about 20 μm of the waist. A finer adjustment was obtained by observing the front surface of the mirror with a long focal length USB microscope. When the mirror was within about 5 μm of the waist, an image of the spatial Fourier transform of the pump beam would appear on the surface of the HR mirror (see Figure G.4). By optimising the intensity of the Fourier image, we were able to find the waist to a higher precision. The location on the HR mirror translation stage was recorded for future reference, since this location did not change if the same mode matching configuration was used. We then continued to translate the HR mirror until a second image formed on the IR-detection disk by the back surface of the mirror. This was done to validate that the first image was indeed coming from the front surface of the HR mirror.

Future implementations of the DWP laser will use either an off-axis parabola or a custom-made achromat as launching optics into the ZBLAN fibre to avoid the complications created by the asphere chromatic dispersion.

Figure G.4: Fourier transform of pump beam observed with the USB microscope when the HR mirror front surface is at the pump waist.

G.3   Aligning pointing direction of pump beams after launching asphere

To ensure high launch efficiency of the pump beams, it was necessary to make the pump beams perpendicular to the fibre end-face. We assumed that the fibre was laid parallel to the top of the optical table and parallel to the table side as well. The high power of the asphere meant any deviation from propagation through its centre resulted in a strong deviation of the beams from being parallel to the table. In addition, even a slight deviation between the different pump beams resulted in their waists not coinciding. Therefore, it was of the utmost importance to ensure both beams were finely co-aligned and pointing in the same direction when entering the launching asphere.

The alignment setup was based on the one used in section G.1 and shown in Figures G.1 and G.2. This consisted of the ordinary DWP laser setup but instead of having the ZBLAN fibre mounted in position, the fibre translation stage was replaced the Ophir 50 W head power meter. The reason for using such a high power head was its large aperture which allows for significant movement of the rapidly diverging beam when

aligning. In addition, the relatively slow response time averaged temporal fluctuation which could cause confusion during the alignment procedure. The pointing direction of the 985 nm pump beam was adjusted using the two mirror adjustment method:

1. Preliminary adjustment of both pump beams' pointing direction was obtained simultaneously:

   (a) The Ophir power meter head was positioned approximately 5 cm behind the HR mirror.

   (b) The dual-axis knife edge apparatus was mounted between the HR mirror and power meter head, with the knife edge approximately at the beam waist location, while ensuring it is not blocking either pump beam (IR card or LCD-thermal paper was used to check for beam obstructions).

   (c) The 980 nm pump diode was turned on and its power was adjusted until a reading of 100 mW was obtained with the Ophir power meter (this corresponded to roughly 330 mA of supply current).

   (d) An IR-detection card (Thorlabs VRC4) was placed between the asphere and the power meter. Markings were placed on the card for the required centre of the pump beam, following the line of the centre of the tapped holes on the optical table and at a height of 75 mm.

   (e) The diverting mirror before the asphere was adjusted in both vertical and horizontal planes until the centre of the 980 nm beam coincided with the markings on the IR-detection card. It was sometimes necessary to slightly shift the asphere in a transverse direction to the beam to ensure the beam went through its centre and maintained its pointing parallel to the table.

   (f) The 980 nm beam was blocked by a beam dump.

   (g) The 1973 nm Tm^{3+} fibre laser was turned on and its power was adjusted until the power meter read 100 mW as well (this required roughly 12.4 A of supply current). When done, the beam was blocked by a beam dump.

   (h) Steps 1e and 1f were repeated with the 1973 nm pump. Instead of the IR-detection card, an LCD-based thermal sensitive paper (Edmund Optics 72-375) was used.

2. The knife-edge apparatus was moved along the optical axis to the approximate waist location found in section G.2. Figure G.5 shows schematically the situation described below.

   (a) The 980 nm beam was unblocked and the power level verified to be 100 mW.

(b) The height of the knife-edge blade that was positioned horizontally was adjusted until it partially blocked the beam and a power reading close to 80 mW was reached.

(c) The second mirror on the 980 nm arm was adjusted in the vertical plane to reduce the power reading value to about 70 mW.

(d) The knife edge apparatus was moved along the optical axis by a couple of mm away from the waist to position 2 in Figure G.5. The power levels measured by the power meter would change drastically (often close to 0 mW or 100 mW).

(e) The third mirror on the 980 nm arm was adjusted slightly in the vertical plane to reach a power level closer to 50 mW.

(f) The knife-edge apparatus was moved back to the waist location (position 1 in Figure G.5).

(g) Stages 2a-2f were repeated while small, incremental adjustments were made (this alignment was very sensitive). Each time stage 2b was repeated, the power level that we were aiming for would reduce to a value closer to 50 mW. As the beam became more parallel to the optical table, the changes in the knife-edge height only made a difference in the power transmitted when the knife-edge was located very close to the waist (position 1). In all other locations, the power readings were very close to 50 mW because the knife-edge was blocking almost half of the diverging beam.

(h) Once 50 mW of power was maintained both at the waist and further away, the knife edge apparatus was moved away from the waist in the opposite direction (position 3 in Figure G.5) and 50% power transmission was verified at this location. If the power in all three locations corresponded to 50 mW, the beam was parallel to the optical table.

3. Once the 980 nm beam was adjusted in the vertical plane, the beam was blocked and the 1973 nm beam was allowed through the asphere. The steps described in stage 2 were repeated, this time with the 1973 nm beam. Adjustments were made using the second 1973 nm beam steering mirror and the dichroic mirror. The centre of the 1973 nm beam had to be located no more than 2 μm away from the centre of the 980 nm beam to ensure both pumps were to be launched simultaneously into the core of the ZBLAN fibre.

4. When the 1973 nm vertical plane was properly adjusted, the knife edge blade used for vertical measurement was retracted and the knifed edge blade used for horizontal measurement was brought to the waist location.

5. The same process detailed in steps 2 and 3 was repeated for the horizontal plane, first for the 980 nm beam and then for the 1973 nm beam.

6. Once both beams were adjusted in both planes, it was necessary to recheck the alignment of both beams in the vertical plane due to cross-talk between the planes of the kinematic mirror mounts used.
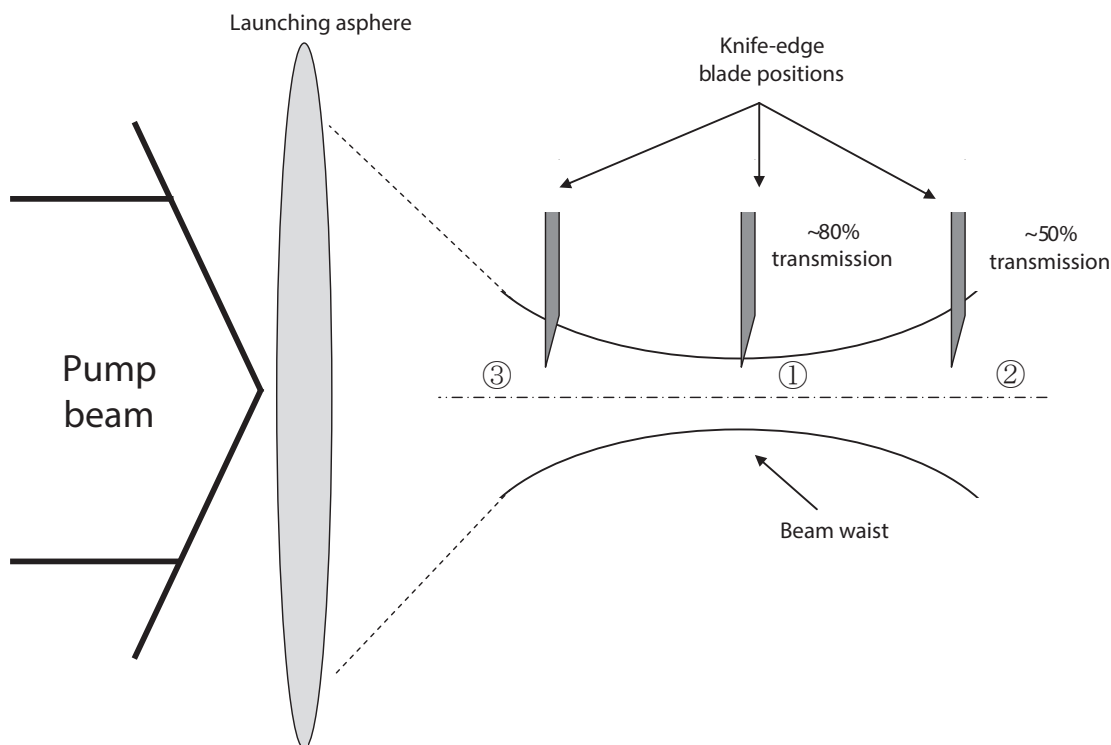

Figure G.5: Schematics of the positions of the knife-edge blade and pump transmission percentage during the beam pointing alignment.

G.4 Fibre laser resonator mirror initial alignment

One of the biggest difficulties in aligning the laser resonator with butt-coupled mirrors was ensuring the mirrors were parallel to the fibre end-faces. Due to the relatively low emission cross-section of this fibre laser, it was essential to ensure complete butting of the fibre with the resonator mirrors. This became an important issue because of the slight angles (2 degrees or less, cleaves with a higher angle were re-cleaved) often obtained when cleaving the fibre and with the difficulty of ascertaining the exact orientation of the mounted fibre. It was decided to align the resonator mirrors with the assumption of a perfectly straight cleave with the fibre being held perfectly parallel to both the top surface and the grid of holes of the optical table. The alignment procedure devised was based on "squaring" a HeNe beam to the table and then aligning the resonator mirrors to perfectly retroflect the HeNe beam. A schematic of the setup used in the process is shown in Figure G.6.
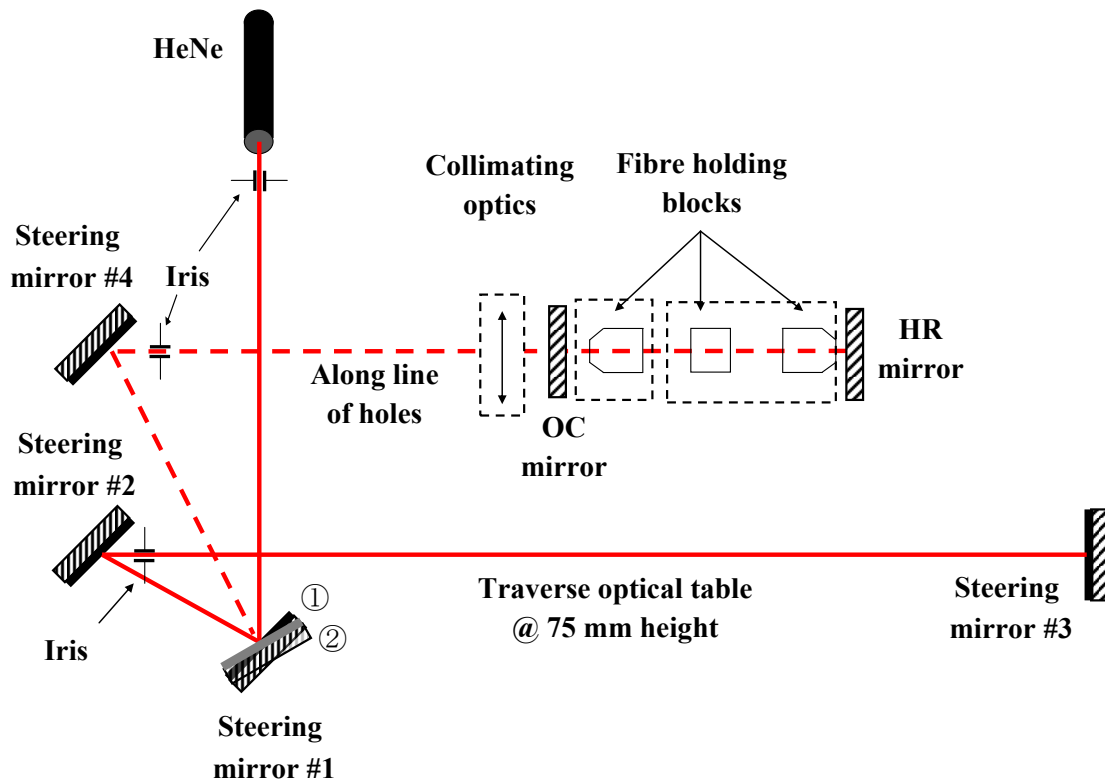
Figure G.6: Schematics of the alignment procedure of the 3.5 μm laser resonator mirrors prior to lasing.

1. A HeNe beam was aligned to traverse between a set of two steering mirrors (1 and 2) and two irises.

2. Steering mirror 1 was adjusted to make the HeNe beam propagate towards a third steering mirror at a constant height of 75 mm above the surface of the table. The height was verified at various points along the table. Mirror 3 retroflected the HeNe beam towards the laser where the spot could be observed at the iris next to the HeNe. Over the 5 m length of the optical table, a good parallelisation of the beam relative to the optical table top was ensured to within 0.2 $mrad$.

3. A fourth mirror was placed in front of the third mirror at the end of the table and retroflected the HeNe beam toward the laser. The fourth mirror was adjusted in the vertical plane to ensure it is normal to the optical table surface.

4. The fourth mirror was repositioned closer to the 3.5 μm laser resonator without changing its vertical alignment so it reflected the HeNe beam towards the OC mirror following a row of holes along the table. At this stage, the HeNe beam incident on the resonator was parallel with the top surface and the grid of holes on top of the optical table.

5. The ZBLAN fibre holding blocks, the OC holder and the resonator's collimating optics were removed.

6. The HeNe beam was turned on and reflected off the HR mirror. The angle of the HR mirror was adjusted in both the vertical and horizontal planes until the retroflected beam passed through the irises next to steering mirror 4 and the HeNe laser.

7. The OC was replaced and the back reflection from the OC was adjusted in both planes by using both irises.

8. All reflections from both the OC and HR mirrors were supposed to overlap with each other. If done properly, weak interference rings appeared on the iris used for beam alignment.

9. The resonator was then aligned for the pump beams and for a perfectly cleaved fibre.

10. Final mirror alignment to fibre was done with very fine angle adjustment at the lasing stage by optimising the output power of the laser.

G.5 Fibre to beam alignment

After both pump beams were straightened, mode matched to the correct beam waist size, co-aligned into the fibre core and the resonator mirrors were "squared" with the table, we could finally mount the fibre and align it to the pump beams. Schematics of the mount holding the fibre input side is shown in Figure G.7.

1. We removed the knife edge apparatus and the power meter standing behind the HR mirror.

2. A length of fibre was mounted on the Thorlabs translation stage. The fibre was mounted on fibre groove blocks that had been milled to achieve a ship's nose profile. This profile enabled the mount to get very close to the mirror without touching any of the mechanical objects surrounding it. It was imperative to mount the fibre on the input side with the coating completely within the groove area, so only uncoated fibre protruded out of it. Otherwise, the strong 1973 nm absorption of the coating could result in the destruction of the fibre during the alignment procedure.

3. A small sheet of indium was placed on top of the fibre. It was necessary to ensure that the indium did not protruded beyond the fibre groove mount, otherwise it could melt due to absorbing scattered pump light. A second fibre groove mount was placed on top of the indium and clamped to the bottom fibre groove mount.
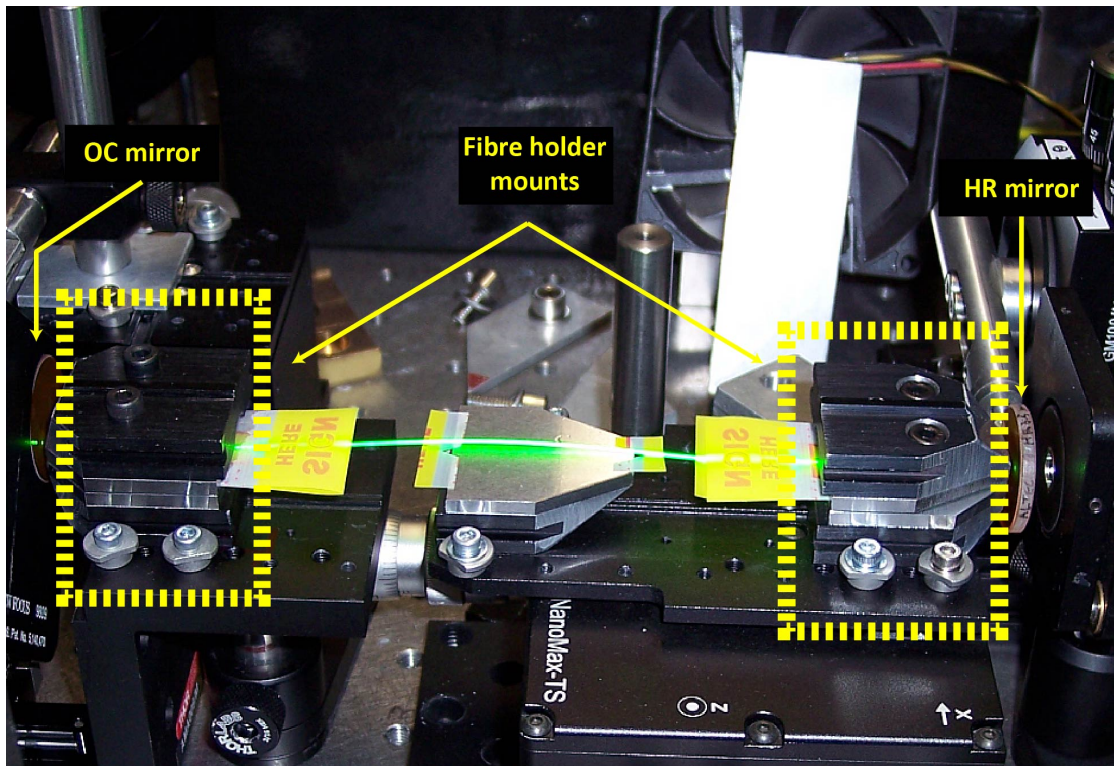
Figure G.7: Image of the mounts holding the fibre and the resonator mirrors. The fibre holder blocks have indium foils in between them for improved heat dissipation. The "post it" sticky flags are used for stress relief at the edges of the blocks and to avoid too much pressure from the edges when the blocks are put into place or removed.

The two mounts were clamped using light finger tightening of the M4 screws but not too tight to avoid damage to the fibre. This was sufficient for achieving light crushing of the indium foil onto the fibre for heat removal.

4. A similar, second set of fibre groove mounts were used on the fibre output side using the same method.

5. The entire translation stage with the fibre mounted onto it was positioned on the optical table. To achieve repeatability, kinematic stoppers on the table allowed for exact mounting of the translation stage to within about ten microns.

6. Using the 980 nm pump on half power (approximately 300 mA driver current), the fibre was moved until faint green fluorescence was observed. This indicated that some pump light was guided by the core.

7. The alignment was first optimised in the lateral direction while increasing the strength of the fluorescence observed visually. The pump driver current was then increased to maximum (700 mA). The fibre was then translated along the optical axis to achieve maximum transmission of power through the fibre. Slight

Figure G.8: Optimal alignment of pump through ZBLAN fibre. Clockwise from top left: Proper alignment to fibre core resulting in mostly LP_{01}, a single transverse mode propagation; poorer alignment resulting in mostly LP_{11} propagation; even poorer alignment resulting in significantly higher order modes and speckle. The images also show that some cladding-modes were present. This image was taken with a 2 cm long fibre; similar behaviour was observed with longer fibres.

modifications in the transverse direction were required as well due to the cross-talk present in the Thorlabs Nano-Max flexure stages.

8. When maximum transmission was achieved according to the strength of fluorescence or when using a power meter, the beam coming out of the fibre was imaged using an IR-card. The alignment was modified until the output beam corresponded to a single transverse mode (see Figure G.8) and no speckle was present. Very slight improvement could be achieved by looking at the 980 nm pump retroflected onto the IR-card iris in the 980 nm pump arm (see Figure G.3). Like the case of reflection from the dichroic surface, when the fibre tip was at the waist, a clear image of the fibre tip would appear and eventually converge completely into the iris.

9. Both pump beams were co-aligned with the waist coinciding, therefore, although not aligned separately, the 1973 nm pump beam should have launched well into the core. To test if this indeed was the case, both 980 nm and 1973 nm pumps were turned on at low power and a strong red fluorescence would appear. This fluorescence

is the result of fluorescence from the $^4F_{9/2}$ level that has significant population under DWP. It was also possible to look at the 1973 nm beam transmitted through the ZBLAN fibre using the Pyrocam and observe a single-transverse mode shape compared with a speckle pattern.

10. Even when well aligned, the mounts would tend to drift slightly after a few hours due to temperature changes in the room, which was only controlled to within $\pm 4°$C. Therefore, everyday when the laser was started, very fine adjustments were necessary. Those included tweaking of the 980/1973 nm dichroic kinematic mount and the third steering mirror on the 980 nm arm. This ensured maximum pump power at both wavelengths was launched into the fibre. Although effective in the short term, this approach only worked temporarily and occasionally, full realignment of the beams and the fibre was necessary. It is expected that if operated in a temperature stable environment, the laser would maintain its alignment for longer periods of time.

G.6   Off-axis parabolic mirror alignment

The output from the ZBLAN fibre laser was collimated using an OAP mirror apparatus (see Figure G.9). The output of the fibre was aligned prior to trying to achieve lasing, since the fibre was not expected to be moved at this stage. Observing the spectrum coming out of the ZBLAN fibre with the spectrometer was necessary for obtaining lasing and this spectrum could not be viewed without the alignment of the OAP.

We started using the OAP apparatus after it became apparent that the chromatic dispersion of an ordinary CaF_2 lens shifted the alignment of the beam entering the spectrometer too much. This required constant adjustment of the alignment to achieve sufficient intensity at the different wavelengths observed (from 550 nm all the way to almost 4 μm). By both collimating the outgoing beam from the fibre and then refocusing using a second OAP into the spectrometer, the chromatic dispersion issue was resolved. However, other aberrations were introduced using this method, especially comma aberrations that had to be addressed. The following alignment method for collimating the beam coming out the fibre was eventually used to achieve best beam shape and ensure easy alignment into the spectrometer or the Pyrocam thermal camera.

The alignment procedure was based on the movement of an apparatus that held the OAP and an additional silver mirror at 45 degrees to the OAP. This design enabled the beam to continue in the same direction as it was coming out of the fibre (although with a slight offset). The arm holding both mirrors was mounted on a three-axis translation stage,
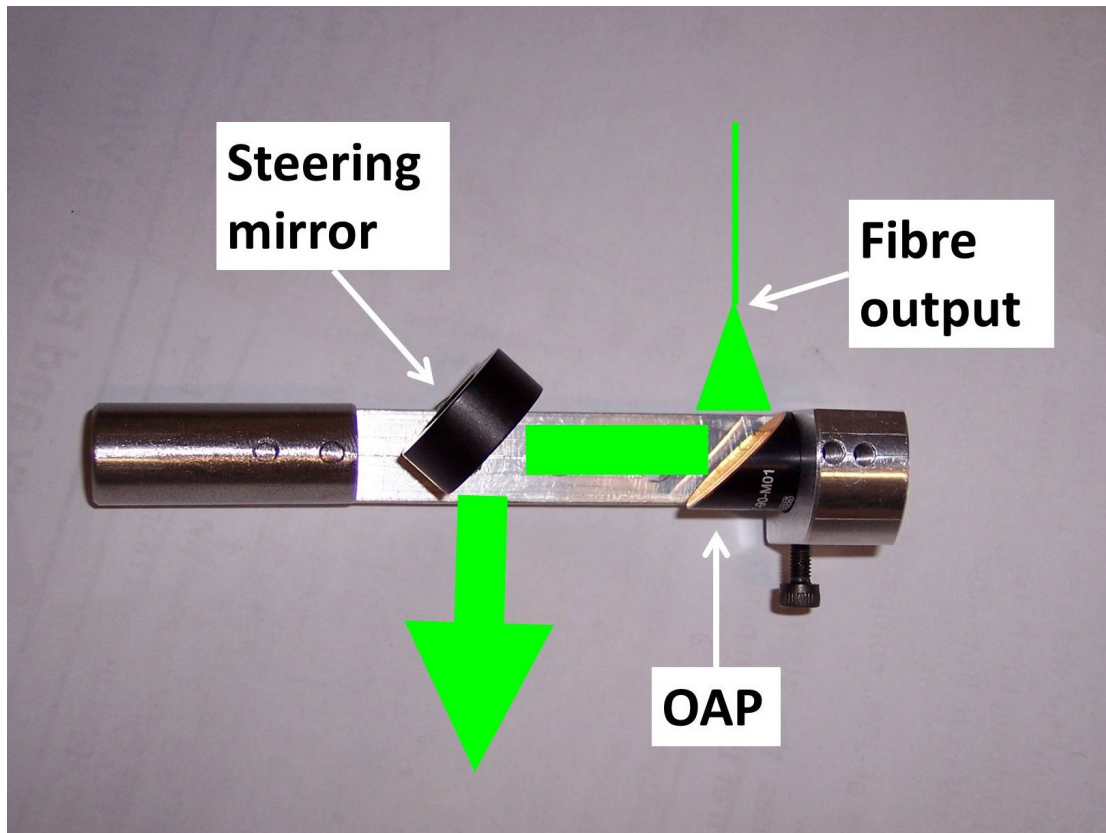
Figure G.9: Off-axis parabolic mirror apparatus. The steering mirror redirects the beam in the same direction as it came from the fibre.

which enabled coarse movement and fine movement on the scale of microns. Figure G.10 shows the schematics of the setup used in the collimating procedure. The steps followed during the collimating procedure were:

1. The apparatus holding the OAP was mounted after the OC at about 25 *mm* from the tip of the ZBLAN fibre.

2. The 980 *nm* pump diode was turned to maximum power, producing a strong green fluorescence beam coming out of the fibre.

3. The mount holding the OAP apparatus was moved on top of the translation stage until a rough collimation was observed using an IR-detection card. At this stage the mount was fastened in place.

4. If the beam was not parallel to the optical table, the OAP was loosened from its mount and rotated slightly to make it run parallel. It was also necessary to ensure that the beam was not clipped by the steering mirror after the OAP. In case of clipping, the mirror location was shifted slightly.
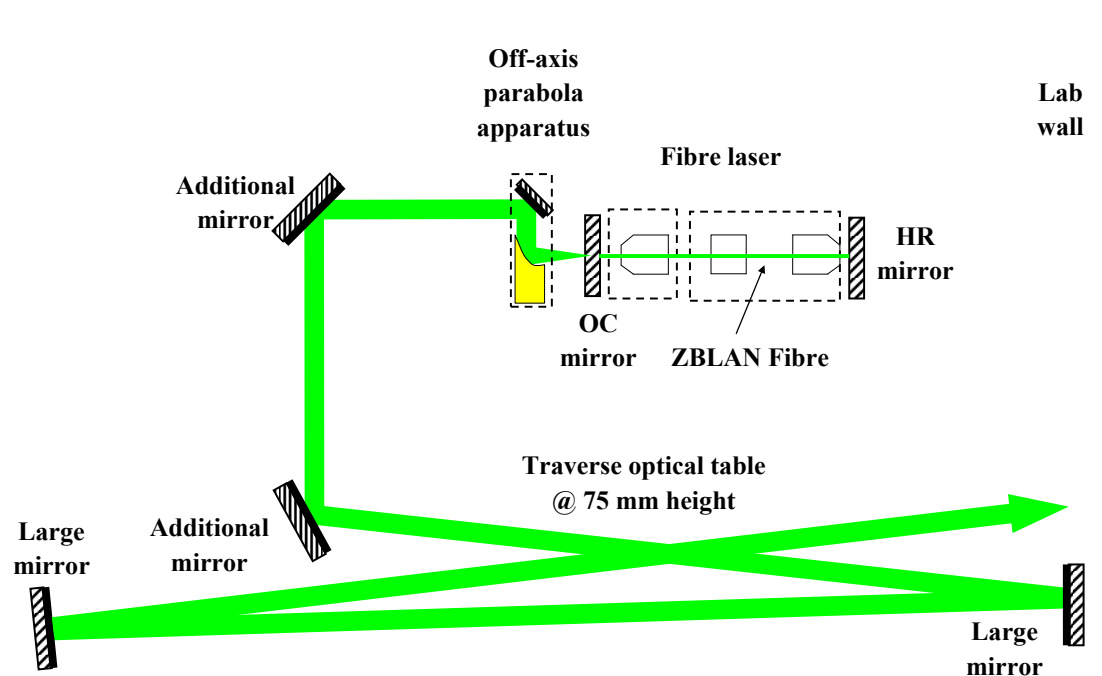
Figure G.10: Schematics of the setup used for collimating the output from the ZBLAN fibre using the OAP apparatus.

5. The translation stage axes were adjusted to obtain a roughly circular beam at a relatively short distance from the OAP apparatus. Beyond this distance, the beam sometimes looked "twisted." A few rules of thumb were used for optimising the appearance of the beam:

   (a) At first the beam was highly astigmatic and the OAP apparatus had to be translated transverse to the beam direction until a roughly circular image would appear (although very much out of focus).

   (b) When the image looked horizontal, the vertical axis of the translation stage needed adjustment. When it looked vertical, the horizontal axis needed adjustment.

   (c) To improve the focus of the image, the OAP arm needed to be translated along the optical axis until what seemed like a good image of the fibre tip appeared.

6. A set of two mirrors were added after the OAP to divert the green fluorescence beam onto the lab wall ($\sim 5\ m$ away) and allow for a finer adjustment of the alignment.

7. The lights in the lab were turned off and the alignment of the two mirrors was adjusted until a green beam was visible on the lab wall.

8. We adjusted the OAP translation stage until a sharp circular image of the fibre endface and its core were observed on the wall (see Figure G.11). The spot was too far away to observe unaided. It was therefore helpful to use a hand-held IR viewer, which enabled seeing the 980 nm pump even under full lighting in the lab. At this stage, adjustments of the translation stage were quite fine.

9. Two large mirrors were positioned along opposite sides of the lab facing each other. The fluorescence beam was pointed towards one of those mirrors. The first large mirror was adjusted to reflect the beam onto the second mirror on the other side of the lab. The second large mirror was then adjusted to reflect the beam back toward the first mirror. This resulted in the image of the core being sent next to the laser on the optical table. The image could be seen by placing a white sheet of paper next to the laser.

10. Final adjustment of the OAP alignment was done to produce as good an image of the core as possible. Once a good image was achieved, the current alignment was sufficiently good to enable launching into the spectrometer. Calculating the imaging condition showed that by using this method of alignment, the OAP was about 15 μm too far from the fibre tip for imaging at infinity (i.e. collimated beam). This additional shift in focal length applied for all wavelengths observed, since the OAP did not suffer from chromatic dispersion. The shift was taken into account when trying to lase in an open cavity configuration requiring perfect collimation.
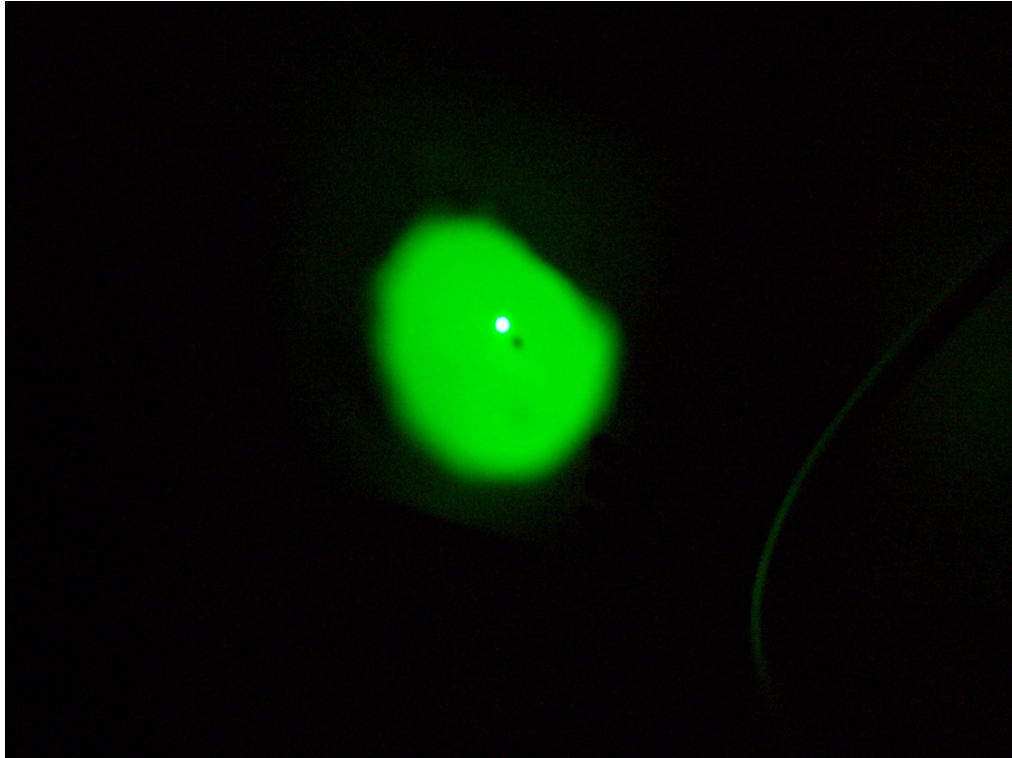
Figure G.11: Fibre endface and core image projected onto the lab wall. This image was taken with a ZDF fibre which had a "D" profile. The core is easily distinguished as the bright spot. The dark spot close to the core was caused by a speck of dust on the fibre endface. This dark spot disappeared after cleaning the fibre tip using an air duster.

G.7 Achieving lasing and optimising output power using fluorescence at 2.75 μm

Up to this stage, the pump beams were aligned and the resonator was roughly aligned but lasing had not yet been obtained. We now describe the method used to achieve lasing when butt-coupling the resonator mirrors to the fibre. This method is associated with the schematics of Figure G.1 and the image in Figure G.7.

G.7.1 Butting the HR mirror

1. The IR-detection disk with was placed on the 980 nm arm with the fluorescence side facing along the beam propagation direction. The pump was turned on to its maximum current (700 mA).

2. We moved the HR mirror as close as possible to the fibre endface while ensuring it did not bump into the fibre.

3. A USB microscope was then aimed at the fibre tip and we continued to move the HR mirror closer to the tip. When getting very close, the fibre green fluorescence started fluctuating as a result of etalon effects between the mirror and the fibre tip modulating the amount of 980 nm pump launched into the fibre.

4. Looking at the IR-detection disk on the 980 nm arm, an image of the fibre core started appearing. The HR mirror was moved further towards the fibre very slowly until the image on the IR-detection disk was at its minimum diameter. On the way to the minimum diameter, dark and bright fringes would fluctuate until the fluorescence stopped fluctuating, when fully butted. To ensure that maximum pump power was launched, it was essential to slightly shift the HR mirror so the image on the IR-detection disk was at a dark fringe. The residual 980 nm power coming out of the fibre was at its peak and the fibre was glowing significantly greener compared to operation on a bright fringe.

5. The 980 nm arm was blocked and the 1973 nm pump was turned on.

6. We measured the 1973 nm power coming out of the fibre. If the power corresponded to the power through the fibre when the HR mirror was far from the fibre tip, then no further action was needed.

7. If the 1973 nm power coming out the fibre was diminished, the HR mirror was shifted very slightly to achieve maximum transmission by reaching the next dark interference fringe of the 980 nm pump. This is because the 1973 nm wavelength is very close to being twice the 985 nm one and thus every second dark fringe of 985 nm corresponded to a dark fringe of the 1973 nm pump.

8. Once the location of the HR mirror was determined, its value was recorded. This value did not change as long as the angle of the mirror was not adjusted.

G.7.2   Butting the OC mirror

1. The 980 nm pump beam was turned on to its maximum current (700 mA).

2. We moved the OC as close as possible to the fibre output tip.

3. Similar to the HR mirror, we used the USB microscope to position the mirror until it was almost butted against the fibre. Fluctuations of the green fluorescence started to appear.

4. We used the spectrometer to monitor the output beam and scanned the 2700-2800 nm band. The peak emission wavelength was determined (usually around 2780 nm or 2800 nm, depending on how close to lasing we were).

5. If the peak was lasing, the intensity read by the spectrometer was adjusted by using a number of PTFE (Teflon®) sheets, as necessary, to scatter the beam and attenuate the signal.

6. We continued to bring the OC mirror towards the fibre tip while maximising the 2800 nm laser line. This line reached a peak value when the mirror was effectively butted against the tip, while at the same time the fluorescence fluctuations ceased to occur.

7. The 1973 nm beam was turned on using a predetermined incident power (for example 0.5 W).

8. A 3000 nm long pass filter was added into the path of the beam coming out of the ZBLAN fibre. This was done to ensure no 2800 nm laser signal was coming through (although the 2800 nm lasing was usually eliminated when the 1973 nm pump was turned on).

9. If lasing at 3.5 μm was achieved by this stage, we were able to observed the 3.5 μm power coming through the filter onto the power meter. It was usually also possible to see the beam using the LCD thermal paper at this stage.

10. When trying to optimise the laser output power, or if lasing was not achieved, the procedure described in section G.7.3 was followed.

G.7.3   Optimising power

After lasing at 3.5 μm was achieved, it was possible to optimise the power using the following adjustments of the resonator mirrors:

1. After the HR and OC mirrors were butted against the fibre completely, they were each pulled away (separately) from the fibre very slowly. In case the mirror induced some movement of the tip which caused it to butt at an angle, this angle was eliminated, resulting in higher power. It was sometimes necessary to repeat this stage multiple times for each mirror, where the mirror was butted against the fibre and pulled away.

2. A very slight tweaking of the angle of either of the resonator mirrors helped to achieve better, flatter butting of the mirror against the fibre tip, which subsequently improved the output power.

3. During the butting process of the fibre input end, it was possible that the tip moved slightly. To compensate for this, the third diverting mirror on the 980 nm pump arm and the dichroic on the 1973 nm arm were adjusted very carefully. The effect of this adjustment was monitored with both the 3.5 μm laser power and with the individual power meters monitoring the 1973 nm and 980 nm pumps (see wavelength separator in section 6.2.4).

Following this procedure, the 3.5 μm laser was usually running in CW with relatively stable power and other measurements such as spectral content or beam quality were performed.

Bibliography

[1] S. D. Jackson. "Towards high-power mid-infrared emission from a fibre laser." *Nature Photonics*, 6(7), 423–431, 2012.

[2] W. A. Gambling. "The rise and rise of optical fibers." *IEEE Journal on Selected Topics in Quantum Electronics*, 6(6), 1084–1093, 2000.

[3] C. A. Brackett. "Dense wavelength division multiplexing networks: Principles and applications." *IEEE Journal on Selected Areas in Communications*, 8(6), 948–964, 1990.

[4] B. Molocher. "Countermeasure laser development." *Proceedings of the SPIE 5989, Technologies for Optical Countermeasures II; Femtosecond Phenomena II; and Passive Millimetre-Wave and Terahertz Imaging II*, volume 5989. 2005.

[5] L. Jun, T. Qiulin, Z. Wendong, X. Chenyang, G. Tao and X. Jijun. "Miniature low-power IR monitor for methane detection." *Measurement: Journal of the International Measurement Confederation*, 44(5), 823–831, 2011.

[6] L. W. Kornaszewski, N. Gayraud, W. N. MacPherson, D. P. Hand, D. T. Reid, J. M. Stone, A. K. George and J. C. Knight. "Mid-infrared methane sensing using an optical parametric oscillator and a photonic bandgap fiber as a gas cell." *CLEO Lasers and Electro-Optics*. 2007.

[7] P. Werle, F. Slemr, K. Maurer, R. Kormann, R. Mücke and B. Jänker. "Near and mid-infrared laser-optical sensors for gas analysis." *Optics and Lasers in Engineering*, 37(2-3), 101–114, 2002.

[8] J. Kottmann, U. Grob, J. Rey and M. Sigrist. "Mid-infrared fiber-coupled photoacoustic sensor for biomedical applications." *Sensors*, 13(1), 535–549, 2013.

[9] D. Guo, X. Chen, S. Vadala, J. Leach, Y. Kostov, W. W. Bewley, C. S. Kim, M. Kim, C. L. Canedy, C. D. Merritt, I. Vurgaftman, J. R. Meyer and F. S. Choa. "Neuron absorption study and mid-IR optical excitations." *Photonic Therapeutics and Diagnostics VIII*, volume 8207, 491–492. SPIE, 2011.

[10] T. H. Maiman. "Stimulated optical radiation in Ruby." *Nature*, 187(4736), 493–494, 1960.

[11] A. Javan, W. R. Bennett and D. R. Herriott. "Population inversion and continuous optical maser oscillation in a gas discharge containing a He-Ne mixture." *Physical Review Letters*, 6(3), 106, 1961.

[12] C. H. Townes. *The first laser.* L. Garwin and T. Lincoln (Editors), *A Century of Nature: Twenty-One Discoveries that Changed Science and the World*, Nature, 126–135, 2003.

[13] A. A. Kaminskii. "Laser crystals and ceramics: recent advances." *Laser & Photonics Reviews*, 1(2), 93–177, 2007.

[14] W. R. Bennett. "Gaseous optical masers." *Applied Optics*, 1(S1), 24–61, 1962.

[15] T. F. Deutsch. "Molecular laser action in hydrogen and deuterium halides." *Applied Physics Letters*, 10(8), 234–236, 1967.

[16] J. Hecht. "History of gas lasers, part 1 - continuous wave gas lasers." *Optics and Photonics News*, 21(1), 16–23, 2010.

[17] T. W. Neely, T. A. Johnson and S. A. Diddams. "High-power broadband laser source tunable from 3:0 μm to 4:4 μm based on a femtosecond Yb:fiber oscillator." *Optics Letters*, 36(20), 4020–4022, 2011.

[18] A. Hemming, J. Richards, A. Davidson, N. Carmody, S. Bennetts, N. Simakov and J. Haub. "99 W mid-IR operation of a ZGP OPO at 25% duty cycle." *Optics Express*, 21(8), 10062–10069, 2013.

[19] J. Faist, F. Capasso, D. L. Sivco, A. L. Hutchinson, S.-N. G. Chu and A. Y. Cho. "Short wavelength ($\lambda \sim 3.4\ \mu m$) quantum cascade laser based on strained compensated InGaAs/AlInAs." *Applied Physics Letters*, 72(6), 1998.

[20] M. Troccoli, A. Lyakh, J. Fan, X. Wang, R. Maulini, A. G. Tsekoun, R. Go and C. K. N. Patel. "Long-wave IR quantum cascade lasers for emission in the $\lambda =$ 8-12 μm spectral region." *Optical Materials Express*, 3(9), 1546–1560, 2013.

[21] Y. Yao, A. J. Hoffman and C. F. Gmachl. "Mid-infrared quantum cascade lasers." *Nature Photonics*, 6(7), 432–439, 2012.

[22] Y. A. Bakhikrin, G. Wysocki, M. P. Fraser, R. Q. Yang and F. K. Tittel. "Sensitive, real-time interband cascade laser based sensor for ethane monitoring." *CLEO Conference on Lasers and Electro-Optics*, 1–2. 2007.

[23] A. Joulli, P. Christol, A. Baranov and A. Vicet. *Mid-infrared 2-5 μm heterojunction laser diodes.* I. T. Sorokina and K. L. Vodopyanov (Editors), *Solid-State Mid-Infrared Laser Sources*, Springer Berlin Heidelberg, 1–61, 2003.

[24] C. Xia, M. Kumar, O. P. Kulkarni, M. N. Islam, J. F. L. Terry, M. J. Freeman, M. Poulain and G. Maz. "Mid-infrared supercontinuum generation to 4.5 μm in ZBLAN fluoride fibers by nanosecond diode pumping." *Optics Letters*, 31(17), 2553–2555, 2006.

[25] M. Michalska and J. Swiderski. "Three-octave spanning supercontinuum generation in a fluoride (ZBLAN) fiber." *Electron Technology Conference 2013*, volume 8902, 89021A–89021A–6. 2013.

[26] K. Liu, J. Liu, H. Shi, F. Tan and P. Wang. "High power mid-infrared supercontinuum generation in a single-mode ZBLAN fiber with up to 21.8 W average output power." *Optics Express*, 22(20), 24384–24391, 2014.

[27] V. Fortin, M. Bernier, J. Carrier and R. Vallée. "Fluoride glass Raman fiber laser at 2185 nm." *Optics Letters*, 36(21), 4152–4154, 2011.

[28] R. Vallee. "Monolithic fiber lasers for the mid-infrared." *Advanced Photonics Congress*, BM2D.1. Optical Society of America, 2012.

[29] M. Bernier, V. Fortin, M. El-Amraoui, Y. Messaddeq and R. Valle. "3.77 μm fiber laser based on cascaded Raman gain in a chalcogenide glass fiber." *Optics Letters*, 39(7), 2052–2055, 2014.

[30] G. S. Edwards, D. Evertson, W. Gabella, R. Grant, T. L. King, J. Kozub, M. Mendenhall, S. Jin, R. Shores, S. Storms and R. H. Traeger. "Free-electron lasers: reliability, performance, and beam delivery." *IEEE Journal of Selected Topics in Quantum Electronics*, 2(4), 810–817, 1996.

[31] T. Kawasaki, J. Fujioka, T. Imai, K. Torigoe and K. Tsukiyama. "Mid-infrared free-electron laser tuned to the amide I band for converting insoluble amyloid-like protein fibrils into the soluble monomeric form." *Lasers in Medical Science*, 29(5), 1701–1707, 2014.

[32] L. S. Rothman, I. E. Gordon, A. Barbe, D. C. Benner, P. F. Bernath, M. Birk, V. Boudon, L. R. Brown, A. Campargue, J. P. Champion, K. Chance, L. H. Coudert, V. Dana, V. M. Devi, S. Fally, J. M. Flaud, R. R. Gamache, A. Goldman, D. Jacquemart, I. Kleiner, N. Lacome, W. J. Lafferty, J. Y. Mandin, S. T. Massie, S. N. Mikhailenko, C. E. Miller, N. Moazzen-Ahmadi, O. V. Naumenko, A. V. Nikitin, J. Orphal, V. I. Perevalov, A. Perrin, A. Predoi-Cross, C. P. Rinsland,

M. Rotger, M. Simekova, M. A. H. Smith, K. Sung, S. A. Tashkun, J. Tennyson, R. A. Toth, A. C. Vandaele and J. Vander Auwera. "The HITRAN 2008 molecular spectroscopic database." *Journal of Quantitative Spectroscopy and Radiative Transfer*, 110(9-10), 533–572, 2009.

[33] H. Waechter and M. Sigrist. *Trace gas analysis with isotopic selectivity using DFG-sources.* M. Ebrahim-Zadeh and I. Sorokina (Editors), *Mid-Infrared Coherent Sources and Applications*, Springer Netherlands, 495–510, 2008.

[34] J. S. Li, W. Chen and H. Fischer. "Quantum cascade laser spectrometry techniques: a new trend in atmospheric chemistry." *Applied Spectroscopy Reviews*, 48(7), 523–559, 2013.

[35] D. Campin. "Environmental regulation of hydraulic fracturing in Queensland." *Proceedings - SPE Annual Technical Conference and Exhibition*, volume 2, 952–998. 2013.

[36] V. A. Serebryakov, E. V. Boîko, N. N. Petrishchev and A. V. Yan. "Medical applications of mid-IR lasers: Problems and prospects." *Journal of Optical Technology*, 77(1), 6–17, 2010.

[37] T. Sumiyoshi, H. Sekita, T. Arai, S. Sato, M. Ishihara and M. Kikuchi. "High-power continuous-wave 3- and 2-μm cascade Ho^{3+}:ZBLAN fiber laser and its medical applications." *IEEE Journal on Selected Topics in Quantum Electronics*, 5(4), 936–943, 1999.

[38] T. H. Risby and F. K. Tittel. "Current status of midinfrared quantum and interband cascade lasers for clinical breath analysis." *Optical Engineering*, 49(11), 111123–111123–14, 2010.

[39] P. Fjodorow, L. Leal, B. Loehden, S. Kuznetsova, K. Sengstock and V. M. Baev. "Real time monitoring of exhaled breath using intracavity absorption spectroscopy with an Er-doped fiber laser." *Lasers, Sources, and Related Photonic Devices*, OSA Technical Digest (CD), LM3B.5. Optical Society of America, 2012.

[40] S.-S. Kim, C. Young, B. Vidakovic, S. Gabram-Mendola, C. W. Bayer and B. Mizaikoff. "Potential and challenges for mid-infrared sensors in breath diagnostics." *Sensors Journal, IEEE*, 10(1), 145–158, 2010.

[41] O. B. Crofford, R. E. Mallard and R. E. Winton. "Acetone in breath and blood." *Transactions of the American Clinical and Climatological Association*, Vol.88, 128–139, 1977.

[42] A. B. Seddon. "Mid-infrared (IR) - A hot topic: The potential for using mid-IR light for non-invasive early detection of skin cancer in vivo." *Physica Status Solidi (B)*, 250(5), 1020–1027, 2013.

[43] J. Hecht. "Half a century of laser weapons." *Optics and Photonics News*, 20(2), 14–21, 2009.

[44] B. D. Nordwall. "NRL laser to counter IR missile threat." *Aviation Week and Space Technology (New York)*, 141(20), 43–44, 1994.

[45] F. Fuchs, B. Hinkov, S. Hugger, J. M. Kaster, R. Aidam, W. Bronner, K. Khler, Q. Yang, S. Rademacher, K. Degreif, F. Schnrer and W. Schweikert. "Imaging stand-off detection of explosives using tunable MIR quantum cascade lasers." *Quantum Sensing and Nanophotonic Devices VII*, volume 7608, 760809–760809–7. 2010.

[46] D. Hofstetter and J. Faist. *High performance quantum cascade lasers and their applications*. I. Sorokina and K. Vodopyanov (Editors), *Solid-State Mid-Infrared Laser Sources*, Springer Berlin Heidelberg, 61–98, 2003.

[47] N. S. Prasad. "Optical communications in the mid-wave IR spectral band." *Journal of Optical and Fiber Communications Reports*, 2(6), 558–602, 2005.

[48] S. A. Diddams. "Frequency comb sources and techniques for mid-infrared spectroscopy and sensing." *CLEO*, OSA Technical Digest (online), JM3K.1. Optical Society of America, 2013.

[49] A. Schliesser, N. Picqu and T. W. Hnsch. "Mid-infrared frequency combs." *Nature Photonics*, 6(7), 440–449, 2012.

[50] A. Ruehl, A. Gambetta, I. Hartl, M. E. Fermann, K. Eikema and M. Marangoni. "Frequency comb synthesizer tunable from 3 to 10 μm." *CLEO: Science and Innovations*, OSA Technical Digest (online), CF2C.1. Optical Society of America, 2012.

[51] E. Sorokin, N. Tolstik and I. Sorokina. "Kerr-lens mode-locked Cr:ZnS laser." *Lasers, Sources, and Related Photonic Devices*, OSA Technical Digest (CD), AW5A.5. Optical Society of America, 2012.

[52] L. Nugent-Glandorf, F. Giorgetta and S. A. Diddams. "Open-air, broad-bandwidth trace-gas sensing with a mid-infrared optical frequency comb." *ArXiv e-prints*, 2014.

[53] C. Wang, T. Herr, P. Del'Haye, A. Schliesser, R. Holzwarth, T. W. Haensch, N. Picqu and T. Kippenberg. "Mid-infrared frequency combs based on microresonators." *CLEO 2011 - Laser Applications to Photonic Applications*, OSA Technical Digest (CD), PDPA4. Optical Society of America, 2011.

[54] W. Shi, Q. Fang, X. Zhu, R. A. Norwood and N. Peyghambarian. "Fiber lasers and their applications [Invited]." *Applied Optics*, 53(28), 6554–6568, 2014.

[55] A. M. Heidt, J. H. V. Price, C. Baskiotis, J. S. Feehan, Z. Li, S. U. Alam and D. J. Richardson. "Mid-infrared ZBLAN fiber supercontinuum source using picosecond diode-pumping at 2 μm." *Optics Express*, 21(20), 24281–24287, 2013.

[56] W. Yang, B. Zhang, K. Yin, X. Zhou and J. Hou. "High power all fiber mid-IR supercontinuum generation in a ZBLAN fiber pumped by a 2 μm MOPA system." *Optics Express*, 21(17), 19732–19742, 2013.

[57] X. Zhu and N. Peyghambarian. "High-power ZBLAN glass fiber lasers: Review and prospect." *Advances in OptoElectronics*, 2010, 2010.

[58] P. France, M. Drexhage, J. Parker, M. Moore, S. Carter and J. Wright. *Fluoride Glass Optical Fibres*. Springer Netherlands, 1990.

[59] C. B. Layne, W. H. Lowdermilk and M. J. Weber. "Multiphonon relaxation of rare-earth ions in oxide glasses." *Physical Review B*, 16(1), 10–20, 1977.

[60] J. Schneider. "Superfluorescent fiber source at 3.9 μm in the attenuation minimum of the atmospheric window 3-5 μm." *International Journal of Infrared and Millimeter Waves*, 16(1), 75–82, 1995.

[61] N. P. Barnes and R. E. Allen. "Room temperature Dy:YLF laser operation at 4.34 μm." *IEEE Journal of Quantum Electronics*, 27(2), 277–282, 1991.

[62] J. F. Pinto, G. H. Rosenblatt and L. Esterowitz. "Continuous-wave laser action in Er3+:YLF at 3.41 μm." *Electronics Letters*, 30(19), 1596–1598, 1994.

[63] V. V. Fedorov, S. B. Mirov, A. Gallian, D. V. Badikov, M. P. Frolov, Y. V. Korostelin, V. I. Kozlovsky, A. I. Landman, Y. P. Podmar'kov, V. A. Akimov and A. A. Voronov. "3.77-5.05 μm tunable solid-state lasers based on Fe^{2+}-doped ZnSe crystals operating at low and room temperatures." *IEEE Journal of Quantum Electronics*, 42(9), 907–917, 2006.

[64] M. Tacke. "New developments and applications of tunable IR lead salt lasers." *Infrared Physics & Technology*, 36(1), 447–463, 1995.

[65] M. Pollnau and S. D. Jackson. *Advances in mid-infrared fiber lasers. Solid-State Mid-Infrared Laser Sources*, Springer Berlin Heidelberg, 315–346, 2008.

[66] M. R. Oermann. *Mid-Wave Infrared Fibre Laser Development.* Ph.D. thesis, The University of Adelaide, 2011.

[67] F. Xiaokang, K. Peiwen, L. Kefeng, Z. Lei, L. Wentao and H. Lili. "A 2 μm continuous wave and passively Q-switched fiber laser in thulium-doped germanate glass fibers." *Laser Physics*, 24(8), 085107, 2014.

[68] A. Haboucha, V. Fortin, M. Bernier, J. Genest, Y. Messaddeq and R. Vallée. "Fiber Bragg grating stabilization of a passively mode-locked 2.8 μm Er^{3+}: fluoride glass fiber laser." *Optics Letters*, 39(11), 3294–3297, 2014.

[69] D. S. Funk, J. W. Carlson and J. G. Eden. "Room temperature upconversion ultraviolet (381 nm) and violet (412 nm) laser in Nd^{3+}:ZBLAN fiber." *Proceedings of SPIE - The International Society for Optical Engineering*, volume 2380 of *UV and Visible Lasers and Laser Crystal Growth*, 108–114. Society of Photo-Optical Instrumentation Engineers, 1995.

[70] D. M. Baney, L. Yang, J. Ratcliff and K. W. Chang. "Red and orange Pr3+/Yb3+ doped ZBLAN fibre upconversion lasers." *Electronics Letters*, 31(21), 1842–1843, 1995.

[71] B. Srinivasan, E. Poppe, J. Tafoya and R. K. Jain. "High-power (400 mW) diode-pumped 2.7 μm Er^{3+}:ZBLAN fibre lasers using enhanced Er-Er cross-relaxation processes." *Electronics Letters*, 35(16), 1338–1340, 1999.

[72] H. Többen. "CW lasing at 3.45 μm in erbium-doped fluorozirconate fibres." *Frequenz*, 45, 250–252, 1991.

[73] J. Schneider. "Fluoride fibre laser operating at 3.9 μm." *Electronics Letters*, 31(15), 1250–1251, 1995.

[74] S. D. Jackson and D. G. Lancaster. *Fiber lasers that bridge the shortwave to midwave regions of the infrared spectrum.* O. G. Okhotnikov (Editor), *Fiber Lasers*, Wiley-VCH Verlag GmbH & Co. KGaA, 233–267, 2012.

[75] P. W. France, S. F. Carter, J. R. Williams, K. J. Beales and J. M. Parker. "OH-absorption in fluoride glass infra-red fibres." *Electronics Letters*, 20(14), 607–608, 1984.

[76] M. Pollnau, C. Ghisler, G. Bunea, M. Bunea, W. Luthy and H. P. Weber. "150 mW unsaturated output power at 3 μm from a single-mode-fiber erbium cascade laser." *Applied Physics Letters*, 66(26), 3564–3566, 1995.

[77] P. S. Golding, S. D. Jackson, T. A. King and M. Pollnau. "Energy transfer processes in Er^{3+}-doped and Er^{3+}, Pr^{3+}-codoped ZBLAN glasses." *Physical Review B - Condensed Matter and Materials Physics*, 62(2), 856–864, 2000.

[78] K. Shinde, S. Dhoble, H. Swart and K. Park. *Phosphate phosphors for solid-state lighting.* Springer, 2012.

[79] M. C. Brierley and P. W. France. "Continuous wave lasing at 2.7 μm in an erbium-doped fluorozirconate fibre." *Electronics Letters*, 24(15), 935–937, 1988.

[80] M. C. Brierley, P. W. France, R. A. Garnham, C. A. Millar and W. A. Stallard. "Long wavelength fluoride fibre system using a 2.7 μm fluoride fibre laser." *Optical Fiber Communication Conference*, volume 5 of *1989 OSA Technical Digest Series*, PD14. Optical Society of America, 1989.

[81] R. S. Quimby and W. J. Miniscalco. "Continuous-wave lasing on a self-terminating transition." *Applied Optics*, 28(1), 14–16, 1989.

[82] C. Frerichs. "Efficient Er^{3+}-doped CW fluorozirconate fiber laser operating at 2.7 μm pumped at 980 nm." *International Journal of Infrared and Millimeter Waves*, 15(4), 635–649, 1994.

[83] S. Tokita, M. Hirokane, M. Murakami, S. Shimizu, M. Hashida and S. Sakabe. "Stable 10 W Er:ZBLAN fiber laser operating at 2:71-2:88 μm." *Optics Letters*, 35(23), 3943–3945, 2010.

[84] W. L. S. Bedö, M. Pollnau and H. P. Weber. "Saturation of the 2.71 μm laser output in erbium-doped ZBLAN fibers." *Optics Communications*, 116(1-3), 81–86, 1995.

[85] V. K. Bogdanov, W. E. K. Gibbs, D. J. Booth, J. S. Javorniczky, P. J. Newman and D. R. MacFarlane. "Energy exchange processes in Er^{3+}-doped fluorozirconate glasses." *Journal of Non-Crystalline Solids*, 256, 288–293, 1999.

[86] M. Gorjan, M. Marincek and M. Copic. "Role of interionic processes in the efficiency and operation of erbium-doped fluoride fiber lasers." *IEEE Journal of Quantum Electronics*, 47(2), 262–273, 2011.

[87] R. S. Quimby, W. J. Miniscalco and B. Thompson. "Clustering in erbium-doped silica glass fibers analyzed using 980 nm excited-state absorption." *Journal of Applied Physics*, 76(8), 4472–4478, 1994.

[88] B. Srinivasan, R. K. Jain and G. Monnom. "Indirect measurement of the magnitude of ion clustering at high doping densities in Er:ZBLAN fibers." *Journal of the Optical Society of America B*, 17(2), 178–181, 2000.

[89] P. Le Boulanger, J. L. Doualan, S. Girard, J. Margerie and R. Moncorg. "Excited-state absorption spectroscopy of Er^{3+}-doped $Y_3Al_5O_{12}$, YVO_4, and phosphate glass." *Physical Review B - Condensed Matter and Materials Physics*, 60(16), 11380–11390, 1999.

[90] S. R. Bullock, B. R. Reddy, P. Venkateswarlu, S. K. Nash-Stevenson and J. C. Fajardo. "Energy upconversion and spectroscopic studies of ZBLAN : Er^{3+}." *Optical and Quantum Electronics*, 29(11), 83–92, 1997.

[91] M. Pollnau, C. Ghisler, W. Lüthy and H. P. Weber. "Cross sections of excited-state absorption at 800 nm in erbium-doped ZBLAN fiber." *Applied Physics B: Lasers and Optics*, 67(1), 23–28, 1998.

[92] M. Pollnau and S. D. Jackson. "Erbium 3-μm fiber lasers." *IEEE Journal on Selected Topics in Quantum Electronics*, 7(1), 30–40, 2001.

[93] D. Piehler, D. Craven, N. Kwong and H. Zarem. "Laser-diode-pumped red and green up-conversion fibre lasers." *Electronics Letters*, 29(21), 1857–1858, 1993.

[94] T. Hebert, R. Wannemacher, W. Lenth and R. M. Macfarlane. "Blue and green CW upconversion lasing in Er^{3+}:$YLiF_4$." *Applied Physics Letters*, 57(17), 1727–1729, 1990.

[95] R. Al-Mahrous, R. Caspary and W. Kowalsky. "Red and orange tunable fiber laser." *12th International Conference on Transparent Optical Networks*. 2010.

[96] A. Sarakovskis, L. Dimitrocenko, A. Misnevs, U. Rogulis and M. Springis. "Up-conversion process in erbium doped lithium fluoride bulk crystal, lithium borate glass and glass ceramics." *Journal of Physics: Conference Series*, 93(1), 2007.

[97] G. Huber, E. Heumann, T. Sandrock and K. Petermann. "Up-conversion processes in laser crystals." *Journal of Luminescence*, 72-74, 1–3, 1997.

[98] R. G. Smart, D. C. Hanna, A. C. Tropper, S. T. Davey, S. F. Carter and D. Szebesta. "CW room temperature upconversion lasing at blue, green and red wavelengths in infrared-pumped Pr^{3+}-doped fluoride fibre." *Electronics Letters*, 27(14), 1307–1309, 1991.

[99] R. Brede, E. Heumann, J. Koetke, T. Danger, G. Huber and B. Chai. "Green up-conversion laser emission in Er-doped crystals at room temperature." *Applied Physics Letters*, 63(15), 2030–2031, 1993.

[100] M. P. Le Flohic, J. Y. Allain, G. M. Stephan and G. Maze. "Room-temperature continuous-wave upconversion laser at 455 nm in a Tm^{3+} fluorozirconate fiber." *Optics Letters*, 19(23), 1982–1984, 1994.

[101] N. Kamata, K. Hoshino, T. Uchida, K. Yamada, M. Nishioka and Y. Arakawa. "Up-conversion luminescence via a below-gap state in GaAs/AlGaAs quantum wells." *Superlattices and Microstructures*, 22(4), 521–528, 1997.

[102] E. B. Mejía. "Ultraviolet emission in Tm^{3+}-doped fluoride fiber pumped with two infrared wavelengths." *Journal of Applied Physics*, 100(11), 2006.

[103] D. V. Talavera and E. B. Mejía. "Blue up-conversion Tm^{3+}-doped fiber laser pumped by a multiline Raman source." *Journal of Applied Physics*, 97(5), 1–4, 2005.

[104] J. Schneider, D. Hauschild, C. Frerichs and L. Wetenkamp. "Highly efficient Er^{3+}:Pr^{3+}-codoped CW fluorozirconate fiber laser operating at 2.7 μm." *International Journal of Infrared and Millimeter Waves*, 15(11), 1907–1922, 1994.

[105] D. Hudson, E. Magi, L. Gomes and S. D. Jackson. "1 W diode-pumped tunable Ho^{3+}, Pr^{3+}-doped fluoride glass fibre laser." *Electronics Letters*, 47(17), 985–986, 2011.

[106] T. Sandrock, A. Diening and G. Huber. "Laser emission of erbium-doped fluoride bulk glasses in the spectral range from 2.7 to 2.8 μm." *Optics Letters*, 24(2-6), 382–384, 1999.

[107] B. C. Dickinson, P. S. Golding, M. Pollnau, T. A. King and S. D. Jackson. "Investigation of a 791-nm pulsed-pumped 2.7-μm Er-doped ZBLAN fibre laser." *Optics Communications*, 191(3-6), 315–321, 2001.

[108] D. J. Coleman, T. A. King, D. K. Ko and J. Lee. "Q-switched operation of a 2.7 μm cladding-pumped Er^{3+}/Pr^{3+} codoped ZBLAN fibre laser." *Optics Communications*, 236(4-6), 379–385, 2004.

[109] X. Zhu and R. Jain. "10-W-level diode-pumped compact 2.78 μm ZBLAN fiber laser." *Optics Letters*, 32(1), 26–28, 2007.

[110] S. Tokita, M. Murakami, S. Shimizu, M. Hashida and S. Sakabe. "Liquid-cooled 24 W mid-infrared Er^{3+}:ZBLAN fiber laser." *Optics Letters*, 34(20), 3062–3064, 2009.

[111] S. D. Jackson. "Single-transverse-mode 2.5-W holmium-doped fluoride fiber laser operating at 2.86 μm." *Optics Letters*, 29(4), 334–336, 2004.

[112] D. D. Hudson, R. J. Williams, M. J. Withford and S. D. Jackson. "Single-frequency fiber laser operating at 2.9 μm." *Optics Letters*, 38(14), 2388–2390, 2013.

[113] T. Hu, D. D. Hudson and S. D. Jackson. "Stable, self-starting, passively mode-locked fiber ring laser of the 3 μm class." *Optics Letters*, 39(7), 2133–2136, 2014.

[114] M. Pollnau and S. D. Jackson. "Energy recycling versus lifetime quenching in erbium-doped 3-μm fiber lasers." *IEEE Journal of Quantum Electronics*, 38(2), 162–169, 2002.

[115] L. Wetenkamp. "Efficient CW operation of a 2.9 μm Ho^{3+}-doped fluorozirconate fibre laser pumped at 640 nm." *Electronics Letters*, 26(13), 883–884, 1990.

[116] C. Carbonnier, H. Többen and U. B. Unrau. "Room temperature CW fibre laser at 3.22 μm." *Electronics Letters*, 34(9), 893–894, 1998.

[117] H. Többen. "Room temperature CW fibre laser at 3.5 μm in Er^{3+}-doped ZBLAN glass." *Electronics Letters*, 28(14), 1361–1362, 1992.

[118] H. Többen. "Temperature-tunable 3.5 μm fibre laser." *Electronics Letters*, 29(8), 667–669, 1993.

[119] J. Schneider, C. Carbonnier and U. B. Unrau. "Characterization of a Ho^{3+}-doped fluoride fiber laser with a 3.9-μm emission wavelength." *Applied Optics*, 36(33), 8595–8600, 1997.

[120] S. F. Carter, M. W. Moore, D. Szebesta, J. R. Williams, D. Ranson and P. W. France. "Low loss fluoride fibre by reduced pressure casting." *Electronics Letters*, 26(25), 2115–2117, 1990.

[121] A. B. Seddon, Z. Tang, D. Furniss, S. Sujecki and T. M. Benson. "Progress in rare-earth-doped mid-infrared fiber lasers." *Optics Express*, 18(25), 26704–26719, NaN.

[122] L. Mescia, F. Prudenzano, L. Allegretti, M. De Sario, T. Palmisano, V. Petruzzelli, F. Smektala, V. Moizan, V. Nazabal and J. Troles. "Erbium-doped chalcogenide fiber ring laser for mid-IR applications." *Proceedings of SPIE - The International Society for Optical Engineering*, volume 7366, 575818. 2009.

[123] L. Mescia, F. Smektala and F. Prudenzano. "New trends in amplifiers and sources via chalcogenide photonic crystal fibers." *International Journal of Optics*, 2012, 2012.

[124] V. Fortin, M. Bernier, N. Caron, D. Faucher, M. El Amraoui, Y. Messaddeq and R. Valle. "Towards the development of fiber lasers for the 2 to 4 μm spectral region." *Optical Engineering*, 52(5), 054202–054202, 2013.

[125] G. E. Snopatin, V. S. Shiryaev, V. G. Plotnichenko, E. M. Dianov and M. F. Churbanov. "High-purity chalcogenide glasses for fiber optics." *Inorganic Materials*, 45(13), 1439–1460, 2009.

[126] F. Prudenzano, L. Mescia, L. Allegretti, M. De Sario, F. Smektala, V. Moizan, V. Nazabal, J. Troles, J. L. Doualan, G. Canat, J. L. Adam and B. Boulard. "Simulation of mid-IR amplification in Er^{3+}-doped chalcogenide microstructured optical fiber." *Optical Materials*, 31(9), 1292–1295, 2009.

[127] L. Wetenkamp, G. F. West and H. Többen. "Optical properties of rare earth-doped ZBLAN glasses." *Journal of Non-Crystalline Solids*, 140(C), 35–40, 1992.

[128] S. D. Jackson, T. A. King and M. Pollnau. "Diode-pumped 1.7-W erbium 3-μm fiber laser." *Optics Letters*, 24(16), 1133–1135, 1999.

[129] L. Wetenkamp, G. F. West and H. Többen. "Co-doping effects in Er^{3+}- and Ho^{3+}-doped ZBLAN glasses." *Journal of Non-Crystalline Solids*, 140(C), 25–30, 1992.

[130] J. Y. Allain, M. Monerie and H. Poignant. "Energy transfer in Er^{3+}/Pr^{3+} -doped fluoride glass fibres and application to lasing at 2.7 μm." *Electronics Letters*, 27(5), 445–447, 1991.

[131] B. Srinivasan, J. Tafoya and R. K. Jain. "High-power 'Watt-level' CW operation of diode-pumped 2.7 μm fiber lasers using efficient cross-relaxation and energy transfer mechanisms." *Optics Express*, 4(12), 490–495, 1999.

[132] X. Zhu and R. Jain. "Numerical analysts and experimental results of high-power Er/Pr:ZBLAN 2.7μm fiber lasers with different pumping designs." *Applied Optics*, 45(27), 7118–7125, 2006.

[133] M. Pollnau. "The route toward a diode-pumped 1-W erbium 3-μm fiber laser." *IEEE Journal of Quantum Electronics*, 33(11), 1982–1990, 1997.

[134] X. Zhu and R. Jain. "Scaling up laser diode pumped mid-infrared fiber laser to 10-Watt-level." *Conference on Lasers and Electro-Optics/Quantum Electronics and Laser Science and Photonic Applications Systems Technologies*, Technical Digest (CD), CTuC3. Optical Society of America, 2005.

[135] V. K. Bogdanov. *Energy exchange processes in erbium-doped fluoride glasses.* Ph.D. thesis, Victoria University of Technology, 1999.

[136] D. Faucher, M. Bernier, G. Androz, N. Caron and R. Valle. "20 W passively cooled single-mode all-fiber laser at 2.8 μm." *Optics Letters*, 36(7), 1104–1106, 2011.

[137] T. Kasamatsu, Y. Yano and T. Ono. "Laser-diode pumping (1.4 and 1.56 μm) of gain-shifted thulium-doped fibre amplifier." *Electronics Letters*, 36(19), 1607–1609, 2000.

[138] T. Kasamatsu, Y. Yano and T. Ono. "1.49-μm-band gain-shifted thulium-doped fiber amplifier for WDM transmission systems." *Journal of Lightwave Technology*, 20(10), 1826–1838, 2002.

[139] S. R. Lüthi, M. L. Sundheimer, W. Margulis and A. S. L. Gomes. "800/1060 nm dual-wavelength pumped TDFA using single active pump source." *Electronics Letters*, 41(25), 11–12, 2005.

[140] R. K. Shori, "Multi-wavelength pump method for improving performance of erbium-based lasers." USPTO. Number 7,633,990, 2009.

[141] B. Aitken and B. Samson, "Broadhead dual wavelength pumped fiber amplifier." USPTO. Number 09/430446, 2002.

[142] T. Kasamatsu, "Laser oscillator and laser amplifier." USPTO. Number 09/527421, 2002.

[143] B. Cole and M. Dennis, "Amplification device utilizing thulium doped modified silicate optical fiber." USPTO. Number 11/151176, 2007.

[144] O. Henderson-Sapir, J. Munch and D. J. Ottaway. "Mid-infrared fiber lasers at and beyond 3.5 μm using dual-wavelength pumping." *Optics Letters*, 39(3), 493–496, 2014.

[145] M. Saad. "Heavy metal fluoride glass fibers and their applications." B. Pal (Editor), *Passive Components and Fiber-Based Devices VIII*, volume 8307 of *Proceedings of SPIE*, 83070N. Optical Society of America, 2011.

[146] R. Caspary. *Applied Rare-Earth Spectroscopy for Fiber Laser Optimization*. Ph.D. thesis, Technical University Braunschweig, Germany, 2001.

[147] X. Zou and T. Izumitani. "Spectroscopic properties and mechanisms of excited state absorption and energy transfer upconversion for Er^{3+}-doped glasses." *Journal of Non-Crystalline Solids*, 162(1-2), 68–80, 1993.

[148] R. S. Quimby, W. J. Miniscalco and B. A. Thompson. "Excited-state absorption at 980 nm in erbium-doped glass." J. F. D. Michel and S. Elias (Editors), *Fiber Laser Sources and Amplifiers III*, volume 1581, 72–79. SPIE, 1992.

[149] M. Poulain, M. Poulain and J. Lucas. "Verres fluores au tetrafluorure de zirconium proprietes optiques d'un verre dope au Nd^{3+}." *Materials Research Bulletin*, 10(4), 243 – 246, 1975.

[150] K. Ohsawa, T. Shibata, K. Nakamura and S. Yoshida. "Fluorozirconate glasses for infrared transmitting optical fibers." 7th *European Conference on Optical Communication (ECOC)*, 1.1–1—1.1–4. Technical University of Denmark, by Peter Peregrinus Ltd, Electromagnetics Inst, Stevenage, Engl, 1981.

[151] M. D. Shinn, W. A. Sibley, M. G. Drexhage and R. N. Brown. "Optical transitions of Er^{3+} ions in fluorozirconate glass." *Physical Review B*, 27(11), 6635–6648, 1983.

[152] F. Gan. "Optical properties of fluoride glasses: a review." *Journal of Non-Crystalline Solids*, 184(1), 9–20, 1995.

[153] Thorlabs. "Multimode fiber attenuation 0.22 NA glass-clad silica." 2014.

[154] Thorlabs. "Mid-infrared optical fiber and fiber patch cables." 2014.

[155] D. J. Richardson, J. Nilsson and W. A. Clarkson. "High power fiber lasers: Current status and future perspectives [Invited]." *Journal of the Optical Society of America B*, 27(11), B63–B92, 2010.

[156] M. Gorjan, M. M. Ek and M. Opi. "Pump absorption and temperature distribution in erbium-doped double-clad fluoride-glass fibers." *Optics Express*, 17(22), 19814–19822, 2009.

[157] M. Bernier, V. Fortin, N. Caron, M. El-Amraoui, Y. Messaddeq and R. Valle. "Mid-infrared chalcogenide glass Raman fiber laser." *Optics Letters*, 38(2), 127–129, 2013.

[158] Agilent. "Agilent Cary 4000/500/6000i Optics." 2011.

[159] L. Wetenkamp. *Charakterisierung von laseraktiv dotierten Schwermeallfluorid-Glasern und Faserlasern.* Ph.D. thesis, Technischen Universitat Carolo-Wilhelmina zu Braunschweig, 25.10.1991.

[160] B. R. Judd. "Optical absorption intensities of rare-earth ions." *Physical Review*, 127(3), 750–761, 1962.

[161] G. S. Opelt. "Intensities of crystal spectra of rare-earth ions." *The Journal of Chemical Physics*, 37(3), 511–520, 1962.

[162] M. J. Weber. "Probabilities for radiative and nonradiative decay of Er^{3+} in LaF_3." *Physical Review*, 157(2), 262–272, 1967.

[163] U. Skrzypczak, M. Miclea, A. Stalmashonak, B. Ahrens, B. Henke, G. Seifert, J. A. Johnson and S. Schweizer. "Time-resolved investigations of erbium ions in ZBLAN-based glasses and glass ceramics." *Physica Status Solidi (C) Current Topics in Solid State Physics*, 8(9), 2649–2652, 2011.

[164] H. Khn, S. T. Fredrich-Thornton, C. Krnkel, R. Peters and K. Petermann. "Model for the calculation of radiation trapping and description of the pinhole method." *Optics Letters*, 32(13), 1908–1910, 2007.

[165] K. Soga, M. Tsuda, S. Sakuragi, H. Inoue, S. Inoue and A. Makishima. "Effects of chloride introduction on the optical properties and the upconversion emission with 980- nm excitation of Er^{3+} in ZBLAN fluoride glasses." *Journal of Non-Crystalline Solids*, 222, 272–281, 1997.

[166] R. Reisfeld and C. K. Jorgensen. "Excited state phenomena in vitreous materials." *Handbook on the Physics and Chemistry of Rare Earths*, 9, 1–90, 1987.

[167] L. A. Riseberg and H. W. Moos. "Multiphonon orbit-lattice relaxation of excited states of rare-earth ions in crystals." *Physical Review*, 174, 429–438, 1968.

[168] Y. V. Orlovskii, T. T. Basiev, I. N. Vorob'ev, E. O. Orlovskaya, N. P. Barnes and S. B. Mirov. "Temperature dependencies of excited states lifetimes and relaxation rates of 3-5 phonon (4-6 μm) transitions in the YAG, LuAG and YLF crystals doped with trivalent holmium, thulium, and erbium." *Optical Materials*, 18(4), 355–365, 2002.

[169] V. K. Bogdanov, D. J. Booth and W. E. K. Gibbs. "Energy transfer processes and the green fluorescence in heavily doped Er^{3+}: fluoride glasses." *Journal of Non-Crystalline Solids*, 321(1-2), 20–28, 2003.

[170] L. Jianfeng and S. D. Jackson. "Numerical modeling and optimization of diode pumped heavily-erbium-doped fluoride fiber lasers." *Quantum Electronics, IEEE Journal of*, 48(4), 454–464, 2012.

[171] J. Li, L. Gomes and S. D. Jackson. "Numerical modeling of holmium-doped fluoride fiber lasers." *IEEE Journal of Quantum Electronics*, 48(5), 596–607, 2012.

[172] L. Jianfeng, L. Hongyu, L. Yong, Z. Lin and S. D. Jackson. "Modeling and optimization of cascaded erbium and holmium doped fluoride fiber lasers." *Selected Topics in Quantum Electronics, IEEE Journal of*, 20(5), 15–28, 2014.

[173] V. K. Bogdanov, D. J. Booth, W. E. K. Gibbs, J. S. Javorniczky, P. J. Newman and D. R. MacFarlane. "Population dynamics in Er^{3+}-doped fluoride glasses." *Physical Review B - Condensed Matter and Materials Physics*, 63(20), 2051071–20510715, 2001.

[174] S. D. Jackson, M. Pollnau and J. Li. "Diode pumped erbium cascade fiber lasers." *IEEE Journal of Quantum Electronics*, 47(4), 471–478, 2011.

[175] D. E. McCumber. "Einstein relations connecting broadband emission and absorption spectra." *Physical Review*, 136(4A), A954–A957, 1964.

[176] R. M. Martin and R. S. Quimby. "Experimental evidence of the validity of the McCumber theory relating emission and absorption for rare-earth glasses." *Journal of the Optical Society of America B: Optical Physics*, 23(9), 1770–1775, 2006.

[177] R. S. Quimby. "Range of validity of McCumber theory in relating absorption and emission cross sections." *Journal of Applied Physics*, 92(1), 180–187, 2002.

[178] M. Eichhorn. "Quasi-three-level solid-state lasers in the near and mid infrared based on trivalent rare earth ions." *Applied Physics B: Lasers and Optics*, 93(2-3), 269–316, 2008.

[179] W. J. Miniscalco and R. S. Quimby. "General procedure for the analysis of Er^{3+} cross sections." *Optics Letters*, 16(4), 258–260, 1991.

[180] H. Többen. *Neue Faserlaser fr das nahe und mittlere Infrarot*. Ph.D. thesis, Technical University Braunschweig, Germany, 1993.

[181] JDSU. "Pump Laser, 980, 720 mW (S30 Series)." 2014.

[182] R. I. Laming, S. B. Poole and E. J. Tarbox. "Pump excited state absorption in erbium-doped fibers." *Optics Letters*, 13(12), 1084–1086, 1988.

[183] S. S. Abbas and S. Popov. "Compact Er^{3+}-doped ZBLAN green upconversion fibre laser." *Proceedings of World Academy of Science, Engineering and Technology*, 78, 756–758, 2011.

[184] M. Pollnau, E. Heumann and G. Huber. "Time-resolved spectra of excited-state absorption in Er^{3+} doped YAlO₃." *Applied Physics A Solids and Surfaces*, 54(5), 404–410, 1992.

[185] D. Piatkowski and S. Mackowski. "Excited state absorption in glasses activated with rare earth ions: Experiment and modeling." *Optical Materials*, 34(12), 2055 – 2060, 2012.

[186] D. Piatkowski, K. Wisniewski, M. Rozanski and C. Koepke. "Excited state absorption spectroscopy of glass ZBLAN : Er^{3+} Experiment and simulation." *Physics Procedia*, 2(2), 365–372, 2009.

[187] D. F. de Sousa, V. Peters, G. Huber, A. Toncelli, D. Parisi and M. Tonelli. "Pump modulation frequency resolved excited state absorption spectra in Tm^{3+} doped YLF." *Applied Physics B: Lasers and Optics*, 77(8), 817–822, 2003.

[188] Y. D. Huang, M. Mortier and F. Auzel. "Stark level analysis for Er^{3+}-doped ZBLAN glass." *Optical Materials*, 17(4), 501–511, 2001.

[189] R. S. Quimby and B. Zheng. "New excited-state absorption measurement technique and application to Pr^{3+} doped fluorozirconate glass." *Applied Physics Letters*, 60(9), 1055–1057, 1992.

[190] NKT Photonics. "SuperK (tm) Compact." 2010.

[191] K. S. Wu, D. Ottaway, J. Munch, D. G. Lancaster, S. Bennetts and S. D. Jackson. "Gain-switched holmium-doped fibre laser." *Optics Express*, 17(23), 20872–20877, 2009.

[192] S. D. Jackson and T. King. "High-power diode-cladding-pumped Tm-doped silica fiber laser." *Optics Letters*, 23(18), 1462–1464, 1998.

[193] D. Y. Shen, J. I. Mackenzie, J. K. Sahu, W. A. Clarkson and S. D. Jackson. "High-power and ultra-efficient operation of a Tm^{3+}-doped silica fiber laser." *Advanced Solid-State Photonics*, Technical Digest, MC6. Optical Society of America, 2005.

[194] E. Slobodtchikov, P. F. Moulton and G. Frith. "Efficient, high-power, Tm-doped silica fiber laser." *Advanced Solid-State Photonics*, OSA Technical Digest Series (CD), MF2. Optical Society of America, 2007.

[195] W. Hofle and H. Többen. "Analysis, measurement and optimization of threshold power of 3.5 μM ZBLAN-glass fiber lasers." *International Journal of Infrared and Millimeter Waves*, 14(7), 1407–1424, 1993.

[196] S. D. Jackson. "Continuous wave 2.9 μm dysprosium-doped fluoride fiber laser." *Applied Physics Letters*, 83(7), 1316–1318, 2003.

[197] M. B. Walter Koechner. *Solid-State Lasers, A Graduate Text.* Springer New York, 2003.

[198] D. Findlay and R. A. Clay. "The measurement of internal losses in 4-level lasers." *Physics Letters*, 20(3), 277–278, 1966.

[199] N. Iwanus, D. D. Hudson, T. Hu and S. D. Jackson. "Aim at the bottom: Directly exciting the lower level of a laser transition for additional functionality." *Optics Letters*, 39(5), 1153–1156, 2014.

[200] FiberLabs Inc. "Fiber technology." `http://www.fiberlabs-inc.com/fiber_technology.htm`, 2013.

[201] W. Rigrod. "Homogeneously broadened CW lasers with uniform distributed loss." *IEEE Journal of Quantum Electronics*, 14(5), 377–381, 1978.

[202] L. Bigot, S. Choblet, A.-M. Jurdyc, B. Jacquier and J.-L. Adam. "Transient spectral hole burning in erbium-doped fluoride glasses." *Journal of the Optical Society of America B*, 21(2), 307–312, 2004.

[203] S. Jarabo, I. J. Sola and J. Sáez-Landete. "Spectral hole burning induced by reflected amplified spontaneous emission in erbium-doped silica optical fiber pumped at 980 *nm*." *Journal of the Optical Society of America B*, 20(6), 1204–1211, 2003.

[204] S. Guy, L. Bigot, I. Vasilief, B. Jacquier, B. Boulard and Y. Gao. "Two crystallographic sites in erbium-doped fluoride glass by frequency-resolved and site-selective spectroscopies." *Journal of Non-Crystalline Solids*, 336(3), 165–172, 2004.

[205] M. Gorjan, M. Marinc ek and M. Copic. "Spectral dynamics of pulsed diode-pumped erbium-doped fluoride fiber lasers." *Journal of the Optical Society of America B*, 27(12), 2784–2793, 2010.

[206] M. A. Couto dos Santos, E. Antic-Fidancev, J. Y. Gesland, J. C. Krupa, M. Lemaitre-Blaise and P. Porcher. "Absorption and fluorescence of Er^{3+}-doped $LiYF_4$: Measurements and simulation." *Journal of Alloys and Compounds*, 275277(0), 435–441, 1998.

[207] M. Mürtz and P. Hering. *Online Monitoring of Exhaled Breath Using Mid-Infrared Laser Spectroscopy*. M. Ebrahim-Zadeh and I. Sorokina (Editors), *Mid-Infrared Coherent Sources and Applications*, Springer Netherlands, 535–555, 2008.

[208] H. Kogelnik and T. Li. "Laser beams and resonators." *Applied Optics*, 5(10), 1550–1567, 1966.

[209] K. S. Wu. *Short Pulse Gain-Switched Mid-Infrared Fibre & Solid-State Lasers*. Honours thesis, University of Adelaide, 2008.

[210] Y. Fan, B. He, J. Zhou, J. Zheng, S. Dai, C. Zhao, Y. Wei and Q. Lou. "Efficient heat transfer in high-power fiber lasers." *Chinese Optics Letters*, 10(11), 111401–111401, 2012.

[211] D. C. Brown and H. J. Hoffman. "Thermal, stress, and thermo-optic effects in high average power double-clad silica fiber lasers." *Quantum Electronics, IEEE Journal of*, 37(2), 207–217, 2001.

[212] M.-A. Lapointe, S. Chatigny, M. Pich, M. Cain-Skaff and J.-N. Maran. "Thermal effects in high-power CW fiber lasers." *Photonics West*, volume 7195, 71951U–71951U–11. 2009.

[213] Y. Fan, B. He, J. Zhou, J. Zheng, H. Liu, Y. Wei, J. Dong and Q. Lou. "Thermal effects in kilowatt all-fiber MOPA." *Optics Express*, 19(16), 15162–15172, 2011.

[214] J. Li, K. Duan, Y. Wang, X. Cao, W. Zhao, Y. Guo and X. Lin. "Theoretical analysis of the heat dissipation mechanism in Yb^{3+}-doped double-clad fiber lasers." *Journal of Modern Optics*, 55(3), 459–471, 2008.

[215] M. Pollnau, T. Graf, J. E. Balmer, W. Lüthy and H. P. Weber. "Explanation of the cw operation of the Er^{3+} 3-μm crystal laser." *Physical Review A*, 49(5), 3990–3996, 1994.

[216] M. Pollnau. "Analysis of heat generation and thermal lensing in erbium 3-μm lasers." *IEEE Journal of Quantum Electronics*, 39(2), 350–357, 2003.

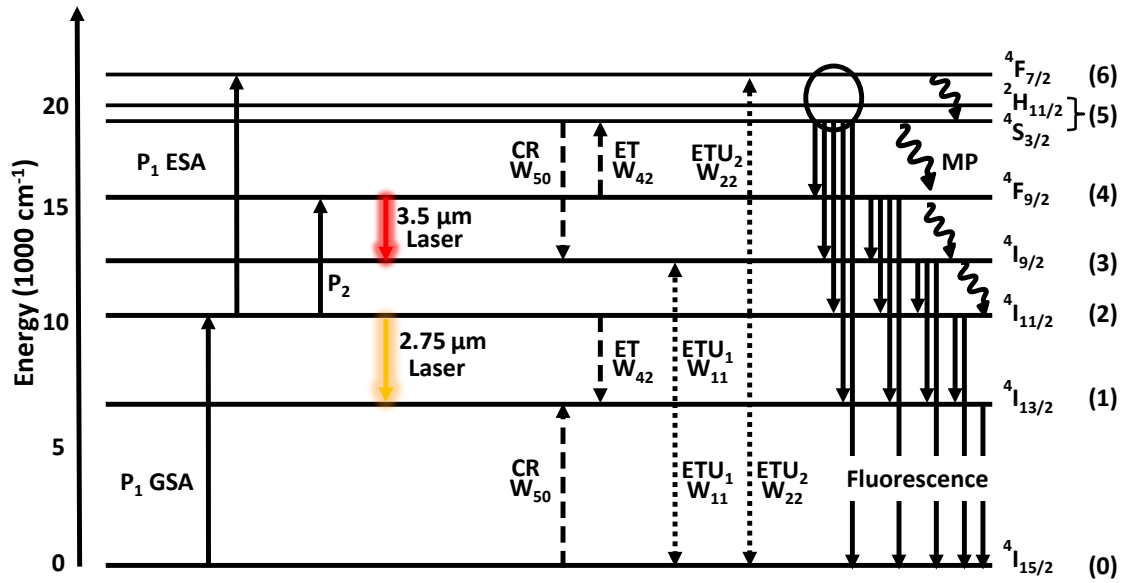[217] A. Siegman. *Lasers.* University Science Books, 1986.

Index

Figure FO.1: Energy levels and spectroscopic processes in Er^{+3}:ZBLAN. $P_{1,2}$ - pump absorption; CR, ET and $ETU_{1,2}$ - cross-relaxation, energy-transfer and energy-transfer-upconversion processes, the indices of W_{ij} indicate the initial levels involved in the process; MP - multi-phonon relaxation. The numbers in brackets to the right represent the number of the rate equation associated with this energy level. Note that $^4S_{3/2}$ and $^2H_{11/2}$ are thermally coupled and share the same rate equation.